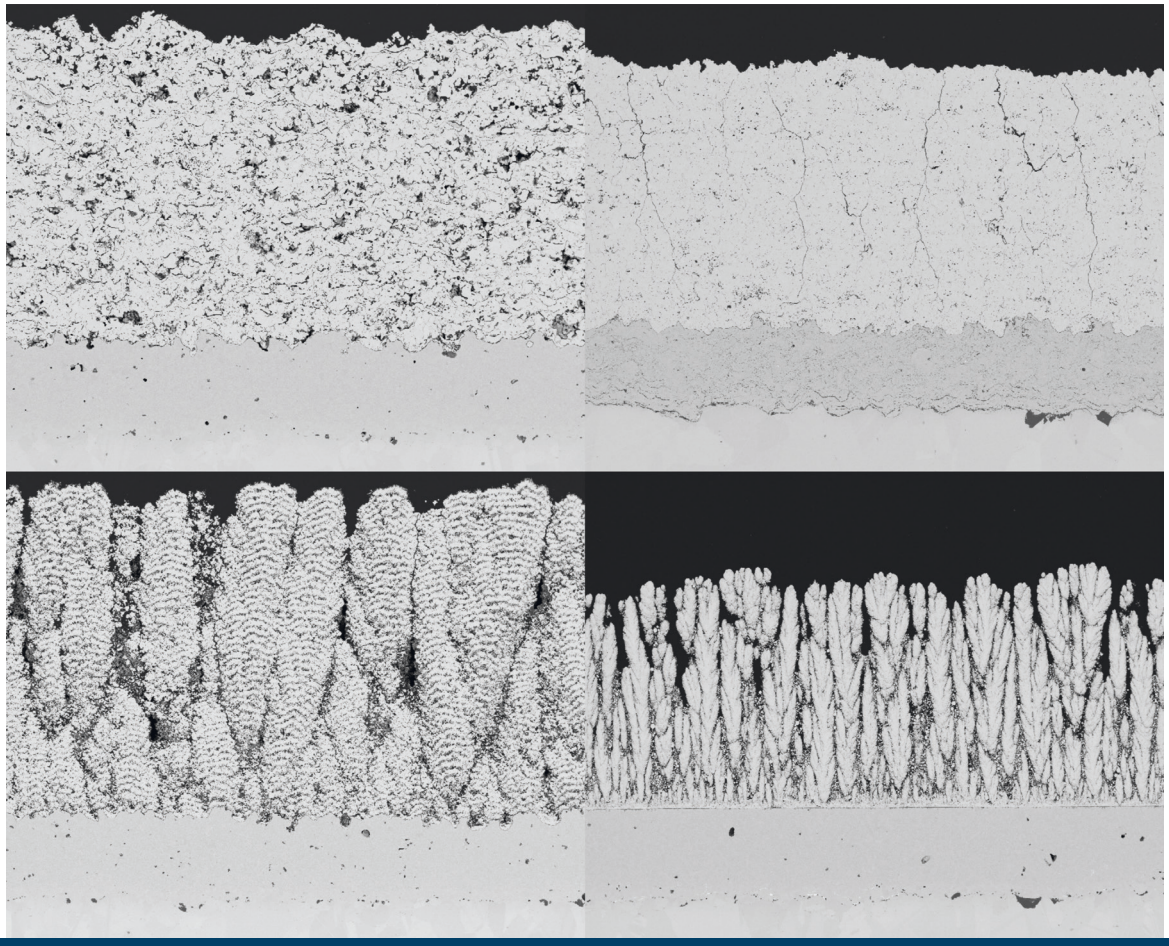

Innovative Plasma Sprayed Thermal Barrier Coatings for Enhanced Flexibility in Gas Turbine Operation

Jens Igel

Energie & Umwelt / Energy & Environment
Band / Volume 665
ISBN 978-3-95806-827-8

Mitglied der Helmholtz-Gemeinschaft

JÜLICH
Forschungszentrum

Schriften des Forschungszentrums Jülich
Reihe Energie & Umwelt / Energy & Environment Band / Volume 665

Forschungszentrum Jülich GmbH
Institute of Energy Materials and Devices (IMD)
Werkstoffsynthese und Herstellungsverfahren (IMD-2)

Innovative Plasma Sprayed Thermal Barrier Coatings for Enhanced Flexibility in Gas Turbine Operation

Jens Igel

Schriften des Forschungszentrums Jülich
Reihe Energie & Umwelt / Energy & Environment Band / Volume 665

ISSN 1866-1793 ISBN 978-3-95806-827-8

Bibliografische Information der Deutschen Nationalbibliothek.
Die Deutsche Nationalbibliothek verzeichnet diese Publikation in der
Deutschen Nationalbibliografie; detaillierte Bibliografische Daten
sind im Internet über http://dnb.d-nb.de abrufbar.

Herausgeber und Vertrieb:	Forschungszentrum Jülich GmbH Zentralbibliothek, Verlag 52425 Jülich Tel.: +49 2461 61-5368 Fax: +49 2461 61-6103 zb-publikation@fz-juelich.de www.fz-juelich.de/zb
Umschlaggestaltung:	Grafische Medien, Forschungszentrum Jülich GmbH
Druck:	Grafische Medien, Forschungszentrum Jülich GmbH
Copyright:	Forschungszentrum Jülich 2025

Schriften des Forschungszentrums Jülich
Reihe Energie & Umwelt / Energy & Environment, Band / Volume 665

D 294 (Diss. Bochum, Univ., 2025)

ISSN 1866-1793
ISBN 978-3-95806-827-8

Vollständig frei verfügbar über das Publikationsportal des Forschungszentrums Jülich (JuSER)
unter www.fz-juelich.de/zb/openaccess.

Abstract

Thermal barrier coatings (TBCs) in power plant turbines are primarily designed for high thermal insulation properties. As a result, they enable a high combustion temperature in the turbine, making the power generation process very efficient. In the future, however, the operational flexibility of modern power plant turbines will become increasingly important to maintain grid stability. Frequent fluctuations in the amount of electricity fed into the grid due to the high volatility of renewable energy sources, as well as changing loads, require constant adjustment of power generation. In the future, this will be made possible by gas turbines that must be started up and shut down quickly and flexibly. The challenges for the coating system arise from the different properties of the materials applied. The different expansion of layers and substrates during temperature changes introduces stresses into the coating system when the turbine is started up or shut down. In addition, the high operating temperatures lead to detrimental phase transformations and sintering of the ceramic top layer, reducing the strain tolerance and thus the flexible application of the coatings.

The objective of this study was therefore to develop an optimized TBC system capable of withstanding rapid mechanical load and temperature changes. The development focused on the optimization of the bond coat as well as the top layer of the TBC system. For the bond coat optimization, aspects such as surface roughness, thermal expansion coefficients and the effect of pre-oxidation of the bond coat on the performance of the coatings during thermal cycling were investigated. In contrast, the effect of different microstructures produced by different plasma spraying processes on the thermal cycling performance of the ceramic topcoats was investigated.

In addition, innovative analysis methods were used for the various plasma-sprayed thermal barrier coatings to investigate coating properties and failure mechanisms in detail. These methods include digital image correlation, which enables to analyze strain changes on the sample surface during thermal cycling. In this way, the forced elongation of the ceramic top layer by the substrate material could be shown, as well as local changes in elongation over the cycles, which finally might result in coating failure. A further method is the laser shock adhesion test. This allows to determine the interfacial bonding of coatings and to introduce specific defects into coating systems. The growth of these defects can be observed during thermal cycling, providing important insights for investigating the failure mechanisms in thermal barrier coating systems.

Overall, the optimizations more than doubled the service life of the thermal barrier coatings compared to a reference coating system as used in today's turbines. In addition, insights were gained into the failure mechanisms that occur with differently structured topcoatings. At the end of the work, further opportunities for improvement were identified that can be investigated in the future.

Kurzzusammenfassung

Wärmedämmschichtsysteme (WDS-Systeme) in Kraftwerksturbinen sind vor allem auf eine hohe thermische Isolationsleistung ausgelegt. Dadurch ermöglichen sie eine hohe Verbrennungstemperatur in der Turbine, was den Prozess der Stromerzeugung sehr effizient macht. In Zukunft rückt jedoch die operative Flexibilität von modernen Kraftwerksturbinen immer mehr in den Fokus, um der Aufrechterhaltung der Netzstabilität gerecht zu werden. Häufig schwankende Stromeinspeisungen in das Netz, durch die hohe Volatilität der Erneuerbaren Energien, sowie sich veränderbare Lasten erfordern eine ständige Anpassung der Stromerzeugung. Dies soll in Zukunft über Gasturbinen ermöglicht werden, wodurch diese schnell und flexibel an und abgefahren werden müssen. Die Herausforderungen für das Schichtsystem ergeben sich dabei aus den unterschiedlichen Materialeigenschaften der verwendeten Materialien. Durch sich unterschiedlich stark ausdehnende Schichten und Substrate bei Temperaturwechseln werden beim An- und Abfahren der Turbine Spannungen in das Schichtsystem eingebracht. Zudem kommt es bei den hohen Arbeitstemperaturen zu nachteiligen Phasenumwandlungen und zum Sintern der keramischen Deckschicht, was die Dehnungstoleranz und somit die flexible Einsetzbarkeit der Schichten reduziert.
Ziel dieser Studie war es daher, ein optimiertes WDS-System zu entwickeln, das in der Lage ist, schnellen Last- und Temperaturänderungen standzuhalten. Die Entwicklung konzentrierte sich dabei sowohl auf die Optimierung der Haftschicht als auch der Deckschicht des TBC-Systems. Bei der Bond Coat Optimierung wurden Aspekte wie die Oberflächenrauheit, die Wärmeausdehnungskoeffizienten und die Auswirkungen einer Voroxidation des Bond Coats auf die Leistungsfähigkeit der Beschichtungen beim thermischen Zyklieren untersucht. Bei den keramischen Deckschichten hingegen wurde der Effekt von verschiedenen Mikrostrukturen, hergestellt über verschiedene Plasmaspritzverfahren, auf die thermische Zyklierbarkeit untersucht.
Darüber hinaus wurden für die verschiedenen plasmagespritzen Wärmedämmschichten innovative Analyseverfahren eingesetzt, um Schichteigenschaften sowie Versagensmechanismen detailliert untersuchen zu können. Zu diesen Verfahren gehört die digitale Bildkorrelation, welche es ermöglicht, Dehnungsänderungen an der Probenoberfläche während der thermischen Zyklierung zu analysieren. Darüber hinaus konnte die Zwangsdehnung der keramischen Deckschicht durch das Substratmaterial gezeigt werden, sowie sich über die Zyklen verändernde lokale Dehnungsänderungen, die schließlich in einem Schichtversagen resultieren können. Ein weiteres dieser Verfahren ist der Laser Schock Adhäsionstest. Über diesen kann zum einen die Grenzflächenanbindung von Beschichtungen am Interface bestimmt werden und es können gezielt Defekte in Schichtsysteme eingebracht werden. Das Wachstum dieser Defekte kann während der thermischen Zyklierung beobachtet werden und liefert wichtige Erkenntnisse bei der Erforschung der Versagensmechanismen in Wärmedämmschichtsystemen.
Insgesamt konnte die Lebensdauer der Wärmedämmschichten durch die Optimierungen, im Vergleich zu einem Referenzschichtsystem wie es in heutigen Turbinen eingesetzt wird, mehr als verdoppelt werden. Zudem konnten Erkenntnisse zu den auftretenden Versagensmechanismen in verschieden strukturierten Deckschichten gewonnen werden. Darüber

hinaus wurden am Ende der Arbeit noch weitere Verbesserungsmöglichkeiten dargelegt, die in Zukunft untersucht werden können.

Contents

Abbreviations and Symbols

Abbreviation/ Symbol	Meaning
AC	Alternating Current
APS	Atmospheric Plasma Spraying
BBD	Box-Behnken Design
BC	Bond Coat
CCGT	Combined Cycle Gas Turbine
CMAS	Calcium-Magnesium-Alumina-Silicate
CMOS	Complementary Metal-Oxide-Semiconductor camera
CTE	Coefficient of Thermal Expansion
DC	Direct Current
DE	Deposition Efficiency
DIC	Digital Image Correlation
DoE	Design of Experiments
DVC	Dense Vertically Cracked
EB-PVD	Electron Beam-Physical Vapor Deposition
EDX	Energy-Dispersive X-ray spectroscopy
fcc	face-centered cubic
FOD	Foreign Object Damage
FZJ	Forschungszentrum Jülich GmbH
GZO	Gadolinium Zirconate
HOSP	Hollow Oxide Spherical Powder
HVAF	High Velocity Air Fuel spraying
HVOF	High Velocity Oxygen Fuel spraying
IR	Infrared camera
LASAT	Laser Shock Adhesion Test

LED	Light-Emitting Diode
mol%	Mole Fraction in percent
NACA	National Advisory Committee for Aeronautics
NASA	National Aeronautics and Space Administration
PSD	Particle Size Distribution
PS-PVD	Plasma Spray-Physical Vapor Deposition
ROI	Region of Intrest
SEM	Scanning Electron Microscopy
SPS	Suspension Plasma Spraying
TBC	Thermal Barrier Coating
TCP	Topologically Closed Packed
TGO	Thermally Grown Oxide
TIT	Turbine Inlet Temperature
VPS	Vacuum Plasma Spraying
wt.%	Weight Percent
XRD	X-Ray Diffraction
YSZ	Yttrium Stabilized Zirconia
β	Al rich NiAl-Phase in Bond coat layer
γ	Ni matrix in Nickel-based Superalloys
γ'	Precipitation phase (Ni_3Al) in Nickel-base Superalloys
κ	Isentropic Exponent

1 Motivation and Scientific Objectives

In the 21st century, the transition of the global energy supply to renewable energies is considered a major challenge. Europe is a good example of an environmentally oriented energy policy, in which the amount of renewable energy in electricity generation is to be increased to 50 % by 2030 and 65 % by 2050 [1]. Germany has been involved in this concept since the energy transition initiated in 2000, which aims to restructure the electricity sector from fossil fuel and nuclear power plants to renewable energies. The Renewable Energy Act (Erneuerbare-Energien-Gesetz), which was introduced as part of the energy transition, regulates the preferential feed-in of renewable energy into the electricity grid. By 2023, nearly 52 % of Germany's electricity demand was covered by renewables [2]. The German government's goal is to cover at least 80 % of gross electricity demand with renewable energy by 2030. Greenhouse gas-neutral electricity generation is then supposed to be achieved by 2045 [3]. However, this transition is complicated by the intention to cover a significant portion of the electricity supply with wind and solar power plants, which are highly volatile. The decision to shut down all nuclear power plants by 2022 and the federal government's roadmap to phase out coal-fired power generation by 2038 further eliminates the power plants needed to secure the baseline energy supply. Achieving the 80 % target will, therefore, require a massive overbuilding of renewable energy generators and reversible storage of the energy generated. Long-term energy storage, however, is currently only feasible with high losses, making it impossible to avoid conventional power plants. Moreover, the variability of renewable energy sources and fluctuations in demand create challenges for maintaining grid stability. Flexible power plants capable of adjusting output rapidly are essential to meet these demands [4], [5], [6].

Combined cycle gas turbines (CCGTs) are particularly suitable for this type of operationally flexible power plants. This is reflected in the German government's decision to build gas-fired power plants with a capacity of about 10 GW over the next few years [7]. These have good operational flexibility and low maintenance requirements. In addition, investment costs are low, and the plants are highly efficient [8]. Modern CCGT power plants achieve high fuel utilization with efficiencies exceeding 60 %. Moreover, there is already operational flexibility concerning the fuel. New gas turbines installed in the future must be H_2-ready, enabling conversion for hydrogen operation. In addition, there are turbine manufacturers who are already distributing hydrogen-capable turbines.

A major challenge for gas turbines is to operate flexibly to compensate for power supply and demand fluctuations. Rapid start-up and shut-down of the turbine, or rapid changes in power output, cause rapid changes of the temperature and mechanical loads in the components. This is particularly stressful for components in the hot section of the turbine. Their service life depends to a large extent on the thermal barrier coatings applied to protect them. A thermal barrier coating (TBC) system typically consists of a ceramic thermal insulation layer applied to a metallic bond coat. While the ceramic layer provides thermal insulation, the bond coat protects the component from corrosion and oxidation while providing a good adhesion base for the ceramic topcoat. However, the combination of ceramic and metallic layers in this system results in high stresses during temperature

changes due to their different thermal expansions, leading to failure of the ceramic layer. Today's TBC systems are typically optimized for steady-state and maximum operating temperatures to achieve high turbine efficiency. However, transient conditions, particularly the cooling and heating phases, significantly impact the coating systems' degradation. Therefore, it is essential for the development of operationally flexible gas-fired power plants to gain a solid scientific understanding of the damage mechanisms during rapid load changes and thus to develop optimized coating systems for operationally flexible turbines.

The main objective of this thesis was to develop a thermal barrier coating system with a service life twice as long as a standard coating system used in power plant turbines under rapid load and temperature changes. To achieve this goal, both the bond coat and the top coat were optimized. The layers of the thermal barrier coating system were all produced using the thermal spray process. Various manufacturing processes were employed to produce different coating microstructures to investigate their effect on cyclability. These processes included atmospheric plasma spraying (APS), suspension plasma spraying (SPS), and plasma spray-physical vapor deposition (PS-PVD). While the SPS and PS-PVD processes were applied to produce columnar coating microstructures, the APS process was used to produce both highly porous and dense vertically cracked (DVC) coatings. The highly porous APS coatings primarily provide excellent thermal insulation, while the segmented DVC coatings and columnar SPS and PS-PVD coatings focus on high strain tolerance.
The optimization of the bond coats involved modifying its surface roughness to explore the impact on top coat adhesion and its ability to prevent crack propagation at the interface, and thus enhancing service life in thermal cycling tests. Additionally, a bond coat material with a different thermal expansion coefficient was studied to examine the influence of expansion mismatch between the bond and top coat on the failure mechanism and the lifetime of the coating system in cycling tests. Furthermore, the effect of pre-oxidation of the bond coat before the application of the ceramic top coat on the thermal cycling lifetime of the coating systems was investigated. Pre-oxidizing offers the advantage that the stresses induced by the initial rapid growth of the oxide layer do not affect the ceramic top layer.
The optimization of the individual surface layers was based on process optimizations that were performed with respect to coating properties important for thermal cycling and turbine use. These properties include coating porosity, microstructural features such as crack/column densities, hardness, elastic moduli, and erosion resistance. Subsequently, the optimized coating systems were subjected to rapid thermal cycling in burner rig tests to determine their lifetime to coating failure. The service life provides a measure of the cycling resistance of the investigated coating system. In addition, metallographic cross-sections of the specimens provided information on the failure mechanisms.
Besides determining lifetimes and identifying failure mechanisms in coating systems with different microstructures and bond layers, high-resolution images of the sample surfaces were taken during thermal cycling. Image correlation was used to determine the strains on the sample surface during a thermal cycle, which in turn was used to determine the stress states within the coatings. Moreover, correlating images across the entire lifetime of the sample was used to detect changes in strain on the coating surface to identify correlations between strain observations and coating failure.

The transferability of the LAser Shock Adhesion Test (LASAT) to determine the interfacial toughness of plasma sprayed coatings was also investigated. This method is well suited to measure this value for Electron Beam Physical Vapor Deposition (EB-PVD) coatings. It is also possible to introduce specific defects with this method into the interface of EB-PVD coatings and observe the defect growth during thermal cycling. This provides insight into the failure mechanisms of thermal barrier coating systems. Therefore, the aim was to transfer this approach from EB-PVD coatings to plasma sprayed coatings.

The following research questions and technical development goals for analytical methods investigating the TBCs can be concluded from these approaches:

(i) How do bond coats with different roughness profiles and thermal expansion coefficients affect the durability of the TBC system under rapid temperature changes?

(ii) What is the influence of pre-oxidation of the bond coat combined with different top coats on the thermal cycling performance?

(iii) How do different coating microstructures influence the thermal cycling performance of thermal barrier coating systems?

(iv) Is it possible to record strains on the sample surface during thermal cycling and correlate these to stresses in the coating system?

(v) Can image correlation be used to predict coating system failure?

(vi) Is the LASAT approach transferable from EB-PVD systems to plasma sprayed coating systems, and can the interface toughness of different plasma sprayed coatings be determined?

(vii) Is it possible to introduce targeted defects into plasma sprayed coatings using the LASAT method and to analyze their growth during thermal cycling?

This work is part of the LaBeGa (Lastflexible Beschichtungssysteme für Gasturbinen) project, which was funded by the Federal Ministry of Economic Affairs and Climate Action (BMWK = Bundesministerium für Wirtschaft und Klimaschutz), Germany, within the framework of the 7th Energy Research Program (FKZ 03EE5045A). Furthermore, the author of this thesis and the research presented in this were additionally funded by two grants. Funding was provided by the MatKat-Foundation under registration number ArL LG.06-11741/526, as well as through the Procope-Mobilité scholarship, sponsored by DAAD and the French Ministries MESR/MEAE, under program number 0185-DEU-23-0008 LG1.

2 State of the Art

2.1 Gas Turbines

Gas turbines are turbomachines wherein a fluid flowing through the machine transfers work to its components. This process involves converting potential or thermal energy into kinetic energy [9]. The power units typically consist of a compressor, combustion chamber and turbine, as illustrated in Figure 2.1 (a). The compressor and turbine can be further divided into low-pressure and high-pressure segments. In aircraft engines, a fan takes in additional air, redirecting part of it around the turbine ("turbofan bypass"). This bypass promotes the main thrust, contributing to increased turbine efficiency [10]. Gas turbines have become indispensable in both stationary power generation and non-stationary aviation applications due to their efficiency, reliability, and suitability for a wide range of applications. Their common use has led to continuous research and development efforts over the decades [11], [12], [13], [14].
Ongoing turbine development predominantly focuses on maximizing efficiency, positively impacting economic and ecological aspects [15]. Improvements in aerodynamics, cooling technology and materials contribute to higher turbine efficiency. Innovative blade designs optimize airflow, reducing frictional losses on blades, while additive manufacturing enables complex designs for improved component cooling [16]. Advanced cooling techniques and materials allow higher turbine inlet temperatures, improving overall turbine efficiency [15], [17], [18], [19]. This relationship can be seen in the ideal thermodynamic cycle, known as the Joule or Brayton process, shown in Figure 2.1 (b). However, it should be noted that the ideal Joule process serves as a theoretical benchmark for assessing gas turbine performance. In real gas turbines, losses occur due to friction, heat dissipation and non-ideal behavior of the process medium [20].

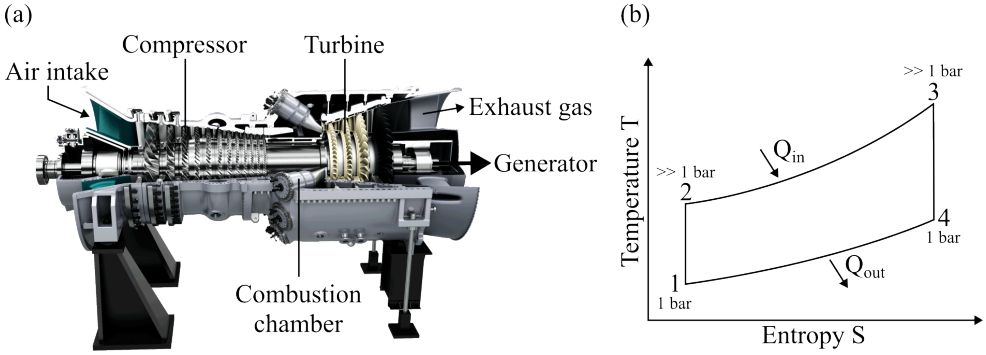

Fig. 2.1 Schematic illustration of the Heavy-duty Gas Turbine SGT5-900HL (50Hz) from Siemens Energy in (a); Ideal Joule (or Brayton) process in a gas turbine in (b) according to [21]

Initially, air is taken into the turbine inlet and is isentropically compressed (constant entropy) within the compressor from state 1 to 2. In the ideal cycle process, this compression is assumed to be adiabatic, which means there is no heat exchange with the environment. Consequently, both the pressure and temperature of the process medium increase. The compressed air is then mixed with fuel in the combustion chamber and ignited, resulting in isobaric (constant pressure) heating from state 2 to 3 (Q_{in}). The temperature and volume of the gas increase. Following this, the gas undergoes an adiabatic expansion through the turbine, driving it by releasing work. This isentropic change of state from 3 to 4 is characterized by a drop in the pressure and temperature of the gas. The work performed on the turbine covers the energy requirement of the compressor and can be used for other purposes, such as electricity generation (Generator). Finally, an isobaric heat release occurs from state 4 to 1 (Q_{out}). [22], [23].
The thermal efficiency of the turbine can be described according to Formula (2.1) [23]. It depends on the pressure ratio after combustion (p_3) to the pressure after expansion (p_4), or the ratio before and after compression. This thermal efficiency, in turn, is linked to the combustion temperature via the ideal gas law. κ is the isentropic exponent, which is approximately 1.4 for air [20].

$$\eta = 1 - \frac{T_1}{T_2} = 1 - \left(\frac{p_4}{p_3}\right)^{\frac{\kappa-1}{\kappa}} \tag{2.1}$$

According to the formula, the maximum combustion temperature has no influence on the turbine's thermal efficiency in the ideal Joule process. The efficiency of the turbine increases with higher temperature changes after compression of the gas (T_2), as the ambient's air temperature (T_1) is usually predefined. However, there are also developments in turbine intake air cooling, in which the air drawn in is cooled with exhaust heat recovery chillers [24], [25]. The increase in T_2 can be achieved by increasing the compression of the gas. However, this also increases the combustion temperature (T_3). In the actual Joule process, this increase in T_3 influences the energy recovered from the process and is therefore of great importance. Figure 2.2 illustrates that the overall thermal efficiency increases with the compression ratio at a higher turbine inlet temperature (TIT). A simulation study conducted by *Ibrahim et al.* demonstrates that the overall efficiency increases with a higher compression ratio and a higher peak temperature ratio within the thermodynamic cycle [26].
When aiming to maximize the TIT, the components directly behind the combustion chamber, specifically the first turbine stage, are particularly exposed to the high temperatures. The limiting factor in this context is the high-temperature stability of the materials used. Especially the blades of the first turbine stage are subject to mechanical, thermal and high-temperature corrosive stresses and are therefore heavily affected [10]. Figure 2.3 shows how various developments have increased the maximum achievable working temperature in turbines. On the one hand, continuous enhancements have been made to the base material from which turbine components are manufactured. The nickel-based superalloys used today are often produced as directionally solidified or singlecrystalline superalloys, as these in particular offer an extended creep life [10]. Another protective mechanism for improving the service life of turbines is the combination of a thermal barrier coating system and component cooling, both of which have been continuously improved over time.

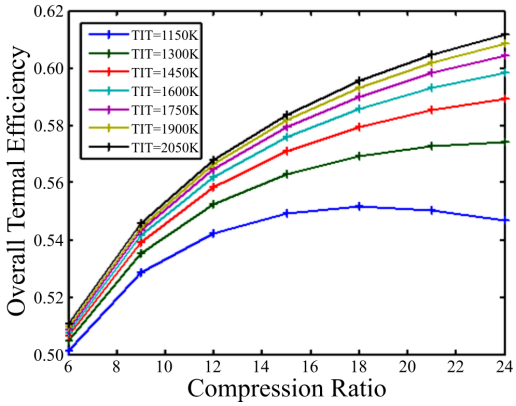

Fig. 2.2 Effect of variation in compression ratio and turbine inlet temperature (TIT) according to [26]

In combination, these allow the turbine inlet temperature to exceed the melting point of the base material improving the turbine efficiency and durability [17]. This protection mechanism is explained in the following section 2.2 before each individual layer of the thermal barrier coating system is described.

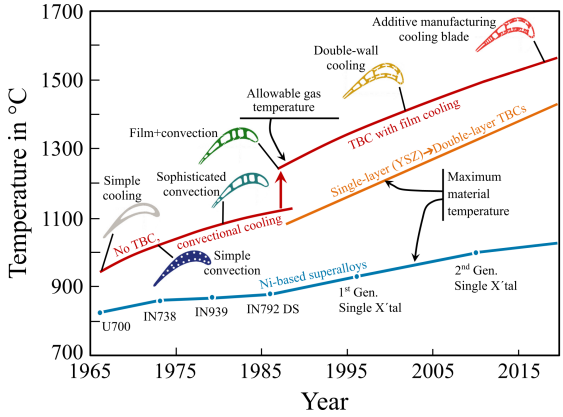

Fig. 2.3 Historical development of base material, cooling technology and coating materials of turbine blades with regard to their maximum working temperatures. Adapted from [19], [27] and, [28]

2.2 Thermal Barrier Coatings

Thermal barrier coating (TBC) systems are primarily applied in stationary gas turbines and aircraft turbines, where these highly resistant coatings fulfill various tasks in the hot sections of the turbines. These tasks include increasing efficiency, extending service life and simplifying the design of the turbine [18]. The hot sections of the turbine include

the combustion chamber, stationary guide vanes, rotating blades, blade outer seals and housings in the high-pressure zone behind the combustion chamber [19]. In all these components, thermal barrier coatings must fulfill important functional requirements in order to protect the components at high temperatures and under dynamic operating conditions [17].

Research on thermal barrier coatings dates back to the late 1940s and early 1950s, when the first ceramic protective coatings were applied to turbine blades at the NACA (National Advisory Committee for Aeronautics), the predecessor of NASA (National Aeronautics and Space Administration) [29], [30], [31]. In the late 1970s, the first two-layer thermal barrier coatings for turbine blades were developed, which had a long service life even at temperatures above 1100 °C [32]. Today's TBCs are still designed according to this concept, shown schematically in Figure 2.4. First, the so-called bond coat, is applied to the substrate - the actual component. The bond coat is highly resistant to oxidation and allows a good adhesion of the second coating. This second coating, the top coat, is a ceramic layer that provides thermal insulation due to its low thermal conductivity. Due to bond coat oxidation during operation, a thermally grown oxide (TGO) layer is formed between the bond coat and the top coat. Consequently, the entire system consists of three layers added to the substrate material [19], [17]. In combination with internal cooling of the components, a thermal gradient is created in the component. This enables the turbine to operate at a TIT above the melting point of the substrate material. Without an increase in substrate temperature, the thermal gradient causes an increase in TIT compared to a system without TBC and thus an increase in efficiency (Figure 2.5 (c)). Alternatively it is possible to reduce the substrate temperature using a TBC while keeping the process gas temperature constant (Figure 2.5 (b)) and therefore increase the durability of the turbine blade [33], [34].

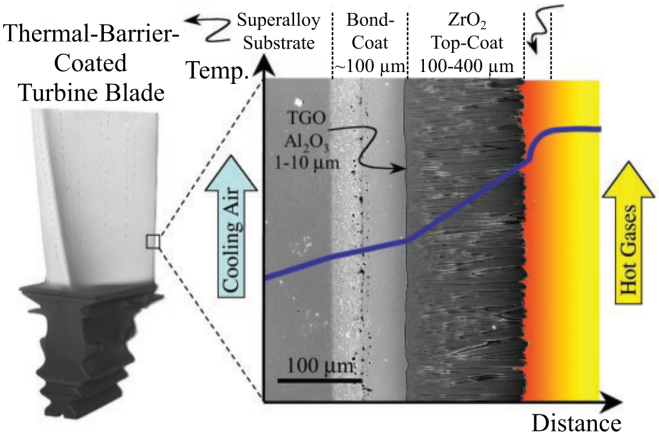

Fig. 2.4 Cross-sectional image of an EB-PVD TBC, superimposed onto a schematic diagram showing the temperature reduction provided by the TBC. The turbine blade contains internal hollow channels for air-cooling [17]

In modern turbine blades, in addition to the conventional internal cooling of the material, an additional airflow is directed to the surface of the turbine blade through cooling holes. This airflow is directed to create a cooling film on the material, reducing the direct contact between the hot gas flow and the blade surface [23]. In current applications, this boundary layer allows to reach surface temperatures on the TBC of up to 1400 °C [35] and turbine inlet temperatures (process gas temperatures) of up to 1600 °C [36]. However, the air used for cooling is taken from the last compressor stages, which means that it is lost in the thermodynamic cycle In addition, the interaction between the cooling flow and the main process gas flow leads to a significant interference, reducing the turbine's overall efficiency [20].

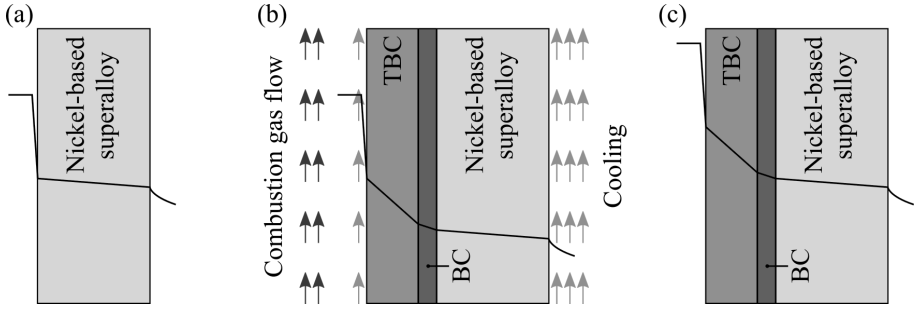

Fig. 2.5 Effect of TBCs considering the heat transfer through a flat wall. (a) without thermal barrier coating, (b) constant hot gas temperature leads to reduced substrate temperature, (c) constant substrate temperature at increased hot gas temperature [33], [34]

TBCs are one of the most important and effective advancements in improving the efficiency of modern turbines, as they do not compromise the overall efficiency of the turbine. All layers of the TBC system must retain their functionality even under the highly demanding conditions in a turbine. This is made even more difficult by the complex interaction of metallic and ceramic materials, which differ considerably in their physical, thermal and mechanical properties. At high temperatures, various thermally activated processes take place simultaneously in the layers of the thermal barrier coating system. These processes include phase transformations, diffusion, oxidation, corrosion, thermal expansion, creep, fatigue and sintering phenomena, which all interact with each other. These interactions between the oxide, the ceramic top layer and the underlying alloys make it necessary to consider all layers and the substrate as a single system. This overall view takes into account that the properties of the TBC system change with time and operating cycles [17]. The different material properties of the layers and substrate are particularly challenging and lead to high stresses during operation, which are further intensified by the changes of the system during operation. As the system heats up, the different expansion coefficients of the materials generate tensile stresses in the ceramic. These stresses relax at high operating temperatures, resulting in compressive stresses in the ceramic after the system cooled down. After a certain period of time, these alternating stresses usually lead to failure of the protective coating system. The specific failure mechanisms within TBC systems are discussed in detail in Chapter 2.3, after the properties of the individual layers have been explained in more detail in the following sub-chapters.

2.2.1 Superalloys used in Turbine Engine Parts

Superalloys describe a group of metallic alloys that are specialized for use under extreme temperatures, high mechanical loads and aggressive environments. These alloys are characterized by an extraordinary combination of high temperature resistance, oxidation and corrosion resistance, high strength and toughness, resistance to creep and good thermal conductivity (important for effective cooling) [37], [38]. The most critical application areas include the stationary guide vanes, the rotating blades, the combustion chamber and the casing in the high-pressure area of the turbine [10]. The use of superalloys as a base material enables turbines to operate efficient with a long service life. As shown in Figure 2.3, the continuous progress in the development of superalloys has led to an increase in the maximum substrate temperature during turbine operation of around 250 ℃ (to approx. 1050 ℃) compared to the start of alloy development [37].
The most common superalloys are mainly based on nickel or cobalt, with nickel-based superalloys being the first choice for turbine blades. This preference results from the higher creep strength of nickel alloys in the desired temperature range [10]. Another advantage is the exclusive presence of nickel in the face-centered cubic (fcc) γ-phase up to the melting point. The γ-phase is characterized by high toughness and ductility and thus fulfils key properties for turbine blades. The high creep resistance is particularly important for the turbine blades, as they are not only exposed to high temperatures, but also to centrifugal forces. For this reason, single-crystal turbine blades are used in the very hot, first stage of the turbine. These have no grain boundaries, significantly reducing the creep of the material at high temperatures. In addition, grain boundaries lead to damage accumulation at high temperatures, which is also prevented by this. In the later, cooler sections of the turbine, it is sufficient to use columnar solidified crystal structures for the blades, as they are cheaper to produce. In these the grain boundaries are in the direction of the centrifugal force, so the grain boundaries hardly contribute to a reduction in creep strength [37], [38].
The latest generation of nickel-based superalloys are highly alloyed, precipitation-hardened variants. These alloys often contain five to ten alloying elements, reaching a total content of up to 40 wt.%. Common alloying elements include Cr, Co, Mo, W, Ta, Re, Ru, Nb, Al, Ti, Hf, C, B, Y, Zr and Fe, each serving to improve certain properties of the base metal, including high temperature strength, ductility, oxidation resistance, hot corrosion resistance and castability [38], [37]. In particular, the addition of the elements Al, Ti, Nb and Ta is of great importance as they are γ'-formers and are necessary for the precipitation hardening. In a supersaturated γ-nickel matrix, these elements generate intermetallic γ' precipitates of the Ni_3(Al,Ti,Nb,Ta) phase [39]. The cubic precipitations are crucial in increasing the strength of the alloy and improving its creep properties. Figure 2.6 shows the microstructure of such a precipitation-hardened single-crystal superalloy with the characteristic γ/γ' structure. The γ-matrix can be further strengthened by the addition of elements such as Mo, W, Nb and Re by solid solution hardening [37].
The strength of the alloys is optimized by increasing the volume fraction and the size of the γ'-precipitates while retaining the γ-matrix. This can be achieved by targeted addition of different elements and adjusted heat treatments. However, reducing the γ-content over a critical amount is problematic as it affects the ductility of the material and makes it more brittle. In addition to their positive properties, alloying elements such as Cr (oxidation and

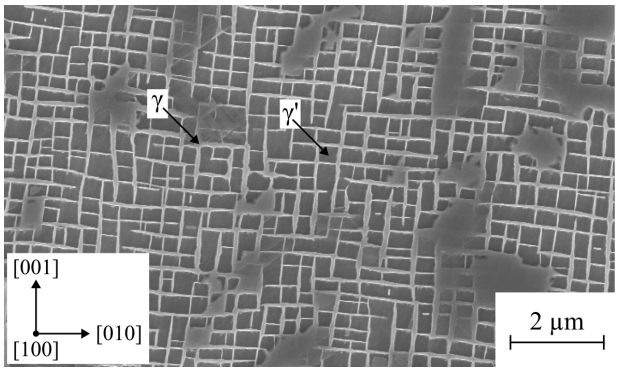

Fig. 2.6 SEM image of the typical γ/γ' microstructure of a single-crystal Ni-based superalloy according to [37]

corrosion protection), W and Re can tend to form brittle phases at high concentrations. A balanced amount of alloying elements must therefore be used. The usual heat treatment consists of two steps. Solution annealing, which compensates for inhomogeneities in the material after casting, and subsequent age hardening, which determines the phase fraction and the size of the γ'-precipitates [37].
Beyond around 900 ℃, critical diffusion processes start in the alloys. The cubic precipitates fuse together to form long, aligned bands, which reduces creep resistance - a phenomenon known as rafting [33]. However, further development of the alloys over the years enables these materials to serve long term operations at an average temperature of around 1050 ℃. Occasional temperature peaks, such as local hotspots (e.g. at blade tips) reaching up to 1200 ℃, can also be tolerated, corresponding to around 90 % of the melting temperature of the materials [37].

2.2.2 Metallic Bond Coats

The metallic bond coat plays a crucial role in the TBC system and complements the thermally insulating ceramic top coat. This layer provides an effective bond between the top layer and the substrate and protects the underlying material from oxidation and corrosion. Two commonly used types are aluminates containing nickel (NiAl) or platinum (PtAl) as well as MCrAlY coatings. The choice of a suitable bond coat depends on the subsequent top coat application method. Aluminide-based coatings are used for the application of electron beam physical vapor deposition EB-PVD coatings, while MCrAlY coatings are well suited for thermal spray coatings [12]. As this thesis focuses on thermal spray coatings, a more detailed description of MCrAlY coatings is given in the following. The term MCrAlY represents a class of bond coats, where M refers to metals such as nickel, cobalt or a combination of both. The exact alloy composition can be tailored to the respective requirements. When selecting the material composition, considerations regarding the desired coating properties and low interdiffusion with the substrate are important. Cobalt-based alloys are suitable for improved corrosion resistance, while nickel-based alloys have better oxidation resistance [40]. Adding chromium, which is typically in the range of

21 and 31 wt.%, further improves oxidation and corrosion resistance. Aluminum is added to the alloy to quickly form a homogeneous and dense oxide layer (usually Al_2O_3) at high temperatures. This layer, known as thermally grown oxide, acts as an oxygen diffusion barrier and protects the underlying metals from fast oxidation. This is important as the overlying ceramic is transparent to oxygen at high temperatures. For this purpose, around 6 - 12 wt.% is added to the alloys. Yttrium is contained in the alloys in a concentration of 0.1 - 0.5 wt.% [41]. On the one hand, it reacts with sulphur, which can be precipitated at the boundary between the bond coat and the TGO, which could lead to early damage of the TBC [38]. Other reactive elements such as Hf, Si, La, Zr and Re show similar effects [42], [43], [44]. On the other hand, yttrium is precipitated at the grain boundaries of the alumina layer, preventing oxygen diffusion along the grain boundaries and slowing down TGO growth - a critical factor for TBC failure, which is discussed in more detail in Chapter 2.3 [45], [46]. However, high concentrations of yttrium lead to the formation of yttrium aluminates in the oxide layer, which serve as fast oxygen diffusion paths and cause stresses in the oxide layer. This stress affects the thermal cycling durability of TBC systems [47], [48], [49].
The metallic MCrAlY interlayers are commonly manufactured using thermal spray processes. Typical processes are atmospheric plasma spraying APS [50], vacuum plasma spraying VPS [51] or high velocity oxygen fuel spraying HVOF [51]. Recently, studies have also been carried out on the production of bond coats using the high velocity air fuel HVAF process [52], [53], [54], [55]. Further details on the spraying processes used in this study are given in Chapter 2.4. The overall aim during the coating process is to minimize coating oxidation. The coating thicknesses for TBC systems are typically between 125 and 250 µm and vary depending on the coating technology selected and the application [11].
The deposited coatings usually consist of a fcc γ-Ni solid solution phase and the β-NiAl phase. The β-NiAl phase plays a crucial role in the high-temperature behavior of the bond coat alloy and serves as an aluminum reservoir for the formation of the TGO [11], [41]. The thermal growth of the oxide layer is discussed in more detail in the following subsection, including the effects on the bond coat itself.
Alongside the formation of the TGO, long-term operation leads to interdiffusion between the bond coat and the substrate. This leads to the depletion of alloying elements in the bond coat, the formation of Kirkendall porosity and the formation of intermetallic phases [56]. Especially the diffusion of aluminum represents a major challenge, as it reduces the amount of aluminum being crucial for the formation of a protective aluminum oxide layer. A depletion zone of the Al-rich β-phase forms below the TGO, which grows further into the bond coat during operation. Interdiffusion leads to a depletion zone of the β-phase in the bond coat on the substrate side, also growing over time. In the substrate, instead, a γ'-depleted zone occurs near the bond coat [57]. The diffusion processes also contribute to the formation of Kirkendall porosity, caused by different diffusion coefficients of the alloying elements. This leads to the accumulation of vacancies that develop into pores [56], [58]. A large number of these pores can lead to a reduced bond between the substrate and the bond coat and even to failure [59]. In addition, topologically closest packed TCP phases can form in the substrate, worsening the mechanical properties of the superalloy [60].

2.2.3 Thermally Grown Oxides

As explained above, the formation of an oxygen diffusion barrier between the top layer and the bond coat is crucial to protect the underlying metal alloys from oxidation. Since the formation of the TGO layer is unavoidable due to the oxygen transparency of the ceramic top layer, the bond coat is developed to form an α-Al_2O_3 layer as described in Section 2.2.2. This oxide is preferred due to its slow growth at elevated temperatures and forms a layer with strong adhesion and good mechanical strength. The slow growth is essential as the thickness of the oxide layer is related to TBC failure. Details can be found in section 2.3 describing the failure modes in TBC systems. The external oxidation of the bond coat takes place as the aluminum has a high affinity for oxygen and is able to diffuse quickly to the surface. The growth of the oxide layer is typically driven by oxygen diffusion through the TGO to the bond coat, but upward diffusion of aluminum into the interface between the TGO and the topcoat is also possible [19].
The aluminum forming the Al_2O_3 layer originates from the β-phase of the bond coat, which serves as an aluminum reservoir. Therefore, a depletion of the Al-rich β-phase in the bond coat takes place during long exposure to high temperatures, especially in the upper bond coat area [61]. The kinetics of the depletion of the beta phase and the resulting aluminum loss in the alloy are primarily influenced by the oxidation properties of the alloy, which depend on its composition [62], the heat treatment [63], [64] and, above all, the oxidation temperature [65]. Below 1000 °C, the oxidation of MCrAlY alloys is slow and no α-Al_2O_3 layer is formed. Above 1000 °C, the oxidation process accelerates exponentially, leading to fast β-phase degradation and aluminum loss. Therefore, the typical operating temperatures for the bond coat layer during testing are 1050 to 1100 °C [66]. The reduced availability of Al leads to the formation of undesirable transient oxides such as NiO, CrO, Cr_2O_3 [67] or spinels such as $NiAl_2O_4$, $CoAl_2O_4$ [43], [68], [69]. These grow faster than Al_2O_3 and have no protective properties. As a result, they can contribute to the failure of the TBC [66]. During these transient transition phases, moreover, metastable phases of aluminum oxide can form. The most common ones are γ-Al_2O_3 and θ-Al_2O_3. These transform above about 1100 °C into α-Al_2O_3. These transformations are associated with a volume decrease of over 10 % [70], which can significantly affect the oxygen diffusion and the subsequent oxidation kinetics as well as stresses arising from the transformation. Therefore, an early transition to or just the formation of α-Al_2O_3 is desirable. This prevents volume changes and the associated stresses due to phase transformations and the α-Al_2O_3 layer slows down the inward-diffusion of oxygen to the bond coat or the outward-diffusion of aluminum due to the denser lattice, in the long term leads to a slowly growing oxide [71].
The volumetric expansion caused by TGO formation leads to growth stresses that can affect the service life of the TBC system [72], [69]. The growing oxide layer has an influence on the stress field in the coating system and leads to a stress reversal in the system when a coating system specific oxide thickness is exceeded, negatively affecting the service life of the coating system [73]. In addition, the formation of Al_2O_3 TGO leads to a depletion of aluminum in the bond coat. This depletion causes mixed oxide formation (spinel formation) of Cr or Co oxides, which tend to grow very rapidly, introducing additional growth stresses into the system and thus promoting failure [66]. The effect of TGO and mixed oxide growth in the transition phase of Al depletion on the failure of TBC systems

is discussed in detail in Chapter 2.3.2. Additional stresses caused by different thermal expansion coefficients in the layers can exceed the fracture toughness of the material when a thick TGO layer is formed. The TGO layer therefore serves as a protective barrier against further oxidation, but at the same time represents a potential weak point within the TBC system, as its formation cannot be suppressed. It is therefore important to create a dense Al_2O_3 layer with a low growth rate during operation.
One possibility for achieving a reduced oxide growth rate during operation, which has increasingly become the focus of research in the recent past, is the targeted pre-oxidation of the bond coat prior to the application of the ceramic topcoat. In 1991, *Chang et al.* showed that pre-oxidation of NiCrAlY bond coats could improve the lifetime of TBC systems with an APS topcoat by about 50 %. In addition, they found that an Al_2O_3 layer with few mixed oxides could be produced under appropriate heat-treatment conditions. In contrast, if the pre-oxidation time was too long or the pre-oxidation temperature too high, the amount of mixed oxides was increased, negatively affecting the service life of the samples during thermal cycling [74].
A systematic study on the effect of partial oxygen pressure (pO_2) on oxide layer formation was later performed by *Matsumoto et al.* They compared the oxidation behavior of CoNiCrAlY bond coats in an air atmosphere and in an argon stream with different pO_2 levels. Subsequently, some of the pre-oxidized samples were further oxidized in air and the TGO surface was examined, while others were coated with an APS topcoat and tested in furnace cycling experiments. The results showed that during pre-oxidation in air (0.2 atm) not only an Al_2O_3 layer but also $(Co,Ni)(Al,Cr)_2O_4$ spinels were formed, whereas after pre-oxidation at low pO_2 values of 10^{-12} - 10^{-17} atm only an Al_2O_3 layer could be detected. Subsequent oxidation of the differently pre-treated bond coats in air and the thermal cycling experiments in the furnace showed that the best performance was achieved with the samples pre-oxidized at a pO_2 of 10^{-14} - 10^{-15} atm. This was attributed to the formation of a highly pure α-Al_2O_3 layer with larger grain size. During further oxidation in air and during thermal cycling, spinels were formed in all samples, but the quantity was lowest at this pO_2. When the samples were pre-oxidized at a lower or higher pO_2, more spinels were formed during subsequent oxidation in air and the total TGO thickness increased, resulting in earlier coating failure. A lower pO_2 lead to the formation of an Al_2O_3 layer with smaller grain size and increasing the pO_2 prevented the formation of a sufficiently thick protective Al_2O_3 layer [75]. In addition, this study showed that at low pO_2, not only α-Al_2O_3 is formed, but also transient γ- and θ-Al_2O_3. The transient Al_2O_3 is believed to be detrimental because the growth rate of θ-Al_2O_3 as TGO is an order of magnitude higher than that of α-Al_2O_3 [76]. Furthermore, the conversion of γ- and/or θ-Al_2O_3 to α-Al_2O_3 at high temperatures is accompanied by a large reduction in volume, which negatively affects the lifetime of TBCs [77]. Comparable results were also found by *Nijdam et al.* using a NiCoCrAlY bond coat and EB-PVD topcoat system [78], as well as by *Kitaoka et al. Joeris et al.* showed that a significant lifetime improvement is also possible for TBC systems with an SPS topcoat and pre-oxidized bond coats [79], [80]. Since these coatings typically fail at the formation of thin oxide layers (~2 µm [81]), the initial rapid oxide growth during thermal cycling can be prevented by pre-oxidation. The presence of an already formed TGO during thermal cycling could influence the stress reversal process and prevent cracking at roughness peaks [80]. Further studies by *Negami et al.* showed

that the initial growth of the TGO is critical for subsequent oxidation. If a dense α-Al_2O_3 layer can be produced, no transient Al_2O_3 oxides or spinels are formed during subsequent oxidation [82], [83], [84]. (Sections of this chapter have been published in [Submitted in Coatings] by the author of this thesis and his colleagues.)

2.2.4 Yttria Stabilized Zirconia Top Coats

The primary function of the ceramic coating is to provide thermal insulation to protect the turbine blade and the bond coat from the high temperatures of the process gas. However, the ceramic coating material must fulfill various requirements to withstand the extreme conditions in a gas turbine. The most important properties the material must offer include a (i) high melting point, (ii) low thermal conductivity, (iii) high coefficient of thermal expansion, (iv) good thermal stability, (v) high fracture toughness, (vi) resistance to erosion and hot corrosion, (vii) good sintering resistance, (viii) chemical inertness and (ix) good adhesion to the metallic bond coat [18], [85], [86]. One material that meets these requirements well is zirconium oxide partially stabilized with 6 - 8 wt.% yttrium oxide (Y_2O_3). This composition was optimized at the end of the 1970s [87] and has been state of the art since the 1980s, making it the most commonly used material for TBCs in gas turbines [88], [89]. However, it should also be noted that the material is limited in its maximum operating temperature during long-term operation. The beneficial properties of the material and its limitations are described in more detail below.

The melting point of pure zirconium oxide (ZrO_2) and its mixtures with yttrium is around 2700 °C and thus far above the operating temperatures of turbines [86], [90]. Yttrium-stabilized zirconia YSZ also has low thermal conductivity, making it an effective insulator. A higher yttrium content further reduces the thermal conductivity of the material [91]. For fully dense YSZ (5.8 wt.% yttrium), the thermal conductivity is about 2.6 - 2.7 W/mK (RT - 1000 °C) [92]. Within the TBC layers, the microstructure and porosity contribute to a lower thermal conductivity of 0.8 - 1.3 W/mK (7 - 8 wt.% yttrium, APS) [93], [92], [91]. The coefficient of thermal expansion of 10 - 11 $\cdot$ 10^{-6} 1/K is relatively high for a ceramic [94], [17] and is close to that of nickel-based superalloys (14 - 16 $\cdot$ 10^{-6} 1/K) [17], [94]. This is crucial for minimizing stresses due to thermal expansion mismatch between the different layers of the TBC system and the substrate. The metallic MCrAlY bond coat alloys have a coefficient of thermal expansion (CTE) of about 17.5 $\cdot$ 10^{-6} 1/K [94]. The forming α-Al_2O_3 TGO layer, has a much lower coefficient of 8 $\cdot$ 10^{-6} 1/K [94]. Moreover, the YSZ has a high hardness (~14 GPa) [17] and a rather high fracture toughness (~1 - 2 MPa $\cdot$ $m^{-0.5}$) [90], making it resistant to erosion and foreign body impact. In addition, YSZ has a low sintering tendency below 1200 °C, an important factor as increased sintering is linked to lower porosity and higher Young's modulus [95]. Reduced porosity has a negative effect on insulation, while a higher Young's modulus increases thermally induced stresses, leading to crack propagation and coating failure [94]. In addition, YSZ has a low density of 6.0 g/cm^3 [90], which helps to reduce weight.

Stabilizing the material with yttrium is essential, as pure ZrO_2 is not phase stable at the operating temperatures in a turbine. These phase transformations, shown in Figure 2.7 are associated with volume changes and lead to stresses that can cause the coating to fail [96]. Especially the martensitic transformation from the tetragonal (t) to the monoclinic (m)

phase is a challenge as it is linked with a volume increase of 3 - 5 % [96], [97], [98]. Pure ZrO_2, which undergoes this transformation during heating at around 1170 °C, therefore cannot be used as a thermal insulation material above these temperatures.

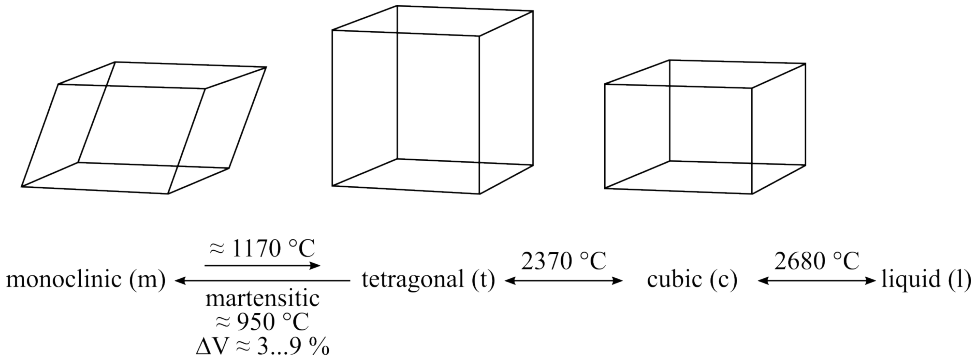

Fig. 2.7 Phase changes in ZrO_2 adapted from [33] and [99]

Stabilizing elements such as Y_2O_3, MgO, CaO or CeO_2 can be added to the ZrO_2 as doping elements. Of these, Y_2O_3 is the most common doping material [33] and is also used in this work. It can be added in different amounts. A small amount of yttrium (4 - 5 wt.%), for example, leads to high fracture toughness [100], [101], but reduced high temperature stability. For complete stabilization of the zirconium oxide, at least 12 wt.% yttrium oxide is required. This, in turn, has reduced mechanical properties due to a lower fracture toughness and tensile strength of the cubic phase, which is formed at this content. Therefore, the already mentioned 6 - 8 wt.% partially stabilized zirconia is usually used for high temperature applications [102]. The corresponding two-phase diagram in Figure 2.8 illustrates the formation of monoclinic (m), tetragonal (t) and cubic (c) phases.
The plasma spray application process, however, deposits this material in the metastable t'-phase. The rapid cooling of the material during the process suppresses the rearrangement of atoms to form the regular tetragonal phase with a low yttrium content and the cubic phase with a high yttrium content. Unlike the t-phase, the resulting t'-phase does not transform into the m-phase during cooling with the associated change in volume. In addition, the t'-phase has a pre-stressed structure due to a modified tetragonal lattice, enhancing the materials toughness. Therefore, the t' is the desired phase for TBC applications [103].
Although called a non-transformable tetragonal phase, the high temperature capability of thermally sprayed YSZ coatings is limited. Above 1200 °C, the t'-phase changes to an equilibrium state by diffusion [104], [105]. This leads to the formation of the tetragonal and cubic phases. The tetragonal phase then transforms into the monoclinic phase with the associated volume change during cooling in turbine operation. The cubic phase formation is accompanied by reduced fracture toughness [106]. However, in a study by *Vaßen et al.* it was shown experimentally that the detrimental monoclinic phase transformation and high energy release rates responsible for crack growth can be influenced by the cooling rate. They showed that rapid cooling from elevated temperatures (> 1500 °C) can be the cause of failure of thermal barrier coating systems. Rapid cooling above 100 K/s resulted in a reduction in service life by a factor of more than 2 due to the high peak energy release

rates. When the cooling rate was reduced to 10 K/s, the TBC systems could be operated in a burner rig at surface temperatures of about 1550 ℃ without any reduction in service life. This defined cooling rate not only avoided the peak energy release rate, but also avoided the tetragonal/monoclinic transformation by cooling to temperatures below 100 ℃. These two factors enabled long lifetime of the YSZ-based coatings despite the extremely high surface temperatures.

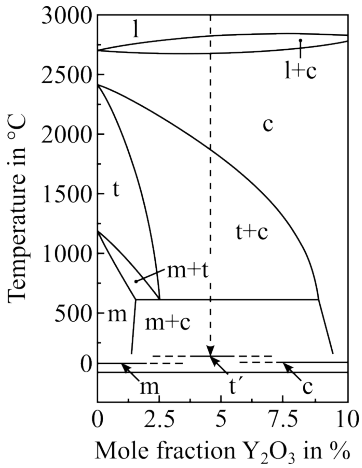

Fig. 2.8 Two-phase diagram of the ZrO_2-Y_2O_3 system according to [33] and [102]

Another aspect that can be adjusted by the application process is the coatings' microstructure. The two most commonly used processes for producing ceramic coatings are atmospheric plasma spraying APS and electron beam physical vapor deposition EB-PVD [107]. The advantages and disadvantages of the coatings produced with these processes are presented below. The different plasma spray processes used in this thesis and the characteristics of the respective coatings are described in more detail in the Chapter 2.4. The coatings produced with the APS and EB-PVD processes differ fundamentally in their microstructure, as shown in Figure 2.10. With the APS process irregular, lamellar structures with enclosed pores and cracks are generated (a) and with the EB-PVD process elongated, feather-like structures known as columns (b) are produced. Between the dense columns there are vertical pores that extend almost across the entire thickness of the coating. APS coatings are designed to incorporate a high cumulative porosity in the coating. This increases the insulation properties, especially by cracks and pores that are perpendicular to the heat flow direction [108], [109], [110]. At the same time, the Young's modulus of the coating is reduced with a higher porosity, improving the strain tolerance of the coating [111], [112], [113]. In comparison to EB-PVD coatings, APS coatings are better in terms of thermal insulation. The APS coatings have a thermal conductivity between 0.6 - 1.3 W/mK for APS, whereas it is 1.4 - 1.9 W/mK for EB-PVD coatings [92], [107], [91]. The higher conductivity of EB-PVD coatings results from the gaps between the columns, which allow the hot gas to get close to the substrate. In addition, the dense columns provide less insulation as the thermally conductive phonons are scattered less

effectively [114]. Another advantage of APS coatings is the significantly lower process costs.
In terms of strain tolerance, however, EB-PVD coatings are superior to APS coatings. Due to the expansion mismatch of the materials in the TBC system, the metallic substrate and bond coat expand more than the ceramic and oxide layer. However, the microstructure of the EB-PVD coating allows them to open up when the substrate expands more. As a result, less stress is built up in the ceramic coating. This can be seen schematically in Figure 2.9. If the TBC system is heated, the higher expansion of the substrate leads to tensile stresses in the ceramic top coat, which are much less pronounced in the columnar coating. In addition, there is less stress relaxation at the operating temperature due to sintering. This leads to a lower stress development during cooling of the coating system (lamellar APS structure has a steeper slope in the stress curve during cooling), and therefore the residual compressive stresses in the ceramic are lower at room temperature. Due to the lower compressive stresses in the columnar structured coating, stress relaxation due to crack growth is also lower. This crack growth represents a critical failure mechanism (see Chapter 2.3) [115].

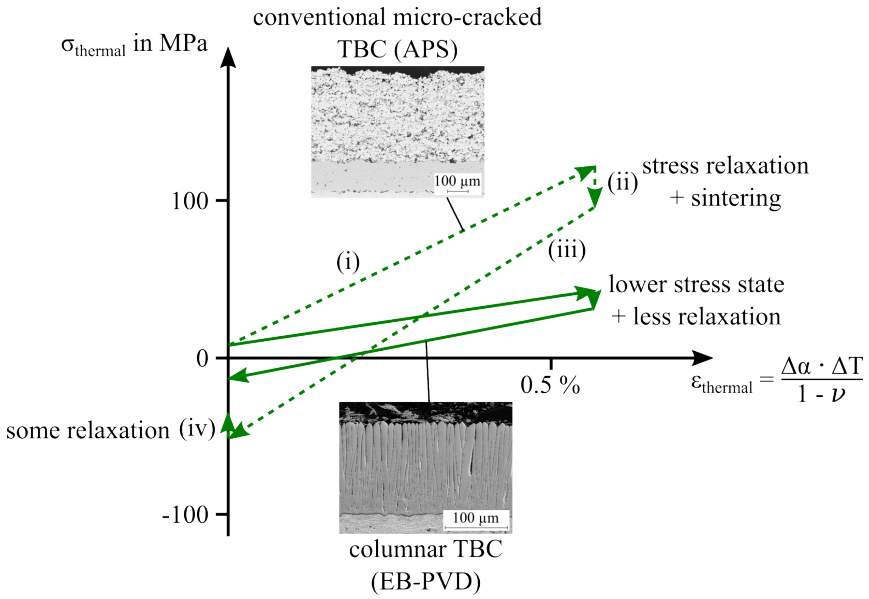

Fig. 2.9 Qualitative stress development within APS (dotted line) and EB-PVD (solid line) TBCs deposited on a nickel-based superalloys during heating (i), dwell time at temperature (ii), cooling (iii) and at room temperature (iv) according to [115]

Due to their superior strain tolerance, EB-PVD coatings are preferred for applications with frequent cycling operation. This is why they are used for small aerospace components, such as turbine blades and guide vanes. These are especially exposed to cyclic loads among others due to take-offs and landings. Large components such as aircraft gas turbine combustion chamber parts or industrial gas turbine blades, on the other hand, are coated with plasma sprayed coatings [18], [114].

In this project, the aim is to develop coating systems for industrial gas turbines that offer flexibility in usage. Therefore, the objective is to develop ceramic coatings that combine the cost efficiency and excellent insulation properties of plasma sprayed coatings with the high strain tolerance of EB-PVD coatings (Figure 2.10 (a)). A key strategy to improve the thermal shock resistance of plasma sprayed coatings is to reduce the tensile stresses in the heated condition, which requires microstructural changes. To achieve this, a various different microstructures were produced and investigated in this project. The APS process was used to produce once, highly porous coatings (Figure 2.10 (b)) , as well as dense, vertically cracked DVC (Figure 2.10 (c)) microstructures. In addition, columnar coatings were produced using suspension plasma spraying (SPS) (Figure 2.10 (d)) and plasma spray physical vapor deposition (PS-PVD) (Figure 2.10 (e)). These coating systems all aim to improve strain tolerance by reducing the tensile stresses before the multilayer coating system is cooled. Further details on the individual processes can be found in the Chapter 2.4 on deposition processes.

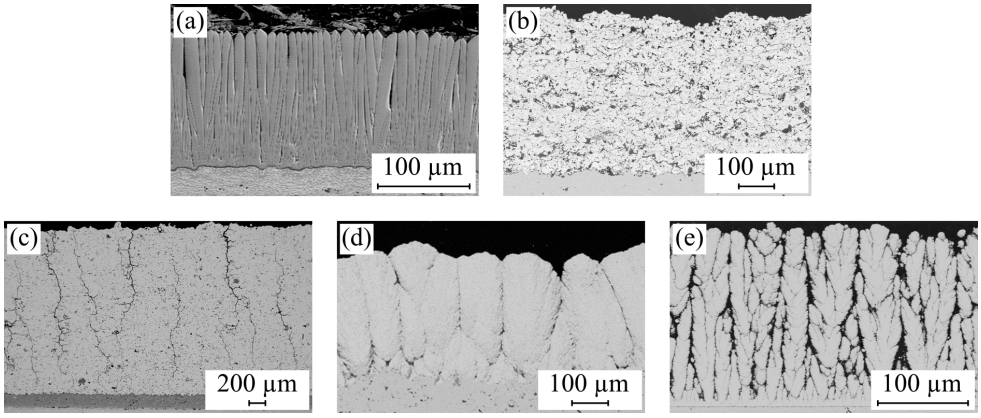

Fig. 2.10 Different microstructures of YSZ TBCs: (a) EB-PVD, (b) conventional APS, (c) thick segmented APS, (d) columnar SPS, (e) columnar PS-PVD accoding to [14] and [116]

2.2.5 Alternative Top Coat Materials

Another approach to increasing the durability of thermal barrier coating systems is to use a top coat material that does not exhibit undesirable phase transformations under the operating conditions in a turbine (above 1200 ℃). Therefore, this chapter focuses on the properties of alternative top coat materials. Sections of this chapter have been published in [Submitted at ACerS] by the author of this thesis and his colleagues.
In the last two decades, pyrochlore materials such as $La_2Zr_2O_7$ or $Gd_2Zr_2O_7$ have become the focus of research [102], [117]. These are characterized by a high melting point, low thermal conductivity, low sintering tendency and phase stability at elevated temperatures [100]. Since gadolinium zirconate ($Gd_2Zr_2O_7$, GZO) is used in this research, it is described in more detail below.

GZO has a melting point of about 2570 °C [118] and a CTE of ($10.5 \cdot 10^{-6}$ 1/K) [119], which are both comparable to the values of YSZ. Compared to YSZ, GZO has improved properties due to its lower thermal conductivity (YSZ: ~2.6 W/mK, GZO: ~1.2 - 1.5 W/mK in dense material) [120], [119] as well as a low sintering rate and high phase stability at elevated temperatures. At high temperatures around 1530 - 1550 °C, the GZO undergoes a transition from the fluorite defect structure (Fm3m) to the pyrochlore structure (Fd3m). This however does not have a detrimental effect on the service life of the coating, as it is the case with the volume expansion in YSZ [121], [122]. Nevertheless, GZO also has disadvantages. Reactions occur between the GZO and the TGO layer in operation, leading to the formation of a $GdAlO_3$ phase. This consumes the protective aluminum oxide layer and can cause an internal oxidation of the bond coat [123], [124]. In addition, the GZO has a relatively low fracture toughness, leading to crack propagation even at low stresses in the material. As a result, GZO monolayers have a lower thermal cycling life than YSZ monolayers [117].
To take advantage of the high thermal stability and low thermal conductivity of GZO while avoiding the disadvantages of low fracture toughness and chemical reactivity with TGO, double layer systems can be used. In these coating systems, a YSZ layer is applied between the bond coat and the GZO top coat. This layer with a high fracture toughness can reduce the growth of cracks due to stresses and prevent the detrimental reaction with the TGO layer. Such double layer systems were introduced by *Vaßen et al.* They were able to show that these double layer systems could have a comparable lifetime with an increase in surface temperature of more than 100 K in burner rig testing [117].
Further, *Bakan et al.* and *Vaßen et al.* reported an extended service life of APS YSZ/GZO double or multilayer systems in gas burner rig testing (1400 °C surface temperature) compared to single layer APS-YSZ coatings. The microstructure and the Young's modulus of the coatings also influence the service life. It has been shown that longer service lives can be achieved for the same cumulative porosity if the Young's modulus of the coatings is lower. In contrast, dense GZO coatings (porosity 10 - 11 %) lead to premature spalling of the GZO top layer, resulting in faster failure compared to single layer APS-YSZ coatings [125], [27]. It has also been observed that at elevated temperatures (1550 °C surface temperature), the main cause of failure of YSZ coatings are not sintering and phase transformation, but the high energy release rates at the beginning of a cooling cycle [126]. For this reason, the investigation of coating microstructures with high strain tolerance, such as dense vertically cracked (DVC) or columnar coatings, are of interest.
Viswanathan et al.'s study on DVC coatings also revealed, that a high Young's modulus induces early coating failure. Furthermore, the coating design significantly affects the failure mechanism. For instance, adequate thickness of the tough YSZ layer (150 µm in a total coating thickness of 300 µm), can shift the failure location from the GZO layer (cohesive failure) to the TGO interface (adhesive failure), thereby increasing the lifetime of the coatings [127].
Multilayer systems produced entirely using the SPS process also showed a longer service life than single layer APS-YSZ coatings in thermal cyclic fatigue tests and gas burner rig tests [128]. *Zhou et al.* investigated the performance of APS-YSZ/SPS-GZO multilayer systems under burner rig test conditions and showed improved cyclic lifetime compared to APS-YSZ monolayers [124].

2.3 Failure Mechanisms of Thermal Barrier Coatings

As described above when considering the individual layers, the different layers in the TBC system interact in a complex manner. These interactions, coupled with different physical properties, lead to aging processes and complex failure mechanisms when subjected to the thermomechanical loads during turbine operation. Failure of the system is determined by the loss of one or more material layers of the system. Typically, the failure can be detected by delamination of the ceramic coating, resulting in loss of thermal insulation and direct exposure of the bond coat to the high-temperature gas stream. Such failures are rarely due to a single factor, but rather result from the combination of several factors, each influencing the others. Nevertheless, this chapter will systematically describe individual failure mechanisms before explaining their interactions. The two main failure mechanisms, crack propagation due to stresses caused by CTE mismatch of the individual layers and failure due to TGO growth, are discussed first. Following this, factors significantly influencing these mechanisms are discussed, including mixed oxide growth due to aluminum depletion, phase transformations, sintering, and thermal gradients exhibited in burner rig tests. Finally, extrinsic factors such as foreign particle erosion (FOD = Foreign Object Damage), hot gas corrosion, and calcium-magnesium-alumina-silicate (CMAS) attack are described.

2.3.1 Thermal Expansion Mismatch

The primary challenge encountered during thermal cycling of TBCs arises from the different coefficients of thermal expansion of the materials used. As described in section 2.2.4 these are about 10 - 11 $\cdot$ 10^{-6} 1/K for the ceramic topcoat and about 8 $\cdot$ 10^{-6} 1/K for the TGO layer, while the values for the metallic bond coat and substrate are 17.5 and 14 - 16 $\cdot$ 10^{-6} 1/K, respectively [94], [17].
In their initial state, thermal barrier coatings have different stress states depending on the coating process and coating temperatures. However, as shown in Figure 2.9, the stress states change with temperature changes. When the systems are heated to the operating temperature of 1200 ℃ or higher, tensile stresses are typically present in all coating systems due to the lower expansion coefficient of the ceramics. These stresses are relieved at high temperatures by relaxation processes. Upon cooling to room temperature, residual compressive stresses are present in all systems, which can lead to crack propagation and coating failure. Due to the microstructure, the total stresses in APS coatings are higher than in segmented or columnar coatings [115].
Assuming the system is stress-free at operating temperature, due to relaxation processes, the resulting stresses at ambient temperature can be described using the equation 2.2. ΔT is the temperature difference from operating to ambient temperature, $\Delta\alpha$ is the difference between the CTE of coating and substrate, and $E_{Coating}$ and $\nu_{Coating}$ are describing the elasic modulus and Poisson's ratio of the coating: [129]

$$\sigma_{Coating} = \frac{\Delta\alpha \cdot \Delta T \cdot E_{Coating}}{1 - \nu_{Coating}} \tag{2.2}$$

However, this equation does not consider the influence of the coating thickness on the stresses, which is described in Figure 2.11. In this example by *Mücke/Vaßen*, it is assumed that systems with different ratios of layer to substrate thickness (h_2/h_1) are heated from room temperature to 1000 K. The tensile stresses in the coating caused by the lower expansion coefficient increase with increasing coating thickness. This can be explained by the fact that a thicker coating hinders the expansion of the substrate to a greater extent. As a result, the expansion and therefore also the stresses in the coating are lower [130].

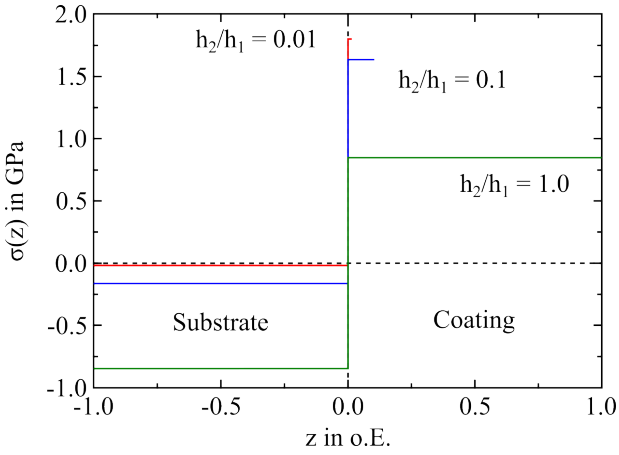

Fig. 2.11 Stress level in a ZrO_2 coating on nickel-based superalloy after heating to 1000 K; h_2/h_1 is the coating/substrate thickness ratio [130]

Although the stresses in the TBC decrease with increasing coating thickness, thicker TBCs tend to fail faster. Thicker coatings store more compressive stress in the form of higher elastic energy during cooling. This energy, referred to as the energy release rate, increases linearly with coating thickness and is described by the area under the curve in Figure 2.11. According to Formula 2.3, the energy release rate results from the coefficient of thermal expansion α, the Young's modulus (E), the ceramic coating thickness d, the maximum temperature drop at the coating surface ΔT, and the average cooling rates at the surface $\dot{T}_{\mathrm{Coating}}$ and in the substrate $\dot{T}_{\mathrm{Substrate}}$ [131].

$$G_{max} \approx \frac{1}{6}(\alpha \Delta T)^2 E d \frac{\dot{T}_{Coating} - \dot{T}_{Substrate}}{\dot{T}_{Coating}} \tag{2.3}$$

When this elastically stored energy exceeds a critical value, cracks begin to propagate and the coating may even delaminate. A study by *Vaßen et al.* has shown that the rapid cooling rates at the beginning of a cooling cycle in gradient tests in particular lead to peaks in the energy release rates, which significantly reduce the service life of coatings [131].

Up to this point, only the effects of the CTE mismatch on the in-plane stresses have been considered. In TBC systems, these are usually determined by the thick substrates, so the thickness of the coatings is negligible. However, local out-of-plane stresses at the interface between the bond coat and the ceramic top coat also have a major impact on the failure

of TBCs. The roughness of the bond coat has a decisive influence on these local stresses, which is shown schematically in Figure 2.12. For description, a system without stresses at operating temperature is considered. During cooling, the higher contraction of the bond coat leads to radial tensile stresses at the roughness peaks and compressive stresses in the valleys of the ceramic coating. The local tensile stresses at the roughness peaks lead to crack growth. The propagation of these cracks is inhibited in the compressive stress regions. However, the formation of the TGO layer during operation changes the local stress conditions. Once a certain TGO thickness is reached, the lower CTE of the TGO causes a reversal in stress sign [132]. As a result, compressive stresses occur at the roughness peaks and tensile stresses occur in the valleys due to cooling. The cracks formed at the roughness peaks continue to grow in the valleys and connect, causing the coating to delaminate [73].

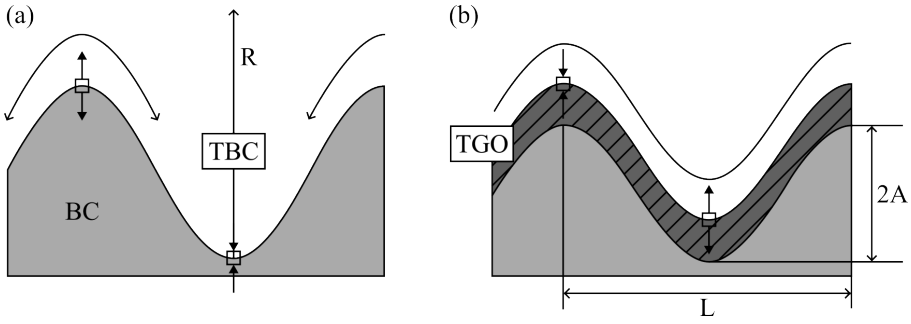

Fig. 2.12 Model of crack growth due to local stresses at roughness peaks and valleys at the beginning of the service life (a) and after TGO growth (b) [73]

2.3.2 TGO Growth

In addition to introducing stress due to the low CTE, the growing oxide layer has other effects that can cause the coating system to fail. The growth of the TGO at operating temperature due to oxygen diffusion leads to an increase in volume. This results in additional compressive stresses in the system [133]. However, beyond a certain TGO thickness, the stress reversal described in Figure 2.12, caused by the CTE mismatch of the TGO, dominates. This specific TGO thickness depends on the coating system under investigation and varies for different coating microstructures [72], [81], [134].
The following sections describe how different bond coat roughnesses affect crack growth and coating failure during TGO growth. For this purpose, the cracking processes in systems with different bond coat roughnesses are shown schematically in Figure 2.13. These are divided into three stages for each system. Stage 1 shows the initial TGO growth, stage 2 describes the crack nucleation and/or growth and stage 3 the crack linking, causing the system to fail. Figure 2.13 (a) - (c) shows the different crack paths in APS systems with different bond coat roughnesses. Figure 2.13 (d) is describing the failure of an SPS coating sysmtem and (e) of an EB-PVD or PS-PVD system.

Figure 2.13 (a) shows a system with a relatively smooth bond coat surface. However, the convex areas of the bond coat are already sufficient to represent the preferred crack nucleation sites. During cooling, the CTE mismatch between the bond coat and the TGO causes tensile stresses at the TGO/bond coat interface, leading to crack nucleation, which is defined as crack mechanism I (Stage 2 (a)). In addition, good adhesion between the TGO and the bond coat can also lead to cracking at the TGO/top coat interface, which is referred to as cracking mechanism II (Stage 2 (a)). The cracks can easily connect along the smooth interface until the coating chips off along the TGO (Stage 3 (a)).
If the roughness of the bond coat is increased (Figure 2.13 (b)), crack mechanisms I and II also occur. In addition, the tensile stresses above the roughness peaks also cause cracking within the brittle top layer, which is defined as cracking mechanism III (Stage 2 (b)). After the critical TGO thickness is reached and the stress sign is reversed, cracking mechanism IV also occurs, causing the cracks to grow into the roughness valleys due to the tensile stresses that have developed there (Stage 2 (b)). When the various cracks formed join, the coating fails. The cracks usually join at the interface between TGO and bond coat, between TGO and top coat, and through the brittle top coat itself, mainly in the roughness valley areas (Stage 3 (b)).
A further increase in bond coat roughness (Figure 2.13 (c)) results in cracking mechanisms I and II again. The cracks form in the convex bond coat areas. However, due to the very rough bond coat surface these convex areas are very small and the arising stress in which the cracks form are very localized (Stage 2 (c)). This prevents the individual cracks from joining, as the cracking process relieves the stresses built up. Further exposure then gradually thickens the TGO and several of these cracks can form on top of each other in the TGO (Stage 3 (c)). Above an elevation of the bond coat in a large scale, cracks also develop due to crack mechanism III in the ceramic top layer (Stage 2 (c)). Since the crack growth in the TGO or its interface is repeatedly inhibited, the cracks in the ceramic top layer grow constantly and finally connect. As a result, the crack in a failed system runs predominantly through the ceramic top layer and partly along large roughness peaks of the bond coat (Stage 3 (c)) [17], [135].
In SPS coatings, crack nucleation usually occurs due to tensile stress development at the roughness peaks on which the columns grow. The cracks usually nucleate near the interface in the ceramic columns, which is equivalent to crack mechanism III in the APS coatings (Stage 2 (d)). These cracks grow during thermal cycling and can either lead to spallation of individual columns, or the cracks can connect by growing through the intercolumnar regions, resulting in spalling of the entire coating near the TGO/top coat interface (Stage 3 (d)) [136].
In the case of smooth, polished interfaces between the bond coat and the top coat, as used in PS-PVD and EB-PVD coatings (Figure 2.13 (e)), local out-of-plane stresses cannot arise. With these coatings, another effect known as rumpling can occur and is shown in Stage 2 (e). Rumpling takes place when the lower expansion coefficient of the substrate puts the bond coat under tensile stress during cooling. In contrast, compressive stresses are present in the bond coat during heating. If the yield strength of the bond coat alloy is exceeded during these processes, or if creep occurs, the bond coat layer will subsequently roughen. The resulting crack nucleation can occur at different locations. The subsequent roughening of the bond coat surface causes crack mechanism I to occur in the interface

between the TGO and the bond coat, as in the other systems previously described. The crack mechanism ii, however, differs in part from the crack mechanism II of the APS coatings. The TGO penetrates into the bond coat, which also causes tensile stresses at the interface to the ceramic layer, resulting in the delamination of the coating (Stage 2 (e)). The roughening has a negative effect on the adhesion of the top coat and can lead to failure of the coating due to mechanism iii. In this case, the coating lifts off the relatively flat bond coat over a large area and buckles upwards due to the compressive stresses in the coating (Stage 3 (e)) [17], [135].
The TGO layer is formed by the aluminum diffusion in the bond coat towards the TGO layer and the diffusion of oxygen from the hot gas stream. As a result, the Al-rich β-phase in the upper part of the bond coat is depleted, as described in Chapter 2.2.2 and 2.2.3. Furthermore, there is an interaction between the substrate and the bond coat under thermal stress. Another depletion zone of the Al-rich β-phase in the lower area of the bond coat is also formed due to diffusion. If there is an exchange of elements with different diffusion coefficients between bond coat and substrate, pores can form, which are also referred to as Kirkendall pores [56], [58].
When the upper and lower diffusion zones grow together, the bond coat is completely depleted of the Al-rich β-phase and only a small amount of aluminum remains in the bond coat. This results in the formation of transient oxides (spinel formation) at the interface with the ceramic top layer. These transient oxides are usually the mixed oxides described in Chapter 2.2.3 [66]. These grow very fast compared to the α-Al_2O_3 layer and provide no protection against further oxygen diffusion. The rapid formation results in high growth stresses which can promote TBC spallation and thus system failure [138].

Failure due to CTE mismatch and TGO growth are the two most important failure mechanisms in TBC systems. However, there are also other effects that influence the service life of thermal barrier coatings by affecting the chemical or mechanical properties of the layers of the system. These are discussed in the following subsections.

2.3.3 Phase Transformation

The rapid cooling processes during the production of YSZ coatings by plasma spray processes lead to the formation of a non-equilibrium tetragonal phase with a high yttrium content. This metastable phase, referred to as t', initially shows no phase transformation with temperature changes. However, during exposure to temperatures above 1200 °C, phase separation into the equilibrium phases is observed. A tetragonal phase with low yttrium content and a cubic phase with high yttrium content are formed [104]. The low yttrium tetragonal equilibrium phase in turn undergoes a transformation to the monoclinic phase during cooling, as discribed in Chapter 2.2.4. This transformation is associated with volume changes that are detrimental to the integrity of the coating. As a result, the phase transformation promotes coating failure [139], [140].

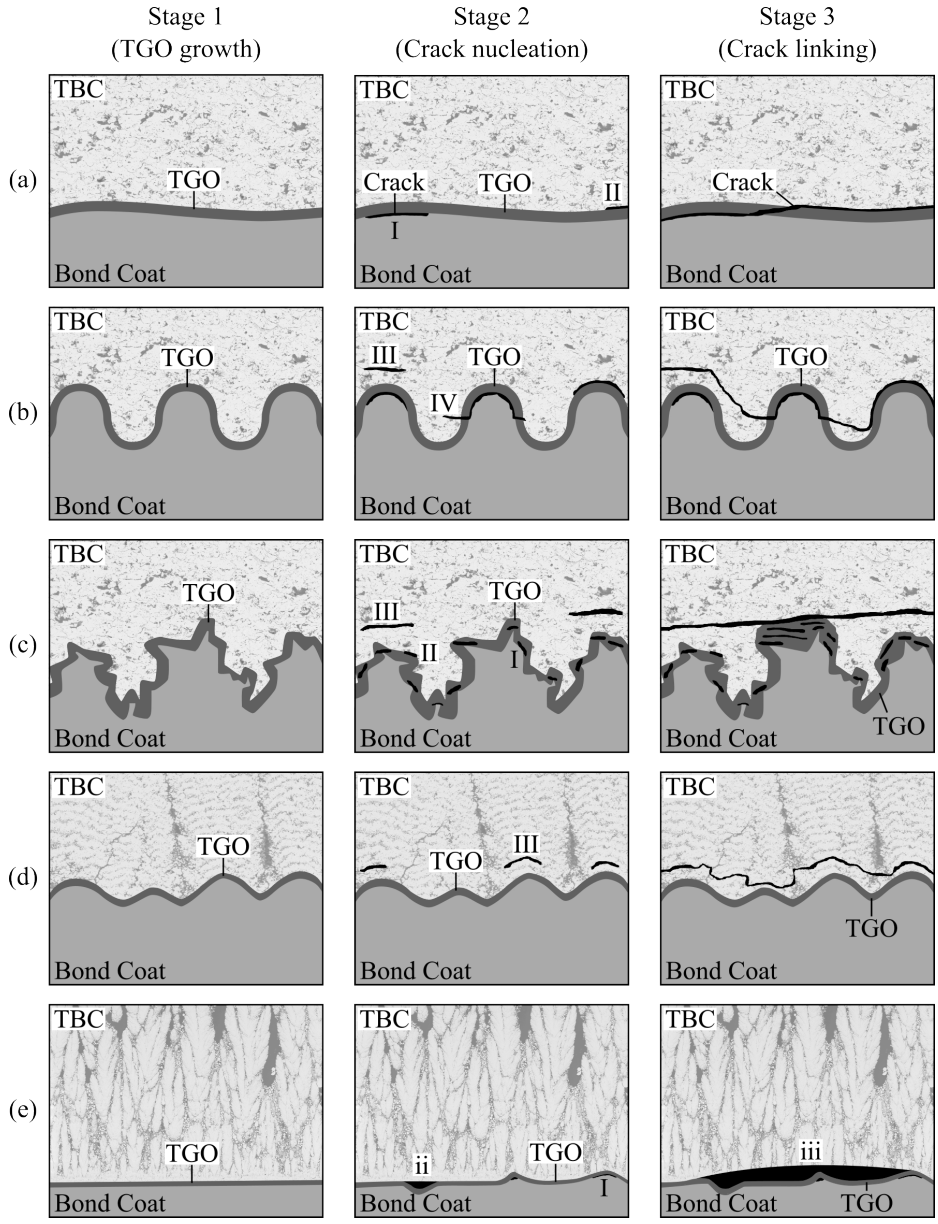

Fig. 2.13 Failure mechanisms in different coating systems at different stages: (a), (b), (c) in APS coatings with increasing bond coat roughness; (d) in SPS coatings, (e) in EB-PVD coatings according to [17], [135] and [137]

2.3.4 Sintering

In addition to phase transformation, above 1200 ℃ there is also increased sintering in the ceramic top coat. The driving force for sintering is the reduction in surface free energy. The sintering process of the ceramic leads to a change in the mechanical properties and microstructure of the coating. The porosity of the coating can be decreased and the elastic modulus increased. One effect of a decrease in porosity is a reduction in the insulating properties of the coating. This, in turn, causes the bond coat temperature to increase, accelerating TGO growth. In addition, the healing of microcracks and pores stiffens the coating, increasing in the Young's modulus. This compromises the strain tolerance of the coating as more elastic energy is stored in the coating during cooling, promoting crack growth. [141], [142]. Furthermore, the compressive stresses in the coating are increased after cooling. This can be seen in the steeper cooling curve in Figure 2.9 after sintering and relaxation have reduced the stresses in the coating. These detrimental developments in the coating due to sintering can promote premature failure of the coating [18].
Another effect that is often observed in burner rig cycling tests is related to the thermal gradient across the coating system. This gradient must be introduced into the coating system when surface temperatures exceed 1100 ℃, the maximum working temperature of the bond coat. To achieve this, the TBC system is cooled from the substrate side like the turbine blade. Because of the temperature gradient, there is already a stress gradient in the ceramic coating due to the different expansion at different temperatures. If the material on the surface then sinters even more due to the higher temperatures near the surface, this effect is further intensified. As a result, individual ceramic splats often chip off the surface at high surface temperatures [143].

Up to this point, the intrinsic failure mechanisms have been considered in isolation. However, since they also influence each other, a simple combined model of the mechanisms is described in the following. This model focuses primarily on the changes that occur in the system over time due to sintering of the ceramic and oxidation of the bond coat.
The sintering of the ceramic increases the Young's modulus of the coating and thus contributes to an increase in the elastically stored energy. This, in turn, contributes to an increase in the energy release rate. As a result, the driving force for crack propagation increases over time. Conversely, the oxidation of the bond coat and the resulting TGO growth reduces the crack resistance at the interface.
The driving force for crack propagation and the corresponding crack resistance can be represented as competing curves, as shown in Figure 2.14 with the changes of the curves over time. The crossing point of the curves represents the failure of the coating in the interface. At this point, the energy release rate exceeds the critical energy release rate (= fracture toughness) of the interface and a crack propagates along the TGO. The different lines for each curve show that increasing the interface temperature T_{min} accelerates the decrease in fracture toughness of the interface (faster oxide growth). Increasing the surface temperature T_{max}, instead, leads to a faster increase in the driving force for crack propagation (stronger sintering = increase in Young's modulus). Thus, both a higher bond coat temperature and a higher top coat surface temperature lead to faster failure of the coatings.

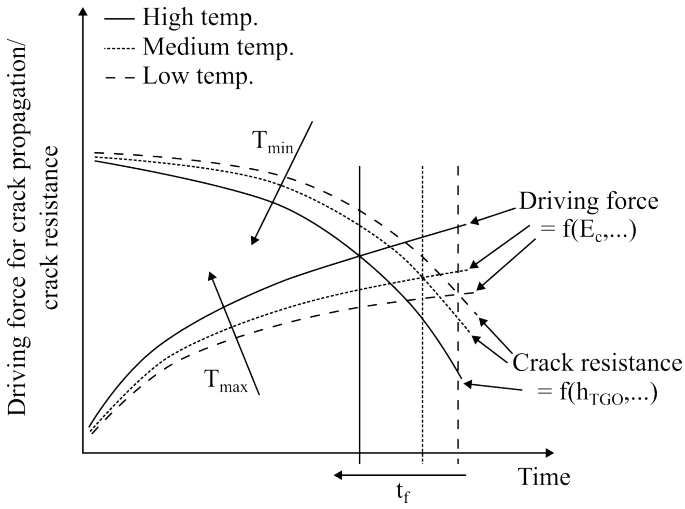

Fig. 2.14 Temperature- and time-dependent curves of the driving force for crack propagation and the crack resistance in the interface area of a thermal barrier coating system according to [144]

2.3.5 Erosion

In addition to the intrinsic failure mechanisms, there are also extrinsic factors that promote or cause coating failure. One of these external factors is foreign object damage (FOD) to the thermal barrier coatings. There are two basic types of FOD. On the one hand, impact of small particles can promote the formation of cracks near the surface. If these cracks join due to increased particle impact, this can lead to delamination of parts of the coating [145]. On the other hand, impingement of large foreign particles can compact the entire coating and worsen its properties or even lead directly to failure [146].
Due to the horizontally oriented splat microstructure of APS coatings and the high number of horizontal cracks, this coating is easily removed by erosive impact. Therefore, APS coatings in general have lower erosion resistance than EB-PVD coatings [147].

2.3.6 Hot Gas Corrosion and CMAS attack

Hot gas corrosion and CMAS (Calcia–Magnesia–Alumina–Silicate) attack are caused by melted foreign particles deposited on the TBC layer. These include particles that enter the turbine by contaminated fuel or air. Hot gas corrosion can be caused by fuel impurities such as sulfur, sodium, vanadium, and others. These impurities oxidize during combustion and penetrate the porous structure of the coating. They react with the components of the top coat and can promote cracking or penetrate into the bond coat and promote oxidation there [148].
CMAS attack is primarily caused by sand or volcanic ash particles that are sucked in with the air, melted, and deposited in the top coat. Chemical reactions with the top coat and substrate also occur. A further problem, however, is the low expansion of the glassy

CMAS compared to the YSZ. This results in high compressive stresses in the top layer as the system is cooled down, increasing the energy release rates of the system [149].

2.4 Plasma Spraying of Ceramic Top Coats

Plasma spraying is a surface coating technology and is part of the thermal spraying processes. A schematic design of a plasma torch used for this method is shown in Figure 2.15. For the deposition of ceramic thermal barrier coatings, a plasma torch with a direct current (DC) source is used. An arc is ignited between a tungsten cathode and a copper anode. Today, plasma torches with cascaded arc control are often used. In these, the anode is divided into several rings separated by electrically neutral rings (neutrode rings). This structure is also called a neutrode stack. When the torch is fully started, only the front anode at the nozzle outlet is electrically connected to the power supply. This design allows the arc length to be artificially extended and fixed. The fixed arc length stabilizes the plasma jet, eliminating power fluctuations and allowing high voltages to be achieved already with low ampere. The torches with cascaded arc control are therefore well suited for processing high-melting materials such as ceramics, and the low power fluctuations allow the production of coatings with uniform properties.

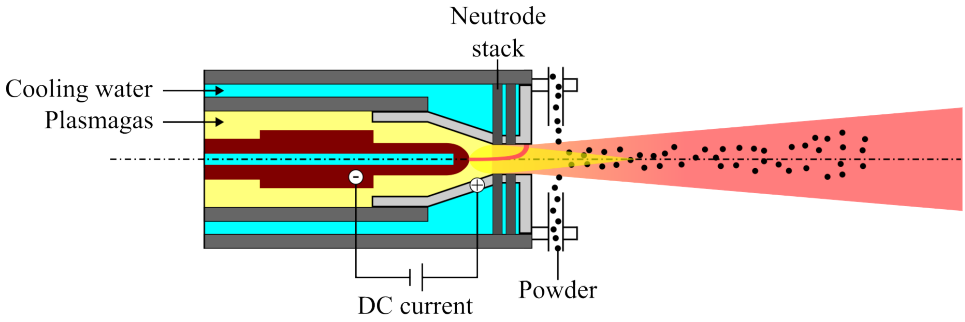

Fig. 2.15 Schematic structure of a single cathode cascaded plasma torch according to [110]

The arc emits electrons at the cathode and the applied voltage accelerates them towards the anode. On their way, the electrons collide with atoms of the process gas, causing ionization and, depending on the process gas, dissociation of the gases. The process gases typically used are argon (Ar), helium (He), nitrogen (N2), hydrogen (H2), or a mixture of these gases. Argon is commonly used as primary gas to which one of the other gases is added as a secondary gas [129]. In some cases, however, nitrogen is also used as the primary gas [150], [151], [152]. While the inert gases argon and helium can only be ionized, molecular nitrogen and hydrogen can also undergo dissociation processes to split into individual atoms before ionization. Accordingly, more energy is required to convert the molecular gases to the plasma state via process excitation, dissociation, and ionization. The energy supplied is present in the plasma as specific enthalpy. As shown in Figure 2.16, hydrogen has the highest specific enthalpy. A higher specific enthalpy means that more energy is available to melt the coating material in the plasma. However, due to the direct

contact of the process gas with the metallic electrodes of the torch, oxidizing and reducing properties must be taken into account to avoid damage. Therefore, pure hydrogen cannot be used as a process gas, so process gas mixtures are used [110]. Finally, recombination of the ionized gases and the free electrons takes place. This process releases a large amount of energy in the form of heat. As a result, temperatures of up to 20000 K can be reached in the plasma.

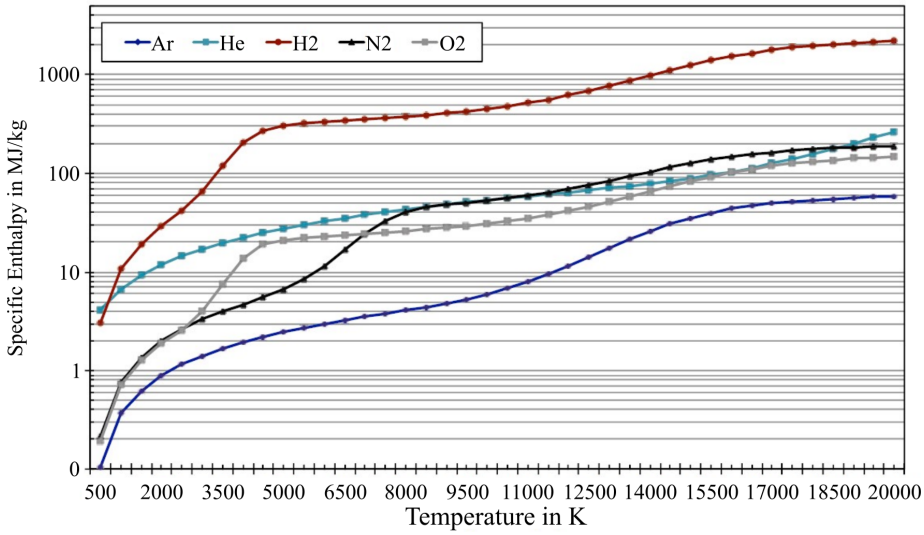

Fig. 2.16 Specific enthalpy of various gases as a function of temperature (Data from [153], graphic from [110]

The plasma spray process can be divided into several sub-processes. The most important ones are Atmospheric Plasma Spraying (APS), Suspension Plasma Spraying (SPS) and Plasma Spray-Physical Vapor Deposition (PS-PVD). These processes differ primarily in the produced coating microstructures, shown in Figure 2.10, which are characteristic for each process. Since these processes were also used to produce the ceramic top coatings in this work, they are described in more detail in the following sections and their differences are explained.

2.4.1 Atmospheric Plasma Spraying

Atmospheric plasma spraying is performed in ambient air. The coating material is injected as a powder into the hot plasma gas stream. There, heat is transferred from the plasma to the powder particles and they are accelerated by the expanding gas. The heat transfer depends on several factors, such as the dwell time in the plasma, the plasma temperature, the thermal conductivity of the plasma and others. The acceleration of the particles depends, among other things, on the velocity of the plasma gas, but also on the particle size and density [154]. The heat transfer from the plasma to the particles and in the particles themselves, as well as the momentum transfer to accelerate the particles, will be described in detail below.

The heat exchange between a single spherical particle and the surrounding plasma proceeds via conduction, convection and radiation. The net energy Q_n [W] absorbed by the particle results from the energy balance between the heat Q_{cv} absorbed by the particle from the plasma by conduction and convection and the heat Q_{sr} emitted by radiation from the surface of the particle to the environment. This energy balance is described by the following Formula 2.4 [155].

$$Q_n = Q_{cv} - Q_{sr} = h \cdot A_p \cdot (T_\infty - T_s) - A_p \cdot \epsilon \cdot \sigma_s \cdot (T_s^4 - T_a^4) \tag{2.4}$$

The heat input into a particle therefore depends on the heat transfer coefficient h [$W \cdot m^{-2} \cdot K^{-1}$], the particle surface area A_p [m^2], the plasma jet temperature T_∞ [K] and the particle surface temperature T_s [K]. The energy emitted by thermal radiation Q_{sr} also depends on the particle surface and its temperature, as well as the particle emissivity ϵ, the Boltzmann constant σ_s [$5.67 \cdot 10^{-8}$ $W \cdot m^{-2} \cdot K^{-4}$] and the ambient temperature T_a [K] [155]. This heat loss should not be ignored, especially for high melting materials like YSZ combined with a large particle surface. The heat transfer in the particle itself $Q_{Particle}$ [$J \cdot s^{-1} = W$] can be described by the particle mass $m_{Particle}$ [kg], the specific heat capacity of the particle $c_{\rho_{Particle}}$ [$J \cdot kg^{-1} \cdot K^{-1}$], and the time-dependent temperature difference $\Delta T/\Delta t$ between the particle core and the particle surface. With low particle thermal conductivity and high energy input, material can evaporate on the surface while the core does not melt. The material vaporized by the overheating of the particle also leads to a heat loss Q_v [129], [156]. In summary, the following Figure 2.17 shows the most important variables of the heat transfer between the plasma and the particle.

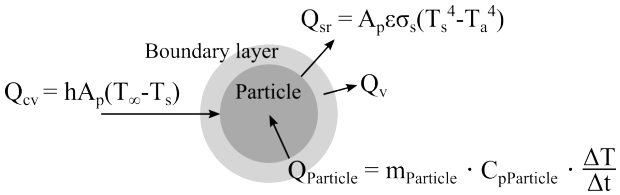

Fig. 2.17 Heat fluxes in a particle during flight according to [156], [110] and [129]

However, the heat transfer is also influenced by the dwell time of the particles in the plasma, which has not yet been taken into account in the relationships described above. As an approximation, it can be assumed that the energy q [$W \cdot s \cdot m^{-2} = J \cdot m^{-2}$] transferred to the particle is proportional to the temperature T_∞ of the plasma, the length l [m] of the plasma jet from the injection point, and the heat transfer coefficient h. In addition, the energy q is indirectly proportional to the velocity of the plasma v [$m \cdot s^{-1}$], resulting in the approximate relationship of equation 2.5 [157]:

$$q = \frac{T_\infty \cdot h \cdot l}{v} \tag{2.5}$$

This formula is only an approximation because it does not consider the effect of the particle size on its acceleration, which also affects the dwell time in the plasma t_A [s]. The dwell time depends not only on the particle radius, but also on the plasma velocity and plasma viscosity. In addition to the plasma temperature and thermal conductivity, these also influence the amount of energy transferred to the particle.

Once the accelerated particles leave the plasma jet, they are no longer supplied with energy and are not further accelerated. They release thermal energy to the environment by thermal radiation, which causes the particle temperature to drop. Moreover, the particles velocity decreases, caused by friction with the air [110]. Due to these effects and the fact that not all particles are completely melted because of plasma fluctuation, radially changing temperature and velocity profile of the plasma and non-ideal injected particles, the particles arrive at the substrate in different conditions. These are shown in Figure 2.18. It is important to note that the particles can arrive at the substrate in any of the stages shown. Stage S0 describes the solid initial particle. If it is heated in the plasma, it can reach state S1, where the shell is molten but the core is still solid. When the particle exits the plasma jet at this stage, it can either reach the substrate in this state, or sufficient thermal energy is emitted to reach stage S2 or S3. At stage S2, the outer shell solidifies again, leaving the core in its initial state, surrounded first by a layer of molten material and then by a resolidified shell. If further energy is released, stage S3 is reached, in which the entire particle is in a solid state again. The core is still in its initial state and the outer region is resolidified material. However, if a particle does not leave the plasma jet in state S1 and further energy is applied, it can melt completely, which is shown in state S4. Again, there is the possibility of leaving or remaining in the hot plasma. If more energy is added, material can evaporate, reducing the particle diameter (stage S5). If the particles leave the plasma jet in stage S4 or S5, again partial or complete solidification can occur. If only the outer shell solidifies and the core remains liquid, stage S6 is reached. If there is a complete resolidification, the particel is described by stage S7. Since particles can be deposited in the coating at any of the stages described, they have a major influence on the coating microstructure. In addition, targeted process control can be used to achieve a desired particle stage when hitting the substrate, to form a specific coating microstructure [158].

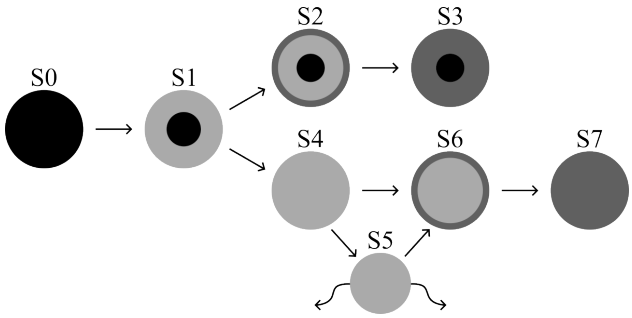

Fig. 2.18 Different conditions in which particles can impact at the substrate according to [158]: unmolten (black), re-solidified (dark gray), liquid/molten (light gray)

When the particles hit the substrate, a coating is formed. Each particle has a specific kinetic and thermal energy due to its particle properties (diameter, velocity, temperature, density, viscosity, etc.). This is decisive for the deformation of the particle on impact. The surface roughness of the substrate or the coating already applied also plays an important role. The molten particles expand greatly on impact and form a flat disk-shaped

structure, also known as a splat (Figure 2.19 (a)), or explode (Figure 2.19 (b)). Since the substrate is at a much lower temperature than the impacting particles, the particles solidify very quickly accompanied by a volume contraction. This contraction results in mechanical interlocking of the particles with the substrate or the previously deposited layer. Mechanical interlocking is the key adhesion mechanism in thermally sprayed TBCs [110]. In addition, the rapid cooling of the particles also ensures the formation of the desirable metastable tetragonal t'-phase mentioned in Chapter 2.2.4.

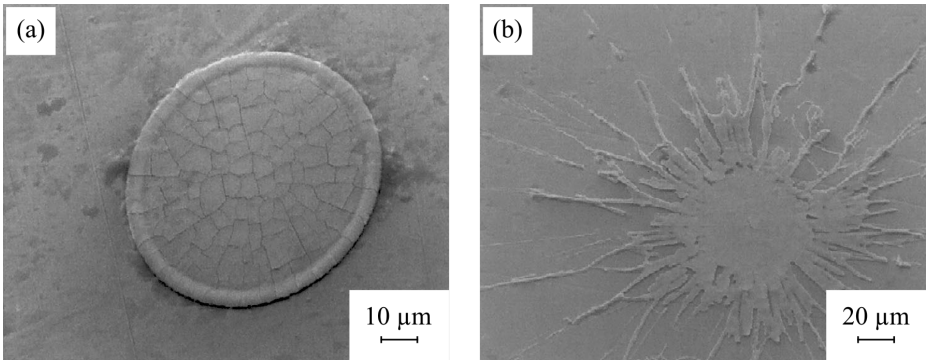

Fig. 2.19 Single splats of plasma-sprayed YSZ: (a) pancake-shaped particle, (b) fragmented particle [159]

The overlapping of individual disk-shaped splats creates the characteristic lamellar coating microstructure of APS coatings, as shown in Figure 2.20. Rapid cooling of the particles leads to the formation of inter- and intralamellar cracks ((i) and (ii)) and globular pores (iii). In addition, particles of state S0, S1, S2 or S3, which were not or only partially melted, are deposited in the coating (iv). As a result, there is material in the coating containing phases of the raw material. Therefore, many powders have a small amount of the monoclinic phase, which undergoes the undesired phase transformation during cooling. The completely or partially unmelted particles also introduce their internal porosity, which depends on the powder manufacturing process, into the system. Pores are also formed by gas inclusions and holes in the coating caused by shadow effects when the lamellae or unmelted particles overlap (v).
The microstructure of the coating is mainly responsible for the physical and mechanical properties of the deposited coating. In particular, the porosity of the coating is important for key properties such as thermal conductivity and Young's modulus. Both the thermal insulation capacity and the elastic modulus of the coating are reduced with higher porosity, which is beneficial for most TBC applications [110]. Higher porosity reduces heat transfer in several ways. The air trapped in the porous structure, which has a lower thermal conductivity, impedes heat conduction. In addition, the porous structure provides greater scattering of thermal radiation, and the increased surface area due to the pores increases radiation emission at high temperatures. Moreover, the microcracks in the coating allow sliding movement between the cracks, increasing the coating's elasticity [112], [111]. However, higher porosity also has a negative effect on the process efficiency and hardness of the coating, reducing its resistance to erosive wear [160], [161]. This can be explained

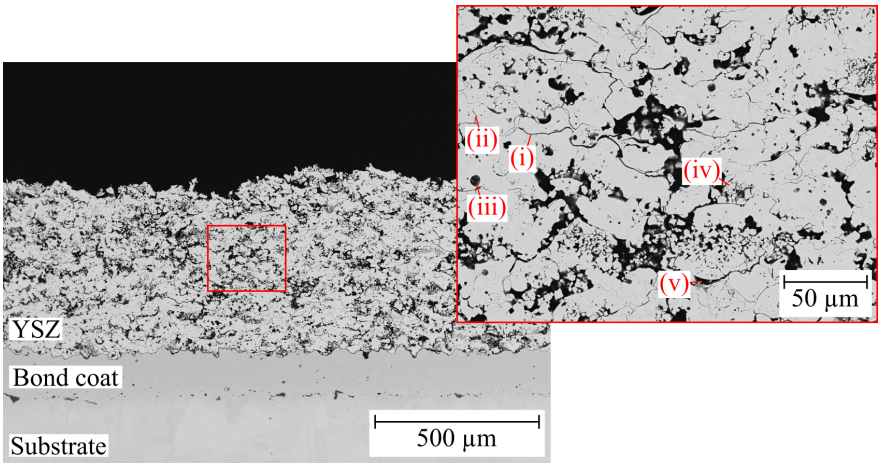

Fig. 2.20 SEM cross-section of an APS coating with (i) intersplat crack, (ii) intrasplat crack, (iii) globular pores, (iv) unmelted particle core, (v) pore due to overlapping splas

by the increased degree of irregular porosity and, in some cases, partially melted or unmelted particles, which affect the cohesion of the coating and cause a tendency for crack propagation [162], [163]. Due to these dependencies, an optimal combination of process parameters is required to achieve the goal of an optimized coating for use in gas turbines. However, targeted process control to achieve the desired coating properties is not always possible. In the APS process, there are 80 to 120 parameters (depending on the author) that influence the process [156]. Some of the parameters interact directly or indirectly with each other and sometimes have oppositional behavior. Since a detailed consideration of the effect of the parameters would be too detailed, the following literature is given for the most important parameters that can be directly influenced. In the literature, current density, process gas flow, spray distance, powder feed rate and carrier gas flow are identified as the most influential of these parameters [164], [165], [166]. Studies that systematically investigate the effect of these parameters and their interaction can be found in [113], [166], [160]. The studies examine either most or all of the listed parameters.
Another way to reduce the elastic modulus of the coating is to introduce vertical cracks into the coating. Such a coating is shown in Figure 2.21, often referred to as segmented or dense vertically cracked (DVC) coating. DVC coatings are typically produced with high plasma power, small spray distances and dense and fine powders. As a result, a large amount of the particles are deposited in the liquid state (S4/S5), creating a dense coating. In addition, the rapid cooling of the splats on the substrate from high temperatures creates large tensile stresses in the coating. These are relieved by the formation of vertical cracks. The cracks act like the columns in an SPS or PS-PVD coating band can reduce the thermally induced stresses in the coating during turbine operation. However, a disadvantage of the coatings is their high density and thus increased thermal conductivity from the surface to the substrate. Parameter studies on the production of coatings with high segmentation crack densities can be found in the references [167] and [168].

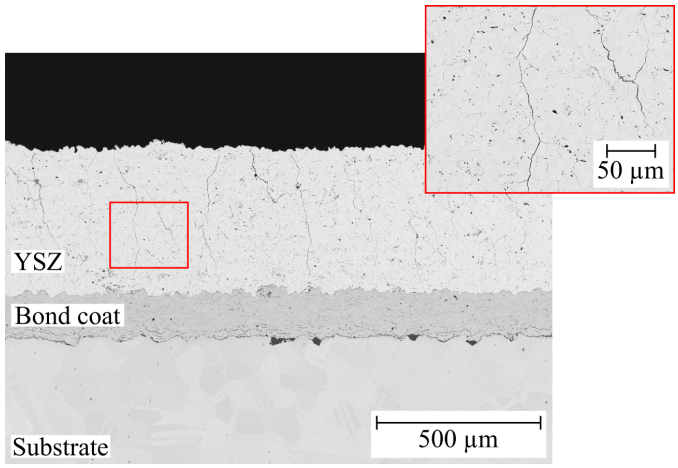

Fig. 2.21 SEM cross-section of a DVC coating with the characteristic vertical cracks

2.4.2 Suspension Plasma Spraying

The difference between the APS and SPS process is how the coating material is injected into the plasma. While in the APS process a dry powder is injected, in the SPS processs a suspension of fine powder particles and a liquid is injected. The liquid is necessary because the very fine powder particles require a carrier liquid to be properly injected into the plasma. Without the liquid, clogging of the feed pipe can occur or high carrier gas flow rates, which negatively affect the plasma, are required for the particles to have sufficient energy to penetrate the plasma. The fluids used are usually ethanol and sometimes water. In addition, a dispersant is added to the liquid/powder mixture, which adsorbs to the particle surface and allows effective dispersion of the particles by electrostatic and steric repulsion [169].

There are two ways to inject the suspension into the plasma: radial injection [169], [170] and axial injection [171], [136], [172]. The plasma and suspension then interact, as shown in Figure 2.22. As the suspension stream enters the plasma, it is atomized into fine droplets, also known as break-up. The suspension is atomized by the shear stresses exerted on it by the plasma [169]. As the droplets break up, they are accelerated and the liquid evaporates. The particles of the droplet form agglomerates as the liquid evaporates. These agglomerates then can split into smaller fragments. The very small particles vaporize in the plasma and the larger particles melt together to form small droplets of molten material. These are further accelerated in the plasma and follow the gas stream towards the substrate. The acceleration and melting of the particles is the same as described for the APS process.

However, the SPS process differs again from the APS process when it comes to coating deposition. The main reason for this is the lower inertia of the very small particles, as shown in Figure 2.22. The plasma gas is deflected and accelerated parallel to the substrate surface in front of the substrate. The small particles follow the deflected plasma gas stream. Flying parallel to the substrate surface, these particles can be deposited laterally on roughness peaks. As the coating grows, the columnar microstructures characteristic

of the SPS process are formed on the roughness peaks. To ensure the particles can be deflected by the plasma gas flow, they must be around 5 µm or smaller [173]. The smaller the particles, the lower their inertia, which increases the deflection in front of the substrate. Due to their inertia, larger particles fly directly towards the substrate without being deflected. Therefore, the efficient atomization of the suspension to form the smallest possible droplets and thus molten particles is particularly important for the formation of a columnar microstructures [174].

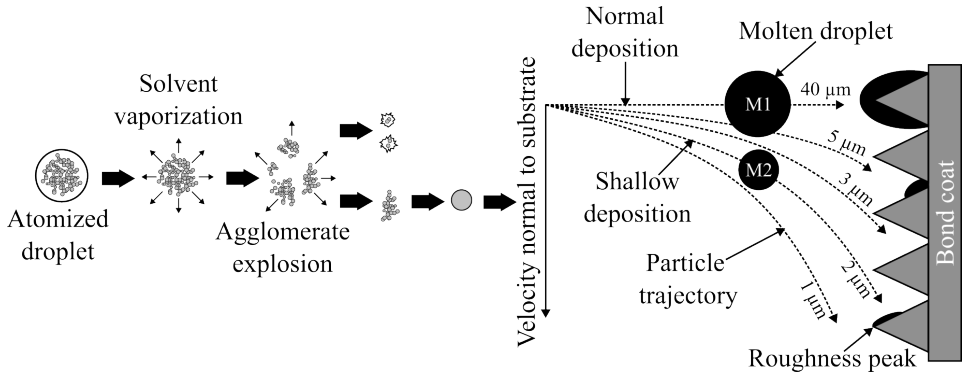

Fig. 2.22 Schematic illustration of the plasma-particle interaction during suspension plasma spraying [175] and the droplet trajectories and their impact on the bond coat asperities [176]

The columnar microstructure characteristic of the SPS process is shown in Figure 2.23. It can be seen that the microstructure is characterized by two alternately stacked layers: Zone (i) is a dense zone consisting of fused, well-bonded particles, and zone (ii) is a porous zone consisting of fine particles deposited individually or as agglomerates in the layer. These are resolidified and have limited cohesion. The larger, fully molten particles are deposited in the dense zone. However, many of the smaller particles resolidify during the longer flight because of the deflected trajectory and are deposited later than (on top of) the larger particles. This is why the porous bands form between the dense areas. During the next pass, the small particles, which are also deflected in front of the large particles in spraying direction, are deposited before the next dense layer is formed [177]. Due to the finely distributed porosity, SPS coatings can even have a lower thermal conductivity than porous APS coatings (0.8 - 1.3 W/mK) with a value of about 0.6 - 0.75 W/mK [114]. Overall, this process, like the APS process, is influenced by a large number of parameters. Systematic studies on the influence of parameters on the coating microstructure in SPS with radial injection, as used in this work, can be found in the references [169], [170], [178].

2.4.3 Plasma Spray–Physical Vapor Deposition

The PS-PVD process differs from the APS and SPS processes as it is not carried out in ambient atmosphere, but at very low pressure. A low chamber pressure and a high torch power are required to transfer the coating material into the vapor phase for the deposition of a fine columnar microstructure. In this process, the pressure of the plasma emerging

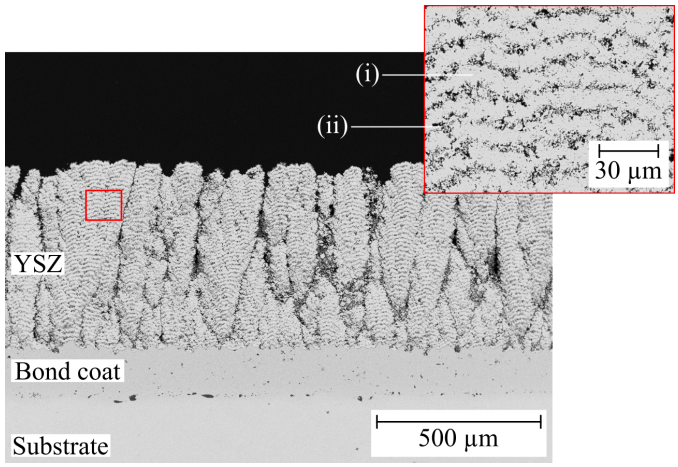

Fig. 2.23 SEM cross-section of a SPS coating with the characteristic microstructure and different layers: (i) dense layer with well bonded splats, (ii) porous layer with re-solidified particles with low cohesion

from the plasma torch is higher than the chamber pressure, which means that the plasma is underexpanded. As a result, the gas expands as it exits the torch, creating a highly linear, long plasma stream. Due to the low chamber pressure, the plasma stream interacts hardly with the surrounding atmosphere and therefore does not cool or slow down much [179].

The growth of the columnar microstructure depends on the degree of evaporation of the injected coating material and can be divided into three stages. Initially, randomly oriented grains form at the bond coat/coating interface, a process known as nucleation. This occurs as a result of condensation of the vaporized material on the relatively cold substrate. In the subsequent structure of the coating, nucleation is replaced by grain growth. This is the growth of elongated grains without crystallographic orientation. In the final stage of the coating structure, the elongated grains grow into large columns. These grow with a preferred crystallographic orientation [180].

The microstructure of a columnar PS-PVD coating is shown in Figure 2.24. The gaps between the columns provide the high strain tolerance of these systems. However, they also have the disadvantage of being in the direction of heat flow, which compromises the insulating properties. In addition, the columns themselves are very dense and do not have microcracks parallel to the coating plane. As a result, the columns themselves are also better thermal conductors than the APS or SPS coatings. How the different process parameters influence the coating deposition can be found in the references [181], [182], [183].

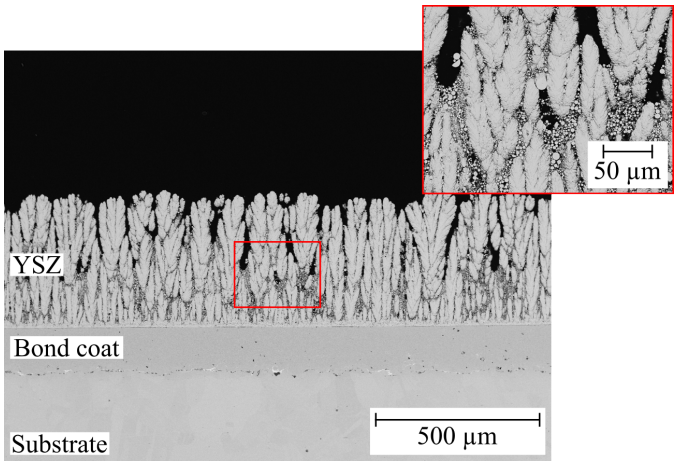

Fig. 2.24 SEM cross-section of a PS-PVD coating with the characteristic microstructure

3 Materials and Coating Facilities

3.1 Materials

3.1.1 Substrates

The TBC systems of this thesis were deposited on superalloys as well as stainless steel and steel substrates. The stainless steel (1.4571) and steel substrates (1.0038) were only used for optimization of process parameters, not for relevant experiments analyzed and discussed in this thesis. Therefore, they are not described in detail.
Vacuum-melted, vacuum-cast nickel-based superalloys with the designations IN738 and C263 were used as substrate materials for the results presented in this thesis. The chemical composition of the two nickel-based alloys is given in Table 3.1. Precipitation hardening of these alloy is caused by precipitation of the γ'-(Ni_3Al,Ti) phase. The main difference between these alloys is that the C263 alloy contains a significantly higher amount of Co, Mo and Cr. This contributes to the excellent oxidation resistance of the material up to about 980 °C. However, at higher temperatures, the Cr_2O_3 phase can form, which evaporates at high temperatures, leading to material degradation. This process is accelerated in the presence of H_2O in the atmosphere [184]. IN738, on the other hand, contains a higher amount of Al and Ti, which is necessary for the formation of the γ'-phase and thus for precipitation hardening. In addition, the IN738 alloy contains the additional elements W, Ta and Nb, which act as carbide formers or precipitate in the γ-nickel matrix. In the γ-phase these elements then leads to solid solution hardening. This combination of precipitation and solid solution hardening in the superalloys gives the IN738 excellent high temperature creep resistance combined with hot corrosion resistance [185].
The melting range of the alloys is 1300 - 1355 °C for C263 and 1230 - 1315 °C for IN738. The densities are comparable at 8.4 and 8.1 g/cm^3, respectively. The thermal expansion responsible for stress generation in the ceramic surface layers is about 10.3 - 18.1 $\cdot$ 10^{-6} 1/K (RT - 1000 °C) for C263 and 12.0 - 15.6 $\cdot$ 10^{-6} 1/K (RT - 1000 °C) for IN738. This means that the thermal expansion of IN738 is lower at high temperatures and can help to reduce the stress caused by the mismatch in coefficients of thermal expansion.

3.1.2 Bond Coats

Two cobalt-based powders and one nickel-based powder served as bond coating powders in this study. The chemical compositions of these alloys are listed in Table 3.2. Each of these powders was manufactured via the gas atomization method, resulting in spherical morphology.
The CoNiCrAlY alloys used are Amdry 9954 and Amdry 995C from Oerlikon Metco (Wohlen, Switzerland), beeing identical in their chemical composition. Due to their composition, CoNiCrAlY alloys combine the advantages of NiCrAlY alloys, which have excellent high temperature oxidation resistance, and CoCrAlY alloys, which have excellent hot corrosion resistance. Although their chemical compositions are identical, the Amdry 9954

Tab. 3.1 Chemical composition of substrate materials in wt.% according to data sheet

	Ni	Cr	Mo	Co	Ti	Al	Ti+Al	W	Ta	Nb	Other
IN738	Bal.	15.7-16.3	1.5-2.0	3.0-9.0	3.2-3.7	3.2-3.7	6.5-7.2	2.4-2.8	1.5-2.0	0.6-1.1	<0.2
C263	Bal.	19.0-21.0	5.6-6.1	19.0-21.0	1.9-2.4	0.3-0.6	2.4-2.8	-	-	-	<2.0

Tab. 3.2 Chemical composition of bond coat powders in wt.% and their respective particle size distribution according to data sheet

	Co	Ni	Cr	Al	Mo	Ta	Si	Y	C	Other	PSD [µm]
Amdry 9954	Bal.	29.0-35.0	18.0-24.0	5.0-11.0	-	-	-	0.1-0.8	-	<1.0	-63 +11
Amdry 995C	Bal.	29.0-35.0	18.0-24.0	5.0-11.0	-	-	-	0.1-0.8	-	<1.0	-90 +45
Metco 2253A	-	Bal.	22.0-28.0	5.0-11.0	3.0-7.0	3.0-7.0	0.4-1.2	0.1-0.8	0.5-1.3	<1.0	-45 +11

and Amdry 995C powders differ in their particle size distribution (PSD). While the Amdry 9954 alloy has a PSD of -63 +11 µm, the Amdry 995C alloy has a PSD of -90 +45 µm. The CTE responsible for the out-of-plane stresses generated in the top layer of the TBC system is 13 - 16 · 10^{-6} 1/K for this type of alloy [57], [186].
The nickel-based alloy applied is the Metco 2253A alloy, also from Oerlikon Metco (Wohlen, Switzerland). This is a NiCrAlMoTaSiYC alloy, featuring the addition of Mo and Ta to enhance thermal cycling life by significantly reducing coefficient of thermal expansion of the alloy. The alloy's CTE is about 15.5 · 10^{-6} 1/K at 1100 °C, but down to 800 °C it is only about 12.0 · 10^{-6} 1/K (other alloys have values of 15 - 16 · 10^{-6} 1/K). This reduction in thermal expansion minimizes stresses in the top coat during thermal cycling. Moreover, the Metco 2253A alloy demonstrates improved creep resistance due to higher microhardness and a slower growth rate of the TGO layer, attributed to a lower aluminum migration rate. The lower outward diffusion of aluminum was attributed in the study to chromium/molybdenum carbide particles, tantalum carbide particles, tantalum and molybdenum atoms in solid solution, which acted as barriers to the diffusion. Furthermore, this alloy offers resistance against sulfidation-based hot corrosion [187]. The PSD of this powder is -45 +11 µm.

3.1.3 Top Coats

The ceramic materials utilized for the top coatings were all provided by Oerlikon Metco. A total of five different yttrium partially stabilized zirconia powders were employed for the APS process. These include the Metco 204C-NS, 204NS, 204F, 233C and 214A, all exhibiting similar compositions, as shown in Table 3.3. The three powders of the 204-family differ only slightly in composition. All three powders are agglomerated, spray dried and plasma densified (HOSP = Hollow Oxide Spherical Powder) powders (Figure 3.1 (a)). These densified, spherical powder particles provide good powder feedability and high deposition efficiency, reducing coating time and powder waste due to overspray. The primary difference between the three powders, Metco 204C-NS, Metco 204NS and Metco 204F, is their PSD, as shown in Table 3.4. The particle size distribution affects the microstructure of the coating. The finer powders are suitable for producing dense lamellar or even dense vertically cracked coatings. The coarser the powders, the more suitable they are to produce porous coating microstructures.
Another powder sprayed with the APS process is the agglomerated and sintered Metco 233C (Figure 3.1 (b)). The agglomerated and sintered powders are easy to feed due to their spherical shape and their porous microstructure makes them particularly suitable for the production of porous TBC coatings. If the particles are not or only partially melted in the plasma and still deposited in the coating, the internal porosity of the particles is retained, increasing the overall porosity. In terms of composition, the Metco 233C differs from the powders of the 204 family only by a slightly higher yttrium content and slightly lower amount of impurity oxides (Table 3.3). As shown in Table 3.4, the particle size distribution is relatively coarse and almost comparable to the largest of the three powders used from the 204 family, which is also beneficial for the production of porous coatings.

Tab. 3.3 Chemical composition of different top coat powders in wt.% according to data sheet; * Maximum amount included in ZrO_2; 6700 an GZO measured with ICP-OE

Metco	ZrO_2	HfO_2*	Y_2O_3	SiO_2	TiO_2	Al_2O_3	Fe_2O_3	Other oxides	Monoclinic Phase
204C-NS	Bal.	<2.5	7.0-8.0	<0.7	<0.2	<0.2	<0.2	<1.0	~10
204NS	Bal.	<2.5	7.0-8.0	<0.3	<0.2	<0.2	<0.2	<1.0	~10
204F	Bal.	<2.5	7.0-8.0	<0.7	<0.2	<0.2	<0.2	<1.0	~6
233C	Bal.	<2.0	7.0-9.0	<0.5	<0.2	<0.2	<0.2	<0.8	<6
214A	Bal.	<2.5	7.0-8.0	<1.0	<0.5	<1.0	<0.5	<1.0	<6
6700	Bal.	~2.0	~7.0	<0.01	<0.01	<0.01	<0.01	<0.01	n.a.
6608	Bal.	<2.5	7.0-8.0	<0.05	<0.05	<0.05	<0.05	-	<10
	ZrO_2	HfO_2*	Gd_2O_3	SiO_2	TiO_2	Al_2O_3	Fe_2O_3	Other oxides	Cubic Phase
GZO	Bal.	~0.9	58.0-59.0	<0.01	<0.01	<0.04	<0.01	<0.04	100

Tab. 3.4 Particle size distribution of the ceramic top coat materials; * Taken from Oerlikon Metco data sheets, ** Size of the particles in a suspension with 25 wt.% solids content

	Nominal Range [µm] *	Measured PSD [µm]			Viscosity	Sufrace Tension	Production method
		d_{10}	d_{50}	d_{90}	[Pa·s]	[mN/m]	
Metco 204C-NS	-147 +45	52.1	77.4	110.9	-	-	HOSP
Metco 204NS	-125 +11	31.4	64.9	98.3	-	-	HOSP
Metco 204F	-45 +15	14.5	23.7	36.4	-	-	HOSP
Metco 233C	-125 +45	57.8	77.2	101.91	-	-	Agglomerated & sintered
Metco 214A	-45 +11	21.4	31.0	44.2	-	-	Fused & crushed
Metco 6700	-30 +1	6.1	10.8	18.4	-	-	Agglomerated
Metco 6608**	n.a.	0.3	0.6	1.3	0.002	22.4	HOSP (milled)
GZO**	n.a.	0.4	1.5	4.9	0.0015	21.6	HOSP (milled)

The fifth powder utilized in the APS process is the fused and crushed powder Metco 214A (Figure 3.1 (c)). This powder is very dense and relatively fine, as shown by the PSD in Table 3.4. The fine and dense particles are designed to melt quickly and completely in the plasma. This makes the powder particularly suitable for producing dense, vertically cracked coatings. Compared to the other powders, the chemical composition in Table 3.3 shows that this powder has the highest amount of impurity oxides.

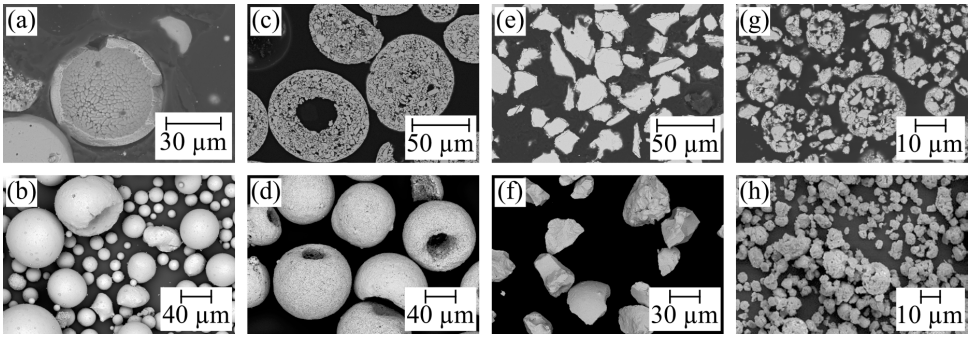

Fig. 3.1 SEM images of ceramic powders produced with different manufacturing processes: (a), (b) HOSP (204NS); (c), (d) agglomerated and sintered (233C); (e), (f) fused and crushed (214A); (g), (h) agglomerated (6700) [188]

Another powder processed in this work is the Metco 6700, which is an agglomerated powder that is atomized and dried from a slurry in a spray drying process (Figure 3.1 (d)). The agglomerated powder is very fine as shown by its PSD in Table 3.4. Thus, it is used to evaporate in the PS-PVD process to form the columnar structured coatings. The chemical composition of this powder is also comparable to the other powders sprayed in this thesis. However the amount of impurity oxides is rather low for this material. Furthermore, the particles in the powder are bound only by a binder, which evaporates in the plasma. In the agglomerates, the particles are present as ZrO_2 and Y_2O_3, but not as YSZ phase [189].

In addition to the powders for the APS and PS-PVD processes, two different suspensions were utilized for suspension plasma spraying. One is a commercial YSZ suspension from Oerlikon Metco and the other is a not yet commercially available suspension with gadolinium zirconate as the solid, which was provided by Oerlikon Metco's research and development center in Westbury, USA.
The commercial YSZ suspension is called Metco 6608 and is made from a high purity HOSP powder. The chemical composition of this powder is shown in Table 3.3. The ceramic solids content of the suspension is 25 wt.%. The powder is mixed with ethanol and then milled to the particle size shown in Table 3.4. A dispersing agent is also added to ensure high stability and low viscosity of the suspension. The viscosity of the suspension was measured to be 0.002 Pa · s and the surface tension to be approximately 22.4 mN/m. Like the YSZ suspension, the GZO suspension was prepared from a powder material. The powder was again mixed with ethanol to reach a ceramic solids content of 25 wt.% in the suspension. A dispersing agent was also added and the powder particles were milled to reduce their size. Since this is a non-commercial suspension, no information is available on

the chemical composition or particle size distribution. Therefore, the chemical composition (Table 3.3) was determined by Oerlikon Metco using the ICP-OE method. The PSD, viscosity and surface tension values determined at FZJ are given in Table 3.4.

3.2 Sample Geometries

In this thesis, various substrate geometries made of different materials have been used. For quick identification in the thesis, the different geometries are named in this section and the exact geometry is defined. An overview is given in Table 3.5.
Rectangular substrates with dimensions of 30 x 25 and 25 x 25 mm^2 were prepared for parameter optimization. Samples of C263 material, with a thickness of 3 mm, were utilized for analyzing the as-sprayed coating of the optimized systems as well as for parameter optimization. In addition, rectangular substrates made of steel (1.0038) and VA steel (1.4571) with a thickness of 2 mm were used for process optimization. These geometries will be referred to as C263, steel and VA steel substrates.
For burner rig tests and thermal cycling experiments in the furnace, cycling buttons were manufactured from IN738. A sketch of the cycling sample geometry is shown in Figure 3.2. These samples measure 30 mm in diameter and 3 mm in thickness, with rounded outer edges to reduce stress levels and prevent edge failure. The outer groove and hole for a thermocouple were added exclusively to the burner rig specimens. The outer groove is used to mount the specimen in the test stand. The specimen geometries are referred to as cycling button and furnace cycling button.

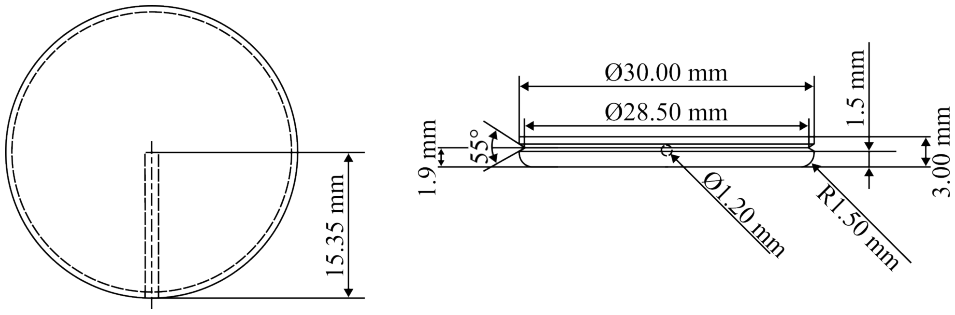

Fig. 3.2 Sample geometry of a standard burner rig cycling sample

For the LASAT tests, samples of various dimensions were used across different test series, which can be found in Table 3.5. The decisive factor for this type of test is the substrate thickness, as it is important for the shock wave propagation. In the initial pre-tests, the substrate thickness was approximately 1.9 and 1.3 mm. Substrates with a thickness of 3 mm were employed for the first systematic test series, while a thickness of 2 mm was chosen for the final test series. All substrates were made of IN738. These samples are referred to below as LASAT substrates or samples. The specific thickness of the substrates is always provided in the text.

Tab. 3.5 Designation of the various substrate geometries used in this study and their applications

Designation	Material	Size [mm]	Application
C263 Substrates	C263	30 x 25 x 3	Parameter optimization
		25 x 25 x 3	As-sprayed analysis
Steel Substrates	1.0038	30 x 25 x 2	Parameter optimization
		25 x 25 x 2	
VA Steel Substrates	1.4571	30 x 25 x 2	Parameter optimization
		25 x 25 x 2	
Cycling button	IN738	⌀ 30 x 3	Burner rig tests
			Furnace cycling tests
LASAT substrates	IN738	⌀ 30 x <2	LASAT pre-tests
		30 x 25 x 3	LASAT tests
		35 x 30 x 2	
Erosion substrates	IN738	25.4 x 50.8 x 3.175 (1 x 2 x 0.125 Inch)	Erosion tests PS-PVD
	1.4571	25.4 x 50.8 x 3	Other erosion tests

For the erosion tests, samples measuring 25.4 x 50.8 x3.175 mm (1 x 2 x 0.125 inches) were produced from IN738 and stainless steel (3 mm thick (1.4571)). IN738 substrates were used for the PS-PVD samples due to the high temperatures encountered during coating. Stainless steel substrates were utilized for the remaining coating systems. Since the substrate does not influence the test results of the erosion experiments, both are referred to as erosion substrates or samples.
All substrates were roughened by grit blasting with F36 Al_2O_3 grit at 4 bar pressure, before applying a coating. After grit blasting the substrates were cleaned first with compressed air and finally in an ultrasonic bath.

3.3 Production of Metallic Bond Coats

3.3.1 Vacuum Plasa Spraying (VPS)

The VPS bond coats utilized in this study were produced by Oerlikon Metco in Wohlen, Switzerland, using the company's MultiCoat system and SinplexPro torch. The coating process involved evacuating the vacuum chamber to a pressure of less than 1 mbar, followed by coating the substrates at a pressure of 30 to 50 mbar. Prior to powder injection and the subsequent coating process, the substrates were preheated with the plasma to a temperature of 400 - 500 ℃. The bond coat powders described in Section 3.1.2 were employed for the preparation and evaluation of different bond coat layers, each deposited with different process parameters. The specific process parameters are listed in Table 3.6, which also includes the names of the various bond coats referred to in this thesis. It should be noted that for confidence reasons only parameter ranges can be given for the parameters used.
The sprayed bond coats include the Standard Bond Coat, the Graded Bond Coat, the Flash Bond Coat and the 2253A Bond Coat. The Standard Bond Coat was once manufactured by Oerlikon Metco and is referred to as Standard Bond Coat. In addition, the standard bond coat from the author's institute, which was produced using the same process and powder on an identical facility at IEK-1 (FZJ), served as a further standard and reference for the other optimized bond coats. This bond coat will be referred to as the Standard

Bond Coat of the FZJ. Its production will not be discussed in detail as it similar to that of the Standard Bond Coat produced by Oerlikon Metco. Moreover, these bond coats were not produced during this thesis. Historical data produced at FZJ with this bond coat was taken as reference.
In the following sections, the manufacturing methods and the respective applications of these different bond coats are explained in more detail. To test the bond coats in thermocycling tests, they were all coated with the Standard Top Coat, the production of which is explained in Section 3.4.1.
The Standard Bond Coat, was used for all optimized topcoat systems to compare their performance independent of the bond coat. Furthermore, a comparison of the optimized top coats with the standard top coat of the IEK-1 should be possible. The Standard Bond Coat is produced with Amdry 9954 powder and the parameters listed in Table 3.6.
To improve the performance of the bond coats, two different strategies have been pursued. The first method is to increase the surface roughness to enhance the adhesion of the ceramic top layer to the bond coat [190]. Studies have shown that increasing the roughness of the bond coat can extend the life of TBC systems during thermal cycling by improving the adhesion of the ceramic and by suppressing crack propagation along the TGO [135]. This approach of increasing the roughness of the bond coat is pursued with the Graded and Flash Bond Coat. In both cases, the particles are less melted in the plasma by reducing the plasma power, or they solidify again in flight outside the hot plasma, resulting in less flattening upon impact on the substrate, thereby increasing the roughness of the bond coat. The parameter ranges for production are given in 3.6. Like the Standard Bond Coat, the Graded Bond Coat was produced with Amdry 9954 powder. The first layers of the bond coat were sprayed with the same parameters as the Standard Bond Coat. For the last layers, the torch power was reduced by decreasing the current and process gas flow, and the spraying distance was extended to increase the amount of resolidified particles. For the Flash Bond Coat, the first layers were also sprayed with the Amdry 9954 and standard parameters. Subsequently, the torch power was also reduced for the last passes and the Amdry 995C powder was used. As described in section 3.1.2, this powder has the same chemical composition as the Amdry 9954, but a coarser particle size distribution, which requires more energy to melt the particles. In combination with the lower plasma power, this results in less melting of the particles upon impact on the deposited layer, increasing the surface roughness.
The other way to optimize the bond coat is to improve the thermomechanical properties of the material used with respect to thermal cycling. In this thesis, the Metco 2253A powder introduced in Section 3.1.2 was utilized for this purpose. This powder was developed by Oerlikon Metco and launched in 2022. The study by *He* associated with the powder's development showed that the lifetime of TBC coatings in furnace cycling tests could be improved by adjusting the CTE of the bond coat. Furthermore reducing the martensitic phase transformation and slowing the TGO growth were beneficial for long lifetimes [187]. However, there are no studies on this material investigating its effect on thermal gradient cycling specimens. Therefore, this is investigated in this thesis. The spray parameter ranges for the production of this coating are also given in Table 3.6.

For the LASAT samples, the Flash Bond Coat was used on the one hand, and on the other hand another a bond coat with a smooth surface was developed. With this the influence of the bond coat surface roughness on the adhesion of the ceramics was investigated. This bond coat was also produced with the Amdry 9954 powder. However, the parameters were adjusted as shown in Table 3.6 under the name Smooth Bond Coat.

After applying the bond coat, the substrate-bond coat systems of the thermocycling samples were annealed under vacuum at 1120 ℃ for 2 hours followed by 845 ℃ for 24 hours. This improves the bonding between the two layers and leads to the formation of the β-rich Al phase from which the TGO grows. Some of the Standard Bond Coats, instead, were pre-oxidized so that a TGO is formed before the topcoat is applied. For this purpose, some Standard Bond Coat samples were annealed not in vacuum but in an argon atmosphere (1 atm, 99.999 % purity) at 1140 ℃ for 2 hours and then at 870 ℃ for 16 hours. This diffusion annealing under argon ensures that a thin TGO layer is formed on the bond coat before the ceramic top coat is applied [80].

3.3.2 High Velocity Oxygen Fuel Spraying (HVOF)

The HVOF process was used at FZJ to produce bond coats. The bond coats were produced using Amdry 9954 powder. They were applied on the MultiCoat system from Oerlikon Metco (Wohlen, Switzerland) equipped with a Diamond Jet - DJ gun from Oerlikon Metco (Wohlen, Switzerland). The processing parameters are also shown in Table 3.7 under the name HVOF Bond Coat. These coatings were applied to samples for parameter optimization and to the furnace cycle samples. The furnace cycling samples were vacuum annealed for 2 hours at 1120 ℃ and then for 24 hours at 845 ℃ after application of the bond coats.

Tab. 3.6 Parameter used from Oerlikon Metco for the production of the different VPS bond coats

Name	Powder	Current [A]	Ar [nlpm]	H_2 [nlpm]	Ar [nlpm]	Ar [nlpm]	1 [g/min]	2 [g/min]	Standoff [mm]	Speed [mm/s]
Standard BC	Amdry 9954	900-1000	80-100	-	4-7	4-7	20-50	20-50	350	n.a.
Graded BC	Amdry 9954	900-1000	80-100	-	4-7	4-7	20-50	20-50	350	n.a.
	+Amdry 9954	400-500	80-100	-	4-7	4-7	20-50	20-50	400	n.a.
Flash BC	Amdry 9954	900-1000	80-100	-	4-7	4-7	20-50	20-50	350	n.a.
	+Amdry 995C	800-900	80-100	0-5	4-7	4-7	20-50	20-50	400	n.a.
2253A BC	Metco 2253A	900-1000	80-100	-	4-7	4-7	15-30	15-30	n.a.	130-170
Smooth BC	Amdry 9954	900-1000	80-100	0-5	5-8	5-8	20-50	20-50	n.a.	130-170

Tab. 3.7 Parameter used for the production of the HVOF Bond Coats

			Process gas		Carrier gas					
Name	Powder	N_2 [nlpm]	O_2 [nlpm]	H_2 [nlpm]	N_2 [nlpm]	Feed rate [g/min]	Standoff [mm]	Speed [mm/s]	Meander [mm]	Passes
HVOF BC	Amdry 9954	460	165	630	20	100	200	500	2	1

3.4 Production of Ceramic Top Coats

The ceramic coatings investigated in this thesis were produced with three different processes: APS, SPS and PS-PVD.The equipment, torches and parameters employed for each process are described in the following subsections. The key parameters of the optimized coating systems for the production of thermocycling, LASAT and erosion samples are listed in Table 3.8. Where the parameter optimization itself is discussed in the results sections, the production parameters are referenced and listed in tables in the Appendix.

3.4.1 Atmospheric Plasma Spraying (APS)

Atmospheric plasma spraying was performed to produce the Reference Top Coat system, LASAT samples, and to generate various optimized coating microstructures. All APS coatings in this work were produced on the MultiCoat system at FZJ (except one parameter study on an identical system at Oerlikon Metco in Wohlen, Switzerland). The different guns were mounted on a six-axis robot that moved the gun over the sample surface. The subsequent subsections detail the application of the top coat, along with descriptions of the gun, materials, and parameters utilized.

Reference Coating System
The Reference Top Coat system, also referred to as the Standard Top Coat, serves two primary purposes. One is to provide a coating for evaluating and comparing the performance of the different bond coat systems in thermal cycling tests. The other is to serve as a reference for evaluating the thermal cycling performance of the optimized topcoats. The parameter set of this reference coating is also applied at FZJ to spray a quality standard (in combination with the Standard Bond Coat of FZJ) for long-term comparison of the performance of the burner rig systems. This provides a large number of data points for this topcoat system in burner rig testing, making it particularly suitable as a reference coating system for this project [191], [14].
Metco 204NS powder was utilized as the spray material for production. The ceramic topcoat was applied using Oerlikon Metco's TriplexPro^{TM} 210 three-cathode cascaded torch. The parameters utilized are listed in Table 3.8 under the name Standard TC. The torch was set up with the short injector holder and a 1.8 mm diameter injector. In addition, the samples were cooled from the front during the process at a pressure of 4 bar.

APS Coatings With Different Surface Roughnesses
APS coatings with different surface roughness were produced for double-layer systems. The TriplexPro^{TM} 210 three-cathode cascaded torch was utilized, and the torch setup was the same as for the reference coatings. Metco 204NS powder was also used. In addition, the first layers of these APS coatings were applied with the spray parameters of the Reference Top Coat. Only the last four passes were sprayed with different parameters. The parameters of the adjusted layers are listed in Table 3.8 as APS2 and APS3. The total number of passes is the sum of the passes with the Standard Top Coat parameter and the four passes with the adjusted parameter. In this way, the effect of the different parameters on the resulting layer structure and properties was minimized and only the surface was modified.

LASAT Top Coats
The top coats for LASAT were produced with Oerlikon Metco's TriplexPro^{TM} 210 three-cathode cascaded gun with the same setup as well. However, the parameters were adjusted to match the powders applied from the Metco 204 family and the desired coating properties. The parameters are listed in Table 3.8 under the designations LASAT porous and LASAT dense. The Metco 204C-NS powder was used to produce the porous coatings with low top coat adhesion. The parameters were selected to deposit the powder under relatively cool conditions. However, due to the coarser powder particles, more power had to be applied to the plasma to melt or partially melt the particles. Therefore, the current, argon flow and helium flow were increased slightly and the carrier gas flow was adjusted accordingly. The Metco 204F powder was instead used to produce the dense coatings with high adhesion. Therefore, hot deposition conditions were created to ensure complete melting of the fine powder particles. This was accomplished by increasing the current compared to the production of the reference system and by using hydrogen as a secondary process gas instead of helium to introduce more power into the plasma. Furthermore, hydrogen increases the heat transfer from the plasma to the particles. In addition, the cooling was eliminated and the spray distance and robot speed were reduced. The amount of powder fed was also reduced to extract less energy from the plasma during powder injection. The carrier gas flow was adjusted to match the changed process parameters.

Highly Porous Coatings
The highly porous APS coating is the first topcoat specifically optimized for thermal cycling tests in the burner rig. It is deposited with Metco 233C powder and Oerlikon Metco's single-cathode cascaded SinplexPro torch. The torch was set up with the long injector holder and two injectors with a diameter of 2 mm. The powder was injected into the plasma from above (0°) and below (180°) the spraying axis. Like the reference coatings, the samples were cooled from the front with 4 bar compressed air. The parameters have been optimized in terms of mechanical properties and microstructure in a study by the author of this thesis and his colleagues [113]. These parameters allow some of the coarse and porous particles to be melted only on the surface, resulting in good adhesion of the coating while maintaining the porosity of the powder particles themselves. The optimized parameters applied to prepare the thermal cycling, erosion and bending samples can also be found in Table 3.8 under the name Opt. APS.

Dense Vertically Cracked DVC Coatings
The second APS topcoat optimized for thermal cycling is the segmented or vertically cracked topcoat. These coatings were also deposited with Oerlikon Metco's SinplexPro single-cathode cascaded torch. Optimization tests were performed spraying Metco 233C and Metco 214A powders as coating materials. High feed rates were applied for the Metco 233C powder, and therefore, as for the highly porous APS coatings, two 2 mm diameter injectors were set up. These were mounted on both the long and short injector holders for different tests. For the Metco 214A powder, only the long injector holder was set up. Due to lower feed rates, a 1.8 mm diameter injector was used for this powder. The Metco 214A, which is specifically designed for the production of segmented coatings, was employed for the optimized parameter. Instead of front-side cooling, rear-side sample cooling of 2 bar

compressed air was utilized. The other parameters are listed in Table 3.8 under the name DVC.

3.4.2 Suspension Plasma Spraying (SPS)

The SPS coatings were also deposited on the MultiCoat facility at FZJ, using the same TriplexPro^{TM} 210 and SinplexPro torch from Oerlikon Metco as for the APS process. A major difference from APS, however, was the suspension feeding system. For SPS a feeding system developed by FZJ was utilized. In this system, the suspension is fed into the plasma from an overpressured tank [170]. The feed rate is determined by the pressure in the tank and the nozzle diameter. In this work, nozzles with diameters of 80 and 120 µm were used. These nozzles did not have an additional atomizer for the suspension. The SPS coatings were produced with a YSZ and a GZO suspension. The setups and optimized parameters for producing the coatings are described in more detail below. When the optimization of the parameters is discussed in the results section, reference is made to the parameters applied, which are listed in tables in the Appendix.

YSZ Monolayer
The monolayer YSZ coatings, optimized for thermal cycling in the burner rigs, were deposited with the SinplexPro torch. It was equipped with the short injector holder and the 120 µm diameter injector. The samples were cooled from the backside with a pressure of 4 bar during coating. The other parameters can be found in Table 3.8 under the name Opt. SPS.

GZO/YSZ Double-layer
The SPS-GZO coating was developed as the top layer of a ceramic double-layer system evaluated in furnace cycling tests. The coatings were produced with the TriplexPro TM 210 torch set up with the short injector holder. For the optimization both, the 80 and 120 µm diameter injector were tested. For the finally optimized coatings, the larger injector was installed. As with the optimized SPS-YSZ single-layer coatings, the SPS-GZO samples were back-cooled with compressed air at 4 bar. A total of two different optimized SPS-GZO topcoats were compared to the reference system in furnace cycling tests. These are designated GZO LP (low process gas flow) and GZO HP (high process gas flow). The corresponding parameters can be found under these names in Table 3.8.

3.4.3 Plasma Spray-Physical Vapor Deposition (PS-PVD)

The PS-PVD coatings sprayed in this work were deposited with Oerlikon Metco's MultiCoat VLPPS (Very Low-Pressure Plasma Spray) system at FZJ, which was modified for PS-PVD operation. Vacuum pumps were used to reduce the chamber pressure for coating to about 2 mbar. An Oerlikon Metco O3CP plasma generator was equipped for PS-PVD operation. The other parameters can be found in Table 3.8 under the name PS-PVD. During coating, the torch is not moved over the samples as in the other processes, but is swivelled at an angle of 8°.

Tab. 3.8 Spray Parameter for different Top Coats; * Parameter only used for the last four passes of the APS coating (before that Standard TC parameter); ** Pot pressure in bar; *** Feed rate solids content; **** minutes not cycles

Name	Powder (Metco)	Current [A]	Process gas Ar [nlpm]	Process gas He [nlpm]	Process gas H_2 [nlpm]	Feeding gas Ar [nlpm]	Feeding gas Ar [nlpm]	1 [g/min]	2 [g/min]	Standoff [mm]	Speed [mm/s]	Meander [mm]	Passes
Standard TC	204NS	420	46	4	-	2	-	30	-	200	500	2	34
APS2 *	204NS	500	46	4	-	2	-	30	-	150	500	2	5 + 4
APS3 *	204NS	380	46	4	-	2	-	30	-	200	500	2	8 + 4
LASAT porous	204C-NS	450	50	5	-	3.5	-	30	-	200	500	2	9
LASAT dense	204F	450	50	-	6	4.5	-	5	-	120	250	2	9
Opt. APS	233C	411	52	-	6.2	3	3	50	50	161	1000	4	12
DVC	214A	675	80	-	10	4.5	-	35	-	110	350	4	11
Opt. SPS	6608	550	64	-	8	1.5 **	-	12 ***	-	60	1000	2	42
GZO LP	GZO	500	46	4	-	1.5 **	-	12 ***	-	70	1000	2	30
GZO HP	GZO	450	80	8	-	1.5 **	-	12 ***	-	70	1000	2	39
PS-PVD	6700	2400	35	60	5	12	12	8	8	1000	30	-	30 ****

4 Characterisation Methods

A wide variety of materials were used to produce the samples as presented in Chapter 3. Since not all information on the materials was available, tests were performed to determine important properties such as particle size distribution (PSD) and, in case of the suspensions, additional values like surface tension and viscosity. The samples were then examined for microstructural and mechanical properties after deposition of the coatings. Samples with optimized coating systems were thermally cycled to evaluate the performance of the coatings in service. Tests were also performed during thermal cycling and on the failed specimens. The equipment and methods used for all of the tests in this thesis are presented in this chapter.

4.1 Powder and Suspension Characterization

4.1.1 Laser Diffraction - Particle Size Distribution (PSD)

The particle size distribution in powders and suspensions has been determined by laser diffraction, a technique based on the principle of light scattering from particles. In this method, the particles are illuminated with laser light and the intensity of the backscattered light at different scattering angles allows the determination of the particle size. In this work, the PSD was measured with a Horiba LA-950 V2 (Horiba Ltd, Kyoto, Japan). The measurements were performed with 15 iterations, and ultrasonic waves were applied to prevent agglomeration of the particles during the measurement. Due to the different particle size distributions of powders and suspensions, different particle size calculation methods were utilized.
The Fraunhofer method was selected to measure the particle size distribution of the different powders. This method is well-suited for larger particles with diameters in the micrometer range, which is relevant for the powders under consideration. When the laser light projected onto the powder particles hits small particles, large scattering angles are produced, whereas large particles tend to produce smaller scattering angles. Particle size can then be determined by analyzing the intensity and backscatter pattern of the light.
The Braun method, also known as Mie theory, was chosen to calculate the particle size distribution within the suspensions, as this method is particularly suitable for fine particles. Unlike the Fraunhofer method, it considers the interference and interaction of the light with the particles. It relates the size of the particles in relation to the wavelength of the light, making it possible to determine particle sizes in the micrometer and submicrometer range.

4.1.2 Viscosity and Surface Tension of Suspensions

To achieve columnar microstructures with suspension plasma spraying, it is important to atomize the suspension into fine droplets. This ensures that the molten particles fly

parallel to the substrate surface and deposit onto roughness peaks [176]. The size of the droplets post-atomization is influenced by several physical properties of the suspension, such as particle size, density, solids content and the properties of the carrier medium, including viscosity and surface tension [192], [193]. Higher viscosity or surface tension of the carrier medium results in larger droplets. When the carrier medium evaporates, the solids from the droplet melt to form a molten particle. Therefore, larger droplets produce larger particles as they contain more solids in total. The droplet size can be reduced by increasing the process gas flow rate and thus, the gas velocity.
A Physica MCR 301 rheometer (Anton Paar, Graz, Austria) was used to determine the viscosity. The dynamic surface tension was determined with a bubble pressure tensiometer (BPT Mobile, KRÜSS GmbH, Hamburg, Germany).

4.2 Process Efficiency

Deposition efficiency (DE) is an important measure from an economic point of view. High efficiency not only helps in maintaining low material costs but also facilitates quicker coating buildup, resulting in reduced process times and overall costs. The DE is calculated based on the deposited coating's weight, representing the percentage of the total sprayed powder effectively deposited in the coating. Alongside the coating weight, factors such as powder feed rate, step width between meander paths, coated area, robot speed and number of passes are relevant for the calculation of DE. It is calculated according to the following equation 4.1:

$$DE = \frac{Coating\ weight\ [g]}{\frac{Feed\ rate\ [g]}{[s]}} \cdot \frac{Meander\ distance\ [mm]}{Substrate\ surface\ [mm^2]} \cdot \frac{Robot\ speed\ \left[\frac{mm}{s}\right]}{Number\ of\ passes} \cdot 100\ [\%] \quad (4.1)$$

4.3 Microstructure Analysis

Various analytical methods were employed to evaluate the mechanical properties (see Chapter 4.5) or the microstructure of the coatings in the as-sprayed state and after thermal treatment. Some specimens were examined on the surface without any further preparation, while others were examined in metallographic cross-sections. To prepare the cross sections, the specimens were embedded in an epoxy resin under low pressure. Embedding in a vacuum bell has the advantage of infiltrating even fine cracks with epoxy resin and no bubbles are formed. This allows to determine after the preparation if defects are caused by preparation or if they were present before (filled with epoxy). Once the resin hardened, the samples were cut using a Accutom-5 (Struers GmbH, Willich, Germany) equipped with a diamond cutting wheel. Afterward the samples were further processed on an ATM Saphir 550 (Struers GmbH, Willich, Germany) grinding and polishing machine. First they were ground with SiC sandpaper up to 2500 grit and then polished to 50 nm. The different analysis methods used on the sample surfaces or cross-sections are presented in the following subsections.

4.3.1 Scanning Electron Microscopy

Cross sections of all plasma sprayed specimens were examined by scanning electron microscopy (SEM) to determine microstructural characteristics. Three different devices were utilized in this thesis. With the Hitachi TM3000 (Hitachi Hightechnologies Europe GmbH, Krefeld, Germany) the majority of the samples were studied. It was used to take overview images to evaluate crack and column densities and other microstructural characteristics. Higher magnification images were also taken to determine porosity and TGO thickness. Details on determining these values are described in Chapter 4.3.2 on image analysis.
When chemical composition analysis by energy dispersive X-ray spectroscopy (EDX) or high magnification images (> 2000x) were required, the Zeiss Ultra 55 SEM (Carl Zeiss AG, Oberkochen, Germany) or Gemini SEM 450 (Carl Zeiss AG, Oberkochen, Germany) with an Ultim® Max 170 EDS detector (Oxford Instruments NanoAnalysis, Abingdon, UK) were utilized.

4.3.2 Image Analysis

The microstructure was categorized (lamellar, dense vertical cracked, columnar) on overview images of cross-sections taken by SEM at low magnification (between x100 and x300). For DVC coatings and columnar SPS and PS-PVD coatings, crack and column densities were determined from stitched images. For this purpose, overlapping images were taken in the SEM at constant magnification (x150 or x200). These were then stitched manually or using the Fiji software. The cracks and columns were counted along a length of 5 - 10 mm to calculate the feature density in 1/mm. A crack was counted as a segmentation crack if its length was at least half a coating thickness.
Porosity, another essential coating property, was also measured with Fiji software on SEM images of sample cross-sections. Ten images were taken at random locations under constant contrast and brightness settings. A magnification of x1000 was employed for the APS and DVC layers, while a magnification of x2000 was utilized for the columnar layers. This is because the finer particles in the SPS process result in smaller pores and cracks that are not visible at lower magnification. Moreover, higher magnification enables the determination of porosity within individual columns for SPS coatings. The ten images were analyzed using the Fiji software. The same Fourier transformation was applied to each image to sharpen and increase contrast. The threshold was then set manually to capture all relevant pore areas. Unrepresentative coating areas e.g., damaged during preparation, were excluded from the porosity measurement. Using this threshold, the grayscale images were converted to binary images from which the porosity values were measured. The mean value of the ten images is taken as the porosity value for the parameter combination. The error of the mean value is described by the standard deviation of the ten measured values.
The thicknesses of the sprayed coatings and the TGO layers formed during thermal cycling were also measured with the Fiji software. Coating thicknesses were determined on the stitched images by calculating the mean value and standard deviation (error) of at least 20 measured values. For the thickness of the thermally grown oxide layer, ten cross-sectional images with a magnification of x1000 were captured at various points in the interface of

the sample. Up to 15 areas were then measured in each image, resulting in up to 150 measured values for the thickness of the thermally grown oxide layer.

4.3.3 Confocal Laser Microscopy

Another method used for microscopic examination of specimens is confocal laser microscopy. In this method, a focused beam of monochromatic laser light is scanned across the specimen's surface using a movable mirror. This scanning process allows for the precise localization of the laser focus within the specimen. By combining the light image captured at each scanned position with the corresponding position of the mirror/focus plane, a three-dimensional representation of the sample's topography can be reconstructed. The confocal laser microscope was used to image the bond coat surfaces and the APS interlayers of the double-layer systems to evaluate their topography, especially the shape of roughness peaks.

4.3.4 Confocal White Light Topography

The surface roughness of the bond coats and the APS-YSZ interlayers of the double-layer systems were measured with the white light topographic profilometer CT 350T (Cyber Technologies, Eching-Dietersheim, Germany) with a CHR1000 confocal white light sensor. These measurements were used to determine the average roughness values R_a and roughness depths R_z. This instrument was also used with a CHR10000 sensor to examine the topography of cycled samples to identify blister caused by the delamination of the coating at the interface. Additionally, thickness measurements for bending samples were conducted on both sides of the bending samples using two CHR3000 sensors.

4.4 Phase Analysis

4.4.1 X-Ray Diffraction

The Chemical composition and crystal structure of the materials were determined by X-ray diffraction (XRD). This method involves measuring the diffraction of an X-ray beam by the crystal lattice as a function of the angle of incidence (θ). This diffraction is also called Bragg reflection. The specific diffraction patterns provide information about the crystal structure and allow assignment to specific materials. XRD analysis was conducted on raw materials (powders), the surface of bond coats in the as-sprayed state and post-diffusion annealing, as well as the top coats in the as-sprayed state and after thermal cycling in the burner rig or furnaces.
The measurements were conducted with a powder X-ray diffractometer D4 Endeavor (Bruker AXS GmbH, Karlsruhe, Germany) using CuK_α radiation. The data were collected in the 2θ range of 10° to 80° with a step size of 0.02° and a counting time of 0.75 s/step. The analysis of the measured data was performed with the program X'Pert HighScore Plus using the PDF-2 (Powder Diffraction File) database from 2004 of the ICDD (International Center for Diffraction Data).

4.4.2 Raman Spectroscopy

Raman spectroscopy has been applied in this thesis to study the oxide formation on the bond coats after diffusion annealing. In this technique, the sample surface is illuminated with monochromatic laser light, which is then scattered. While most of the scattered laser light retains the same wavelength as the incident light, a small fraction interacts with lattice atoms of the sample, leading to scattered phonons with altered energy. This effect is called Raman scattering. The frequency shift of the Raman-scattered light relative to the incoming laser light is termed the Raman shift and is characteristic of materials and enables the determination of the chemical components of a sample.
Raman mapping was performed using the inVia^{TM} Qontor$^{®}$ (Renishaw GmbH, Pliezhausen, Germany) with a 532 nm laser (~2.5 mW) and a 2400 l/mm grating. The spectra were recorded over an area of 80 µm × 40 µm with a step size of 1 µm in both axial directions, with each measurement requiring one second. The spectra were then processed. Cosmic radiation was removed, each measurement was normalized, and then the multiple spectra were averaged into a single spectrum.

4.5 Investigation of Mechanical Properties

Various mechanical parameters were measured throughout this thesis. Indentation tests were conducted to determine the hardness values and elastic moduli of coating systems. These hardness values were further correlated with coating wear in erosion tests. Additionally, three-point bending tests were executed to measure the Young's modulus of free-standing coatings. Laser shock adhesion tests (LASAT) were employed to measure adhesion between top and bond coats, as well as adhesion within the coatings themselves. Details of the methods used to determine the mechanical properties of the coating systems are given in the following subsections.

4.5.1 Indentation Tests

Different devices were utilized for indentation tests. Two different devices were used for Vickers indentations on polished cross sections and one Rockwell indenter for indentations on the specimen surfaces.
The Duramin A300 instrument (Struers, Willich, Germany) equipped with a Vickers indenter was utilized for HV5 (5 kg load) measurements. For the hardness values of the coatings, a mean value was calculated from ten measurements, with the error corresponding to the standard deviation of these measurements. To prevent mutual interference, the indentations were spaced at a distance of at least three times the indent's diameter. These measurements provide a more global hardness of the coatings, as they are not taken in the bulk material, but also include a large number of pores. The high test load and resulting large indentation helped to avoid a large scatter in the measurement results as the overall hardness of the coating was determined. Since these values were measured for the coatings in the as-sprayed and cycled states, they can be used to analyze the effect of sintering on hardness, as sinternecks grwo and microcracks and pores are closed during thermal treatment.

The second Vickers indenter used in this work is the Vickers H-100 Fischerscope microindenter (Helmut Fischer GmbH, Sindelfingen, Germany). These measurements were also taken on metallographically prepared cross-sections. Due to the higher accuracy of the indenter at low load ranges, it was selected for coatings where measurement with a high test load is not possible due to insufficient coating thickness. In addition, some of the thicker coatings were measured with both Vickers indenters. The ESP (Enhanced Stiffness Procedure) was used with the H-100 Fischerscope, in which the indenter is gradually loaded and unloaded. Eight load steps were used, with 50 % relief after each step before the next higher load was applied. A maximum load of 500 mN was specified. This method can be used to determine the Young's modulus EIT, Vickers hardness HV, and indentation hardness HIT for different load ranges at the same specimen location. Seven indentations were made for each specimen measured.
It is important to note, that the hardness values determined with the two devices are not comparable. In contrast to the high load measurement, the low load measurement is primarily intended to determine the hardness in the bulk material and to minimize the influence of pores. Therefore, the measured hardness is higher with the low load. However, the influence of the bond between the individual splats can be determined, which is reflected in both the hardness values and the elastic moduli.
The third version of the indentation tests was conducted with the Duramin-160 (Struers GmbH, Willich, Germany), equipped with a Rockwell indenter utilizing the HR15N (15 kg load) method. The maximum load was maintained for 4 seconds. Unlike the previous methods applied on cross-sections, these indentations were directly applied to the surface of the sprayed coatings. The mean value was again calculated from ten measurements per sample, with the error calculated from the standard deviation of the individual measurements. This test was performed on all optimized coating systems in the as-sprayed condition, as these coating systems were also tested for resistance to erosive wear in the same state. This allows a correlation between the erosive wear and the hardness values measured on the surface.

4.5.2 Three-Point Bending Tests

Three-point bending tests were performed to determine the time-dependent elastic load capacity and stress relaxation of free-standing coatings at room temperature. Rectangular specimens 15 mm in length and 4 mm in width were cut from free-standing coatings using a diamond saw. The coatings were electrochemically etched as described by *Vaßen et al.* [194]. The thickness of each sample was precisely determined using the Cyber Technologies CT 350T profilometer. The elastic properties and viscoplastic deformation of the free-standing coatings were examined using the TMA dilatometry system Setsys TMA-18 from Setaram Inc. (now: KEP Technologies, Mougins, France). The schematic representation of the test setup is illustrated in Figure 4.1 (a), with a distance of 12 mm between the support points (L). During testing, four loads (15, 30, 45, 60 g) were successively applied to each sample and maintained for 30 seconds. The duration of stress relaxation was incrementally increased between the loads (60, 120, 180, 240 seconds). At least five bending specimens were tested for each spray parameter, and an average value was calculated from the measurement results.

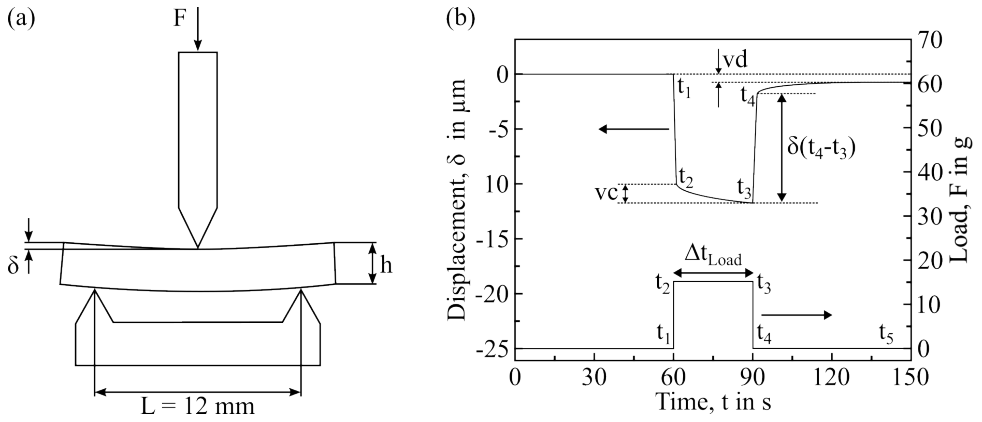

Fig. 4.1 a) Schematic setup of three-point bending test in TMA facility; b) typical progression of loading with time and the resulting viscoelastic/viscoplastic response of the material to in-plane strain [113]

The evaluation was done by fitting the Burger model to the data as described in the literature [111]. The deformation of the sample (δ) was measured continuously. A schematic representation of a strain curve is shown in Figure 4.1 (b). During the application of the load (from t_1 to t_2), the coating undergoes elastic and possibly plastic deformation. After reaching the maximum load, it is maintained constant (from t_2 to t_3). During this period, viscous creep (vc) of the ceramic occurs due to splat sliding, leading to further deformation. When the sample is unloaded (t_3 to t_4), the elastic response decreases again. Additionally, when the load is removed (after t_4), there is a partial recovery of the creep behavior. Nevertheless, a residual displacement remains at the end (t_5), which is called viscoplastic deformation (vd). The elastic modulus was calculated using the displacement during unloading $\delta(t_4 - t_3)$ to exclude the influence of creep during the loading period. Since different loads were applied during the measurement, the force-displacement relationship was taken as the slope of the force-displacement function, which was assumed to be linear. The Young's modulus was then calculated using Equation 4.2. The geometric factor λ is described by the width (b) and height (h) of the specimen, along with the distance (L) between the support pins.

$$E = \frac{F}{\lambda} \cdot \frac{1}{\delta\,(t_4 - t_3)}, \qquad \lambda = \frac{4bh^3}{L^3} \tag{4.2}$$

4.5.3 Erosion Tests

The erosion tests were conducted to evaluate the wear resistance of various top coats against foreign particle impact, adhering to GE erosion test standards at Oerlikon Metco in accordance with ASTM G76-13 [195]. Samples with a geometry of ~25 x 51 x 3 mm (1 x 2 x 0.175 inches) were tested. Since this is not the geometry for the thermal cycling tests, the coating systems were tested only in the as-sprayed condition. A schematic representation of the test setup is provided in Figure 4.2. The sample is mounted at an angle of 20 ± 2° to the nozzle axis. The distance from the center of the sample to the

nozzle outlet is 101.6 ± 1.5 mm (4 inches). The nozzle itself has a length of 95.25 mm (3.75 inches). Al_2O_3 with a grain size of 40 - 80 µm (Biloxit BIR 220) was used as the abrasive material.

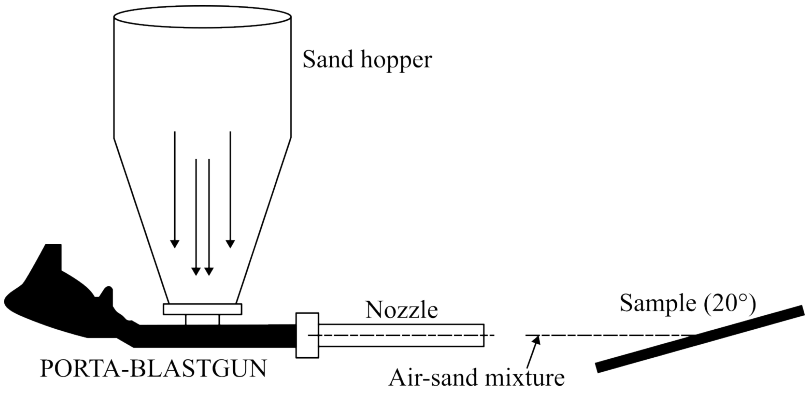

Fig. 4.2 Schematic setup of erosion test stand at Oerlikon Metco

Before measuring the erosive wear, the thickness of the samples is determined and a calibration is done. For this purpose, Lexan plates (Lexan polycarbonate 9030-112) are sandblasted and the exact time is recorded. The parameters are set to remove 1 mil (1/1000 inch = 25.4 µm) of Lexan per 6 ± 0.5 seconds. As a result, the Al_2O_3 particles in this study were accelerated onto the substrate surface at a pressure of 2 bar and a flow rate of 6.5 g/sec. The test duration was set to 30 seconds and several samples of each system were tested.
During the test series, the determination of material removal on the Lexan reference material is repeated multiple times. The difference in coating thickness on the test samples is then measured at the point where the highest removal rate was observed on the Lexan. This approach helps mitigate the influence of irregularities on the coating surface. The coating thickness is measured using a dial gauge with a ball diameter of 5 mm. Determining the Lexan erosion is crucial as the results are presented as a normalized erosion value, denoted as E_{Normal} [sec/mil]. This ensures comparability of measurements over multiple test series. E_{Normal} is calculated according to the Formula 4.3, utilizing the target removal of the Lexan (E_{Target}, 6 sec/mil), the coating removal (E_p, blasting time in sec/removal depth of the material in min), and the actually measured removal of the Lexan (E, blasting time in sec/removal depth in mil).

$$E_{Normal} = \frac{6.0(E_{Target}) \left[\frac{sec}{mil}\right] \cdot E_p \left(\frac{Blasting\ time\ coating\ material}{Depth\ of\ coating\ material\ removal}\right) \left[\frac{sec}{mil}\right]}{E \left(\frac{Blasting\ time\ Lexan}{Depth\ of\ Lexan\ removal}\right) \left[\frac{sec}{mil}\right]} \tag{4.3}$$

4.5.4 LASAT Tests

The aim of LASAT (LAser Shock Adhesion Test) is to introduce controlled defects, if possible, at the interface between the bond and top coat of the coating system, to investigate several aspects. These include damage prediction, as well as determination of

bond strength and remaining life time to failure of the ceramic coating due to aging, which provide important data for understanding and preventing TBC spallation [196]. In particular, predicting the time to failure of the ceramic layer is one of the major challenges in thermal barrier coating system cycling [197]. Especially the TGO layer formed during operation is critical for coating spallation due to energy concentrations from growth and thermal expansion mismatch. As a result, coating spalliation usually occurs at the bond coat/TGO or TGO/topcoat interface. Common tests used to determine coating lifetime untill delamination are the high temperature cycling tests described in the following subsection 4.6. In these the number of cycles to failure is counted to measure the cycling resistance of the coating. In this test, the intrinsic mechanical adhesion is not measured, but evaluated indirectly by the interfacial damage. LASAT instead can be used to determine the interface strength between the metallic bond coat and the ceramic top coat [198]. This is an efficient method for measuring the adhesion of coatings as it is quick and simple and allows easy observation of damage [196]. In addition, the method offers the possibility to observe the development of controlled introduced defects in-situ in cyclic tests, which allows to draw conclusions about the damage progression in the investigated coating system [199].

LASAT Method

The LASAT process is shown schematically in Figure 4.3. A high-power, short-pulse laser is focused on a small area of the sample to be tested (A). At the point where the laser beam is focused, it leads to material ablation. The ablation process (B), generates a plasma, which expands rapidly creating a high-pressure shock wave in the material. The pressure shock wave propagates through the material and coating (C) and is reflected at the opposite free surface. In this process, the compressive shock wave is converted into a tensile shock wave that travels in the opposite direction. As this tensile shock wave moves through the interface between the substrate and the coating, it can interact with the tensile load following the main shock wave and detach the coating if the applied energy is higher than the internal interface strength. If this is the case, cracking will occur at the interface (E) [196], [198].

For thick substrates, such as the 2 mm substrates used in this work, the shock wave propagation must be described in a two-dimensional model, because edge effects change the radial localization of the maximum tensile stresses responsible for the detachment of the coating. This is shown schematically in Figure 4.4. The initial shock wave generated by the expansion of the plasma corresponds to the diameter of the laser shock. However, as it propagates through the material, the presence of edge effects causes a spherical expansion of the wave front. These propagate outward from the shock direction as pressure waves, while the parts facing the shock represent a relief [200], [201]. When the main wave hits the free surface, it is reflected and thrown back as a release wave. When this release wave interacts with the subsequent tensile stresses caused by edge effects, the waves are superimpose, resulting in a maximum tensile stress in the material. The radial location of the maximum tensile stress therefore varies depending on the wave profile, which is related to the thickness of the target and the impact diameter.
The two-dimensional propagation of the shock wave can also explain the increase of the decohesion diameter as a function of the applied laser energy for the same shock diameter,

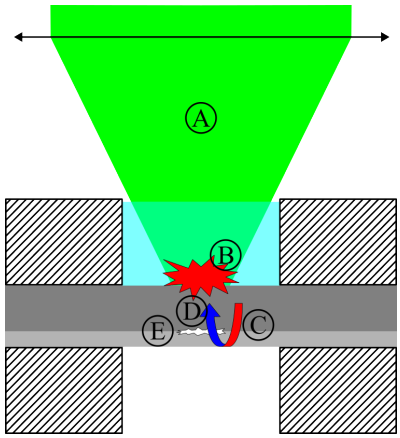

Fig. 4.3 Schematic representation of the LASAT process with: (A) focusing the laser, (B) material ablation and expansion of plasma, (C) compressive shock wave propagation, (D) reflection into tensile shock wave, (E) crack initiation according to [196]

documented in the literature [202]. The intensity of the shock wave gradually decreases with increasing distance from the shock axis. As the applied laser energy increases, the radial area subjected to tensile stresses greater than the fracture strength increases, and consequently the diameter of the decohesion zone also increases. However, for an accurate description of the stresses in the coating system and the shock propagation velocities, interfacial reflections and material specific properties must be considered [203], [204].

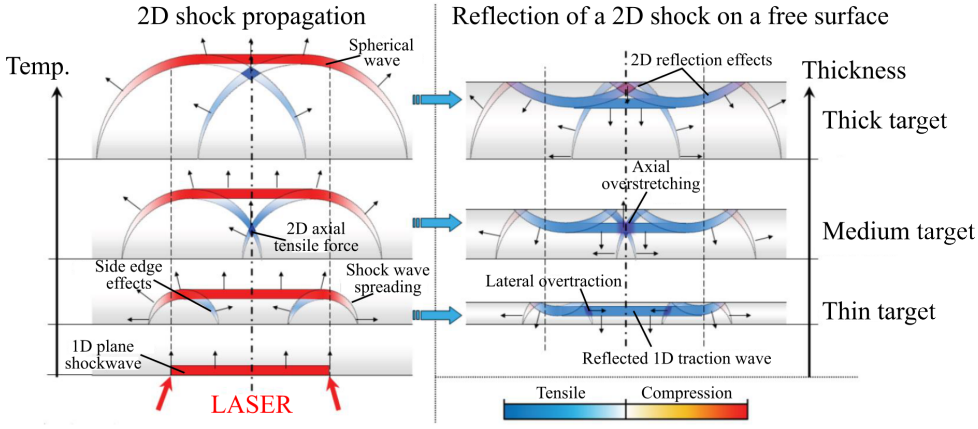

Fig. 4.4 2D propagation of the shock wave and related edge effects [201]

Many studies have been carried out on EB-PVD coating systems using the LASAT method. It was introduced by *Fabre et al.* for this type of coating system and it was shown in the study that cracks can be introduced specifically in the interface [196]. Further studies

on this process, where the shock is applied either on the metallic substrate side or on the ceramic top layer side, as well as tests in the as-sprayed state and after thermal cycling without coating failure, have been published by *Bégué et al.* [202]. The evolution of LASAT induced damage during thermal cycling has been reported by *Guipont et al.* [205] and *Maurel et al.* [197]. Additionally, *Mahfouz et al.* integrated analyses based on this methodology with Finite Element (FE) models to determine failure mechanisms in blisters within EB-PVD coatings [206]. Thus, the LASAT method can be used in coating systems with an EB-PVD topcoat to determine the adhesion energy of the topcoat, or to specifically introduce defects into cycling samples to observe and analyze their development during cycling. This in turn allows to draw conclusions about the damage progression and failure mechanisms of the EB-PVD coatings.
However, there have been no studies on plasma sprayed thermal barrier coatings using this method or analytical approaches similar to those used for EB-PVD coatings. Therefore, the objective of this work was to transfer the approaches used for EB-PVD coatings to the investigation of plasma sprayed coatings.

LASAT Hardware Setup and Sample Treatment
The LASAT investigations were performed at Centre des Matériaux at Mines ParisTech (Paris, France) using the facility shown in Figure 4.5. A SAGA model Nd:YAG laser source (Thales, Paris, France) is installed in this system. The laser operates within the green spectrum, emitting light at a wavelength of 532 nm. The amount of energy acting on the sample can be adjusted between 0.1 and 2 J with a polarization device. The transmitted energy of the laser beam is monitored by a joule meter. The laser source generates pulses with a half-life of 5.2 ns at a frequency of 10 Hz. In the investigations presented in this thesis, the laser was operated in single pulse mode, so that a single pulse of 5.2 ns duration is applied to the samples.

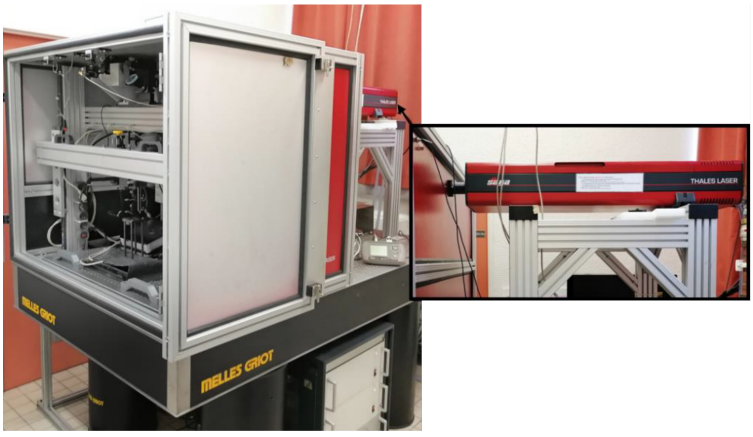

Fig. 4.5 LASAT device of the Center des Matériaux [199]

An additional confining medium can be used at the focal point of the laser. For this purpose, water, glass or a transparent adhesive tape can be applied, of which the adhesive tape with a thickness of 50 µm (3M) was chosen in this work. The confining medium limits the plasma expansion, allowing to generate higher and longer pressure loads with the same laser parameters (power density peak, pulse duration, wavelength) than without a confining medium [207]. Furthermore, two different shock modes can be employed. On the one hand, the shocks can be applied to the metallic substrate side and on the other hand to the ceramic top layer. This changes the shock wave path through the material and is mainly used when it is not possible to apply a shock to the substrate side. This is the case, for example, when coatings are tested on turbine blades. To protect the ceramic, a black adhesive tape, which acts as an ablative medium, is then applied under the transparent adhesive tape, which is used as the confining medium. An approximately 200 µm thick black PVC adhesive tape (3M) was used for this purpose. This could be evaporated by the laser pulse without damaging the underlying coating.
The diameter of the applied shock (D) can be adjusted by the focal plane of the laser. In combination with the laser energy (E) and the laser pulse duration (τ), a surface-related power density of the laser impact can be determined according to the Formula 4.4. This surface-related power density is then utilized to generate the so-called LASAT curves. These curves plot the defect diameters caused by the laser impact against the applied surface energy. An important value that is determined is the LASAT threshold, also known as fracture threshold. This threshold represents the minimum power density above which decohesion is detected in the coated system.

$$\Phi\left[\frac{GW}{cm^2}\right] = \frac{4 \cdot E[J]}{\tau[ns] \cdot \pi D^2_{shock}[cm^2]} \tag{4.4}$$

In this work, the diameters of the introduced defects were investigated with two different methods. On the one hand, non-destructive infrared thermography was employed to detect changes in temperature caused by the defects changing the heat flow. This method allows for immediate evaluation after impact, to evaluate the result and adjust the laser energy for further shocks based on the result obtained [208]. On the other hand, metallographic cross-sections were prepared after the application of all planned tests. These cross-sections were then examined in the SEM, enabling the measurement of crack diameters through analysis of the captured images.
For infrared thermography, an active approach was employed wherein the sample was subjected to a continuous heat source. In this setup, a heating plate maintaining a constant temperature of 60°C served as the heat source, with the sample positioned on top of it and heated from the substrate side. A thermal imaging camera was then mounted above the sample and focused on the coating surface. In this study the infrared camera TITANIUM 520 (CEDIP Infrared Systems GmbH, Munich, Germany) was utilized. The resulting image, known as a thermogram, depicts local disruptions in radiation flow, visualizing defects present. The energy of the thermal radiation can then be directly related to the temperature of the target object if its thermal emissivity is known. The size of the defect was then measured manually from the images generated.

4.6 Thermal Cycling Tests

The thermal cycling resistance of the various thermal barrier coating systems studied was evaluated with two different cycling tests. These are the burner rig test and the furnace cycling test. In both tests, the cycling buttons presented in Section 3.2 were used. Only the hole for the thermocouple was missing on the furnace test specimens.
Thermal cycling in the burner rigs is performed with a thermal gradient through the layers of the system, simulating the thermal conditions in a real turbine. This type of test was performed on the coating systems with the various optimized bond coats and YSZ top coats. Instead, the dual-layer YSZ/GZO topcoats were subjected to furnace cycling tests. The reason for this is that the furnace cycle test generates higher accumulated stresses in the ceramic layers due to the thermal expansion mismatch. Consequently, the stress tolerance of the double-layers can be examined more effectively. This is particularly important for testing the GZO layer, which has low fracture toughness, and for evaluating the adhesion between the two ceramic layers.

4.6.1 Burner Rig Testing

The thermal shock resistance of the various thermal barrier coating systems was investigated in a burner rig test, creating a thermal gradient in the specimen. Due to the specimen geometry used, the results obtained in this work can be compared with those of previous specimens tested on the same test rig, including the historical date of the reference coating system [209]. The test rig utilized is shown in Figure 4.6.
To generate a thermal gradient, the samples were heated from the front side using a flame generated by the combustion of a natural gas-oxygen mixture, while the back side was cooled with compressed air. An automated cycle of seven minutes consists of five minutes of heating and two minutes of cooling. During cooling, the sample is additionally cooled with compressed air from the front side, resulting in a gradient inversion in the coating system as the thin ceramic cools faster than the thick substrate. This gradient inversion and the rapid cooling at the surface imposes significant stress on the coating system. Cooling the front side simulates the flow of cold air in a turbine after shutdown, as the compressor continues to run down and conveys cool air to the components.
Temperatures in the substrate and on the sample surface are monitored during the entire test. The substrate temperature is measured with a thermocouple inserted through a hole to the center of the substrate (see Figure 3.2). The surface temperature of the ceramic is measured with a KT15.99 IIP infrared pyrometer (Heitronics, Wiesbaden, Germany). An average value is calculated over a 10 mm diameter area in the center of the sample. The wavelength range of the pyrometer is 9.6 - 11.5 µm, with a constant emissivity of 1 set for the ceramic. This emissivity value serves as an approximation, however, realistic emissivity values for 8YSZ TBCs in the wavelength range of the pyrometer typically are around 0.98 [210]. The approximated emissivity value leads to an underestimation of the surface temperature of less than 3 %, while the measurement uncertainty of the pyrometer itself is less than 1 %. However, the emissions from the flame, which are in the same spectral range, cause a slight increase in the pyrometer reading, compensating the effect of the overestimated emissivity. Since it is difficult to assess these competing effects accurately, a limited underestimation of the surface temperature is assumed [131].

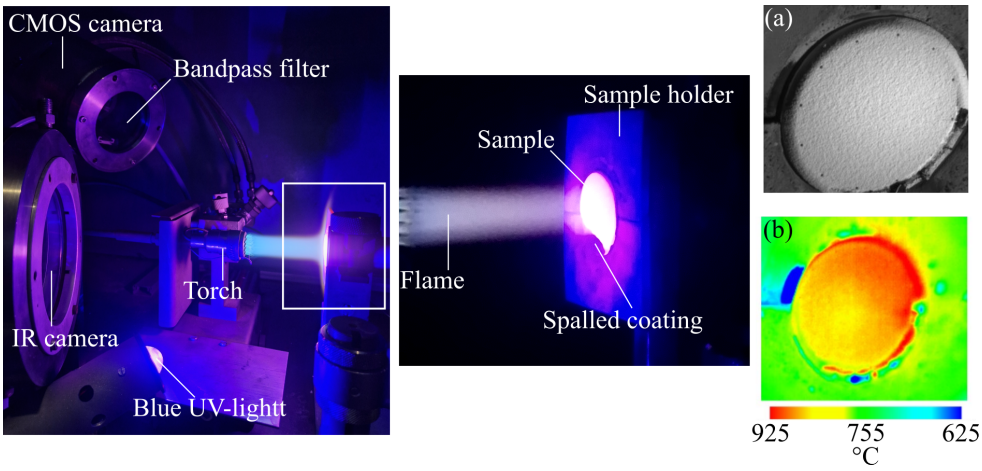

Fig. 4.6 Images of the Burner Rig test bench and images taken with (a) the CMOS camera and (b) the IR camera

At the onset of the tests, the process parameters were adjusted based on temperature recordings. Initially, the gas flows were manually adjusted to achieve the desired surface and substrate temperatures. Subsequently, an automatic control system readjusted the process gas flows over the first 20 cycles to compensate for influences arising from the heating of the test stand and initial sintering of the ceramic. After 20 cycles, the process parameters were kept constant until the sample failed. In this study, the temperatures were initially set to approximately 1400 ℃ on the surface and approximately 1050 ℃ in the substrate. However, due to the long lifetime of the coating systems, these temperatures were increased to 1450 ℃ and 1100 ℃, respectively, maintaining the thermal gradient.
Coating failure is defined as either spalling of the thermal barrier coating on more than 30 % of the sample area or an increase in temperature difference between the substrate and the surface of more than 50 ℃. In this case, it can be assumed that the ceramic coating has detached from the bond coat over a large area and the integrity of the coating is no longer guaranteed. The temperature of the bond coat at the interface to the topcoat also plays a critical role in TBC system failure. Although this temperature cannot be directly measured, it can be calculated using the equation 4.5. It was calculated based on the assumption of linear, homogeneous and one-dimensional thermal flow in the center of the specimen, taking the different thicknesses and thermal conductivities of the layers in the TBC system into account. T_x indicates temperature values, d_x layer thicknesses, and λ_x thermal conductivities. X = BC stands for Bond Coat and TC for Top Coat. The substrate and surface temperatures were determined using the thermocouple and pyrometer, respectively.
For the calculation, it is important to note that different thermal conductivities of the topcoats were assumed for the different coating systems when calculating the interface temperature. Thermal conductivities of 1 W/mK were assumed for the APS [147] and SPS [211] coatings. For the PS-PVD coatings, a thermal conductivity of 1.5 W/mK

was considered due to the dense columns and large gaps between the columns (comparable microstructure to EB-PVD) [147]. For the very dense DVC coatings, the thermal conductivity was assumed to be 1.8 W/mK [211].

$$T_{BC} = T_{Surface} - \frac{\frac{d_{TC}}{\lambda_{TC}}}{\frac{d_{TC}}{\lambda_{TC}} + \frac{\frac{1}{2}d_{Substrate}}{\lambda_{Substrate}} + \frac{d_{BC}}{\lambda_{BC}}} \cdot (T_{Surface} - T_{Substrate}) \tag{4.5}$$

4.6.2 Furnace Cycling

The furnace cycling tests of the double-layer APS-YSZ/SPS-GZO coating systems were conducted in air in a SPLF 12882 furnace (Carbolite, Neuhausen, Germany). The heating cycle lasted 120 minutes at 1100 °C. The specimens were then removed from the furnace and cooled in an air stream generated by a fan for 15 minutes. The failure criterion for the coating was defined as a spallation of the ceramic coating in an area of 30 % or more of the surface area. Since the process was automated, the samples were checked for failure every 20 cycles. In addition to the double-layer systems, single-layer standard APS-YSZ coatings were also tested as a reference. Three samples from each of the double-layer systems and two APS single-layer samples were tested.

4.7 Digital Image Correlation during Burner Rig Testing

Digital Image Correlation (DIC) is an effective tool for quantitatively measuring the deformation of a flat object surface using images. It provides full-field displacements with sub-pixel accuracy and full-field strains by comparing digital images of a test object surface taken before, during, and after deformation. DIC is a non-interferometric method based on digital image processing and numerical calculations that determines surface deformation by comparing gray-scale changes of the object surface. The advantages of 2D-DIC include a simple test setup and sample preparation. Only a fixed camera is needed to capture the digital images of the sample surface, and no sample preparation is required if the texture of the sample in the captured images has a random gray level distribution. In addition, the requirements for the measurement environment are low, as natural light can be used for illumination in many cases. Furthermore, the range of measurement sensitivity and resolution is wide. However, the disadvantages of 2D-DIC are that the measurements are highly dependent on the quality of the imaging system and the accuracy of strain measurement is currently lower than that of interferometric methods [212].
With a suitable image acquisition setup and appropriate image processing and evaluation, DIC can be used to identify inhomogeneities in the strain distribution on the sample surface [213]. This in turn makes it possible to describe damage, crack initiation sites [214], [215], crack growth [216], and the failure behavior of specimens [217] in addition to local strain exaggerations [218].

4.7.1 DIC Basics

To calculate displacements, the features on the surface in the loaded state are assigned to the corresponding features on the surface in the unloaded state. For correlation, two approaches with regular and random surface patterns are used. Employing irregular surface patterns in correlation offers the advantage of utilizing the natural surface structure of the sample to determine deformation, eliminating the need for complex preparation. Due to the natural surface roughness of plasma-sprayed samples, image correlation is possible without the requirement of a defined pattern.
Since the random surface patterns of the samples were chosen for image correlation in this work, the analysis using such patterns is described in more detail below. The sample surface is first defined as a Region of Interest (ROI) in which the image correlation is computed. This ROI is then divided into subsets. These subsets are square image areas of a defined size, measured in pixels x pixels and can be varied as desired. For example, Figure 4.7 shows a 7 x 7 pixel subset. Each pixel in the subset has a specific gray value, which in the example image can range from 0 to 255 (8-bit image), giving each subset a unique average in gray scale. This gray value is assigned to the subset center. The brightness distribution in the subset of the undeformed sample is then searched for in the images of the deformed sample. The shift of the subsets can be computed by assigning those subsets in the distorted image to the subsets in the undistorted image. For this reason, a suitable speckle pattern with a high variance in the gray value distribution is required to minimize the measurement noise.

191	191	255	255	255	255	191
191	191	255	255	191	191	191
255	255	255	191	127	127	191
255	255	191	127	63	63	127
255	191	127	63	0	63	127
191	191	127	63	63	127	191
191	255	191	127	127	191	255

Fig. 4.7 Brightness distribution (gray scale) using the example of a subset with the size of 7 x 7 pixels [219]

In this study, subset tracking in deformed images was conducted utilizing the normalized error squares. The determined displacement of the subsets is assigned to the subset center point P (Figure 4.8 (a)). An additional point Q is defined to calculate the strain (Figure 4.8 (b)). Its change in distance from Q' to the subset center P' is determined in comparison to the distance in the undeformed image (Q to P). This procedure is repeated for any number of successive images to determine the strain evolution in a cycle. The calculated displacement and strain can be related either to a reference image or to the preceding image in the sequence.

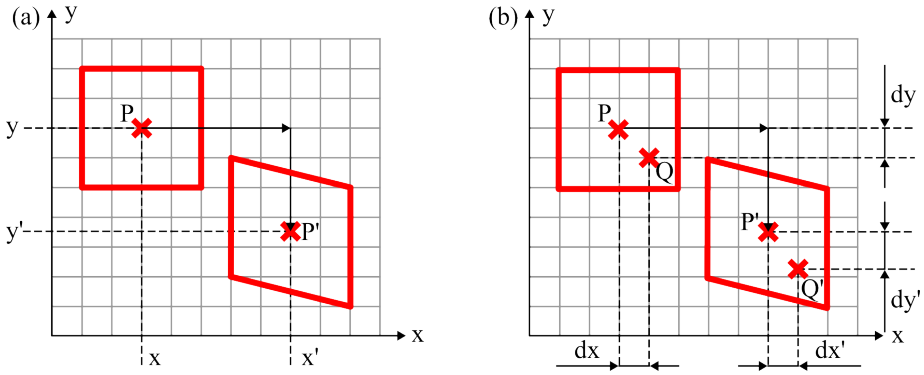

Fig. 4.8 Schematic representation of the displacement (a) and strain (b) determination on a subset according to [220]

The subset size and the step size influence the calculation result. Large subsets enable reliable correlation even with images difficult to correlate, as the amount of information in each subset is higher. However, the disadvantage of large subsets is that the displacement and strain are averaged over larger distances. Smaller subsets, on the other hand, provide better resolution of local strain exaggerations, but may be more challenging to reliably assign due to their lower information content. In some cases, it is possible that no or several areas suitable for a subset match are found, which prevents the correlation [221]. The step size defines the intervals at which displacement and strain calculations are performed. This parameter therefore has a significant impact on the computation time. Halving the step size will increase the calculation time of displacements and strains by a factor of four. However, too large a step size leads to a loss of information. Therefore, the step size should be significantly smaller than the subset size.

4.7.2 DIC Hardware Setup and Image Processing

Digital Image Correlation is carried out on samples during thermal cycling in the Burner Rig. In addition to the pyrometer and thermocouple for temperature recording, an infrared camera (IR camera) is utilized to record the temperature distribution on the sample surface (Figure 4.6 (b)). A FLIR IR camera of the A655 sc series with an optical filter (BBP-9650-11250c nm) from Spectrogon was used for recording. With this setup, the sample can be recorded in a temperature range of 300 - 2000 °C with a resolution of ~300 x 300 µm/pixel. In addition, the sample surface was captured for digital image analysis using a Prosilica GT 1930 complementary metal-oxide-semiconductor (CMOS) camera from Allied Vision. The objective lens equipped was the FL-BC7528-9M from Ricoh. With this setup, the images for strain and displacement calculation of the sample surface are recorded. The images are captured in 16-bit format at 50 Hz with a resolution of ~30 x 30 µm/pixel.
During the development of the test stand, different lighting conditions were applied for image analysis. It was started with the natural ambient light in the test stand. An additional halogen light source was then directed at the sample, providing better

illumination of the specimen and a more pronounced speckle pattern on the surface. This light source was replaced with a blue light-emitting diode (LED) light source as the work progressed. The exact reasons for replacing the light sources are discussed in more detail in the Section 6.3.2. In addition, a bandpass filter by Edmund Optics Inc. was installed in front of the camera lens when using the LED light source. The bandpass filter allows the light in the wavelength range of the LED illumination to pass through and cuts out other wavelengths. In an ideal setup for a 2D-DIC application, the sample must be flat and no part of the sample should move out of the plane toward or away from the camera. In addition, the sample must be planar to the camera sensor. This is not possible due to the design of the test stand, as the camera would have to be mounted directly in front of the sample at the location of the torch. Therefore, the camera has to be mounted in the test stand at an angle to the specimen plane, making distortion correction of the images is necessary to avoid incorrect strain calculations 4.6 (b)).
The distortion correction prior to further image processing was carried out using a Python script written at FZJ. This script warps the images using a predefined grid pattern, where certain positions on the planar sample surface are known. An image of a sample with a defined grid pattern, which was prepared for the determination of the rectification vectors, is shown in Figure 4.9 (a). The image clearly shows the sample distortion due to the angled image acquisition. The grid pattern on the sample surface was introduced into the coating by laser ablation. The size of the squares and the line widths are therefore known. New coordinates are assigned to specific pixel based on the known distances between these points in the grid. The warping vectors of the other pixels are calculated based on this specified correction. After warping, an image is created as shown in Figure 4.9 (b). However, it is important to note that the information content of an image is always highest in its initial state. Any correction can produce artifacts, such as masking errors. With this type of error, previously hidden areas of the image become visible, meaning that these areas cannot be displayed correctly after perspective correction due to a lack of information. In image 4.9 (b), the masking error can also be seen at the lower right edge of the sample. The rounded edge of the sample was masked by the camera positioning and therefore does not appear in the corrected image. In contrast, the camera-facing edge of the sample appears too large after perspective correction (top left). However, since these miscalculated areas do not lie on the redefined plane (sample surface), they do not cause any problems in further image processing. This is because the Region of Intrest, in which the displacement and strain of the sample surface is calculated, is placed only on the planar sample surface. There are no distortion errors on this planar surface.
The actual digital image correlation was then carried out with the VIC-2D Digital Image Correlation software (version 7.0.16) from Correlated Solutions. With this, different image series were processed. On the one hand, image series of a single cycle were analyzed. This makes it possible to analyze the shrinkage of the sample surface during cooling or heating, when examining the image recorded during the cooling or heating period. In combination with the calculation of the expected strains of the individual layers in the considered temperature ranges, conclusions can be drawn about the stress states in the layers of the system at different stages. On the other hand, the condition of the sample was evaluated over different cycles to analyze the long-term changes of the sample. For this purpose, individual images from each cycle (or cycles at defined intervals) were compared.

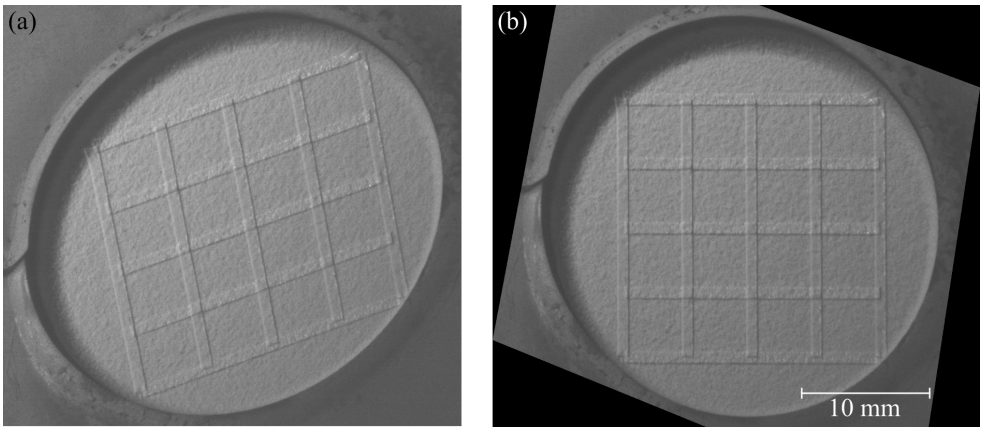

Fig. 4.9 CMOS image taken in the Burner Rig test stand (a) in the original state and (b) in the rectified state

It is crucial to ensure that the temperature distribution of the sample is consistent across all analyzed images. Therefore, in this work, images at room temperature or maximum temperature were chosen to compare the evolution of the sample over different cycles.
The aim of DIC is to determine the strain states on the sample surface in situ during thermal cycling. This, in turn, should allow to drawn conclusions about local stresses and thus to predict damage. In combination with damage specifically introduced by the LASAT process, it should also be possible to observe local crack growth in the future. As shown in literature, the chosen method is suitable for this purpose even at high temperatures, but there is currently no method that has been used for the investigation of TBC systems in thermal gradient tests.

5 Investigation of Optimized Bond Coat Systems

The different bond coats used in this work for thermal gradient cycling in the burner rigs are Standard, Graded, Flash, and 2253A Bond Coat. The parameters for their preparation can be found in Chapter 3.3, Table 3.6. In addition, some Standard Bond Coats were pre-oxidized in an argon atmosphere. In this chapter first the microstructural properties of the bond coats are described, then the phases of the bond coat surfaces before and after annealing are discussed. In the subsequent section, the effect of the different bond coats on lifetime during thermal cycling is evaluated and the different damage mechanisms occurring are analyzed. In the failure mode analysis, aluminum depletion zones, TGO thickness, spinel growth, crack propagation paths and more are compared. For comparability, the Standard, Graded, Flash and 2253A Bond Coat analyzed in this chapter are all coated with the Standard Top Coat System. The comparison between pre-oxidized and non-pre-oxidized bond coats is made in Chapter 6, since optimized topcoat systems were used in these tests.

5.1 Microstructure Analysis of Different Bond Coats

Three approaches were utilized in the production of bond coats to enhance the service life of TBC systems in thermal cycling tests. As described in Chapter 3.3, one method involved increasing the surface roughness of the bond coats, followed by the Graded and Flash Bond Coat. For the second approach, the 2253A Bond Coat has been applied because of its lower coefficient of thermal expansion, resulting in a reduced expansion mismatch between the bond and top coat, and thereby reducing the radial stresses leading to cracking at roughness peaks. The third strategy has been to pre-oxidize the bond coat before applying the ceramic topcoat. The pre-oxidation ensures that the high growth stresses caused by the initial rapid oxide growth do not increase the stress state in the ceramic topcoat.
Since the bond coat roughness is an important factor affecting the thermal cycling behavior of the TBC systems, the bond coat surfaces have been analyzed using the white light topographer and the confocal laser microscope regarding the morphology. The average roughness R_a and roughness depth R_z, analyzed with the white light topographer as well as the coating thickness of the bond coats are given in Table 5.1 and the laser microscope images of the bond coat surfaces are shown in Figure 5.1. Adjusting processing parameters for the Graded Bond Coat increased the average roughness R_a from approximately 7.0 µm (Standard Bond Coat) to around 9.5 µm. That difference can also be seen in the laser microscope images. While the surface of the Standard Bond Coat in Figure 5.1 (a) is relatively uniform, the Graded Bond Coat (b) shows larger circular shaped elevations. These may indicate unmolten or resolidified particles that are less flattened on impact. This difference is also reflected in the average roughness depth R_z, which is ~50 µm for the

Tab. 5.1 Coating thicknesses and roughness values of different bond coats

Bond Coat Name	Coating Thickness [µm]	Average Roughness R_a [µm]	Roughness Depth R_z [µm]
Standard	~150	7.0 ± 0.6	49.8 ± 2.8
Graded	~220	9.6 ± 0.4	65.2 ± 2.7
Flash	~280	17.0 ± 1.0	117.0 ± 14.9
2253A	~150	6.2 ± 0.1	44.9 ± 0.9
Pre-oxidized	~150	8.3 ± 0.7	60.4 ± 5.0

Standard Bond Coating and ~65 µm for the Graded Coating with less flattened particles. The Flash Coating more than doubled the average roughness R_a to ~17.0 µm compared to the Standard Bond Coat. The laser microscope images also reveal a significant roughening of the Bond Coat caused by the coarse powder used to produce the Flash Coat (c). Again, large globular peaks can be seen, indicating unmolten particles beeing deposited in the coating. This observation is supported by the average roughness depths, with an R_z value of 117 µm for the flash coat.
Bond Coat 2253A manufactured with the alternative material had an R_a value of ~6.2 µm, which is slightly lower than the Standard Bond Coat (R_a ~7.0 µm). The laser microscopic image (d) reveal a uniform surface with some elevated globular features of larger height. Consequently, the overall average roughness depth R_z is approximately 45 µm, which is again slightly less than that of the Standard Bond Coat (R_z ~50 µm).
In addition, the surface of the Standard Bond Coat pre-oxidized in argon atmosphere has been analyzed. The process of oxidation leads to an increase in the average roughness value R_a from 7.0 to 8.3 µm. The laser micrograph (e) displays similar characteristics to the Standard Bond Coat sample (a), featuring a uniform surface with few globular peaks. The roughness depths appear more pronounced, as according to the increase in the R_z value to about 60 µm (from ~50 µm). However, these differences are estimated to be insignificant for the thermal cycling performance and are therefore not considered in the following.
Cross-sections of each bond coat system are shown in Figure 5.2. The Standard Bond Coat (a) shows a dense coating of well bonded particles. However, individual particles can also be seen, presumably deposited in a more solid state (i). Due to the diffusion annealing after the application of the bond coat, the γ- and β-phase microstructure typical for MCrAlY bond coats can be seen in Figure 5.2 (b). The β-phase is uniformly distributed in the bond coat, but there are some larger areas of Al-rich β-phase (ii).
The Graded Bond Coat has a similar microstructure and also contains some unmolten particles and the characteristic γ- and β-phases. After heat treatment, there is also a 20 µm thick depletion zone of the β-phase on the side facing the substrate. However, differences can be seen on the surface of the bond coat, where layers were applied with reduced torch power and increased spraying distance to modify the surface roughness. An increased number of spherical particles that have not melted or resolidified during the coating process can be seen in Figure 5.2 (c), indicated by number (iii). These barely deformed particles lead to the roughening of the coating surface as indicated by the roughness measurements described above. However, the cross-section also shows that these particles are poorly bonded to the rest of the bond coat due to their unmolten state during impact. During

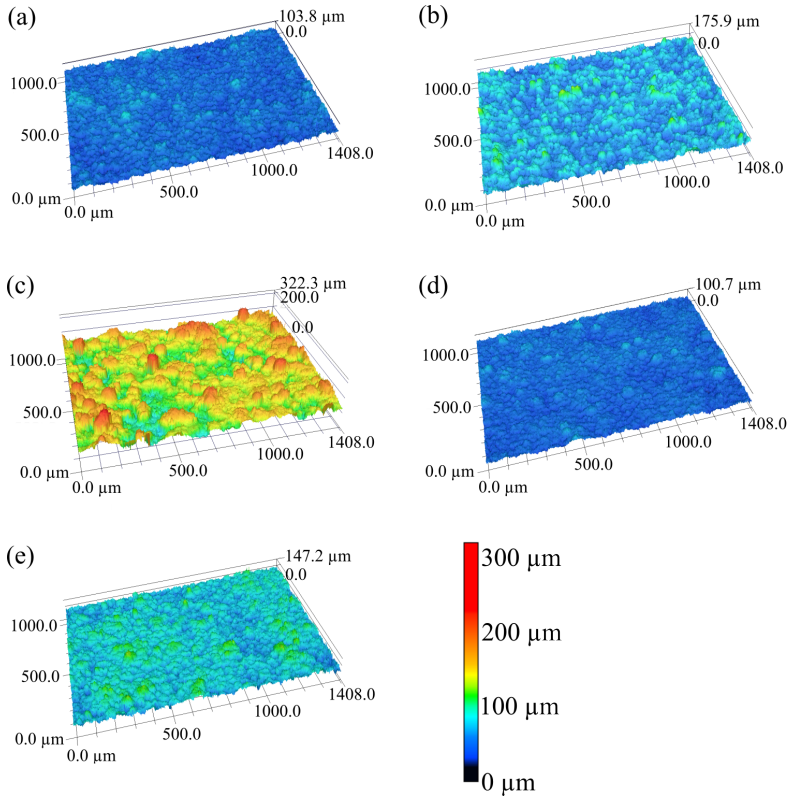

Fig. 5.1 Roughness profiles taken with the confocal laser microscope: (a) Standard, (b) Graded, (c) Flash, (d) 2253A, (e) Pre-oxidized Bond Coat

diffusion annealing, the γ- and β-phase structure is also formed in these isolated particles. With the Flash Coat, shown in Figure 5.2 (d), the bonding of the additional surface modification layers is again better and there are very few poorly bonded particles. In addition, despite the high R_a and R_z values, the surface of the bond coat appears relatively smooth and uniform at the microscopic level. However, it can also be seen that the maximum roughness depths are the highest of all the bond coats. As with the two other bond coats, the γ- and β-phases and the depletion zone are also present. The higher coating thicknesses of the Graded (c) and Flash Bond Coat (d) shown in Table 5.1 are also evident in the cross sections. These are caused by the surface modification layers beeing applied to a Standard Bond Coat.

The cross-section of the 2253A Bond Coat made from the alternative bond coat material is displayed in Figure (e). It's thickness, R_a and R_z are in good agreement to the Standard Bond Coat. However, the surface morphology in the micrographs appears to be slightly less rough than that of the standard coatings. A lamellar structure can be seen in the microstructure of the bond coat (f) due to pores in the splat boundaries. This indicates that the process parameters were not optimally adjusted during the VPS process. Due

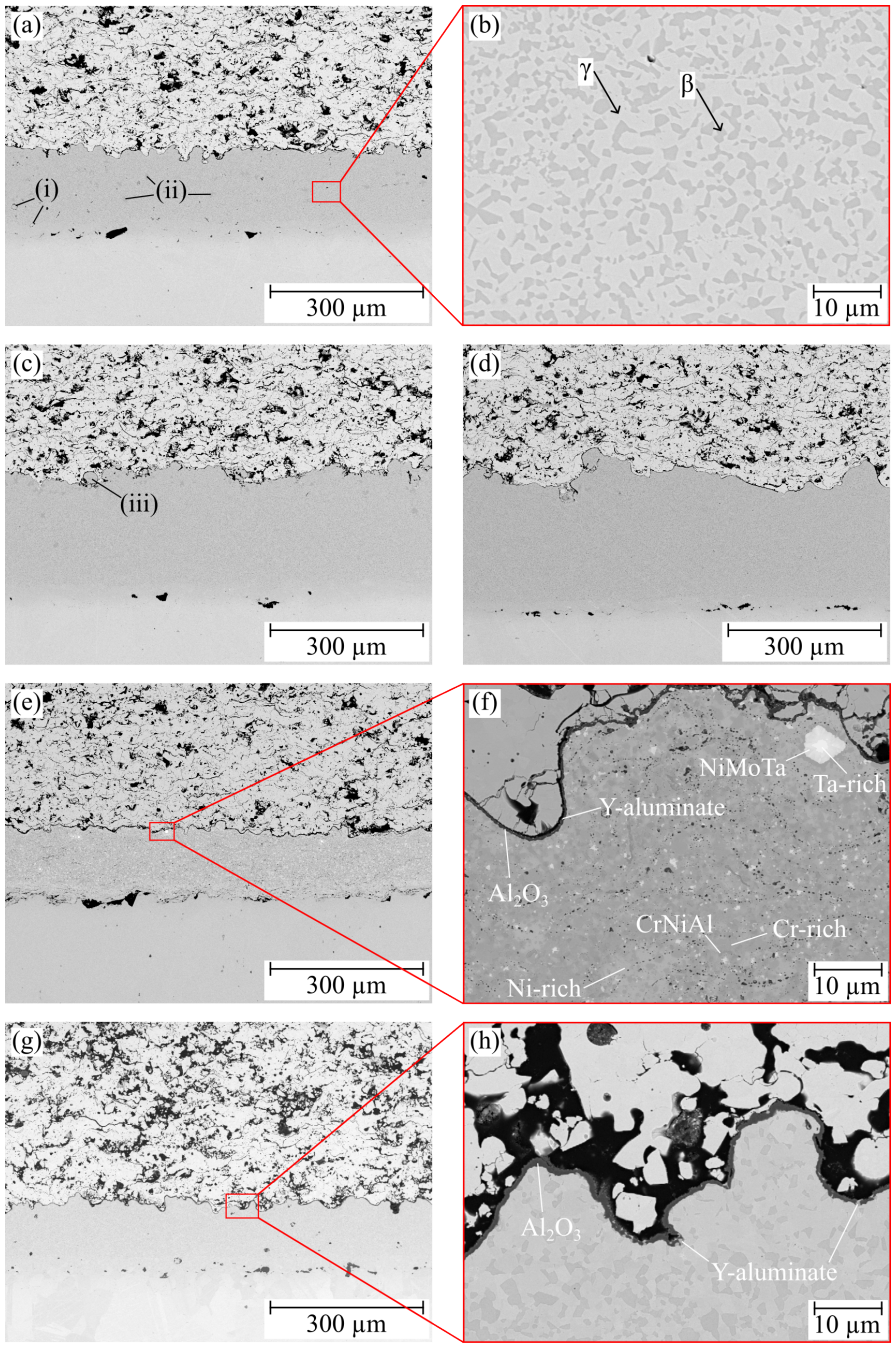

Fig. 5.2 SEM Cross-Sections of (a, b) Oerlikon Metco Standard, (c) Graded, (d) Flash, (e, f) 2253A, (g, h) Pre-oxidized Standard Bond Coat; (i) unmolten or resolidified particles in the bond coat, (ii) large accumulations of β-phase, (iii) unmolten or resolidified particles on the bond coat surface

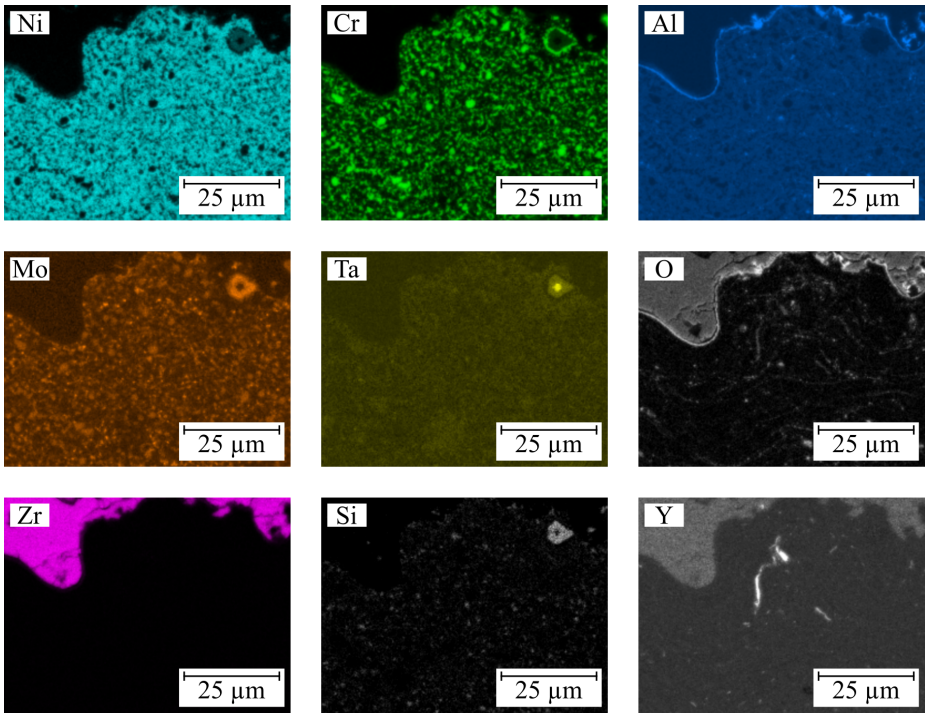

Fig. 5.3 EDX Maps of Metco 2253A Bond Coat after vacuum annealing and top coat application

to the modified chemical composition, the typical γ- and β-phases do not form in this bond coat during diffusion annealing. Instead, the aluminum is evenly distributed in the bond coat. Additional EDX point measurements and mappings have been carried out on this bond coat. The point measurements showed that the white phase is a Ta-rich phase and the nearly white phase is a NiMoTa phase. The matrix of the bond coat consists of a light gray Ni-rich phase and a slightly darker Cr-rich phase. There are also isolated small, even darker CrNiAl precipitates. The EDX mapping was performed on the image from Figure 5.2 (f) and the results are shown in Figure 5.3. In addition to the already identified phases of the bond coat, the mapping revealed that a thin alumina layer has already formed on the surface of the bond coat during diffusion annealing. The TGO layer can also be seen in the cross section at high magnification in Figure 5.2 (f). This is not the case with the previously presented bond coats. The thickness of this oxide layer is less than 0.5 µm. In addition, the lamellar structure can also be observed in the mapping images and the partially formation of alminum oxide at the splat boundaries. If this internal oxidation of the bond coat also leads to the formation of the aluminum oxide layer during heat-treatment needs to be clarified. Furthermore, an area with a very high concentration of yttrium was identified.

An oxide layer can also be found on the surface of the Standard Bond Coats after pre-oxidation in argon atmosphere (Figure 5.2 (g)). In this TGO, the typical Al_2O_3 phase and

yttrium-aluminates can be seen in the SEM image in Figure 5.2 (h). In the upper ~5 µm of the bond coat, the Al-rich β-phase is present in a lower amount than in the rest of the bond coat due to TGO growth, but there is no complete depletion zone. The thickness of this specifically adjusted oxide layer is greater than that of the 2253A bond coat, with an average thickness of around 1 µm.

Additional XRD and Raman spectroscopy measurements were conducted on the surfaces of the various bond coats to further characterize the oxide layers. The results of the XRD measurements are shown in Figure 5.4 (a). All the different bond coats after vacuum annealing as well as the bond coat oxidized in argon were compared. Three samples of the Standard Bond Coat (two from a 2022 batch and one from a 2023 batch) were also examined.
In the evaluation, it is assumed that any observed oxidation was induced by heat treatment in vacuum or argon atmosphere. A study by *Joeris et al.*, using XRD and Raman spectroscopy, showed that in CoNiCrAlY coatings no oxides could be detected after vacuum plasma spraying [172]. In the XRD analysis, the peaks are most prominent at a 2-θ angle of approximately 44° for all bond coat surfaces. With the exception of the 2253A bond coat, all the other bond coats are based on Co, which has its XRD-peaks at 43.9, 51.1, and 75.1°. However, these peaks are expected to overlap with the nickel peaks of the material at approximately 44.6, 51.3, and 76.0°. Since nickel is the major component of Metco 2253A alloy and Co is not present in this material, the same peak position supports this assumption. The peak to the right of the main peak can be assigned to the β-phase of the bond coat layer [75].
To identify oxide peaks, the graphs must be viewed at higher magnification. Figure 5.4 (b) shows the XRD pattern for a 2-θ angle of 20 - 40°. The gray vertical lines show the peak positions characteristic of Al_2O_3 at 25.6, 35.2 and 37.8°. However, there may be some overlapping with AlCr oxide peaks which could be present at 25.6, 35.1 and 37.8°. A clear assignment is therefore not possible, but based on the EDX measurements it can be assumed that an Al_2O_3 layer is present. However, it is apparent that the peaks are most prominent for the bond coat annealed in argon and for the bond coat 2253A. This suggests that the oxide thickness is the highest for these coatings, which is consistent with the SEM images since an oxide film was only visible on these two bond coats in the cross-sections of the as-sprayed samples. The peaks can also be identified in the other measurements, but they are almost lost in the measurement noise, although the curves are normalized. In contrast, no peaks can be identified on the Standard Bond Coat (number 1 of batch 2022 - black line), which may indicate that no measurable oxides were formed during vacuum diffusion annealing on this bond coat.
To gain further information about the oxides present, Raman spectroscopy measurements have been carried out on all bond coats. The Raman spectroscopy measurement spectra are shown in Figure 5.5 and can be matched to the color of the XRD spectra in Figure 5.4. The Raman spectroscopy results confirmed the absence of oxides on the Standard Bond Coat 2022 - 1 sample. Although various points were measured, no Raman signals could be detected. The missing peaks indicate that a metallic surface is still present. In the measurements of the other bond coats, several Raman signals were identified after heat treatment. Similar to the reports of *Vande Put et al.* [222] and *Joeris et al.* [80], most of

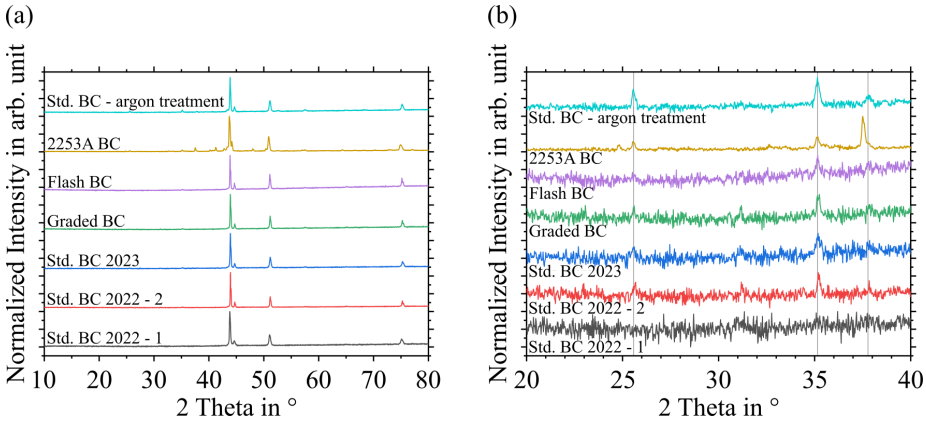

Fig. 5.4 XRD results measured on different bond coat surfaces at a 2-θ angle of (a)10 -80° and (b) 20 - 40°

the signals can be assigned to the $YAlO_3$ phase [223]. This phase was also measured as a reference powder and is represented by the black line in Figure 5.5. However, there are some small differences in the intensity and shape of the $YAlO_3$ signals of the samples and the $YAlO_3$ reference powder. This might be due to an artifact of additional elements in the sample system, such as Co, Ni and Cr, which could affect the $YAlO_3$ structure. In addition to $YAlO_3$, the samples also show signals of Al_2O_3 at 418 cm^{-1} [224]. It should be emphasized that Al_2O_3 was also measured in previous reports [80], where it was shown that the Al_2O_3 has a much lower signal intensity compared to $YAlO_3$. Therefore, it is possible that even low concentrations of $YAlO_3$ show more intense signals compared to Al_2O_3. The low concentration of $YAlO_3$ can be assumed because only small precipitates were identified in the SEM images and the signal remained below the detection limit in the XRD measurements.

Another oxide phase found at 556 cm^{-1} is Cr_2O_3, which has also been found in similar studies [225]. This signal could be identified in the Graded and Flash Bond Coat with the increased surface roughness as well as in the 2253A Bond Coat. In the case of the bond coats with increased roughness, it is possible that an insufficient amount of Al has diffused to the surface quickly enough, to form a dense Al_2O_3 layer. The greater roughness implies a larger surface area needing protection, requiring more Al. If there was not enough Al or Y available for oxide formation, Cr oxides could have formed instead. The 2253A bond coat alloy is also designed for slow Al diffusion to achieve slow oxide growth rates [187]. Therefore, it is also possible that a non-sufficient amount of Al has diffused to the surface fast enough to form a dense Al_2O_3 layer. Nevertheless, it is not clear why a thicker oxide layer forms on the 2253A alloy than on the other bond coats, even though both are treated in vacuum. Therefore, in the future, this bond coat should also be analyzed in the as-sprayed condition. In contrast to the CoNiCrAlY alloys, it is possible that oxides are already present on the surface after the coating has been applied.

Another strong signal is found at 758 cm^{-1}, which is not present in each of the samples analyzed. A specific assignment to a phase could not be made due to missing data or

strong signal discrepancies to other possible secondary phases. However, the Raman signal has already been reported by another group, which at least allows a possible interpretation. There, *El-Turki et al.* assign the signals to Ni(II) and Cr(III) oxides and also give an indication of the presence of nickel chromite [226].

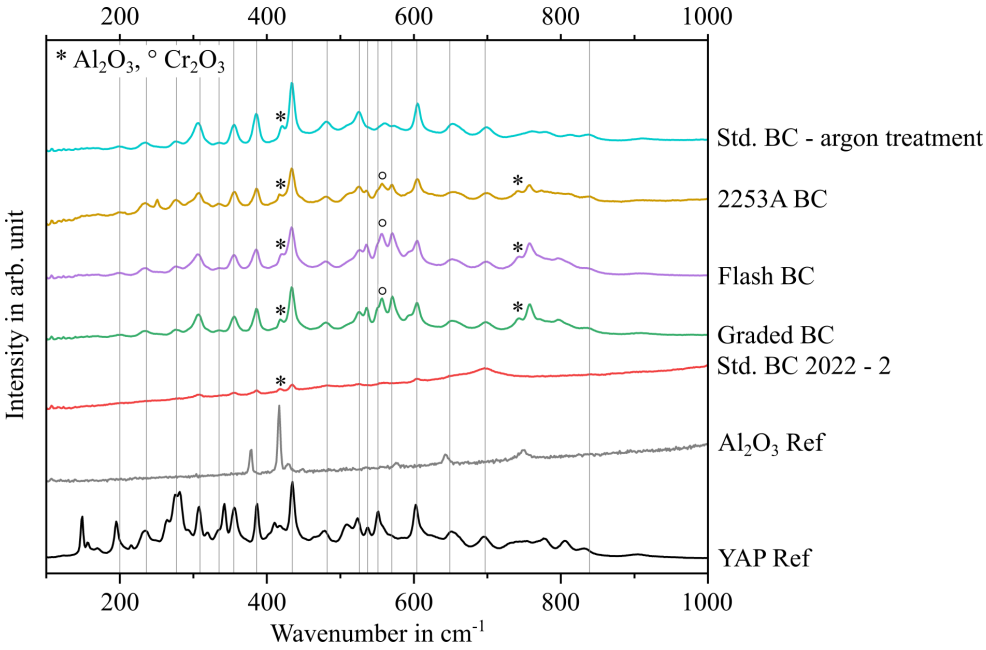

Fig. 5.5 Raman Spectroscopy results measured on different Bond Coats

The differences in the spectra of the samples could be partially explained by the effects of the atmosphere during heat treatment. However, there are still uncertainties that need to be clarified in further investigations.
A strong difference could be observed in the Standard Bond Coat samples from 2022, which showed either weak signals of oxide phases, or in some case no oxides signals at all. This might be due to a very low pO_2 value during the vacuum annealing, not sufficient to cause a comprehensive oxidation of all bond coats. The effect of the different bond coats on the thermal cycling life is evaluated in the following Section 5.2 for the vacuum annealed bond coats. The results of the pre-oxidized bond coats, on the other hand, are discussed in Chapter 6.2, since they were applied with optimized top coats.

5.2 Thermal Cycling Lifetime of Different Bond Coats

To compare the performance of the different bond coats in thermal cycling tests, the samples were evaluated based on the number of cycles completed without failure and the bond coat temperature present. There is a linear relationship between the logarithmic time to failure and the inverse of the bond coat temperature for oxide growth related

failure of TBC systems [191]. Reducing the bond coat temperature by 30 °C doubles the time to failure. Figure 5.6 shows the time to failure of the different bond coat systems based on the inverse of the calculated bond coat temperature. To determine the time, only the heating period of each cycle was calculated, i.e., a 5-minute cycle was assumed. The exact calculation of the bond coat temperature is described in Chapter 4.6.1.
The black line in Figure 5.6 describes the doubling of lifetime when reducing the bond coat temperature by 30 °C. The straight line is placed in the center of the two black squares, indicating the lifetime measured for standard samples from the author's institute, cycled at an earlier time on the same test rig as the coating systems studied in this work. This line therefore represents the service life of the reference system used in this work. This line therefore represents the service life of the reference system used in this work. This system was selected as a reference because the relationship between bond coat temperature and service life was determined based on a comparable coating system at the institute of the author of this work [191].
The blue triangles represent the service life of the Graded Bond Coat samples. These coating systems had comparable lifetimes to the FZJ standard during the thermal cycling tests. The other coating systems with the Standard Bond Coat, produced by project partner Oerlikon Metco, the Flash Bond Coat, and the 2253A Bond Coat had much longer lifetimes, more than twice as long as the FZJ standard system.

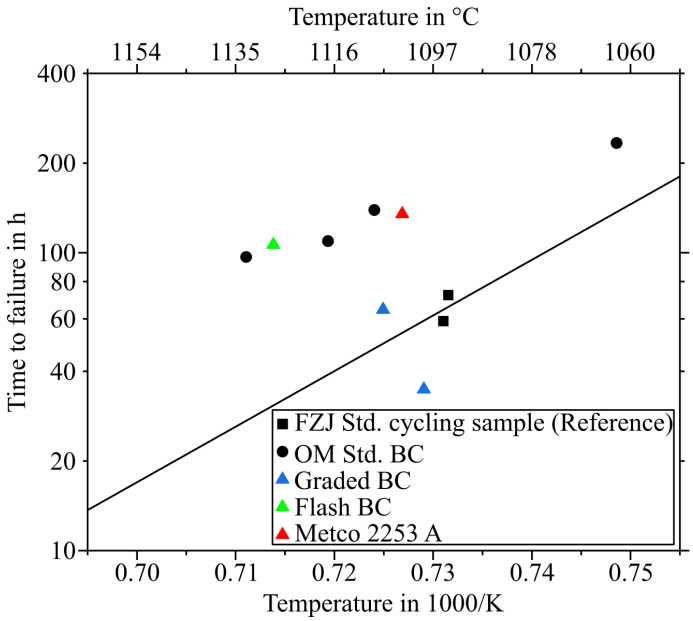

Fig. 5.6 Arrheniusplot Service life to failure as a function of the inverse bond coat temperature for YSZ TBCs with different bond coats at 1400 - 1450 °C surface temperature; black line shows service life of FZJ Standard Bond Coat, red line shows failure due to Al depletion

To understand the reason for these significant differences in lifetime during the thermal gradient tests, further analysis have been carried out on the failed specimens. Photographs

of the failed samples and SEM cross-sections are presented in Figure 5.7. The different localization of the cracks leading to failure is related to the surface roughness of the bond coats. For the two smoother bond coat surfaces on the Oerlikon Metco Standard (a) and 2253A (d) bond coat, the cracks propagated almost completely along or through the TGO layer, desribed as failure mechanism in Figure 2.13 (a). In contrast, with the Graded (b) and Flash Bond Coat (c) cracks were predominantly within the ceramic topcoat. The cracks propagate along the roughness peaks and from there through the ceramic. This is described by failure mechanism (c) in Figure 2.13. Thus, the roughening of the bond coat surface was able to suppress the failure at the interface, as intended. The higher roughness of the bond coat ensures that crack propagation along the TGO is inhibited so that the cracks grow in the ceramic as soon as there is sufficient elastically stored energy [135]. However, for the Graded Bond Coat samples, this approach did not result in an increase in performance. Therefore, the cycled samples and the resulting oxide layers are analyzed in detail below.

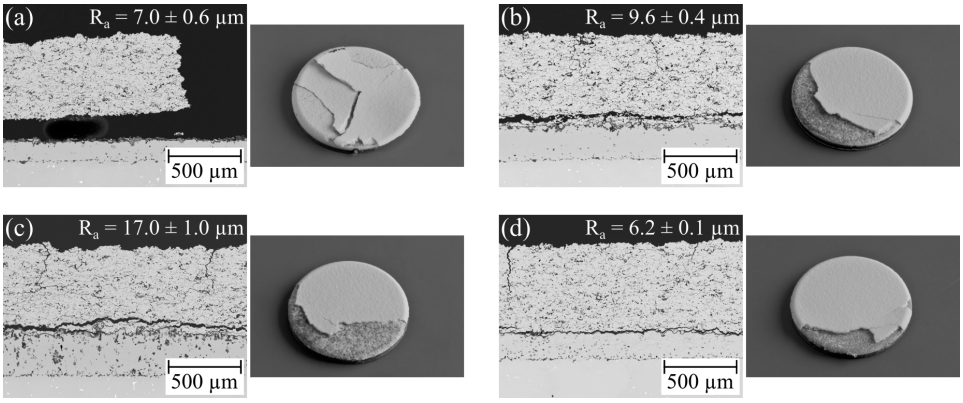

Fig. 5.7 SEM Cross-Sections and Photographs of the failed samples with (a) Oerlikon Metco Standard, (b) Graded, (c) Flash and (d) 2253A Bond Coat

Thick TGO layers can lead to failure of the coating systmes during thermal cycling. The average thickness of the TGO in the reference samples was ~3.5 µm (Al_2O_3). The thickness of the grown oxide layers of the other bond coat systems is shown in Table 5.2. It is evident from the table that the Al_2O_3 layers all exhibit similar thicknesses. The TGO of the Graded Bond Coat, however, is slightly lower due to the shorter duration at high temperature of the sample. Mixed oxides of Ni, Co and Cr were also formed in the Standard, Graded and Flash Bond Coat. In the Standard Bond Coat, these formed very locally. The localized strong thickening of the mixed oxides also occurred in the other two bond coats, but these also had thin mixed oxide films growing ontop of the Al_2O_3 layer in many places. The thickness of these films is also given in the table 5.2. Only in the case of the 2253A bond coat no mixed oxides could be identified in the cross-sectional images, which is in agreement with the results of the study by *He*, investigating this type of bond coat after furnace thermal cycling [187].

Tab. 5.2 Al_2O_3 TGO and Mixed Oxide thicknesses of different bond coats after thermal cycling

Bond Coat Name	Thickness Al_2O_3 [µm]	Thickness Mixed Oxides [µm]
Oerlikon Metco Standard	4.1 ± 1.1	-
Graded	2.5 ± 0.6	0.7 ± 0.3
Flash	3.1 ± 0.6	1.1 ± 1.0
2253A	3.1 ± 0.5	-

The early failure of the Graded Bond Coat system is caused by the poorly bonded particles. As shown in the high magnification image of the bond coat in Figure 5.8 (a), a continuous Al_2O_3 layer with small zones of yttrium-aluminates in it and a thin mixed oxide film on the Al_2O_3 TGO forms below these particles. The poorly bonded particles, on the other hand, are depleted of aluminum early, so there is only a very thin (i) or no (ii) Al_2O_3 layer on them. This is followed by partial internal oxidation of these particles (i). Finally, mixed oxides grow on the particles (iii), or the particles are completely oxidized (ii). The rapid growth of the mixed oxides then causes growth stresses in the ceramic top layer, resulting in cracks propagating from these particles through the ceramic layer. Due to the early failure of the Graded Bond Coat systems, a wide band of the Al-rich β-phase remains in the bond coat.

Poorly bonded particles can also be seen in the Flash Bond Coat, but significantly fewer than in the Graded Bond Coat. As shown in Figure 5.8 (b), internal oxidation of the bond coat at formed pores (iv) is more likely to occur in the Flash Bond Coat. It is assumed that poorly bonded particles promote oxygen diffusion into the inner bond coat, leading to internal oxidation at the cavities. The formation of these pores is analyzed and discussed in more detail in 6.2.2, as they were also common in the bond coats of the optimized topcoat systems. Due to the lower spinel growth and the associated lower stress build-up in the top layer, the Flash Coat was able to withstand the thermal cycling load for a longer period of time than the Graded Bond Coat samples. In this bond coat, the Al-rich β-phase was also still detectable in every part of the bond coat at the time of failure.

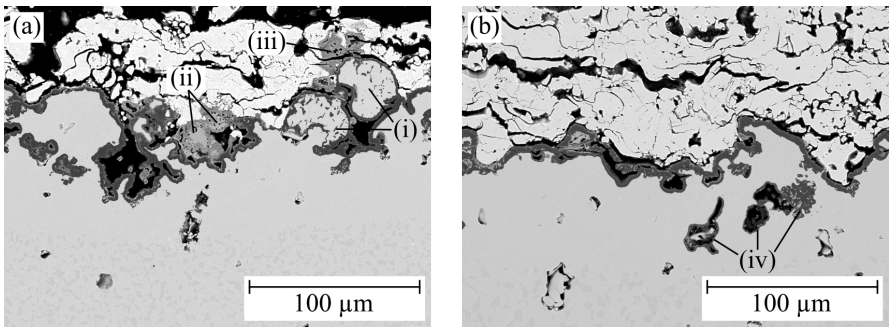

Fig. 5.8 SEM cross-sections with high magnification images of the TGO zone of the failed samples with (a) Graded and (b) Flash Bond Coat; (i) internal oxidation and (ii) complete oxidation of poorly bonded particles, (iii) mixed oxide growth on isolated particles, (iv) internal oxidation of bond coat

This is different for the reference samples and samples with Oerlikon's Standard Bond Coat, shwon in Figure 5.9. Due to the thinner bond coats, aluminum depletion occurred in some parts of the bond coat. The complete depletion is located where the topcoat failure occurred. In the specimen shown in Figure 5.9, the depletion zone extended from the side of the failed topcoat to the center of the specimen (a), where cracks in the interface and ceramic still occur. On the opposite side of the failed topcoat, however, the β-phase is still present, as it can be seen in image (b). A higher bond coat temperature, which can occur due to a slight misalignment of the flame during burner rig operation, could be responsible for the increased depletion on one side of the specimen. However, this could not be confirmed by analyzing the infrared images recorded during thermal cycling. The observation of various cycles distributed over the entire lifetime of the sample showed that the hotspot was always at the center of the sample. Therefore, the effect of uneven aluminum depletion has not yet been clarified and requires further investigation. It can also be seen from the images that the pores occurred predominantly in the aluminum depleted area, but occasionally in the area where the β-phase is still present. Figure 5.9 (a) also shows bright spots in the pores (i), which could be identified as yttrium oxides using EDX point measurements.

The reason for the considerable differences in lifetime between the Reference System, prepared with the FZJ Standard Bond Coat, and the System containing the Standard Bond Coats of Oerlikon Metco is also not yet known. Although the coatings were produced on different facilities with different torches, this does not explain such significant differences. From the reference samples, taken for the data points of the Arrhenius plot, only the cycling results and laser microscope images were available, which are shown in Figure AF1 in the Appendix. No mixed oxides can be determined on these samples due to the imaging method. Therefore, additional reference coating systems should be prepared, cycled, and analyzed. In addition, a detailed analysis of the newly produced bond coat is proposed, which can be compared with the XRD and Raman measurements from this work. Moreover, it is suggested to perform an oxygen analysis on the as-sprayed bond coats produced by Oerlikon and FZJ to detect possible oxidation of the particles in flight during coating production. A possible reason for the difference in performance could be annealing in different vacuum furnaces. Oxides of different grain sizes may have formed, which can affect subsequent diffusion [78].

In cross sections of the samples with a Metco 2253A bond coat, the aluminum depletion zone is not directly visible due to the different phases compared to the other bond coats. However, EDX mappings as shown in Figure 5.10 (b) revealed a significant depletion of aluminum within the bulk of the bond coat. Aluminum was mainly present in the Al_2O_3 layer in the interface and partly in pores in the bond coat inner, which were created by the stacking of the splats during the coating process. The Al accumulations in the interface to the substrate are particle residuals from the sandblasting process. Furthermore, it can be seen that the MoSi-rich phase (white) is only found in the upper part of the bond coat (Figure 5.10 (a)). It is not clear whether this phase migrated there or was dissolved in the lower area by diffusion with the substrate. The pores were also formed in this bond coat during thermal cycling.

The objective of the investigations in this chapter was to increase the service life of bond coats either by modifying the surface roughness or by using an innovative bond coat alloy

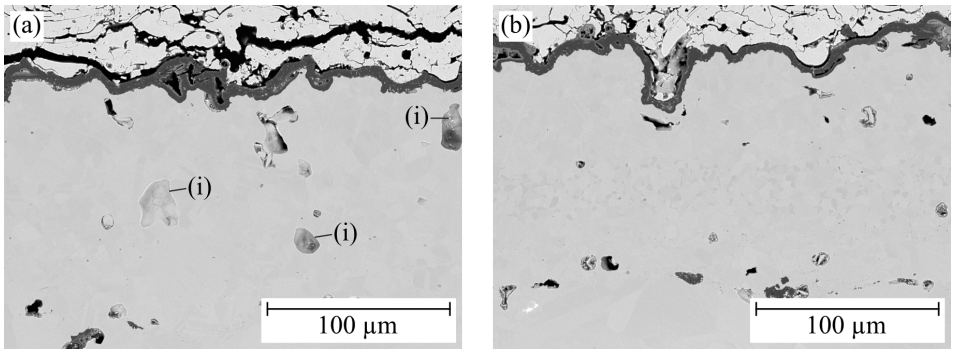

Fig. 5.9 SEM Cross-Sections with high magnification images of the TGO zone of a failed Oerlikon Metco Standard Bond Coat samples (a) in the middle of the sample (b) opposite side to failed coating; (i) white dots in pores are yttrium oxides

with a significantly reduced coefficient of thermal expansion to reduce out-of-plane stresses. In summary, it was observed that roughening the bond coat surface with the same chemical composition could shift the failure location from the interface to the ceramic top layer, which aligns with findings by *Nowak et al.* [135]. However, this shift does not necessarily correlate with an increase in service life. The Graded Bond Coats, with their increased roughness, showed a service life comparable to that of the Reference Coating System from Forschungszentrum Jülich. The failure of the Graded Bond Coat was attributed to aluminum depletion from poorly bonded particles. This led to the early formation of mixed oxides, increasing the stresses in the system and thus contributing to the failure of the coatings.

In contrast, the other bond coats all had longer lifetimes in the thermal cycling tests. The lifetimes of Oerlikon Metco's Standard Bond Coat, the Flash Bond Coats, and 2253A Bond Coats are comparable. The Flash Bond Coats successfully relocated the failure to the ceramic top coat. The cracks leading to failure did not propagate in the interface due to the high roughness, but formed within the ceramic close to the interface and at the tips of roughness peaks. Failure also occurred due to spinel formation, even though the bond coat still contained β-phase. The thinner and smoother Oerlikon Metco Standard Bond Coat and the 2253A Bond Coat specimens instead failed at the interface due to the comparatively smooth surfaces. The failure always occurred in the area of complete aluminum depletion of the bond coat. In some bond coats, the Al-rich β-phase was completely depleted over the entire sample cross-section. The depletion of the β-phase then led to the formation of mixed oxides, causing the spallation. The time of failure due to depletion is estimated by the red line in Figure 5.6. It is possible that these coating systems would have achieved an even longer service life with a thicker bond coat and thus a larger aluminum reservoir. Furthermore, the reasons for the significant differences in service life between the Standard Bond Coats from FZJ and Oerlikon Metco will be investigated in the future. One possible explanation is that different oxides were formed during the heat-treatments in the different furnaces. In addition, the precipitation of different elements at grain boundaries can have a significant effect on subsequent oxygen

diffusion. Moreover, the heat treatment may have led to different nucleation of the oxides, which in turn determines the grain size in the subsequently formed oxide layer, which also influences the oxygen diffusion. These assumptions will be verified using EBSD and TEM. The effect of pre-oxidizing the bond coats is described in section 6.2. In addition, the cross sections revealed, that pores formed in the bond coats during long service life. Since this phenomenon also occurred in the optimized top coats, it is also discussed in the section 6.2.

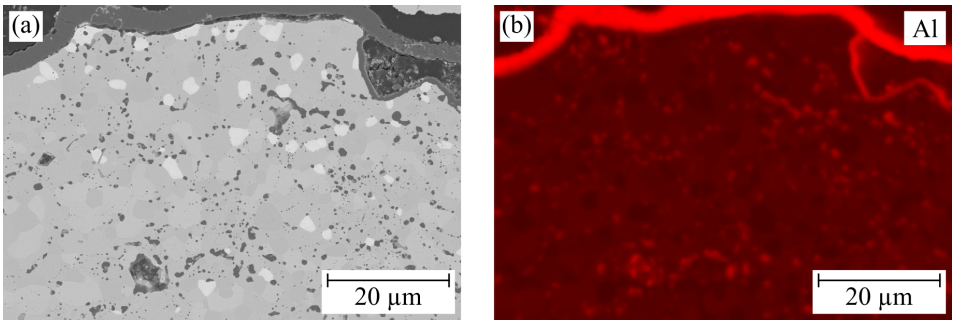

Fig. 5.10 SEM cross-section with high magnification images of the TGO zone of a failed 2253A Bond Coat sample (a) and its EDX map of Al (b)

6 Investigation of Optimized Top Coat Systems

6.1 Microstructure Analysis of As-sprayed Coatings and their Optimization

Parameter studies were performed for each process to identify suitable parameters for the production of strain tolerant coating microstructures. Variables identified in the literature as the most influential were varied. These include the variables current, process gas flows, carrier gas flow, spraying distance, robot speed, feed rates and several others. The deposited coatings were evaluated by image analysis based on metallographic cross-sections. Values such as porosity, crack or column density and other microstructural properties like the presence of unmolten, partially molten or resolidified particles were determined. In addition, the process efficiency for the production of each coating system was calculated. Mechanical properties like hardness and Young's modulus were also determined for some of the coatings. The optimization of the parameters for the different processes and the microstructures of the cycling samples sprayed with these optimized process parameters are discussed in the following subchapters.

6.1.1 Reference/Standard APS Top Coat

The reference top coating was not optimized as the FZJ quality standard (Reference system) was employed. This has been used for more than a decade to check the performance of the burner rigs and to compare optimized coatings [191], [14]. The microstructure of the coating deposited with the parameters listed in section 3.4 is shown in Figure 6.1. The only difference from the quality standards used at FZJ is the higher number of passes, which results in a slightly higher coating thickness. Typically, the reference top coat has a thickness of 400 - 450 µm. However, due to the collaboration with project partner Oerlikon Metco, it was decided to investigate thicker coatings that could generate a higher temperature gradient between the surface and the bond coat. The thickness of the Standard Top Coats used in this work is ~540 ± 20 µm. The porosity was determined to be 12.6 ± 0.6 %. The process had an efficiency of about 15 %. In Figure 6.1, the lamellar microstructures typical for the APS process can be identified and a large number of intra-splat cracks (i) are present. In addition, finely distributed inter-splat cracks (ii) and some resolidified particles can be observed in the coating microstructure. These Standard Top Coats have been applied to both, the Standard Bond Coats of FZJ and Oerlikon Metco.

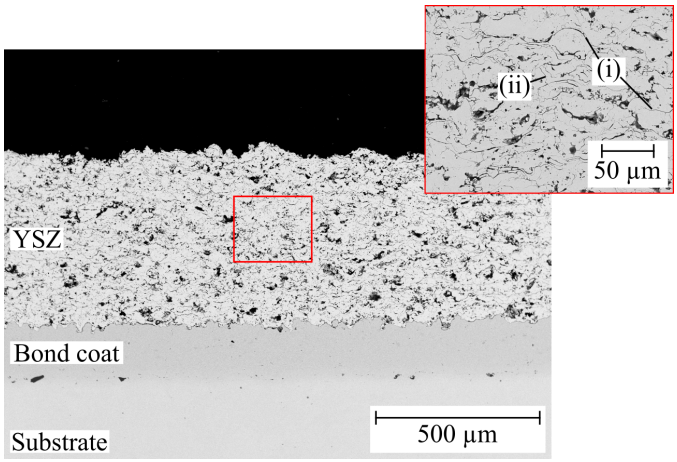

Fig. 6.1 SEM image of the coating microstructure of standard coating system (benchmark system); (i) intra-splat cracks, (b) inter-splat cracks

6.1.2 Optimized highly porous APS Top Coat

A systematic study was performed to optimize the process parameters for the production of strain tolerant, highly porous APS coatings. This was published by the author of this thesis and his colleagues, in a paper with the title "Systematic Approach to Optimize Technological and Economical Aspects of Atmospheric Plasma Sprayed Thermal Barrier Coatings" [113]. The goal of the study was to optimize the porosity and mechanical properties of the coatings with regard to high strain tolerance. A higher porosity not only improves the thermal insulation performance, but also reduces the stresses occurring during operation and thus, the growth of microcracks [110]. Nevertheless, the microcracks are desired in a coating, as they allow sliding movement between the flattened particles (splats) that form the coating, increasing the coating's strain tolerance (low Young's modulus) [111], [112], [227]. Besides its positive effects, a higher porosity is often linked to a negative effect on coating deposition rates and thus, process efficiency, which are both important in keeping manufacturing times and costs low [110]. As porosity increases, the hardness of the coating also decreases, reducing its resistance to erosion wear [161], [160]. This can be explained by the increased degree of irregular porosity and, in some cases, poorly bonded particles (partially molten, unmolten or resolidified), which affect the cohesion of the coating and cause a tendency for crack propagation [163], [162]. Due to these dependencies, it was important to find an optimal combination of process parameters to achieve an optimized coating for flexible gas turbine operation with high deposition efficiency, high porosity and simultaneously advantageous mechanical properties.
Prior to the actual systematic parameter study, screening experiments were performed to identify the most influential process parameters and to create a design of experiments (DoE). After these screening experiments, it was decided to vary the current between 400 and 500 A, the spraying distance between 160 and 220 mm, and the secondary process gas flow of hydrogen between 5 and 8 nlpm. The primary process gas flow of argon was

kept constant at 52 nlpm to analyze the effect of hydrogen content. At a hydrogen flow of 8 nlpm, the process gas flows resulted in parameters exceeding the process window of the gun. However, this was chosen to better analyze the effects of the hydrogen content in the process gas. Within this range of parameters, any combination of the input parameters could be used to produce a coating thickness sufficient for analysis, as well as desirable deposition rates and porosities. These parameters were then used to generate a DoE according to the Box-Behnken Design BBD. The BBD does not explore extreme combinations of all parameters, so the prediction accuracy in these areas is low. However, based on the preliminary tests, it can be assumed that the ideal parameter combination is in the middle of the investigated parameter range. The BBD is well suited for such an investigation due to its high prediction accuracy in this range. The resulting design matrix is shown in Table 7.2 in the Appendix. The design allows the estimation of linear, two-factor interactive and quadratic effects of the variables on the system responses. The results were calculated using Design-Expert software, which was used to create models for predicting system responses. In the following, only the results of the study are described. Details on the methodology can be found in the study [113].

In terms of process efficiency, the current was found to have the greatest influence of the three variables studied, followed by the spraying distance and finally the hydrogen content. The higher arc current generates more power and increases the specific enthalpy and temperature of the plasma. As the temperature increases, the density of the plasma decreases, which increases its velocity [228]. A higher hydrogen supply also increases the specific enthalpy, temperature and velocity of the plasma, and also increases the specific heat capacity and thermal conductivity of the plasma. The higher temperatures and faster heat transfer outweigh the shorter dwell time of the particles in the plasma due to the higher velocity. As a result, the particles are melted more effectively and the deposition rate is increased [110]. These factors also lead to low porosity of the coatings at higher plasma temperature and velocity. An influence of the spraying distance on the porosity could not be determined for the considered parameter range of the DoE.

In addition to process efficiency and porosity, mechanical properties were also analyzed in the study. The hardness and elastic modulus of the coatings were determined. Both were found to be highly dependent on coating porosity, shown in Figure 6.2. Even though the error bars of the measurements are large due to the high inhomogeneity of the coatings, a clear trend between the extreme values could be identified. These correlations between microstructural and mechanical properties are also known from literature [160], [229]. The decrease in hardness with increasing porosity is due to the fact that cracks propagate more easily in existing microcracks and pores. Under load, stress peaks are generated at these points, leading to crack propagation. This effect is amplified because the stresses are not uniformly distributed in the inhomogeneous coating [230]. In addition, viscous creep occurs under load between poorly bonded splats, reducing the hardness values [111]. Furthermore, the large indent volume results in more pores and cracks being penetrated, also reducing the hardness of the coating measured, due to the smaller volume of material. The numerous pores and microcracks also weaken the microstructure and reduce the effective cross-sectional area of the material, decreasing the coating's Young's modulus. [160]. Another effect reducing the Young's modulus is sliding motion between unbonded

splats and along defects. This viscoplastic deformation could also be seen in the force-displacement curves of the bending tests (shown in the study). Under constant load, the deformation due to creep increased significantly more for the porous specimens than that of the denser specimens.

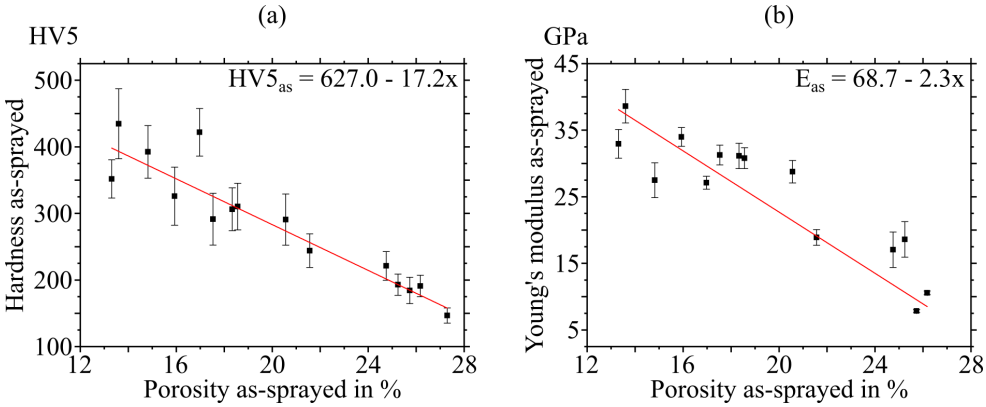

Fig. 6.2 Dependence of mechanical properties on coating porosity: (a) hardness, (b) Young's modulus

In addition to analyzing the porosity, hardness, and Young's modulus of the as-sprayed samples, the coatings were also investigated after heat treatment. Therefore, free-standing coatings were heat treated at 1200 °C for 100 h in a furnace at ambient air. As with the as-sprayed coatings, a high correlation between porosity and hardness was found. The correlation between porosity and Young's modulus remained, but was significantly lower. In the highly porous coatings, it was observed that only areas with fine microcracks could be closed by sintering. However, porosity was retained in areas with partially molten particles, unmolten particles, or areas with wide cracks. The dense coatings had mainly finely distributed cracks in the as-sprayed state, which were also closed by sintering. Because large areas of high porosity were still present in the porous coatings, sintering increased the hardness by only about 25 HV5. In the dense coatings, however, sintering produced large areas of completely dense material, increasing the hardness of these samples by up to 125 HV5. Therefore, in terms of hardness, sintering had a greater effect on the dense samples, where the overall porosity was reduced to a greater extent. In contrast, the effect on Young's modulus was greater for the porous coatings. It is assumed that the aging temperatures of 1200 °C were only able to provide sufficient activation energy to trigger surface diffusion. This allowed the formation of sinter necks to seal fine cracks, as these were mainly present in the dense coatings. However, the temperature was not sufficient to densify the porous coatings with large pores. Again, only sinter necks were formed. However, the formation of sinter necks created a bond between loose splats, resulting in the increase in Young's modulus. This also prevents sliding between cracks and along defects within the coating during deformation, which was previously possible with the porous coatings. This was also reflected in a decrease in viscoplastic creep after heat treatment during three-point bending tests. It was significantly lower after heat treatment than in the as-sprayed samples. However, it should be noted that the samples

were sintered as free-standing coatings, which leads to stronger sintering than in coatings applied to a substrate [231]. Further details about these results can be found in the study [113].

The parameter prediction models generated from the DoE were then used to generate a model for numerical optimization of the output values using the Design Expert software. The difficulty with this is that the results sometimes influence each other in undesirable manners. For example, increasing the porosity improves the insulation performance and reduces the stiffness, which increases the efficiency and durability of the coating in operation. However, it also reduces hardness and efficiency in the manufacturing process, which is detrimental. Higher hardness protects the coating from erosive wear, and high deposition efficiency is important from an economic point of view to enable time-efficient and therefore cost-effective production of the components. For the numerical optimization, the optimum of the input variables current (400 - 500 A) and spraying distance (160 - 220 mm) was searched in the whole design space. To keep the process within the operating window of the torch, the upper limit of the third input variable, hydrogen flow, was lowered from 8 to 6.5 nlpm. Therefore, the optimum optimal hydrogen flow rate was searched for between the values of 5 and 6.5 nlpm. For the system responses, the upper and lower limits were defined by the maxima and minima occurring in the individual prediction model of each result value. The system responses that should be maximized during optimization are deposition efficiency, porosity, and hardness in the as-sprayed state and after heat treatment. The Young's modulus in the as-sprayed state and after heat treatment should be minimized. The importance of porosity was prioritized in the model and therefore given a higher priority than the other system responses. This was chosen because porosity has the greatest influence on the mechanical properties and is the determining factor for the thermal insulation and therefore the efficiency of the turbine in service. Deposition efficiency, instead, was given a lower priority since the focus of the study was to produce a durable coating in service under cycling loads. In addition, the economic efficiency of the process is ensured by the high feeding rate, which keeps the processing time low. Further details of the numerical optimization model can be found in the study [113]. The developed numerical model was tested at the end of the study by spraying different parameter combinations. The results obtained were consistent with the predicted results.

The parameters optimized with the DoE according to the BBD are those described in Chapter 3.4 under the name Opt. APS in Table 3.8. The coating shown in Figure 2.20 was deposited using these parameters. The coating thickness of the Opt. APS samples is ~500 ± 30 µm and the porosity is 22.6 ± 2.0 %. Although the coating porosity is higher compared to the standard coatings, these coatings could be produced with a much higher efficiency of about 42 %. In addition to a large number of inter- and intrasplat cracks, the microstructure also shows many partially molten or unmolten particles in the coating. These are shown in the figure at point (iv). The microstructure of the agglomerated and sintered powder is still present, which can be identified by the small angular particles and high porosity in these areas. Including such areas in the coating was also the goal when selecting the powder with internal porosity.

6.1.3 Segmented APS Top Coat (DVC)

For the segmented APS coatings, the optimization was initially performed with the porous, agglomerated and sintered powder Metco 233C. In the study [232] by *Chen et al.* it was shown that the particle size distribution and the manufacturing process of the powder have almost no influence on the segmentation crack density. Therefore, optimization was first attempted with the relatively coarse powder and its internal porosity. For the first preliminary tests, parameters were identified from the literature that have a significant influence on the microstructure and properties of the resulting DVC coatings. As with the optimization of the highly porous coatings, these parameters were screened to define a parameter range within which DVC microstructures can be produced and the hot deposition conditions do not lead to coating failure during production. The most influential parameters identified from literature are power, spraying distance, powder feed rate and robot speed [167], [168], [232], [233]. These parameter were investigated in the screening tests. In addition, the influence of the injection point of the powder into the plasma torch was investigated by using a long and a short injector holder and the type of substrate cooling (backside only or backside and front side simultaneously). The properties studied were deposition efficiency, porosity and crack density.
By using two different injector holders, the preliminary tests can be divided into two test series. In the first series, the long injector holder was used with an injection point 12 mm behind the nozzle outlet, and in the second series, the short injector holder was used with an injection point distance of 4.6 mm from the nozzle outlet. In the first test series, the parameter combinations where the highest and lowest deposition temperatures were assumed were investigated for screening. The investigation of these extreme values should allow the definition of a test range for further tests to determine the optimum parameter combination. For the highest expected deposition temperatues, a high torch power, a small spraying distance and a slow robot speed were set, while the opposite was chosen for the lowest expected temperatures. The exact parameters used are shown in Table 7.3 in the Appendix. In addition to the parameters mentioned above, which significantly influence the deposition temperature, the effect of feed rate and substrate cooling was also investigated.
Under the low deposition temperatures (low power, high spraying distance, high robot speed), the feed rate had a significant impact on the deposition efficiency. It is about 7 % higher at a feed rate of 50 g/min (54.4 %) than at a feed rate of 100 g/min (47.2 %), as more energy per mass of powder is available in the plasma. However, even with the high efficiency, the microstructure in Figure 6.3 (a) shows that a large number of particles were only partially molten. As a result, a high porosity of ~20 % or more remains in all coatings sprayed with the low torch power output. The quenching stresses cannot build up sufficiently to produce vertical cracks. Under "hot" deposition conditions, the substrate temperatures increased from a maximum of ~380 °C under cold deposition conditions to a maximum of ~780 °C. As shown in Figure 6.3 (b), this also resulted in the formation of vertical cracks of up to 1.4 1/mm, which propagate through almost the entire coating. However, the porosity remained very high at around 20 %. At the high feed rates of 100 g/min, the hottest deposition temperatures were reached. These lead to delamination of the coating at the interface.

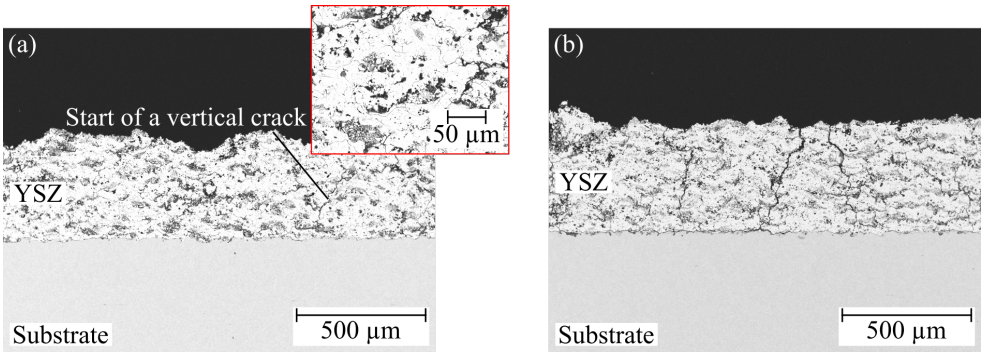

Fig. 6.3 Images of cross sections from the DVC screening tests: (a) cold conditions high feed rates, (b) hot conditions high feed rates

Due to the spallation of some of the coatings in the first test series, the power was adjusted for the second test series, investigating the short injector holder. These adjustments did also not lead to the production of dense, vertical cracked coatings with a sufficiently high crack density. A maximum crack density of ~2.5 1/mm could be achieved with parameter No. 10 from Table 7.4 in the Appendix. Despite the injection point in the hotter region of the plasma, there were still many unmolten or semi-molten particles in the coating and thus the porous structure of the particles remained in the coating. It is assumed that the heat flow in the particles themselves is too low to cause complete melting. Since it is not possible to produce dense vertical cracked coatings with the Metco 233C powder, the results will not be discussed further and the production of DVCs with Metco 214A powder will be described below.

The powder Metco 214A was provided by Oerlikon Metco along with two different sets of parameters for depositing the powder as DVC coatings. The parameter variations tested, with this powder are listed in Table 7.5 in the Appendix. The highest crack density was obtained with the DVC1 parameter. However, the microstructure of the coating sprayed with this parameter, shown in Figure 6.4, had horizontal cracks that can significantly affect the thermal cycling capability of the coating. Therefore, the coating with the next highest crack density was selected for the production of the thermal cycling buttons. This is produced using parameter DVC from Table 3.8 (DVC3 from Table 7.5 in the Appendix) and the coating microstructure is shown in Figure 2.21. Using these parameters, the coatings were produced with a process efficiency of approximately 53 %. The coatings have a thickness of ~445 ± 15 µm and a porosity of about 4.6 ± 0.3 %. The crack density is about 3.5 1/mm. Looking at the high magnification of the coating microstructure in Figure 2.21, it can be seen that the majority of the microcracks in the coating run in a vertical direction and only a few microcracks run horizontally to the substrate. This indicates good adhesion between the splats. The vertical cracks are then caused by the quenching stresses as the splats cool down. Some of the vertical microcracks in the coating join to form long vertical cracks. These occur both on the surface of the coating and in the lower coating area. Some run almost through the entire coating thickness from the

surface almost to the bond coat. These are the ones that are counted as cracks according to the crack density per mm.

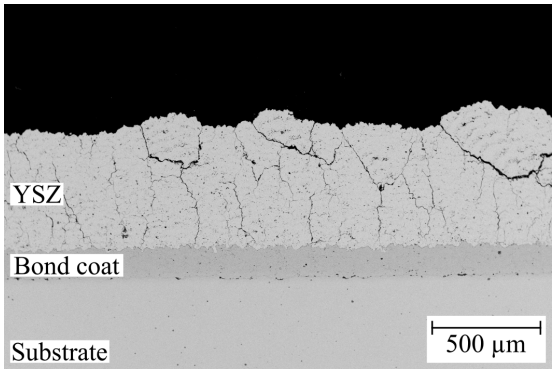

Fig. 6.4 Microstructure of DVC coating with detrimental horizontal cracks, sprayed with DVC1 paramerter

6.1.4 Optimized Suspension Plasma Sprayed Top Coat

After preliminary screening tests, the two different injectors without atomizers with a diameter of 80 and 120 µm were compared. Therefore, samples were sprayed with the same parameter at different spraying distances and the results were evaluated on the basis of the coating microstructures. The cross-sections of the coatings produced are shown in Figure 6.5. For both injectors, the deposition efficiency decreased with increasing distance and the porosity increased. For the 80 µm injector, the efficiency decreased from around 42 to 28 % and the porosity increased from around 24 to approximately 40 %. For the 120 µm injector, the efficiency decreased from about 55 to about 35 % and the porosity increased from about 19 to about 29 %. In general, it can be expected that a lower feed rate with the small injector (at constant pressure) will result in better melting of the agglomerated particles and an increase in deposition efficiency. However, this was not observed in the tests performed. Since the feed rate with the thin injector temporarily dropped to almost 0 g/min, it is assumed that this deviation was due to insufficient suspension feed, resulting in the suspension not being properly injected into the plasma. This caused the lower deposition efficiency and higher porosity with the thin injector. Further details on injector clogging are discussed below.
A striking feature in the microstructures are the very dense areas in the coatings sprayed with the small injector and a spraying distance of 60 and 70 mm. In both coating runs, the feed rate had temporarily dropped because the injector was probably slightly clogged. It was assumed that this caused the coating to re-melt due to the plasma treatment. The feed rate temporarily dropped to about 0 g/min. As a result, the suspension is no longer being fed into the plasma and there is no heat exchange between the plasma and the suspension. As a consequence, all of the thermal energy from the plasma is retained, re-melting the deposited material. When heat is partially transferred to the suspension under normal

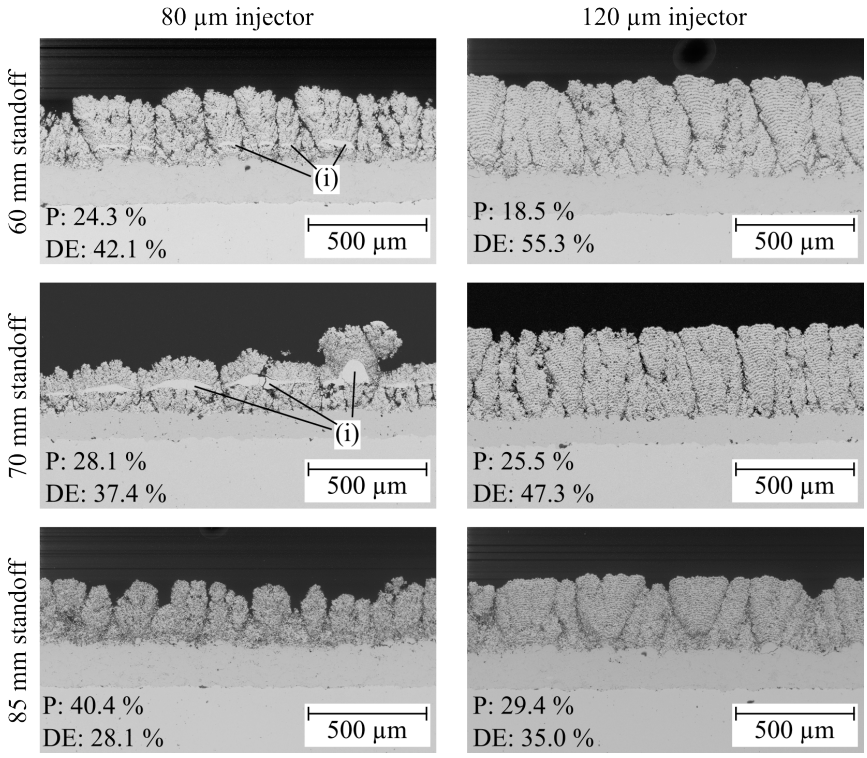

Fig. 6.5 Microstructure of SPS coatings sprayed with the 80 and 120 µm injectors at different standoff distances; P = Porosity, DE = Deposition Efficiency, (i) Remelted areas

feeding conditions, not all of the heated particles are deposited in the coating, resulting in a loss of some of the heat transferred to the particles. The heat lost in this way appears to be sufficient to prevent the deposited coating from re-melting. This theory was checked in further experiments. First, two samples with columnar coatings were produced. Then the suspension supply was stopped and the torch with plasma only was passed over the sample. One of the samples was passed over ten times and the other twice. Images of the sample surfaces and cross sections are shown in Figure 6.6. It can be seen that the surface was re-melted and the very dense coating areas were formed. This seems to confirm that the heat of the plasma, without suspension injection, is sufficient to re-melt the applied coating at short standoff distances. Since it was not possible to achieve a constant feed rate over an entire coating run with the feeding system used and the small injector in a large number of coating runs, it was decided to use only the large injector with a diameter of 120 µm for further investigations to ensure process reliability. In addition, after these preliminary tests, the spraying distance was set to 60 mm as with this the highest column density could be achieved.

The robot speed was also not varied further because tests with the GZO suspension (see section 6.1.7) showed that a lower robot speed results in thick porosity bands between the

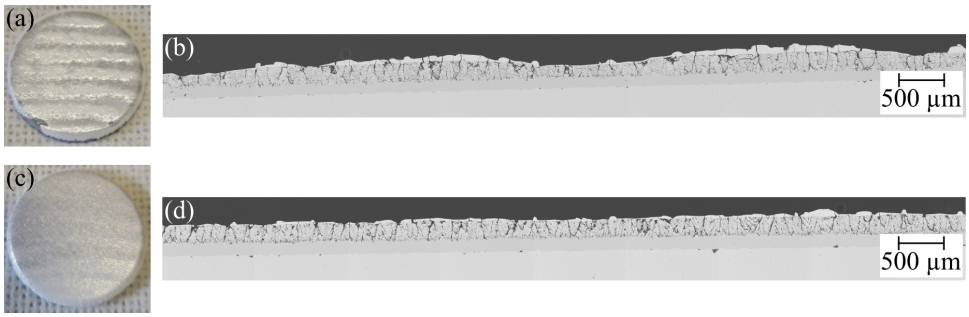

Fig. 6.6 Surface photograph and SEM cross-section of samples with a columnar microstructure and subsequent plasma treatment: (a) and (b) 10 times and (c) and (d) 2 times traversed with plasma without injection of suspension

individual layers of the coating containing horizontal cracks. Therefore, in the following tests, the process gas flows and the current were varied while the other parameters were kept constant. The total process gas flow was increased from 45 nlpm argon and 5 nlpm hydrogen to 52 and 6.5 nlpm and 64 and 8 nlpm respectively. These parameters relate to the limit of the process window with the highest possible hydrogen content in the plasma gas. Cross-sections of these samples are shown in Figure 6.7. Increasing the total process gas flow resulted in a slight decrease in deposition efficiency (from ~55 to ~51 %). The porosity remained comparable for all process gas flow rates (between 18.5 and 20 %). However, the column density increased with the higher gas flow (from ~5.9 to ~6.9 to ~8.4 1/mm). This can be explained by an increasd velocity of the plasma at higher process gas flow. As a result, the suspension is atomized into finer droplets due to the higher aerodynamic forces acting on it, resulting in more fine molten particles that are deflected in front of the substrate forming the columns [169].

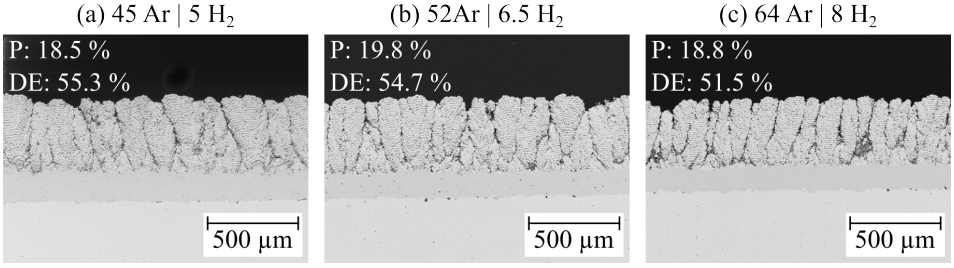

Fig. 6.7 SEM cross-sections of columnar microstructures produced with different process gas flows: (a) 45 nlpm Ar and 5 nlpm H_2; (b) 52 nlpm Ar and 6.5 nlpm H_2; (c) 64 nlpm Ar and 8 nlpm H_2

The microstructures created during production at different process currents are shown in Figure 6.8. It was found that as the current was increased, the deposition efficiency increased and the porosity decreased. The higher current causes more particles to melt and deposit in a dense layer, as the plasma enthalpy increases. The column density increased only slightly with increasing current, indicating that column growth is primarily driven

by the process gas flow. Since the highest process gas fluxes and the highest current tested achieved the highest column density, the optimized SPS samples were sprayed with the high process gas flow of 64 nlpm argon and 8 nlpm hydrogen and the highest current of 550 A. (Table 3.8). The cycling buttons were produced with an efficiency of about 54 %. The coating thicknesses were about 520 ± 30 µm and the porosities about 20.4 ± 1.5 %. The average column density of these coatings was ~7.6 1/mm. A cross section of a coating produced with the optimized parameters is shown in Figure 2.23. The columnar microstructure also shows the porous bands between the denser layers where many fine spherical resolidified particles are found. In the study by *Joeris et al.* such structured porosity bands were able to increase the thermal cycling life of the samples [80].

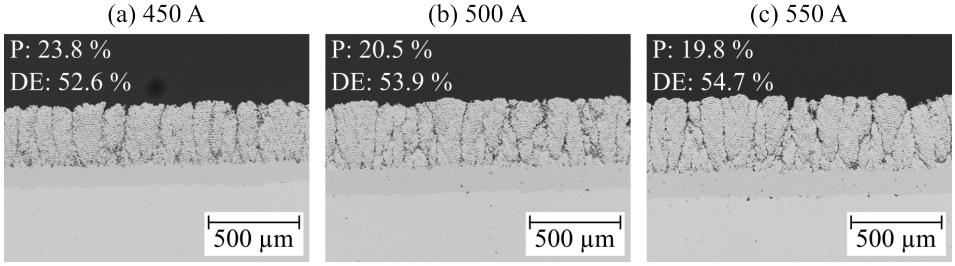

Fig. 6.8 SEM cross-sections of columnar microstructures produced with different current: (a) 450 A; (b) 500 A; (c) 550 A

6.1.5 Plasma-Spray - Physical Vapor Deposition Top Coat

Due to the significantly higher process costs of the PS-PVD process compared to processes performed at atmosphere, this process was not focused on. However, it was used to evaluate the coating performance of the optimized coatings. The PS-PVD coatings were therefore not optimized, but produced with a parameter set already optimized by FZJ. The parameters are described in Table 3.8 and the coating microstructure produced with these parameters is shown in Figure 2.24. The coatings produced for the thermal cycling experiments have a thickness of about 335 ± 45 µm and a porosity in the columns of about 9.8 ± 0.8 %. The column density of approximately 15 1/mm is the highest of the coatings analyzed in this work. However, a large number of spherical, resolidified, non-vaporized particles can also be found between the columns. This indicates that the process parameters could be further optimized. Nevertheless, due to the very high column density, the coatings were used for thermal cycling in the burner rig tests.

6.1.6 Comparison of YSZ Coatings Tested in Burner Rigs

Microstructure and Phase Analysis

This chapter presents a comparative analysis of optimized YSZ topcoat systems, subjected to cycling with a thermal gradient in a burner rig. Key microstructural properties and assumed thermal conductivities are summarized in Table 6.1. These values can be used to calculate the interface temperature. Since the Standard Bond Coat was used for all

coating systems listed in the table, it was comparable for all samples with a thickness of ~150 µm. The polished standard bond coat for the PS-PVD coating was also in this range. The thicknesses of the Standard, Optimized APS and SPS topcoats were comparable at around 500 µm. The thickness of the DVC coatings is slightly lower and is further reduced for the PS-PVD coatings. On the one hand, the thinner coating thickness reduces the amount of stored elastic energy in the coating during thermal cycling, which has a positive effect on the cycling properties of the coating. On the other hand, it is more difficult to achieve the same bond coat temperature at a constant surface temperature as with the other coating systems. This is further complicated by the fact that the thermal conductivity of the thinner coating systems is higher than that of the APS and SPS coatings due to the high density and, in the case of the PS-PVD coating, the additional large gaps between the dense columns.
Oerlikon Metco's Standard Bond Coat was used for all samples to compare the different topcoats. The only exception is FZJ's Standard Coating System, which was at least produced with the same bond coat alloy. Therefore, it is assumed that the TGO thickness will grow similarly at the same bond coat temperatures. Considering the fracture mechanics model of Oechsner from Figure 2.14, the fracture toughness at the interface should therefore decrease uniformly. However, the driving force for crack propagation differs between the systems due to the different microstructures and Young's moduli.
The difference in the driving force for crack propagation is the elastically stored energy in the coatings. With APS coatings, the entire coating is forced to follow the strains of the substrate. As a result, tensile stresses are present through the entire coating thickness during heating. After stress relaxation at high temperatures and subsequent cooling, compressive stresses are present. These stresses can only be reduced at the edge of the specimen, where the coating is not forced to stretch. Since the Young's modulus plays a critical role in the driving force for crack propagation, it can be assumed that a coating with a high Young's modulus will store more elastic energy and therefore exceed the critical energy density more quickly, leading to coating failure. In the case of APS coatings, the Young's modulus is closely related to the porosity of the coating **??**. As a result, the highly porous Optimized APS coatings should have better cyclability than the Standard APS coatings.
In coatings with segmentation cracks or columns, the stress state and therefore the distribution of elastically stored energy in the coating is different. In these, the strain at the coating surface is not dictated by the substrate. As with the APS layers at the edge of the sample, the gaps within the coating create regions throughout the sample where the coating can expand and contract flexibly. As a result, the stresses within the segments and columns decrease with increasing layer thickness toward the surface. As a result, a large amount of elastic energy is stored in and near the interface, decreasing toward the surface. This can be particularly problematic when a heat front passes rapidly through the coating. For example, if the sample is cooled with compressed air, the coating can contract freely at the surface. Close to the substrate, however, it is forced to stretch further caused by the hot, elongated substrate. This creates additional stresses in the system that can cause the critical elastic energy to be exceeded, resulting in crack propagation. Also critical to the rapid transit of a heat front through the coating is the thermal conductivity, which is higher for the segmented and PS-PVD coatings than for the APS and SPS coatings.

Tab. 6.1 Summary of key properties of YSZ coating systems for burner rig testing, * Measured only in columns

System	Thickness [µm]	Porosity [%]	Cracks/Columns [1/mm]	Termal conductivity [W/mK]
Standard	540 ± 20	12.9 ± 0.6	-	1.0
Opt. APS	500 ± 30	22.6 ± 2.0	-	1.0
DVC	445 ± 15	4.6 ± 0.3	~3.5	1.8
SPS	520 ± 30	20.4 ± 1.5*	~7.6	1.0
PS-PVD	335 ± 45	9.8 ± 0.8*	~15	1.5

To evaluate possible phase changes due to thermal cycling, an XRD measurement was performed on all topcoats in the as-sprayed condition. The results are shown in Figure 6.9 (a). The left graph shows the peaks of the metastable tetragonal phase typical of thermally sprayed YSZ caused by the rapid cooling of the material upon impact with the cold substrate. Notable differences between measurements emerge when considering the area surrounding the main peak. Enlarging the section of the 2-θ angle between 25 and 35° reveals peaks of the monoclinic phase (Figure 6.9 (b)). The peaks located at approximately 28.2° and 31.5° can be identified in the two APS coatings and in the PS-PVD coating. In the latter, they are slightly shifted, which could be caused by a tilted sample during measurement. In contrast, the peaks are not present in the DVC and SPS coatings. As the monoclinic phase is present in all raw materials, it is assumed that it is converted during the DVC and SPS processes. After rapid cooling from the molten phase, the metastable tetragonal phase is then formed. Even if deposited in a re-solidified state, as observed in the SPS coatings, the monoclinic phase underwent a transformation due to the complete melting. In the APS process, partial or unmelted particles are also deposited in the coating. These, in contrast, do not transform the monoclinic phase, leaving the monoclinic phase present. The occurrence of the monoclinic phase in PS-PVD coatings can be explained by the properties of the powder. Since it is not pre-alloyed, yttrium oxide and zirconium oxide are present as a single phase. During melting in the coating process, no YSZ alloy is formed. As a result, pure zirconia particles are still present, which form the monoclinic phase during cooling.

Mechanical Properties

Vickers and Rockwell indentations were performed as mechanical tests on the various as-sprayed samples, alongside erosion tests. Vickers indentations were used to determine hardness in the cross sections. These results can be correlated with porosity to verify its influence on hardness. In addition, these values are utilized to validate the influence of sintering during thermal cycling, comparing the HV5 values of the as-sprayed samples with those after cycling. Rockwell hardness instead is measured on the surface of the coatings. Therefore, these measured values are compared with the erosive wear of the coating systems to evaluate the influence of the different microstructures and hardnesses on the erosive wear.

The results of the Vickers hardness tests (HV5) are compared with the porosity of the coating systems in Figure 6.10 (a). This graph illustrates a consistent trend of decreasing hardness with increasing porosity across all considered coating systems. However, it was

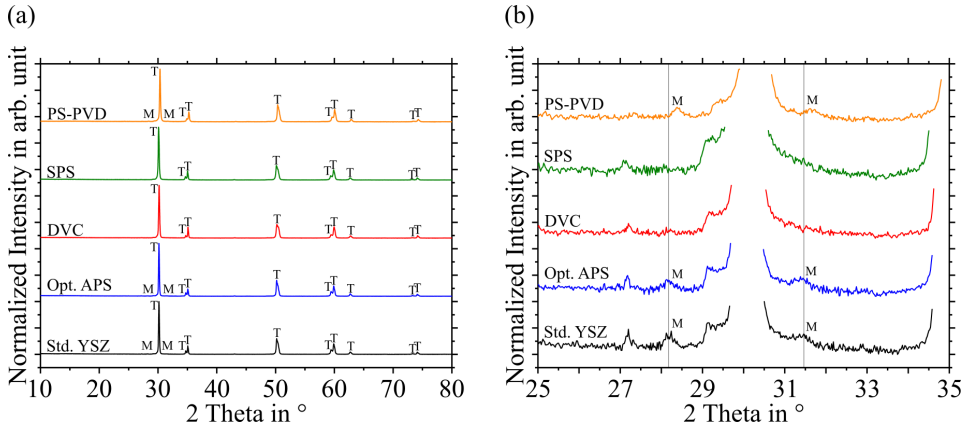

Fig. 6.9 XRD Analysis on as-sprayed TBCs in (a) at an 2-θ angle of 10 - 80° indicating peaks of the metastable tetragonal (T) and moniclinic phase (M) and in (b) enlarged view at an 2-θ angle of 25 - 35° indicationg peaks of the monoclinic phase (M)

not possible to measure the hardness of the PS-PVD system using the selected measurement method because the indentations were too large for the thin columns, resulting in coating failure.

In contrast, when measuring Rockwell hardness, the influence of the coating microstructure is different. A comparison of the results in Figure 6.10 (b) with the results in Figure 6.10 (a) shows that the Rockwell hardness of the SPS coating measured on the surface is closer to that of the Standard Top Coat and not, as with the Vickers hardness, to that of the Optimized APS coating. This implies that the SPS coating with a porosity of about 20.5 % has a comparable Rockwell hardness to the APS coating with a porosity of about 12.5 %. Thus, the dependence of the Rockwell hardness seems to be less closely linked to the porosity than the Vickers hardness. Similarly to the Vickers method, it was not possible to measure values for the PS-PVD coatings using the Rockwell method, as the columns collapsed due to the indent, indicating coating failure.

The erosion tests likewise demonstrate a pronounced impact of microstructure on material removal (Figure 6.10 (b)). While material is removed rapidly from the APS coatings, the material removal rate is low for the DVC and SPS coatings. In the PS-PVD coatings, as in the hardness test, the widely spaced columns spall due to lateral particle impact, resulting in immediate coating failure.

The poor performance of APS coatings in erosion tests is known from the literature. According to *Eaton and Novak*, plowing, secondary fracture and tunneling via pores are failure mechanisms for porous APS ceramics [234]. It is assumed, that the high removal rates are caused by splats beeing removed individually (secondary fracture), and that cracks also propagate parallel to the direction of particle impact along pores (tunneling via pores), resulting in the removal of large pieces of coating. Especially for the highly porous Optimized APS coatings, large pieces seem to be removed quickly. Here, cracks can easily propagate through the many microcracks and large pores, as well as along poorly bonded, partially or unmolten particles.

In contrast, the DVC coatings show the lowest erosion rates despite the lamellar microstructure resulting from the APS process. This finding is consistent with prior literature, which has compared DVC coatings with APS and SPS coatings [211], [235]. Due to the high hardness and toughness of the dense DVC coatings, crack propagation as described by *Eaton and Novak* is inhibited. Similarly, SPS coatings also display high erosion resistance, aligning with trends reported in the literature [236], [211], [235]. The finely distributed microcracks and predominantly well-bonded splats, facilitated by complete melting, contribute to preventing crack propagation due to particle impact.
For PS-PVD coatings, however, there are conflicting results in the literature. While *Cernuschi et al.* reported the highest erosion resistance for PS-PVD coatings among the plasma sprayed coatings tested [237], *Wännman* found that PS-PVD coatings experienced the highest erosive wear among the plasma sprayed coating systems investigated [238]. The results of this work align with Wännman's findings, as coating failure occurred directly as a result of particle impact. The wide gaps between the columns and the v-shaped grain boundaries in which some unmelted and resolidified particles can be found (Figure 2.24) suggest that even a small amount of energy from the lateral impact is sufficient to remove large column areas.
Despite the consistency of many erosion test results with findings from the literature, these tests were performed, as none of the previous studies examined all the coating systems considered in this work simultaneously. Furthermore, different erosion behavior could have been detected, as the microstructures can vary considerably even when using the same coating process.

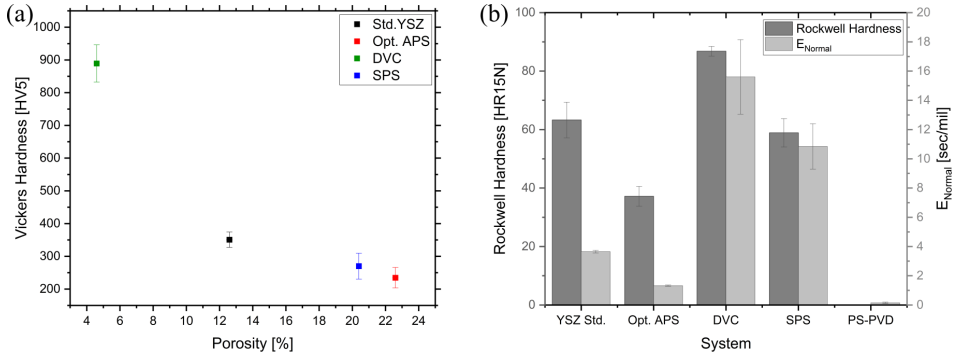

Fig. 6.10 Dependence of Vickers hardness on porosity for the as-sprayed samples in (a), comparison of Rockwell hardness and erosion wear in (b)

6.1.7 Alternative Top Coat Material Gadolinium Zirconate

The results obtained regarding alternative top coat materials are described separately from the single layer YSZ coatings, as these samples were tested in furnace cycling and not in the burner rigs. GZO was selected as an alternative to YSZ. Due to the low fracture toughness of GZO, it was deposited in a double-layer system with YSZ as interlayer. The optimized specimens were tested in furnace cycling tests, as these produce higher accumulated

stresses due to the thermal expansion mismatch than burner rigs. The coatings durability and failure mechanisms were compared with single-layer YSZ Standard Top Coats. The results were published in a paper by the author of this thesis and his colleagues with the "Extended Lifetime of Dual Layer Yttria Stabilized Zirconia APS/Gadolinium Zirconate SPS Coatings in Furnace Cycle Tests" [Submitted in JACerS]. The optimization of the parameters, to produce strain tolerant GZO topcoat microstructures described in this study, is summarized here.

Since there was no previous experience with the non-commercial GZO suspension and continuous stream injection, screening tests were first carried out to determine a process window for the production of strain-tolerant SPS coatings. It was found that a high robot speed of 1000 mm/s was required to keep the interpass porosity sufficiently low to prevent horizontal cracking in the coatings. The effect of robot speed can be seen in the microstructure images in Figure 6.11. These coatings were produced with the GZO LP parameters from Table 3.8. The robot speed was only reduced from 1000 to 500 mm/s for the sample in the left image (a). At the lower robot speed, the individual layers produced with each pass can be identified and the horizontal cracks between these layers are clearly visible. A small spraying distance and minimal gun power are also required to produce strain-tolerant microstructures. The standoff distance was set to 70 mm. To keep the porosity as high as possible, which is important for insulation and performance [80], the gun power should not be too high, otherwise dense layers may be formed [172]. Therefore, a power of about 47 kW was specified. This is influenced by the current as well as the volume and composition of the process gas. The amount of plasma gas also affects the atomization of the suspension and thus the droplet size. This is particularly important because the suspension is injected radially into the plasma and no additional gas is used for atomization. The size of the droplets then affects their trajectory, which influences the microstructure of the resulting coating [129], [239], [176]. Therefore, different currents and process gas flows were tested to achieve the defined performance. Of these, the two combinations GZO LP and GZO HP described in Table 3.8 were finally selected to produce the furnace cycling samples and to analyze the influence on microstructure and lifetime in detail.

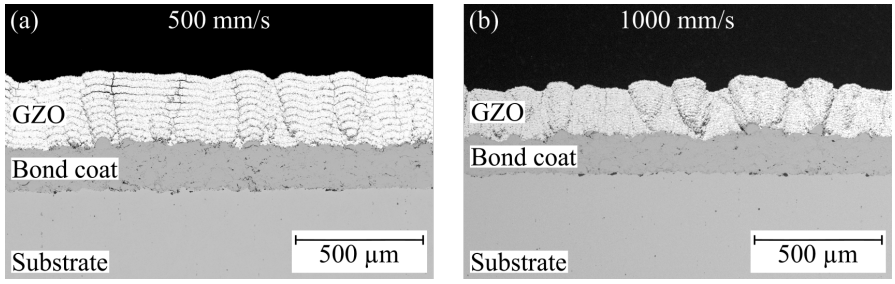

Fig. 6.11 SEM cross-sections of GZO-SPS microstructures produced with different robot speeds: (a) 500 mm/s; (b) 1000 mm/s

These parameters were then applied to APS-YSZ interlayers with different surface roughness to investigate the effect of the interlayer on column formation. The interlayers were prepared

with parameters APS1, APS2 and APS3. The surface roughness was analyzed with a white light topographer. The standard APS-YSZ layers (APS1) without surface modification and the APS layers deposited with the reduced torch power (APS3) had a comparable roughness value of R_a ~9.5 µm. However, attempts to further reduce the power to increase the roughness values resulted in poor bonding of the deposited particles and low process efficiency. By increasing the torch power (APS2), the roughness could be reduced to R_a ~7.5 µm.

In the cross-sections, different microstructures were found in the SPS-GZO layers sprayed onto the APS layers with different surface roughness. On the smoother APS2 interlayer, there was almost no column formation, as shown in Figure 6.12. Due to the lower roughness, the fine particles deflected by the plasma gas flow in front of the substrate cannot deposit laterally on it and no columns are formed [176]. Instead, vertical cracks form in the GZO layers. Due to the small number of microcracks in the coating, tensile stresses build up when the splats cool down after impact, leading to the formation of segmentation cracks [240]. Segmented coatings are also suitable for strain-tolerant coatings [14]. In this case, however, the vertical cracks are combined with horizontal cracks along the interpass porosity of the coatings, especially in the SPS coating produced with high process gas flow (GZO HP parameter). These horizontal cracks originating from the vertical cracks are also referred to as branching cracks in the literature. They have been observed in a large number of studies on SPS coatings [172], [81], [174], [54], [241]. When comparing the occurrence of these cracks, it is noticeable that they always occur in coatings deposited on rather smooth substrates. Furthermore, they always grow in the porous interlayers of the SPS coating microstructures. Deposition on the smooth surfaces leads to the formation of DVC structures, which also have a uniform surface of the top layer without large differences in height. Therefore, the porosity bands run parallel to the interface and are not waved, providing an easy path for crack propagation. In addition to the poor adhesion of the coatings within the porosity bands, the low fracture toughness of GZO can also promote crack propagation within the coating. On polished substrates, the coating may also buckle, indicating compressive stresses in the coatings. Compressive stresses after production can occur when high deposition temperatures are reached and the substrate contracts more than the ceramic topcoat contracts from its deposition temperature. Compressive stresses can also favor the formation of branching cracks in the weakly bonded porous interlayers. The branching cracks can have a negative effect on the thermal shock resistance of the coating. Therefore, it was decided to produce the cycle samples only with the interlayers with parameters APS1 and APS3.

A total of four combinations of APS-YSZ and SPS-GZO were produced from these parameters for furnace cycling tests. The sprayed microstructures are shown in Figure 6.13. Table 6.2 lists the parameters used to produce the various double-layer systems and the resulting coating thicknesses according to the Figure 6.13. This table also gives a designation for each of the systems, which will be used in the discussion about the furnace cycling results. The GZO A system consists of the standard APS1 intermediate layer and the GZO-LP coating, which is produced with the low process gas flow. The GZO B system also consists of the standard APS1 coating and the GZO-HP coating, which is produced with a high process gas flow. The GZO C and GZO D systems consist of the reduced power APS3 layer and the low (GZO LP) and high (GZO HP) process gas flow

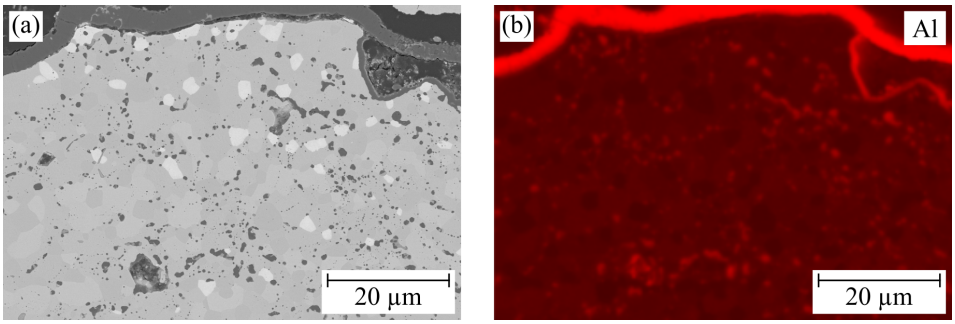

Fig. 6.12 SEM cross-sections of GZO-SPS microstructures produced with (a) GZO LP and (b) GZO HP parameter on smoothest APS interlayer (APS2 parameter)

Tab. 6.2 Comparison of TGO thickness in different faild TBC Systems

Image	System name	Parameter used	Thickness APS [µm]	Thickness SPS [µm]
a	A	APS1 + GZO LP	233.3 ± 17.5	265.5 ± 19.1
b	B	APS1 + GZO HP	223.9 ± 19.2	263.6 ± 22.8
c	C	APS3 + GZO LP	223.3 ± 20.9	281.5 ± 11.4
d	D	APS3 + GZO HP	223.5 ± 20.6	254.0 ± 16.2

top layers, respectively. All ceramic layers produced are of comparable thickness. The porosity of the YSZ interlayers is about 14.6 ± 0.9 % for all systems. No influence of the parameter variation on the porosity could be determined. In contrast, an influence of the process parameters on the porosity could be determined for the SPS-GZO coatings. For the coatings with low process gas flow, the porosity was higher with a value of 11.1 ± 1.4 % than for the coatings with high process gas flow, where the porosity value was 8.8 ± 0.8 %. As expected, the columns grew at the roughness peaks. In contrast, vertical cracks formed in areas with few roughness peaks. The microstructures of the specimens always contained a mixture of columnar and vertical crack structures. Therefore, all cracks and gaps in the columnar microstructure were counted to determine the crack and column density. Overall, the crack and column densities measured in the systems were approximately 10 1/mm. The phases present in the coatings and the mechanical properties of the coatings are described in the analysis after furnace cycling tests (Chapter 6.2.2) and are directly compared with the changes caused by thermal cycling.

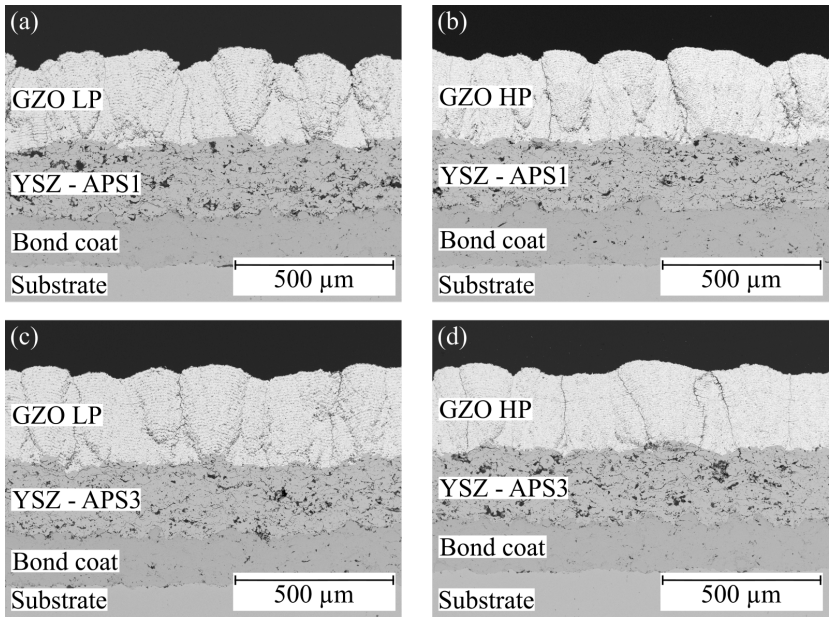

Fig. 6.13 SEM cross-sections of four different APS-YSZ/SPS-GZO microstructures for furnace cycling experiments

6.2 Thermal Cycling Lifetime of Different Top Coats

This chapter will cover the results of cycling tests in a burner rig with a thermal gradient and the results of isothermal furnace cycling tests. The different YSZ topcoats (Standard, Opt. APS, DVC, SPS, PS-PVD) have been investigated in burner rig tests, as this test setup closely simulates the thermal conditions in a turbine. Therefore, these results are the most representative for the coating systems under consideration. The alternative topcoat material GZO, which was used in a double-layer system with a YSZ interlayer, was tested in isothermal furnace cycling tests. The furnace tests generate higher accumulated stresses due to the isothermal temperature distribution during the test. The furnace tests generate greater thermal stresses due to the isothermal temperature distribution during the test. Since the ceramic expands less than the metallic components, the stresses are maximized. The burner rig test instead, reduces the expansion mismatch as the ceramic reaches a higher temperature than the metallic components. The furnace cycling test is therefore particularly suitable to investigate the strain-tolerance of the low fracture toughness material GZO as well as the adhesion between the two ceramic top layers. The results of the burner rig tests are discussed below, followed by the results of the furnace cycling tests.

6.2.1 Burner Rig Testing Results

Comparison of Time to Failure for different Top Coats

The graph in Figure 6.14 describes the life of the samples plotted over the average inverse bond coat temperature during the test. The two black squares again describe the performance of the reference specimens described in Section 5.2. The black line running through the two black squares describes the doubling of the service life when the bond coat temperature is reduced by 30 ℃ [191]. The two black circles, on the other hand, describe the performance of the Standard top cpat produced with the HOSP powder Metco 204NS deposited on the Standard Bond Coat from Oerlikon Metco. As described in chapter 5.2, these had a longer service life than the reference samples produced at FZJ.

The blue triangles show the lifetime of samples with the Optimized APS Top Coat. The triangles with the tip up represent the samples with the Standard Bond Coat, and the triangles with the tip down represent the samples with the Bond Coat pre-oxidized in argon. The samples without the pre-oxidized bond coat have a slightly higher average lifetime than the Standard Top Coat samples. The samples with the pre-oxidized bond coat again slightly exceed the lifetime of the samples without the pre-oxidized bond coat and the optimized APS Top Coat. The increase in service life is attributed to slower growth of the oxide layer during thermal cycling. This growth is slowed down by the previously formed, dense Al_2O_3 layer. As the oxide layer was formed in a reduced argon atmosphere, it is assumed that a very dense oxide layer has formed, which prevents diffusion through vacancies.

The green triangles describe samples with an SPS top coat. Again, triangles with the tip pointing upwards represent samples sprayed on with the Standard Bond Coat and triangles with the tip pointing downwards represent samples sprayed on Bond Coats pre-oxidized in argon. The Standard Bond Coat samples only had a lifetime slightly improved compared to the reference system. However, pre-oxidizing the bond coat significantly improved the cyclability of the SPS coatings. The lifetime was increased by a factor of about 2. This improvement of the lifetime of the coating system in thermal gradient tests is consistent with the results of the study by *Joeris et al* [80].

The DVC coatings are marked by the red rhombus in the diagram. These systems have a comparable durability to the FZJ Standard Coating System. The increased bond coat temperatures are due to the high thermal conductivity of the dense coatings. With a thermal conductivity value of ~1.8 W/mK, it is assumed to be much higher as with the other porous YSZ coatings (~1 W/mK). However, despite the strain-tolerant, vertically cracked microstructure, the DVC coatings do not exhibit good cyclability, considering the linear relationship of a factor of 2 improvement at 30 ℃ lower bond coat temperature.

The measured values of the PS-PVD samples shown in the diagram by the orange triangles pointing to the left also had a higher bond coat temperature. Again, this is due to the higher thermal conductivity of this coating system, which is assumed to be ~1.5 W/mK. For this reason, further samples of this coating systems should be tested at an adapted bond coat temperature to correlate the service life with the other coating systems.

Failure of Different Coating Systems

First, the coating systems were examined for the type of failure mechanism by investigating the cross-sections. Crack propagation paths, TGO thicknesses, and microstructural changes

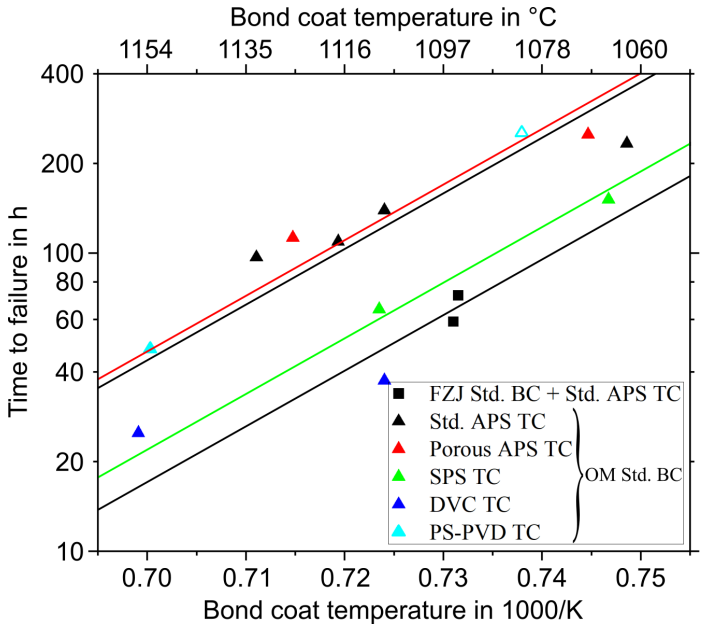

Fig. 6.14 Service life to failure as a function of the inverse bond coat temperature for YSZ TBCs with different top coatings; Except FZJ Std. all samples had Oerlikon Metco Standard Bond Coat; Surface Temperatures 1400 - 1450 °C

were analyzed. This analysis is described below for the various optimized single-layer YSZ coating systems deposited on the Standard Bond Coats. The systems analyzed include the Standard Top Coat System, the Optimized APS, DVC, SPS and PS-PVD Coatings. The effects of pre-oxidizing the bond coats will be discussed in more detail later. A photograph and SEM cross section of a failed sample from each coating system is shown in Figure 6.15.

The standard coating system (Figure 6.15 (a)) has already been described in the analysis of the different bond coats in Section 5.2. Failure in this system was caused by crack growth at the interface along or through the TGO. Due to the low roughness of the bond coat, crack propagation in the interface could not be suppressed, allowing the cracks in this area to propagate and interconnect until the coating spalled. This type of failure also occurred with the highly porous optimized APS coating (Figure 6.15 (b)). This indicates that the critical energy release rate was exceeded in the TGO itself or near the interface, in poorly bonded splats of the ceramic. Considering the fracture mechanics model of Oechsner (Figure 2.14), it can be assumed that the same bond coats used experience the same decrease in fracture toughness. However, due to the higher porosity and lower Young's modulus of the Optimized APS coating, this approach would expect it to store less elastic energy, resulting in a longer service life. Figure 6.14, however, shows that the service life of the APS coating systems with Oerlikon Metco Standard Bond Coat is comparable.

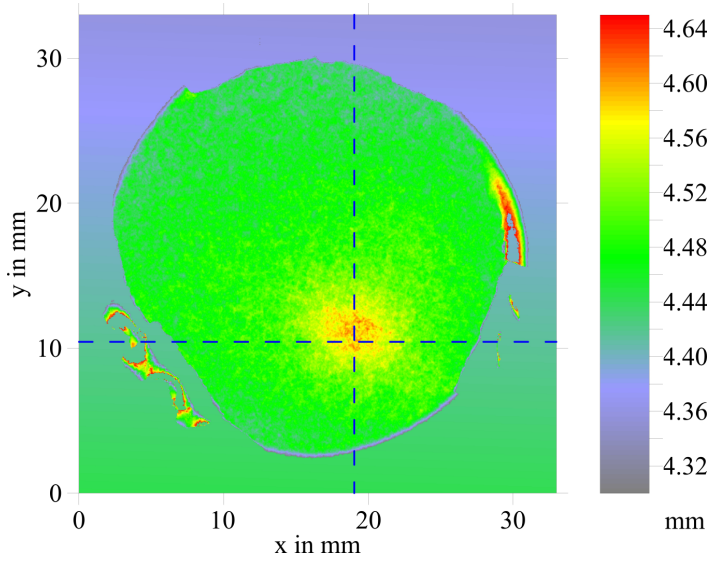

Fig. 6.15 Photographs and SEM cross-sections of the failed samples with different top coats: (a) Standard, (b) Opt. APS, (c) DVC, (d) SPS, (e) PS-PVD Top Coat

On the one hand, this could indicate that the driving force for crack propagation has a minor influence. On the other hand, Figure 6.15 and 6.16 show in the cross-sections that more cracks propagate through the porous Optimized APS coating and also reach higher into the ceramic. These cracks formed near the interface between splats with low adhesion. Such a crack pattern can be seen for the Standard Coating System in Figure 6.16 (a) and for the Optimized APS System in (b). In the left image (a) of the Standard coating, there are areas where the crack runs along the interface (i), through the TGO (ii), and through the ceramic (iii). These three crack paths can also be seen in the right image (b) of the Optimized Topcoat. In the case of the Optimized APS coating (b), it can be seen that the crack propagates into the ceramic coating in the area of unmolten particles with low adhesion (iii). These also affect the fracture toughness of the ceramic. Like Young's modulus, fracture toughness is related to porosity. Lower porosity increases the Young's modulus, which increases the driving force for crack propagation, but also increases the fracture toughness, which increases the resistance to crack propagation. Therefore, these effects seem to balance each other for the coatings investigated. Thus, both coating systems appear to withstand thermal cycling to the point of mixed oxide formation due to Al-depletion of the bond coat.

In the coating systems with segmentation cracks (Figure 6.15 (c)) and columnar SPS microstructure (d), the crack paths are different. Although the cracks also occur close to the interface, they predominantly expand through the ceramic coating. Since the bond coat system is the same as for the APS coatings, the modified top coat must be responsible for the different crack paths. Higher magnification images of the interface are shown in Figure 6.17 (a) for the DVC system and (b) for the SPS system. The cracks leading to

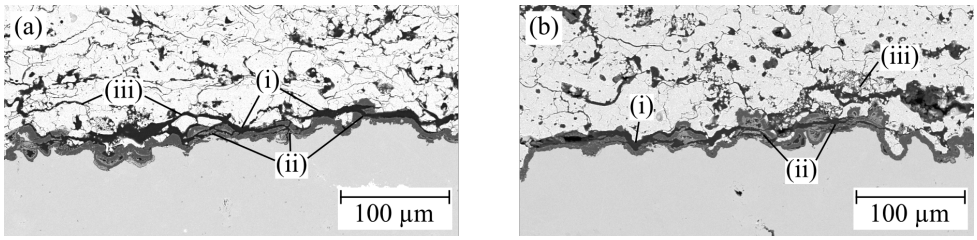

Fig. 6.16 High magnification of the crack in the interface: (a) Standard, (b) Opt. APS Top Coat; (i) Crack along the interface, (ii) through TGO, (iii) through ceramic

coating failure propagate along the roughness peaks of the bond coat, but do not follow the interface and TGO. Instead, they propagate almost completely through the ceramic near the interface. It is assumed that the cracks form above the roughness peaks in the interface or in the ceramic close to the interface due to the radial stresses created by the expansion mismatch between the bond coat and the top coat during thermal cycling. From there, the cracks expand through the ceramic. This indicates that the critical energy release rate (fracture toughness) of the coating system has been exceeded at this point. The segmentation cracks and columns in the coatings absorb the elastically stored energy, especially near the interface. The reason for this is that the segments and columns are flexible in the upper region and only the lower region is forced to stretch by the substrate. The tips of the coating therefore experience less or no stress and the elastically stored energy is lower. In the case of DVC coatings, the thinner layer also causes the temperature front to pass the coating more quickly during cooling, further increasing the stresses at the interface. In the SPS coatings, the porosity bands provide low fracture toughness due to poor particle bonding, resulting in a low critical energy release rate. As a result, large amounts of elastic energy are introduced near the interface and the critical energy release rate is exceeded early during thermal cycling, leading to coating failure.

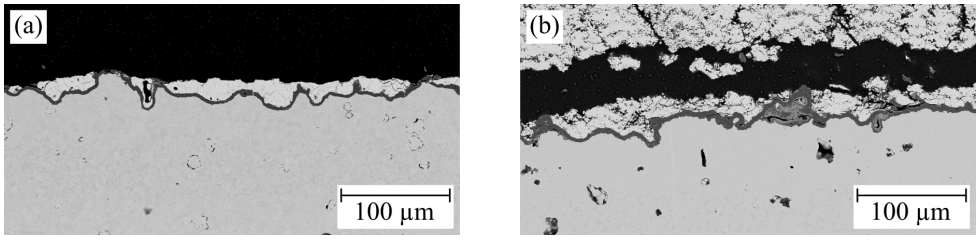

Fig. 6.17 High magnification of the crack in the interface: (a) DVC, (b) SPS

The failure mechanism in the PS-PVD system (Figure 6.15 (e)) is not comparable to the others as the bond coat was polished before the PS-PVD coating was applied. Due to the changed morphology of the surface, radial stresses no longer occur at roughness peaks. This means that expansion mismatch between the ceramic and metallic layers occurs only in plane. This mismatch can be compensated due to the high column density of the PS-PVD coating and therefore high strain-tolerance. However, the different CTE of the substrate

Tab. 6.3 Comparison of TGO thickness in different failed TBC Systems, all applied to Standard Oerlikon Metco Bond Coats; Tested at surface temperatures between 1400 and 1450 ℃and bond Coat temperatures between 1050 and 1100 ℃

Top Coat System	Al_2O_3 [µm]
Standard	4.1 ± 1.1
Opt. APS	3.9 ± 0.8
Opt. APS + pre-ox. BC	3.2 ± 1.0
DVC	2.7 ± 0.5
SPS	3.6 ± 0.8
SPS + pre-ox. BC	3.3 ± 0.6
PS-PVD	2.5 ± 0.4

and bond coat can lead to subsequent roughening of the bond coat, referred to as rumpling beeing explained in Chapter 2.3.2. This effect is shown in Figure 6.18 (a). It occurs when the lower expansion coefficient of the substrate causes the bond coat to experience tensile stress during cooling. In contrast, compressive stresses occur in the bond coat during heating. When the stress buildup exceeds the yield strength of the bond coat, creep results and the bond coat roughens. At these points, the ceramic layer detaches from the formed TGO, as shown in Figure 6.18 (a). Such cracks then easily propagate along the smooth TGO/topcoat interface. This results in delamination of the coating at the interface, leading to spallation of the coating. The delamination of the coating can be seen in Figure 6.18 (b).

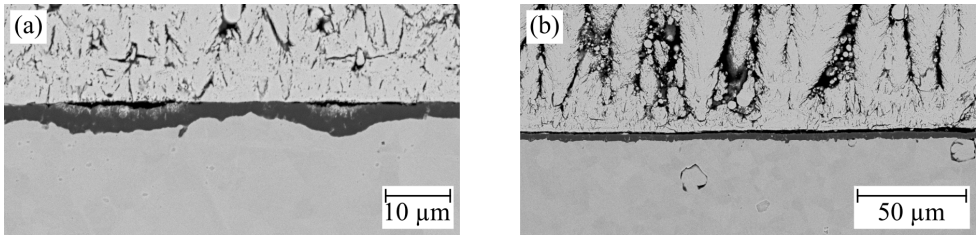

Fig. 6.18 SEM cross-sections of failed PS-PVD coating (a) at high magnification and (b) in an overview image

A comparison of TGO thicknesses is given in Table 6.4. The values listed there are the average values of all samples tested of the respective coating type. It can be seen that the TGO thickness is comparable for all samples. The TGO thickness for the samples with a shorter run time (DVC and PS-PVD) is slightly lower, but not significant, so this difference is not considered further. This means that the TGO thickness alone cannot be the determining factor for the different lifetimes of the coatings. As described in Chapter 5.2, CoNiCr spinels formed only very locally in the samples with the Standard Top Coat System. This is also the case for all other top coat systems deposited on the same bond coat. Only in the PS-PVD sample with the polished bond coat no mixed oxides were formed. Since no significant differences can be found to explain the different lifetimes of the samples, the microstructural changes in the top coats are analyzed in more detail in the next section.

The comparison of the service life of vacuum-annealed and pre-oxidized bondcoat samples is shown in Figure 6.14. This shows that the service life of the samples with the Optimized APS topcoat and the vacuum-annealed bond coat (blue line) considerably exceeds that of the SPS coatings on this bond coat (green line). Comparing the results of the systems with the bond coats pre-oxidized in an argon atmosphere, the lifetimes are more similar. However, it should be noted that both the APS and SPS topcoat systems showed an improvement in service life as a result of pre-oxidation, which is consistent with the results of the studies presented in Chapter 2.2.3. To understand why the improvement in service life was particularly pronounced for the SPS topcoat systems, the SEM cross-sections of the samples after failure were also examined.

The APS and SPS coatings applied to a pre-oxidized bond coat exhibited the same failure mode as the samples with coatings applied to the vacuum annealed bond coats. The APS coatings also failed within the TGO, and for the SPS coatings, the crack leading to failure propagated within the porosity bands close to the interface. Since there were no differences in the topcoats, the extended lifetimes of the specimens with the pre-oxidized bond coats must be due to the pre-oxidation. When comparing the TGO thicknesses of the pre-oxidized bond coats after thermal cycling, they are in the same range as for the vacuum annealed samples. It was therefore assumed that the TGO growth during testing is reduced due to the formation of a dense Al_2O_3 layer before the ceramic top coat is applied. The reduced atmosphere during the argon treatment enables the slow and dense growth of this layer. After thermal cycling, a partial depletion of the Al-rich β-phase in the bond coat was observed in both the APS and SPS coatings applied to the pre-oxidized bond coat, resulting in the formation of mixed oxides. This was the same for the samples with the Optimized APS Top coat on the vacuum annealed bond coat. The SPS top coat on this bond coat instead failed before the depletion of the Al-rich β-phase.
In the case of the APS coatings, the slowed oxide growth due to pre-oxidation only slightly extended the service life of the coatings. However, in the case of the SPS coatings, it is assumed that the formation of the TGO prior to the application of the ceramic top coat could change the stress distribution within the coating system. As the initial rapid growth of the oxide layer occurred mainly before the topcoat was applied, it did not affect the ceramic topcoat during thermal cycling. As a result, the specimens only failed when there was a partial depletion of aluminum in the bond coat. However, the lowest fracture toughness was still in the ceramic itself, which is why the sample failed in the top coat and not at the interface. Therefore, the lifetimes of the APS coatings with pre-oxidized bond coat are still longer than those of the SPS topcoats, as they failed when the critical energy release rate of the TGO was exceeded. In contrast, the SPS coatings failed before this fracture occurred at the TGO. This failure mode differs from the results of the study by *Joeris et al.* on the pre-oxidation of TBCs with an SPS top coat [80]. There, the pre-oxidation shifted the failure location to the TGO as well. It should therefore be investigated whether the top coat needs further optimization or whether the pre-oxidation can be further adapted for the coating system under consideration in order to create ideal conditions for thermal cycling.

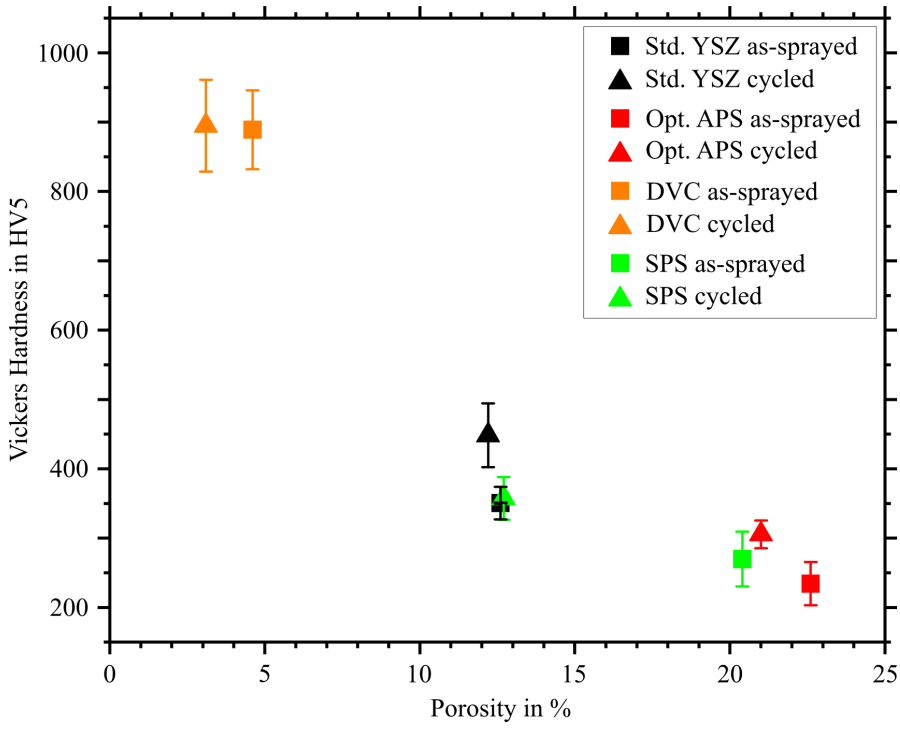

Fig. 6.19 Dependence of Vickers hardness on porosity of the different top coats before and after thermal cycling

Influence of thermal cycling on microstructure and mechanical properties of the top coats

The thermal cycling tests revealed an impact on the microstructure all of the coating systems investigated. However, the changes in mechanical or microstructural properties were very different. Since no hardness measurements could be done on the PS-PVD coatings, these are not considered in the following section on mechanical properties, but will be considered later when determining the phase changes caused by thermal cycling. Figure 6.19 shows the change in hardness (HV5) and porosity of the different coating systems after burner rig testing. In case of the two APS coating systems, there was an increase in hardness from about 350 to 450 HV5 for the standard system and from about 235 to 305 HV5 for the optimized APS system. These values were associated with a slight reduction in porosity. For the DVC system, the porosity decreased slightly but the hardness did not change. The SPS system experienced the greatest changes. The porosity decreased significantly with an increase in the measured hardness. While the measured porosity of the other systems decreased only slightly (between 0.4 and 1.6 % on average), the measured porosity of the SPS coatings decreased by almost 8 %. Such a high sintering rate was also found in other studies for SPS coatings with high porosity in burner rig tests [137].

To understand these differences, microstructural changes from high magnification SEM images were analyzed in more detail. For this purpose, Figure 6.20 shows the coatings of the optimized APS, DVC, and SPS systems in the as-sprayed state on the left and after failure of the respective test specimen on the right. The highly porous Optimized APS coatings (a) and (b) show minor changes in microstructure. The large pores and areas with partially molten or unmolten particles remain unchanged. Only in the already very dense areas the microcracks have been closed by sintering processes, which could explain the slight decrease in porosity and the increase in hardness. It should be noted, however, that the error bars of the porosity measurements before and after thermal cycling overlap for both APS systems, indicating that sintering might not influence the coating porosity significantly. It is assumed that sinter necks have formed, which change the mechanical properties (hardness) of the porous layers. However, the activation energy is not sufficient to lead to a densification of the coatings.
A significant decrease in porosity observed in the DVC coatings and is attributed to the low error bars resulting from the small number of pores. The high magnification SEM images reveal that microcracks, initially present in (c), are notably less present after cycling, in (d). The sintering of these microcracks is also reflected in a widening of the segmentation cracks, which can be observed both in (d) and in the overview image of the failed DVC sample in Figure 6.15 (c). In addition, globular pores rather than microcracks are found in the sintered coating. However, there is no effect on the hardness. It is assumed that the bonding between the splats is already strong in the as-sprayed state due to the high deposition temperatures that the healing of the microcracks has no influence. Moreover, the influence of pores on the hardness measurement is very low because of the high density.
The large difference in porosity in the SPS layers is also evident in the cross-sectional images. In the initial state (e), the porosity bands are clearly visible, with a large number of small resolidified particles. In between there are the dense areas with well attached splats and finely distributed microcracks. These features disappear completely during sintering (f). In the cross-section of the cycled sample, the porosity bands are still visible, but many dense interconnected areas have formed between the initially dense layers. The microcracks in the initially dense areas have also densified. Instead, numerous spherical pores are formed, which have the lowest free surface energy and are therefore the preferred geometry formed during sintering, indicating high sintering activity in the material. Overall, the porosity decreases and the hardness increases to such an extent that the SPS layer becomes comparable to the Standard YSZ system in terms of both values.
To better compare the changes between the different systems, the percentage changes in porosity and hardness for each system are listed in Table 6.4. This reveals that the sintering tendency for the coatings with finely distributed pores and microcracks (DVC and SPS) is significantly higher than for the coatings with large pores and wide microcracks (APS). In addition, the hardness appears to increase uniformly with high porosity due to the sintering of microcracks. This is concluded from the observation that only the microcracks closed in the APS coatings while the other porosities remained. Nevertheless, the hardness increased to the same extent as in the strongly sintered microstructures of the SPS coatings. However, beyond a certain porosity threshold, the hardness does not appear to increase further with decreasing porosity, as in the case of the DVC coatings. This is

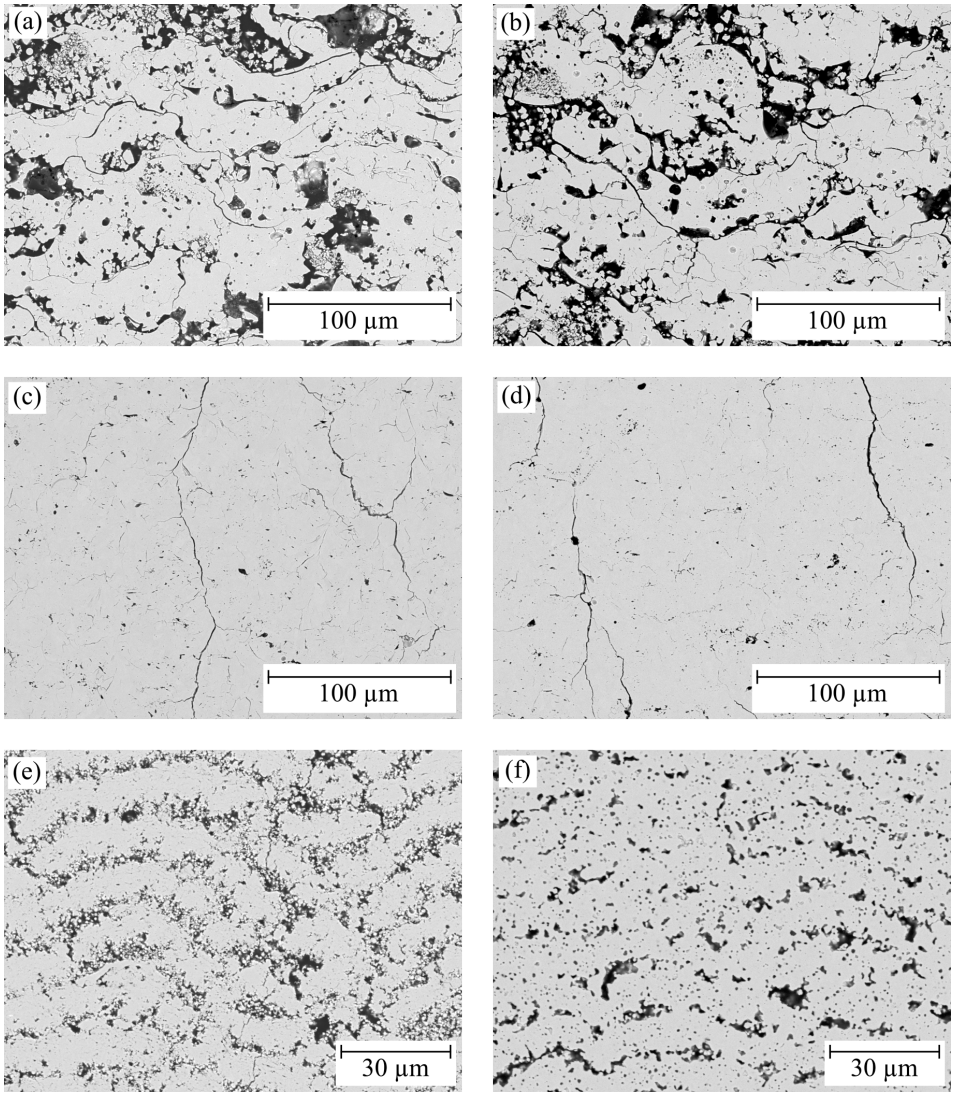

Fig. 6.20 SEM images with high magnification showing the sintering in different top coats: Opt. APS (a) as-sprayed, (b) after heat treatment (ht); DVC (c) as-sprayed, (d) after ht; SPS (e) as-sprayed, (f) after ht

Tab. 6.4 Changes of porosity and hardness due to thermal cycling in %

System	Std. YSZ	Opt. APS	DVC	SPS
Porosity Change [%]	-3.2	-7.1	-32.6	-37.7
Hardness Change [%]	27.9	30.3	0.6	32.4

attributed to the fact that, at a certain point, almost only dense material is penetrated by the indentation.

During cycling above 1200℃, not only sintering but also phase transformations might occur in YSZ thermal barrier coatings. One potential phase transformation for plasma sprayed YSZ is the transformation of the metastable tetragonal phase t', formed due to the rapid cooling of the splats during the coating process. This transformation leads to the formation of the cubic and tetragonal phase t. Upon cooling, the tetragonal phase t can further transform into a monoclinic phase. Due to the different densities of these phases, additional stresses are introduced into the thermal barrier coating system, which can contribute to the failure of the system [96].

The XRD plots for determining the phases present in the coatings are shown in Figure 6.21 (a). Zooming in on the 2-*theta* ranges of 34 - 36°, 58 - 62°, and 72 - 76° in Figure 6.21 (b) reveals typical ranges where peaks change during thermal cycling. The red line of the cycled DVC coating represents the appearance of the coatings in the specified ranges before cycling, as no phase transformations occurred in the DVC coating. This can be attributed to the short lifetime of this coating, which prevented the formation of the tetragonal phase with low yttrium content and the cubic phase with high yttrium content. In contrast, the XRD curves for the other coating systems exhibit the peaks characteristic of the cubic phase in these regions, indicating a rearrangement of the atoms to form the cubic and tetragonal phase. The peaks of the cubic phase are marked with the letter C in Figure 6.21 (b).

However, looking at the 2-*theta* ranges from 25.7 - 29° and from 31 - 32° in Figure 6.21 (c), the peaks of the monoclinic phase at about 28.2 and 31.5° are only clearly visible in the Optimized APS sample with a very long lifetime (3000 cycles). Since the peaks of the monoclinic phase were even more pronounced after coating or could be identified in the measurement curves of other coating systems as well (Figure 6.9), it is possible that the monoclinic phase is transformed into the tetragonal phase at the high temperatures during cycling. However, when the cycling samples are rapidly cooled by the compressed air cooling, there is not enough time for the phase to transform back to the monoclinic phase.

The thermal cycling results revealed different types of failure mechanisms across the different coating systems. While the coating systems with an APS top coat failed at the interface along the TGO, the DVC and SPS coatings developed a crack that propagated from roughness peaks of the bond coat through the ceramic. The critical energy release rate of the TGO was exceeded for the APS coatings. This resulted in failure in or near the TGO. The highly porous optimized APS coating also had a low fracture toughness near the interface due to poorly bonded or unmolten particles. These provided an additional crack propagation path. With the DVC and SPS coatings, the critical energy release

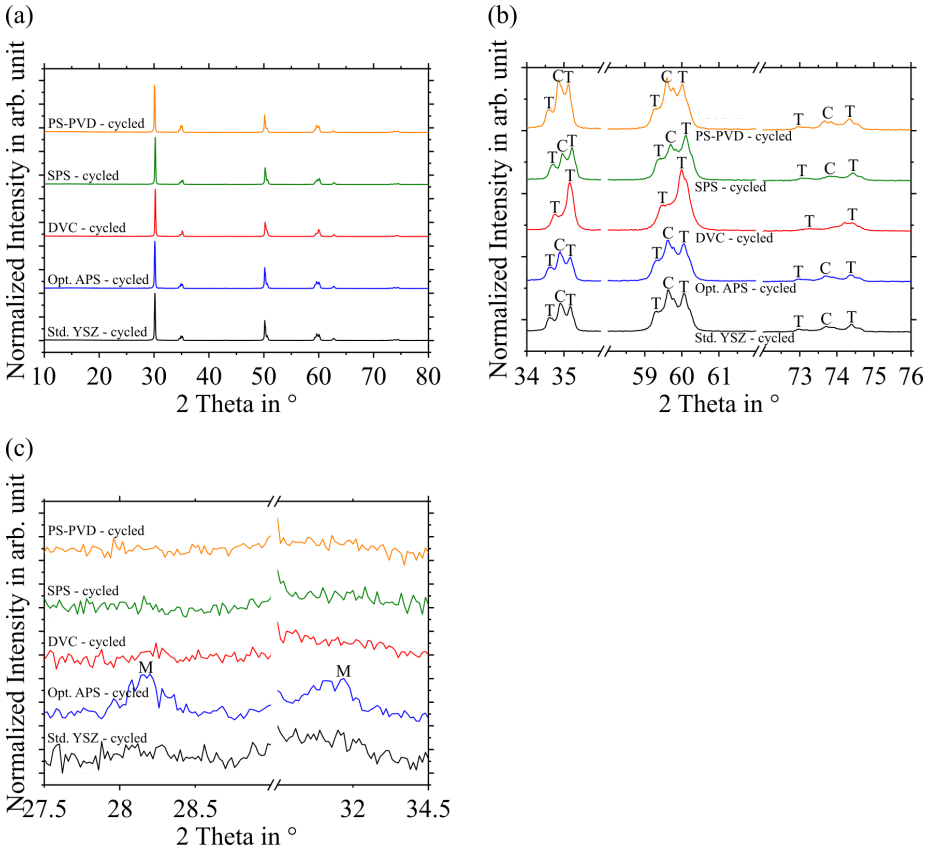

Fig. 6.21 XRD curves of the samples after thermal cycling at 1400 - 1450 ℃ with the characteristic peaks of the metastable tetragonal (T), cubic (C) and monoclinic (M) phase

occurred in the ceramic near the interface. This is where the highest elastically stored energies were accumulated in these coatings. In addition, areas such as the porosity bands in the SPS coating offered areas with low fracture toughness. Pre-oxidizing the bond coats extended the service life of the coating systems. The slowed growth of the TGO slowed the decrease in the critical energy release rate. In addition, the introduction of the initially high TGO growth stresses could prevente an early failure of the SPS coatings. Failure of PS-PVD coatings is caused by rumpling, which occurs when the polished bond coat is roughened during operation, causing coating areas to delaminate at the interface. Since the flat surface of the bond coat does not prevent crack growth, these delaminations are quickly joined by crack growth, resulting in a large area of coating delamination along the TGO/topcoat interface.

The analysis of the failed coatings showed the change from the metastable tetragonal t'-phase into the cubic and tetragonal phases. However, the rapid cooling of the coating system prevented the formation of the critical monoclinic phase in most cases. Only for

the optimized APS coating, weak peaks of the monoclinic phase were detected by XRD after failure of the samples.
During the cycling tests, an influence of the coating microstructure on the sintering of the materials at high temperatures was observed. In particular, fine microcracks and pores were closed during sintering. Therefore the porosity in the DVC and SPS layers, which have a large number of fine cracks and pores, was reduced to a greater extent. In contrast, the wide cracks and large pores in the APS layers were only slightly changed by sintering. Overall, the samples with a standard bond coat from Oerlikon Metco and a standard APS or optimized APS coating, as well as the samples with a standard APS or SPS coating deposited on a pre-oxidized bond coat, achieved comparable lifetimes in the cycling tests, considering the bond coat temperature. This similarity in performance could be attributed to a partial or complete depletion of the bond coat over the cycling duration, leading to spinel growth and subsequent failure of the samples. As a result, an accurate assessment of the cyclability of these topcoats is not possible.

6.2.2 Furnace Cycling Tests of Alternative Top Coat Material

The results presented in this chapter on the furnace cycling of the double-layer APS-YSZ/SPS-GZO coatings, like the optimization process of this system described in chapter 6.1.7, have been published in a study by the author of this thesis and his colleagues [Submittet at JACerS]. Therefore, the results are summarized here, whereby some parts of the passages from the evaluation of the study have been partially adopted here.

Coating Lifetime
The lifetime of the four different coating systems tested during the furnace cycling tests is shown in Figure 6.22. The values used in the graph represent the number of cycles after which the system was still intact. Failure then occurred within one of the following 20 cycles. It can be seen that all of the double-layer systems exhibited longer lifetimes than the APS-YSZ reference coatings. The two single-layer reference coatings both failed between 120 and 140 cycles. The best individual performance was achieved by a sample from system C, which remained intact after 240 cycles. Depending on the exact time of failure, this represents around a doubling of service life compared to the reference coatings. Additionally, it should be noted that the coating thicknesses of the double-layer systems were higher than those of the reference system. This increases the elastic energy stored in the ceramic due to thermal cycling, which even contributes to the spalling of the ceramic. However, based on this experimental data, it is not possible to interpret the effects of the APS surface and the GZO microstructure on service life separately. Further testing would be required to determine which of the two factors has the greatest influence on service life. Factors that were not considered in this study, such as a different particle size distribution of the GZO suspension, may also have a significant influence on the microstructure of the resulting surface layer [176]. Nevertheless, it can be concluded that the double-layered structure of lamellar, porous YSZ interlayer and columnar/vertically cracked GZO top layer prolongs the lifetime of TBCs in furnace cycling tests, even at medium temperatures.

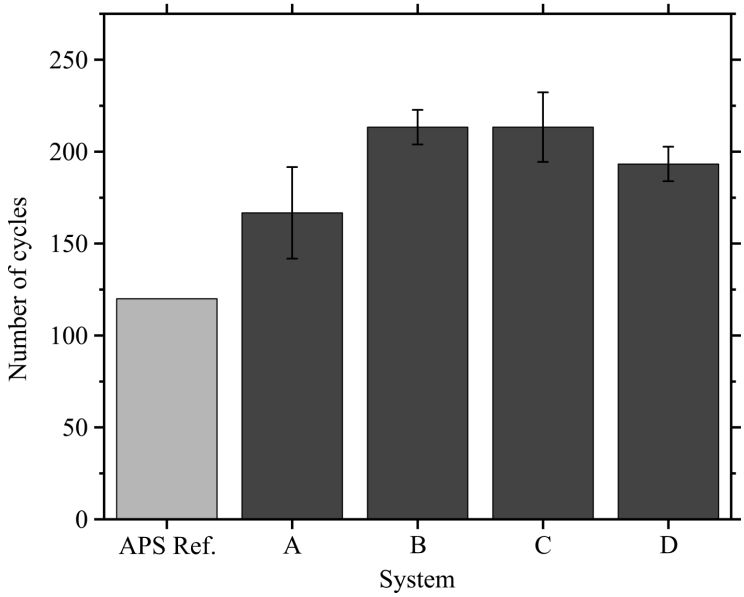

Fig. 6.22 Service life of the single-layer APS-YSZ reference system and the different APS-YSZ/SPS-GZO double-layer systems: A APS1 + GZO LP, B APS1 + GZO HP, C APS3 + GZO LP, B APS3 + GZO HP

Failure Mode

The cracks that led to failure of the APS monolayer systems propagated within the ceramic near the TGO, within the TGO itself, or between the TGO and the top or bond coat, as displayed in Figure 6.23 (a). A combination of these three localization zones was observed in both reference samples, resulting in almost complete detachment of the coating from the bond coat layer. The 9.0 ± 2.2 µm thick Al_2O_3-TGO layer formed from the Al-rich phase of the bond coat and led to a depletion of the bond coat near the TGO. In addition, yttrium oxides were found in the Al_2O_3 layer and spinels grew on the TGO. However, small amounts of β-phase remained in the bond coat. The porosity of the ceramic layer remained almost unchanged at 13.5 ± 1.4 %.

The twelve bilayer systems of the four different coating systems all exhibited the same failure mode as the two reference samples. Figure 6.23 shows SEM cross sections and photographs of a failed sample from each system. Again, in all samples, the entire coating detached at the interface between the bond coat and the topcoat. Furthermore, there was no difference in the thickness of the oxide layer, although the bilayer systems had significantly longer lifetimes than the reference system samples. The thickness of the TGO layers for systems A to D was 8.7 ± 3.6 µm, 8.4 ± 3.4 µm, 8.0 ± 3.3 µm, and 8.2 ± 3.6 µm, respectively. One possible explanation is that the oxide layer undergoes rapid growth at the beginning of thermal cycling, but then forms a dense oxygen diffusion barrier, resulting in slow subsequent growth. Another explanation is that the aluminum-rich β-phase in the reference system is almost completely depleted, leaving little aluminum available to form the Al_2O_3-TGO. Therfore its growth ist limited to the thickness found here. This indicates

that the oxide thickness is not the driving force for the failure of the coating systems. It is suggested that the increased service life of the double-layer systems is attributed to the increased strain tolerance of their design. In addition to the Al_2O_3 layer, more Co, Cr and Ni spinel oxides with the lighter color were identified in the cross sections compared to the reference systems. Their growth suggests Al-depletion in the bond coat due to TGO formation, as these typically form when the Al content in the bond coat has dropped below a critical level [242]. This observation is supported by the absence of an Al-rich β-phase in the bond coats of the doubl-layer samples.
The cross sections in Figure 6.23 also demonstrate that the two-layer design effectively prevents crack propagation from the top layer to the interface. Existing vertical cracks or cracks formed along the columns in the GZO did not propagate into the YSZ. This can directly prevent crack propagation with its high fracture toughness. Moreover, no cracks were detected at the interface between the YSZ and GZO, indicating good bonding between the APS and SPS layers. Some horizontal cracks formed in the GZO layer, originating from vertical cracks and extending through the porous bands between the individual layers of the GZO coating (Figure 6.23 (d)). However, no part of the GZO coating spalled.

Phase Composition of GZO Before and After Thermal Cycling
The XRD diffractograms of the powder from the dried suspension, a GZO layer after spraying, and two GZO layers after cycling are displayed in Figure 6.24 (a). These measurements compare samples produced with the GZO LP parameter. The measurements on the raw powder and the as-sprayed coating show no characteristic pyrochlore peaks (331, 511, 531, etc.), indicating the presence of a defective fluorite phase. The rearrangement of the GZO pyrochlore phase into the metastable defective fluorite phase during plasma spraying has been described in other studies [117], [125], [243]. The rapid cooling of the molten particles on the cool substrate prevents the formation of the ordered pyrochlore structure, resulting in the metastable defect fluorite phase. However, in the studies mentioned, the powder itself was present in the ordered pyrochlore structure, which is not the case for the suspension used in this study. This discrepancy is likely attributed to the manufacturing process of the powder in the suspension.
After thermal cycling, the diffractograms show slight peaks at locations characteristic of the pyrochlore phase, indicating the conversion of part of the fluoride phase to the pyrochlore phase (Figure 6.24 (b)). However, these peaks are very narrow and may indicate only a low transition rate, since the temperatures during the test are only 1100 ℃. The main phase is still present as defective fluorite. Nonetheless, the quantity of transformed phase is not of major importance as it does not change the volume or thermal conductivity of the material [244]. Therefore, the phase transformation is not expected to affect the lifetime of the coatings. In addition to the pyrochlore phase, further secondary peaks appeared in the cycled samples. These are the peaks marked with red and green dots, which were identified as Gd_2O_3 and Al_2O_3 (Figure 6.24 (a) and (b)). The Al_2O_3 originates from deposits of the sample holder, which is made of this material.

Change in Microstructural and Mechanical Properties by Thermal Exposure
Treatment of the material at 1100 ℃ resulted in sintering of the material and thus changes in the coating microstructures, mainly affecting the GZO. The APS layers did not change

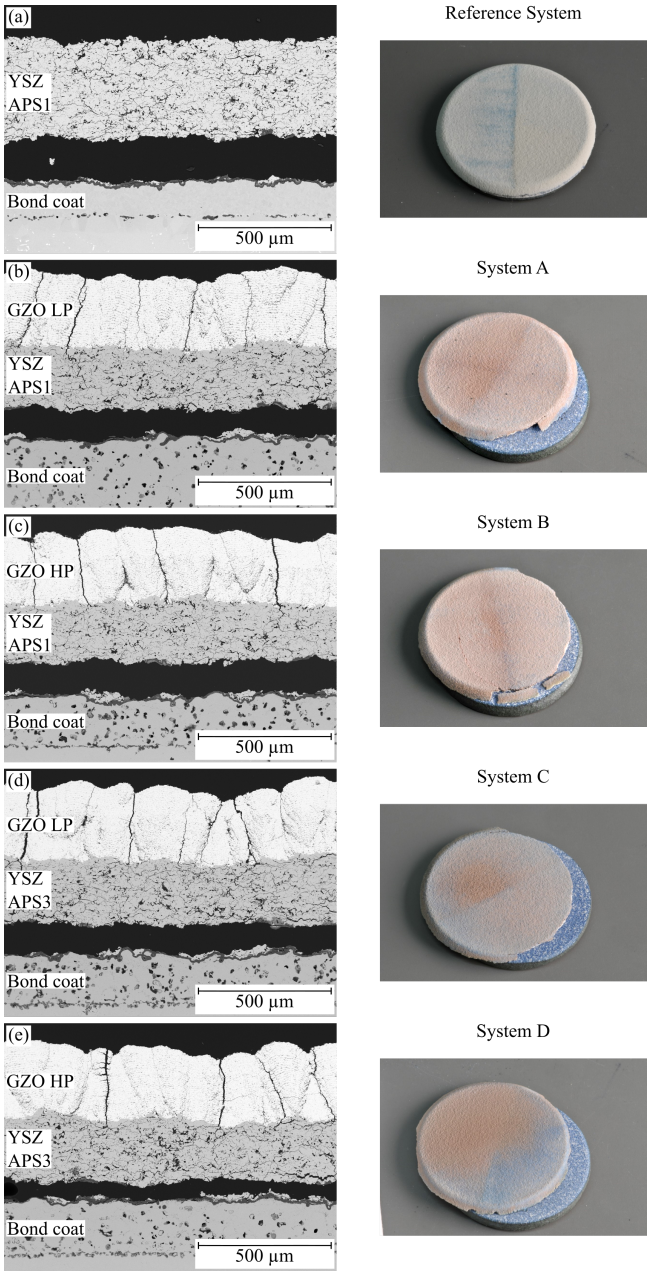

Fig. 6.23 SEM cross-sections and photographs of the failed furnace cycling samples

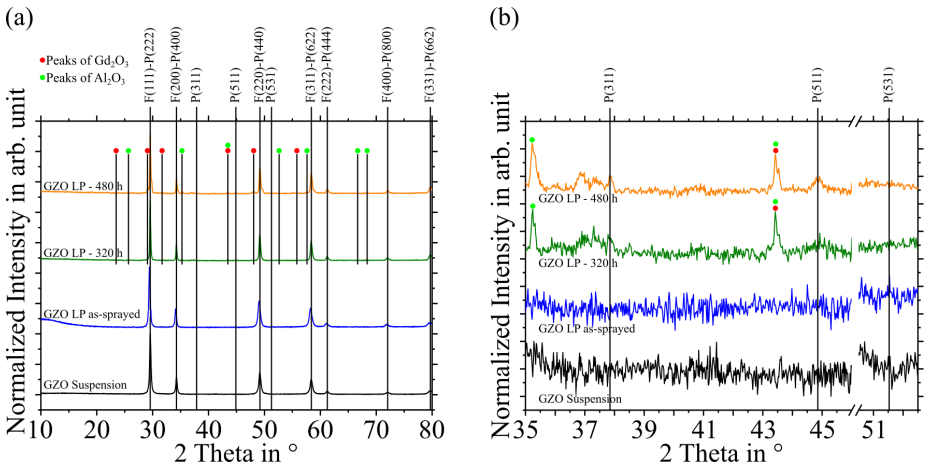

Fig. 6.24 XRD curves of the GZO Supsension, one sample in the as-sprayed state and two samples after furnace cycling at 1100 °C: (a) 2-θ range of 10 - 80°, (b) 2-θ range of 35 - 52°

and retained a porosity of 14.2 ± 1.4 %. For the GZO, the porosity values for the coatings produced with low gas flow (GZO LP) decreased from 11.1 ± 1.4 % to 9.0 ± 1.3 % and for the high gas flow (GZO HP) from 8.8 ± 0.8 % to 8.0 ± 1.0 %. Since the GZO material is reported to have a lower sintering tendency [245], the microstructural effect differs the sintering of the materials, similar to the SPS samples of the YSZ monolayers in the burner testing. This effect can also be seen in the highly magnified images of the respective layers of the bilayer systems before and after cycling in Figure 6.25. In the as-sprayed state, a large number of finely distributed microcracks can be observed in the GZO layer (a). After thermal cycling, these are closed by the sintering processes and some larger pores remain (b). In contrast, in the APS layers, only a few very fine microcracks are present in the as-sprayed coating, along with some wider cracks between the dense areas (c). After thermal cycling, the few fine microcracks disappear, but the large cracks are not closed by sintering. Although a change in the crack surface is noticeable, no bond forms between the separated areas ((d), (e)).

Another visual indication of a change in the GZO surface layer is the width of the cracks in the cross-sections after thermal cycling. Compared to the cracks and gaps next to the columns of the as-sprayed samples (Figure 6.13), they are significantly wider after thermal cycling (Figure 6.23). This indicates shrinkage and compaction of the segments between the cracks, causing the gaps to widen.

This change due to sintering is also reflected in the mechanical properties of the coatings. The elastic modulus measurements in Figure 6.26 (a) also show an effect of the heat treatment on the GZO coating. The Young's modulus increased by an average of 30 to 40 GPa for all systems. This elevation in the elastic modulus implies a higher stress level in the coating systems during heat treatment. However, a direct influence of the process parameters used and the resulting coating structures cannot be inferred from this measurement. In contrast, as with the porosity measurements, the APS coatings show no change in Young's modulus after thermal cycling.

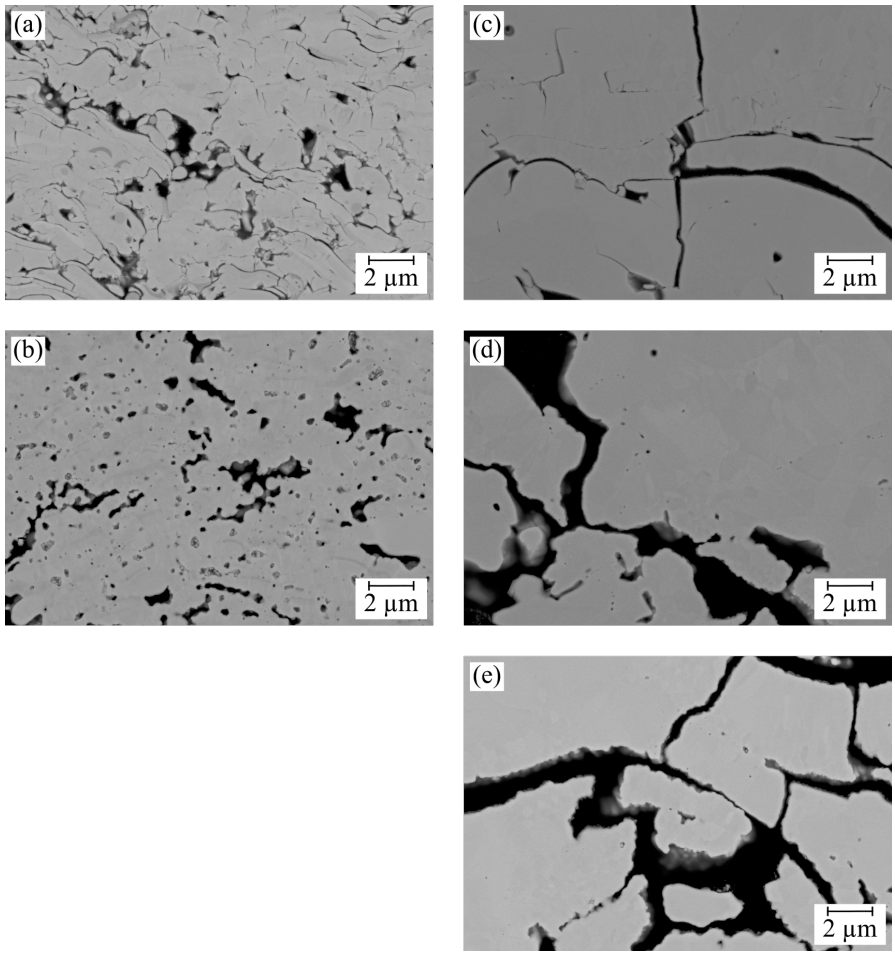

Fig. 6.25 SEM images with high magnification showing the sintering in different layers of the double layer system top coats: SPS-GZO (a) as-sprayed, (b) after heat treatment; APS of double layer (c) as-sprayed, (d) after heat treatment; APS of monolayer reference system (e) after heat treatment; Theramal cycling at 1100 ℃

This behavior is also evident in the hardness measurements presented in Figure 6.26 (b), as the hardness significantly increased only in the GZO layers as a result of the thermal load. From this it can be concluded that, contrary to the assumption of a higher sintering tendency of the YSZ, changes only occurred in the GZO as a result of its different microstructure. These findings are in agreement with the results of *Frommherz et al.*, who demonstrated forAPS-GZO structures that the GZO sintered more than YSZ at 1100 ℃. However, at 1300 ℃ the GZO showed a lower sintering tendency than YSZ. The authors were able to explain this by the specific microstructure of the GZO layers, which in their case had a higher defect density than the YSZ [246]. Furthermore, it should be noted, that

it is not possible to compare the hardness values determined here with the HV5 values measured for the coating systems tested in the burner rigs, since a considerably lower number of pores was measured due to the low test force. As a result, the hardness values are also higher.

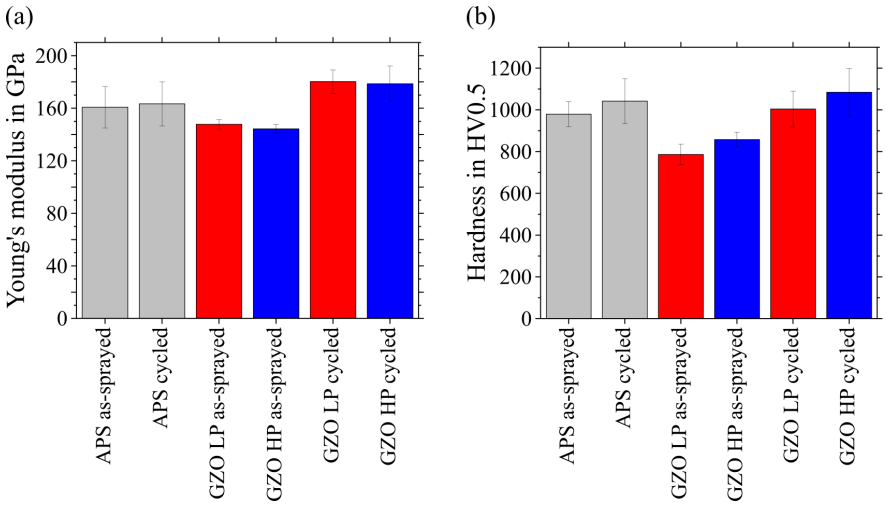

Fig. 6.26 Young's modulus (a) and hardness (b) of the different double layer systems before and after thermal cycling in the furnace at 1100 °C

Pore Formation in Bond Coats During Long Exposure Times

In addition to the depletion of aluminum in the bond coat, dispersed pores formed in the bond coats of the dual-layer systems due to extended exposure time in the furnace. These pores are similar to those found in the optimized bond coat and top coat systems during long exposure times in the burner rigs. Since this part of the thesis has been referred to in the previous chapters, the occurrence of pores in the bond coat will be discussed here. To explain this phenomenon, analyses of samples from the double-layer system are presented alongside samples from the burner rig testing. This comprehensive approach allows for a deeper understanding of the factors contributing to the formation of pores in the bond coat.

The phenomenon of pore formation in the bond coat, known as Kirkendall porosity, arises when the bond coat is depleted of alloying elements due to TGO growth and interdiffusion with the substrate during long-term operation. The different diffusion coefficients of the alloying elements lead to the accumulation of vacancies, which become pores [56], [58]. Since these pores often occur at the interface between the substrate and the bond coat, as shown in the cross-sections in Figure 6.23, they affect the adhesion of the coating and can lead to failure [59]. In both the HVOF bond coats of the furnace cycling samples and the VPS bond coats of the burner rig samples examined in this study, pores also occurred at the substrate/bond coat interface. However, pores also formed in the center of the bond coat and near the TGO, so it remains to be investigated how the pores formed there.

To investigate a possible loss of material in the bond coat, EDX point measurements were taken before and after furnace cycling. The measured points are marked in Figure 6.27 for the as-sprayed state in (a) and for the cycled state in (b). The respective measured values of the spectra are listed in Table 6.5. In the left image (a), the β-phase is clearly visible. This is also reflected in the measured values. In the dark β-phases, the Al concentration of ~12 wt.% is higher than in the light-colored matrix, where the Al concentration is only about 7 wt.%. The calculation of the mean values of the individual point measurements leads to a composition of Co 32Ni 21Cr 9Al 0.1Y wt.%. To validate the mean values calculated from the point measurements, two EDX mappings were also carried out on the as-sprayed sample, to determine the phase fractions over larger bond coat areas of the sample. The mean values of the samples from the point measurements correspond well with the mean values of the mappings, which are also given in Table 3.2 (Amdry9954). In addition, the values determined with the EDX are within the composition ranges specified in the alloy data sheet.

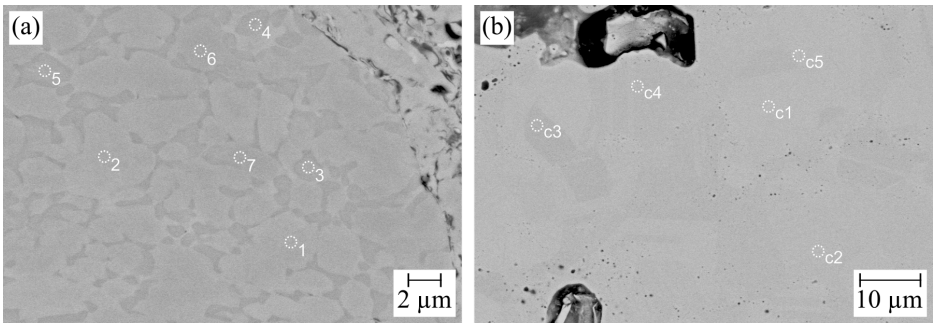

Fig. 6.27 SEM images of the bond with measuring points of EDX analysis: (a) after vacuum-annealing, (b) in the cycled state

The Al concentration decreases as expected during thermal cycling due to the formation of Al_2O_3. Therefore, it is on average around 4 wt.% after cycling instead of the ~9 wt.% in the as-sprayed state. However, it is also noticeable that there is a considerable loss of Co. The main element of the alloy, which was present at around 38 wt.% in the as-sprayed state, is only present at around 33 wt.% in the bond coat after thermal cycling. The different contrasts in the SEM image do not appear to represent different phases, but crystal orientation contrasts, as all the measured values are very similar. Due to the loss of Co, the relative proportions of Cr and Ni increase and Ni becomes the main component of the bond coat.

Even if the results of a quantitative EDX analysis must be treated with caution due to a high error probability with inhomogeneous material compositions, a cobalt loss due to thermal cycling can be clearly identified on the basis of the measurements, in addition to the aluminum loss. However, exact quantification is not possible. Furthermore, at the time, it is not yet clear how the cobalt reduction occurred. Cobalt can either diffuse towards the substrate or towards the TGO and form spinels there. An indication of upward diffusion is provided on the one hand by the spinels found above the TGO, and on the other hand

Tab. 6.5 Chemical composition according to EDX point measurements in wt.% for the standard bond coat in (a) initial state and (b) after thermal exposure

	Al	Cr	Co	Ni	Y
Spectrum 1	7	22	41	30	0
Spectrum 2	7	22	41	30	0
Spectrum 3	13	18	34	35	0
Spectrum 4	12	19	32	36	1
Spectrum 5	10	21	37	31	1
Spectrum 6	7	22	41	30	0
Spectrum 7	7	22	41	30	0
Spectrum c1	4	22	33	40	0
Spectrum c2	4	22	32	40	0
Spectrum c3	4	22	33	40	0
Spectrum c4	4	22	33	39	0
Spectrum c5	4	22	33	39	0
Map 1	9	21	38	32	0
Map 2	8	21	38	32	1

by a blue coloring ontop of the furnace cycled samples after failure, which is attributed to Co-oxides. However, no SEM images or EDX measurements were taken of the surface before embedding in epoxy. The surfaces were only analyzed with XRD after cycling. No oxide peaks could be identified with this technique, as they are below the detection limit, if present. No oxide deposits on the surface can be seen in the cross-sections in the SEM either. The reason for the loss of the cobalt is therefore not clear, but is seen as a possible cause of the pore formation, which should be investigated in further tests.

The pores may have formed due to the loss of Al and Cr if insufficient material diffused from the substrate. However, a closer look at the as-sprayed bond coats and various pores provides another theory for the formation of the pores. Figure 6.28 shows various bond coats after failure of each coating system. In Figure (a), the bond coat of a DVC sample with the shortest lifetime reveals significant depletion of the β-phase due to high bond coat temperatures. In addition, particles can be seen that have been deposited in the coating in the solid state. Such particles were also found in the as-sprayed bond coats in Figure 5.2. If there are unmolten or resolidified particles in the coating, poor bonding and pore formation might occur. Figure 6.28 (b) shows the bond coat of a PS-PVD sample, which has run about twice as long as the DVC sample in burner rig testing. It can already be seen that the voids around the particles have increased in size. It can be clearly seen that these particles are only partially or no longer attached to the bond coat on the cross-sectional plane. In Figures (c) and (d), the particles have broken out of the coating in many areas due to preparation of the cross-sections. In Figure 6.28 (c), the bottom of a pore can be seen in each of the three red circles. EDX measurements identified the white dots as yttrium oxides. Figure 6.28 (d), on the other hand, shows that oxygen can also diffuse into the bond coat, resulting in the formation of oxides at the pores in the upper regions.

Therefore, it is assumed that the large voids in the bond layers are not caused by the loss of Al and Co material alone. It is suggested that unmolten or resolidified particles were deposited in these areas. During thermal cycling, the pores surrounding these particles acted as nucleation sites for further pore growth during the depletion of Al and Co. The pore growth around the particles further dissolves the few poorly bonded areas and causes

the particles to be pulled out during preparation, leading to an overestimation of the pore size.

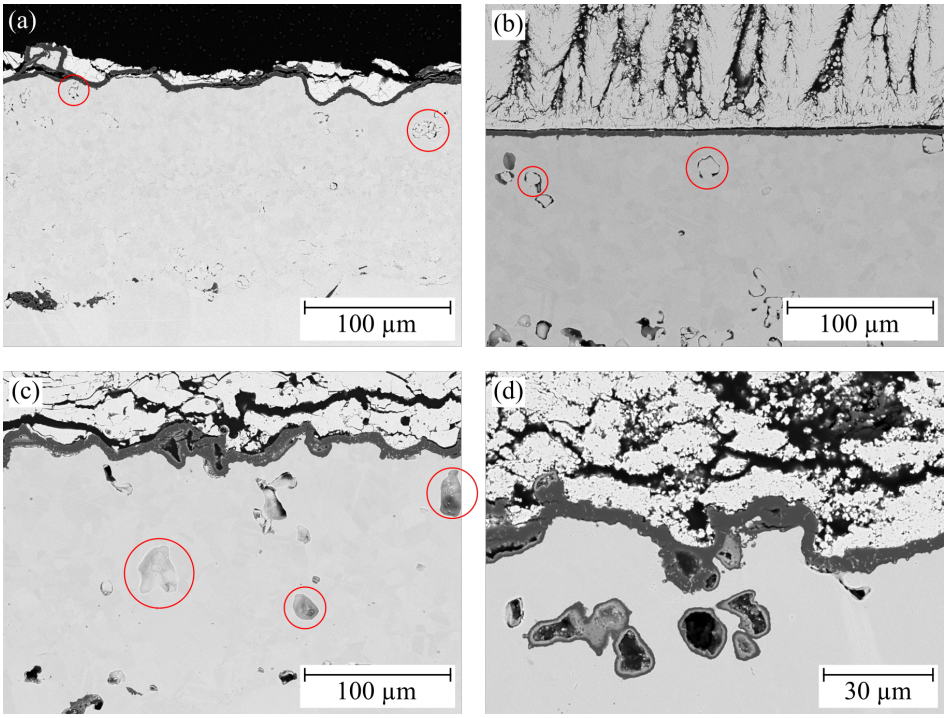

Fig. 6.28 SEM cross-sections of different samples after failure, red circles show areas with unmolten particles: (a) DVC, (b) PS-PVD, (c) Standard APS, (d) SPS

6.3 Digital Image Correlation Results

6.3.1 Optimization of Image Acquisition

Initial tests of the camera setup were performed without an additional light source. Without this, the illumination of the sample was not sufficient to capture a suitable speckle pattern with sufficiently high contrast and constant brightness over a cycle suitable for digital image correlation. For this reason, in further experiments, the sample was illuminated from the side with a halogen spotlight. This was used to generate a speckle pattern on the sample surface based on the roughness peaks of the sample, which was found to be sufficient for digital image correlation. This setup was therefore used to make evaluations with the VIC-2D software. However, it was not possible to analyze complete cycles using digital image correlation. As shown in Figure 6.29 ((a) and (b) red frame), problems occurred during sample acquisition, especially at high temperatures, preventing image processing.

At elevated temperatures, the sample itself emits light that surpasses the intensity of the light shining on it, resulting in the absence of a visible shadow on the sample created with the halogen light source. Consequently, no speckle pattern can be detected, only a noisy image as shown in Figure 6.29 (a) (red frame). Moreover, contrast and intensity variations occur at high temperatures (b) (red frame). These variations make correlation within an image series impossible for these temperatures. Additionally, hot air streaks distort the image. The issue of streaks and visible thermal radiation emitted by the sample is also documented in the literature for high-temperature DIC [247], [248]. During heating, the flame in front of the sample also caused distortions in the images, making these unusable as well. Therefore, the images were only processable when recorded during the cooling phase below a surface temperature of approximately 900 °C. Below this temperature, the sample stopped emitting light and the halogen spotlight again cast a shadow, revealing the speckle pattern. The illumination then produced a continuous gray value distribution between a surface temperature of about ~900 °C and room temperature, which was well suited for image processing.

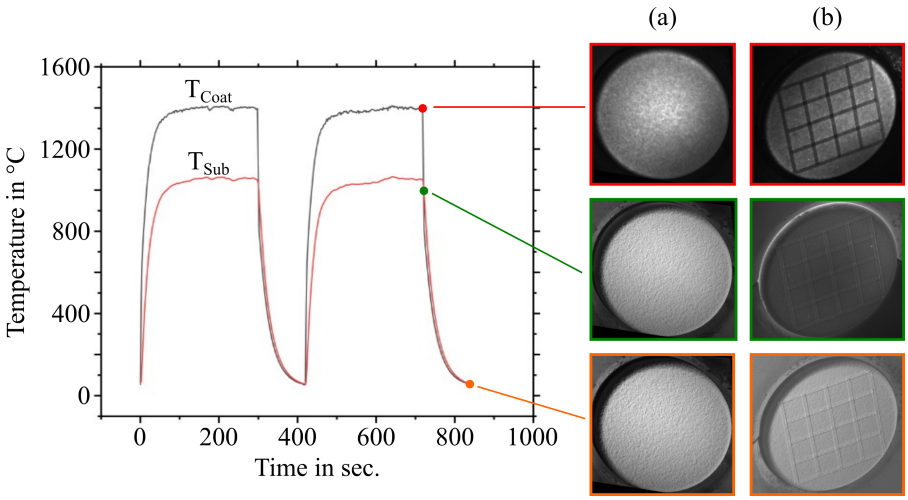

Fig. 6.29 Temperature profile in substrate and at the coating surface during thermal cycling with CMOS images taken at different temperatures ((a) and (b))

This setup was used to perform initial image correlation experiments between surface temperatures of around 900 °C and room temperature. During the analysis within a cycle, it was found that there is a displacement vector during cooling. As shown in Figure 6.30 (a), the sample moves toward the right edge of the image during cooling. However, this movement of the entire sample is not only the shrinkage of the sample itself, but also a displacement of the sample in the image as the sample holder contracts in this direction during cooling. Similar to the other artifacts of image distortion described in Chapter 4.7, this displacement is not problematic because the elongation of the sample surface is not

determined by a point outside the ROI (colored area), but between defined points within each subset to the respective subset center.

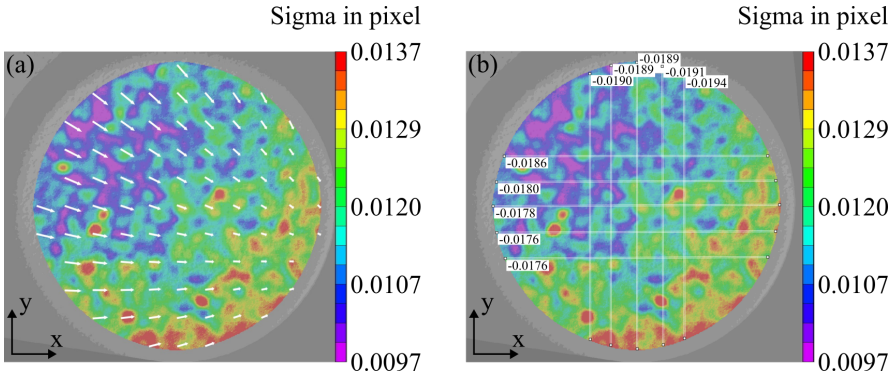

Fig. 6.30 Displacement vectors on sample surface in (a) and lines at which strain was measured in (b); the colored background indicates the standard error of correlation of the subsets

To verify the accuracy of the measured strains, the expected shrinkage of the individual layers in specific temperature ranges was determined using the temperature data obtained from the sample surface (Pyrometer) and in the substrate (Thermocouple). These were calculated using the Equation 6.1. ϵ is the elongation in percent and is calculated from the coefficient of thermal expansion of the respective layer (α) and the temperature difference (ΔT [K]) in the area under consideration. Due to the reversal of the thermal gradient during cooling, the temperature in the substrate (Formula 6.2) is higher than the temperature of the surface (Formula 6.3) in this calculation. The specified strains represent the values by which free-standing layers would contract in the temperature range under consideration.

$$\epsilon = \alpha \cdot \Delta T \cdot 100 \ [\%] \tag{6.1}$$

$$\epsilon_{Substrate} = 16 \cdot 10^{-6} \cdot (1285 - 290) \cdot 100 \ = \ 1.59 \ \% \tag{6.2}$$

$$\epsilon_{Coating} = 10.5 \cdot 10^{-6} \cdot (1140 - 290) \cdot 100 \ = \ 0.89 \ \% \tag{6.3}$$

The strains measured by digital image correlation were determined using five lines each in the x and y directions, as depicted in Figure 6.30 (b). Mean values were then calculated from the respective measurements for each axis direction and plotted against temperature. This is shown in Figure 6.31 for a system with Optimized APS Top Coat (a) and SPS Top Coat (b). The slope of the lines shows that the strain at the sample surface between 800 and about 100 °C corresponds to the expected strain of the substrate material (about -1.6 %). Since the coatings are thin relative to the substrate, they have no effect on the strain of the system. Therefore, the coating is forced to deform by the substrate during thermal cycling. This result is in agreement with calculations by *Vassen et al.* on stresses in systems with different coating thicknesses and thermal expansion [130].

However, with the setup shown, only the total strains on the sample can be determined in a limited temperature range. In addition, above the temperature of 800 °C, there was a kink in the measured strain. As a result, the total strain measured from about 950 °C was almost -2.0 %, also shown by the graphs in Figure 6.31. To identify the cause of this overestimation and to address the problem of image acquisition with a self-radiating sample, further improvements to the setup were made, as described below.

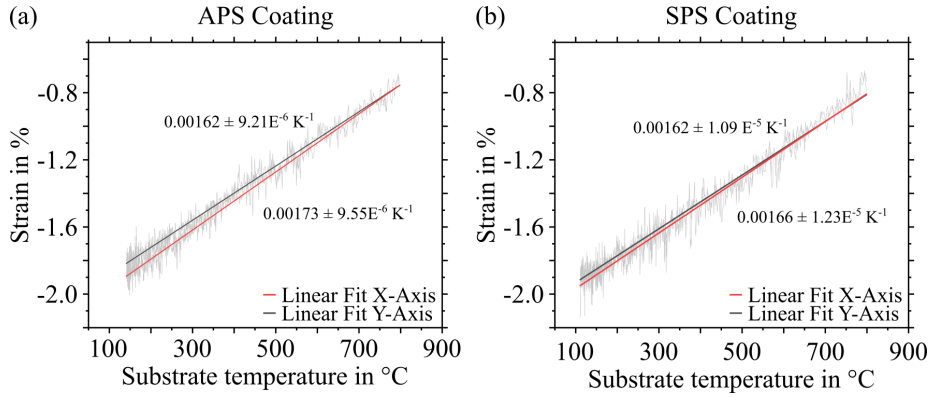

Fig. 6.31 Averaged strain of the sample surface of an APS and SPS system during cooling of the sample; determined by five lines, as shown in Figure 6.30 (b)

A monochromatic blue LED light and a bandpass filter in front of the camera lens were implemented in the test stand to overcome the problem of the self-radiating sample above 900 °C surface temperature and the flame interference during image acquisition. Such a setup has already been successfully demonstrated in the literature by *Pan et al.* for another application of DIC at high temperatures with self-radiating samples [249]. In the present work, however, a different wavelength range of light and bandpass filter were used. A light with a wavelength of 405 nm was chosen, alongside a bandpass filter that transmits light in this wavelength range while blocking other wavelengths. The reason for this choice is that both the sample itself, which is similar to a blackbody radiator, emits hardly any light in this wavelength range in the temperature range used (< 1800 K) (Figure 6.32 (a)), and the CH_4/air flame of the burner rig also emits very little in this wavelength range (Figure 6.32 (b)). Consequently, only a very limited amount of ambient light, self-emitted light from the sample at high temperatures, and the burner flame can pass through the filter in the bandpass range. As a result, these light sources contribute insignificantly to the intensity of the recorded image compared to the active monochromatic light. This allows images to be recorded with constant image contrast regardless of whether the burner flame is in front of the sample or the sample itself is emitting bright light.
One issue that cannot be solved with this setup is the blurring of the image due to heat flickering in front of the sample. However, this problem can be solved by averaging the gray values of image series at constant temperature. The result of such an averaged image is shown in Figure 6.33. With this final setup, image processing and correlation were performed on different coating systems, which is described in the following chapter 6.3.2.

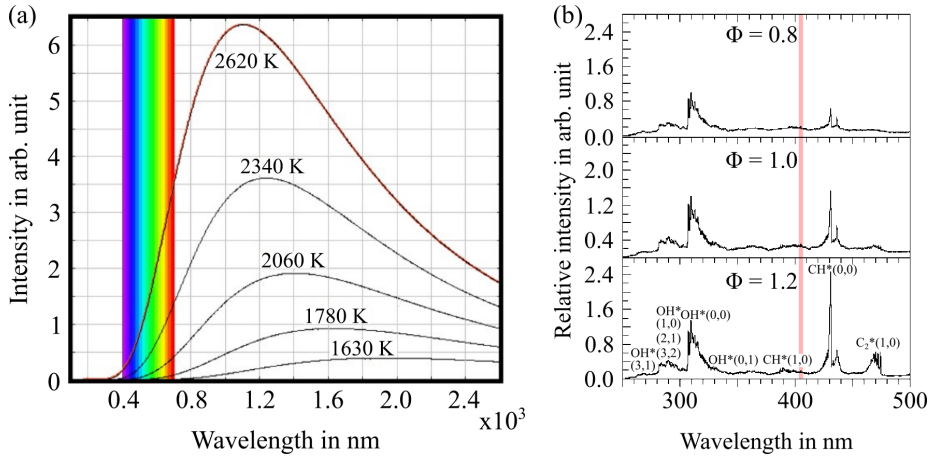

Fig. 6.32 Spectral distribution of a black body radiation at different temperatures (a), Spectrum of the light emitted by the burner rig flame (b) [250]

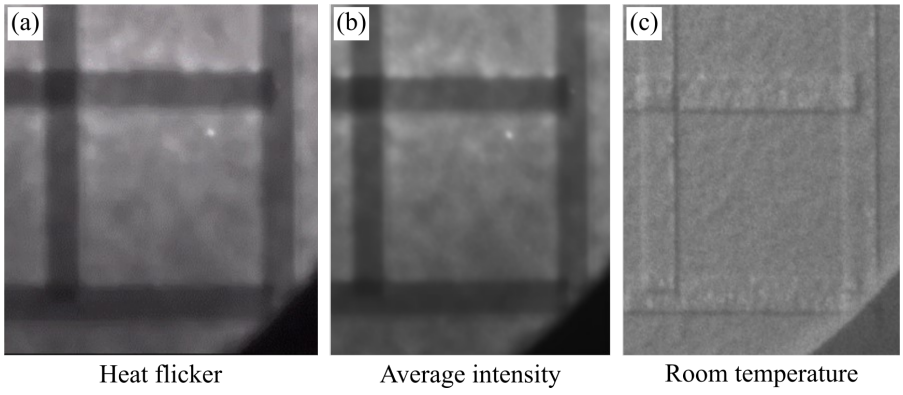

Fig. 6.33 Effect of averaging gray values over several images at constant surface temperature: (a) uncorrected image distorted by heat flicker, (b) averaged image, (c) image at room temperature

6.3.2 Strain Analysis on Different Coating Systems

The first step was to determine if this setup could provide realistic and consistent strain values for complete cycles, or if there was still an overestimation of the strain on the sample surface. In addition, it was checked whether the measured strain on the surface of the topcoat corresponds to the strain of the substrate, independent of an overestimation of the strain. For this purposes, a sample without topcoat was first heated to a temperature of 1050 - 1100 ℃ in the substrate using the burner rig. The dark bond coat surface was also high enough in contrast for image correlation due to the illumination setup. Subsequently, a Standard YSZ sample was heated to 1450 ℃ on the surface and 1090 ℃ in the substrate. The strain curves determined by image correlation during heating and cooling of a cycle are shown in Figure 6.34 (a) for the sample with no top coat and (b) for the Standard Top Coat sample. The plots show an average of the strains in one axial direction for each image in the image series. The horizontal guideline at 1.7 % strain shown in both plots corresponds to the maximum expected strain of the substrate at the temperatures investigated. This means that the measured strains overestimate the realistic value by about 0.4 - 0.6 %. The reason for this overestimation remains to be clarified. There may also be a curvature of the substrate due to the thermal gradient in it, increasing the strains measured. This could be checked with a 3D setup of the image correlation, providing additional information on strains in z-direction, outside the samples plane.
However, the measurements reveal that the strain measured on the surface of the standard sample approximately corresponds to the strain measured on the sample without a top coat. This supports the assumption that the strain in the coating system is entirely determined by the substrate. Moreover, continuous strain curves can be recorded, enabling the identification of time-related changes over many cycles or local strain differences within a cycle on the sample surface. Thus, the system is capable of qualitative analysis, but not quantitative analysis due to the misrepresentation of strain values.
For further investigation on different specimens with different coating systems, the focus was on long-term strain development over the entire lifetime of the samples. For this purpose, images from each cycle or from cycles at regular intervals were compared under constant conditions. Images taken just before the start of the cooling cycle or just before the start of the heating cycle were compared. The former allowed for a comparison at maximum surface temperature, while the latter enabled comparison at room temperature. To increase the accuracy of the measurements, especially at high temperatures, the gray values of several images were averaged into one image for evaluation.
The result of such a comparison sequence is shown in Figure 6.35 for an SPS system with a preoxidized bond coat at high temperature and in Figure 6.36 for the same sample at room temperature. The infrared images in the top row reveal the formation of a hotspot with increasing number of cycles. The formation of this hotspot has also caused the temperature difference between the surface and the substrate to increase, as shown in Figure 6.37 illustrating the temperature difference. This indicates a delamination of the coating in the area of the hotspot as the heat can no longer be effectively transferred to the cooler substrate.

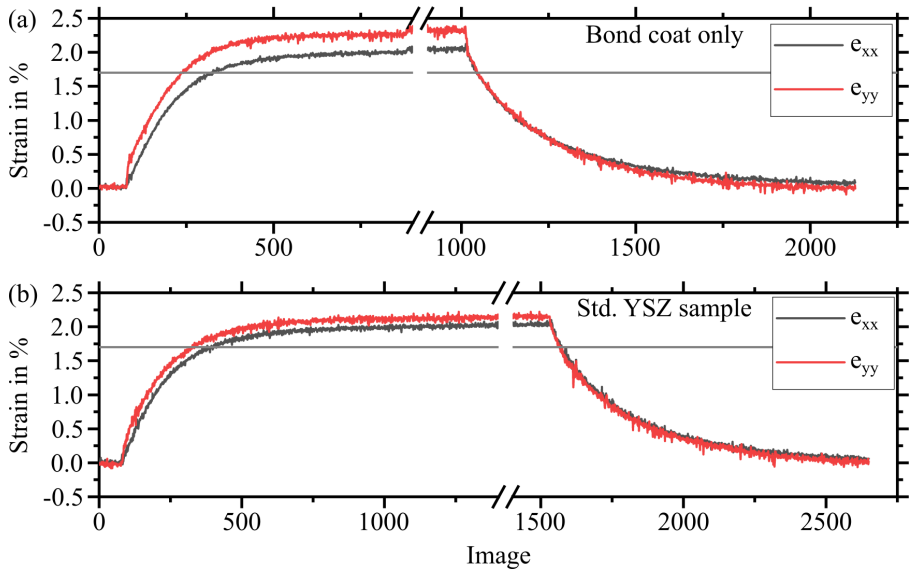

Fig. 6.34 Strain calculated via image correlation on the surface of a sample without top coat in (a) and a standard sample in (b)

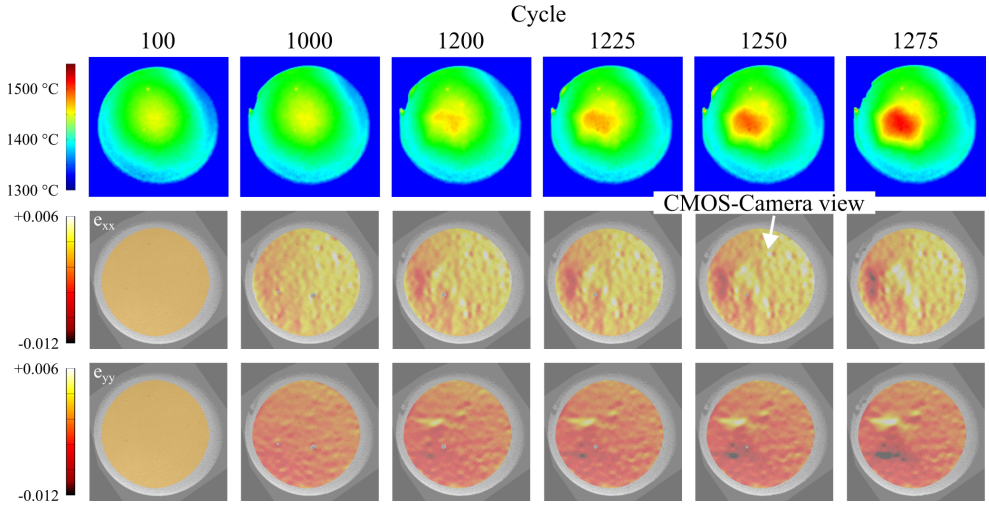

Fig. 6.35 Development of the surface temperature (top) and the change in strain in the x (middle) and y (bottom) directions over several cycles at maximum test temperature; SPS coating is investigated

Examining the local strains associated with the infrared images in the x and y directions (Figures 6.35), it can be seen that there is also a change in strain at the surface at the location of the hotspot. To better interpret this observation, it is important to note that in the rectified images shown here, the camera was pointed at the sample from above. The viewing direction of the CMOS camera is indicated by the arrow in Figure 6.35. In both the x and y directions, there are local strain increases in the bright areas. From the camera's point of view, however, dark areas appear behind the bright areas, corresponding to lower strain than in the reference image. This phenomenon suggests the formation of a blister, where the coating on one side is tilted towards the camera sensor. This increases the distance visible between two speckles, which results in a calculated increase in elongation. Conversely, on the side of the blister facing away from the camera, the strains appear smaller, resulting in darker regions. This trend can be observed not only at high temperatures, but also at room temperature (Figure 6.36). The elongation on the side facing the camera increases again, which can be seen in the light color, and the side away from the camera behind the blister appears dark due to the negative elongation. This suggests that the blister is present both at room temperature and at high temperature.

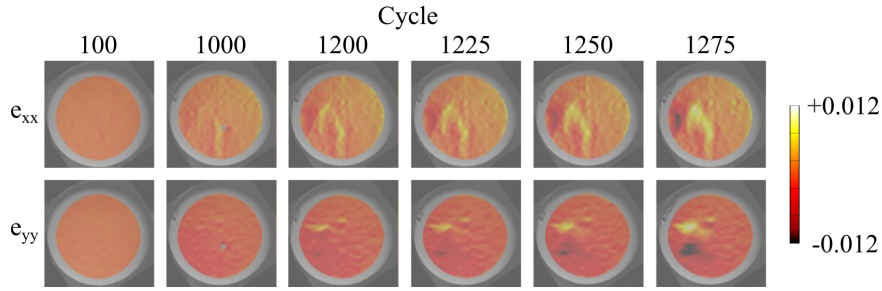

Fig. 6.36 Determination of the strain change in x (top) and y direction (bottom) over different cycles at room temperature; SPS coating is investigated

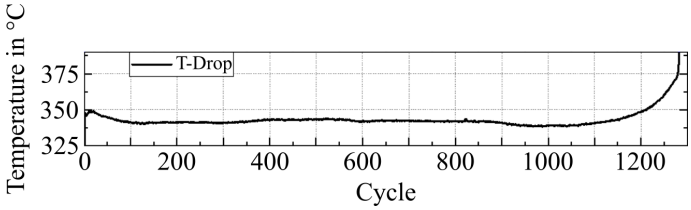

Fig. 6.37 Development of the temperature difference between top coat surface and the substrate of the SPS sample investigated in Figures 6.35 and 6.36

Figure 6.38 compares these calculated changes in strains with the finally failed sample and the resulting crack in the top coating. In the image, the strain field recorded in cycle 1275, when the specimen had not failed, is superimposed on the image of the specimen that failed after cycle 1283 (only every 25th cycle was recorded). For both axial directions,

it can be seen that the crack propagates between the dark and light areas indicating the strain changes. This observation provides further evidence supporting the theory of the blister at this location.

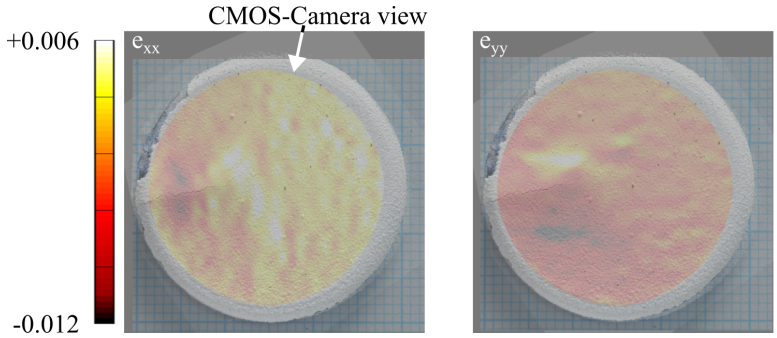

Fig. 6.38 Superimposing of the images of the determined strain change after Cycle 1275 and the failed specimen after Cycle 1283 shows correlation of the determined strain change and crack initiation

A lifting of the coating during thermal cycling was also demonstrated using another sample type. This was a sample of a Standard APS Top Coat of Metco 204NS ceramic powder. Figure 6.39 shows the evolution of the sample in terms of surface temperature distribution and surface strain between cycle 100 and 1587 at maximum test temperature (1450℃ target). Similar to the previously examined SPS sample, the hotspot spreads as the number of cycles increases, after about 1500 cycles. It expands from the center of the sample to the lower right, indicating possible delamination of the surface layer in this area. This observation is further supported by images processed with the (DIC) software, revealing a local change in strain at the hotspot, particularly in the Y-direction. As described for the previous sample, this is particularly pronounced in this direction as the coating is tilted toward the camera sensor due to the positioning of the camera. Behind the tip of the blister, in contrast, the coating bends away from the sensor, decreasing the visible distance between the speckle features and thus being identified as negative strain.
This effect was observed not only at high temperature but also at room temperature, as depicted in Figure 6.40 for the same cycles after the sample had cooled to ambient temperature. This indicates that the coating exhibits blistering at both high and room temperature. At low temperatures, the top coat experiences compressive stress due to the stronger contraction of the substrate, resulting in lifting of the coating in the detached area. At high temperatures, however, it is often assumed in literature that the topcoat is stress-free before cooling due to relaxation processes, or that it is under tensile stress due to the larger expansion of the substrate. Theoretically, this should cause the blister to flatten out again, which is not the case as shown in Figure 6.39. Several factors could contribute to this observation. One possibility is that plastic deformation prevents the blister from flattening reversibly at high temperatures. Another possibility is that the plastic deformation has stretched the coating over the blister to such a length that its total elongation during heating is greater than that of the substrate in the detached area. It is also possible that the length of the ceramic layer above the blister is that large, it

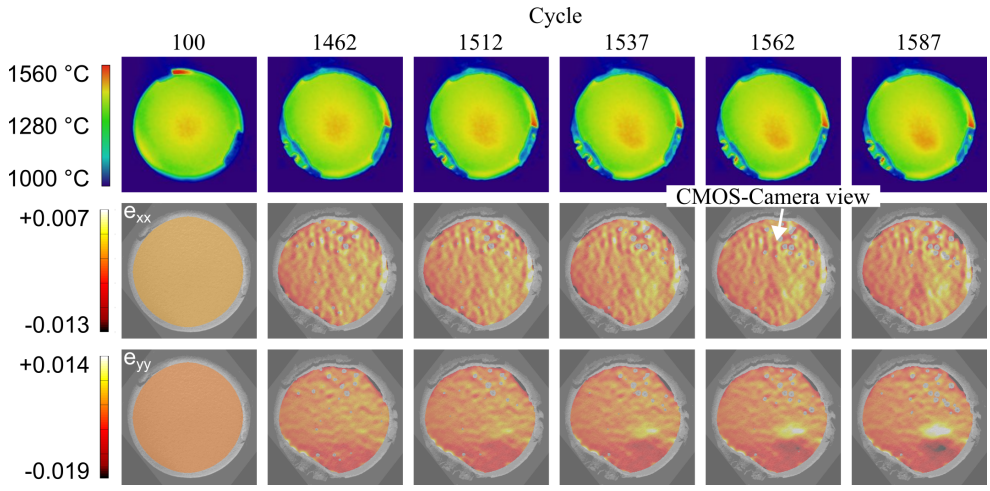

Fig. 6.39 Development of the surface temperature (top) and the change in strain in the x (middle) and y (bottom) directions over several cycles at maximum test temperature; APS standard coating is investigated

expands to a similar extent as the straight substrate under the blister. To calculate this, however, it is necessary to know the exact height of the blister, at high temperatures as well. This in turn could also be checked with a 3D setup for image correlation.

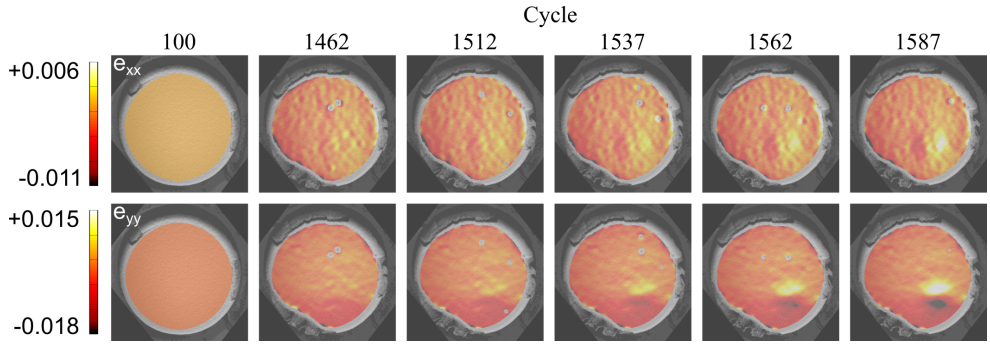

Fig. 6.40 Determination of the strain change in x (top) and y direction (bottom) over different cycles at room temperature; APS standard coating is investigated

The blister height at room temperature was also determined after cycle 1598 using a white light topographer. The corresponding height profile is shown in Figure 6.41 and confirms the presence of a local elevation at room temperature. This has a maximum height of about 120 µm. However, it is not possible to determine the exact height at high temperatures. It also cannot be determined from the strains, as they are displayed incorrectly. Therefore, it is not possible to compare the strains at high and low temperatures as they are also calculated using different reference images at their respective temperatures. To determine

blister height at high temperature, a 3D view of the sample would be required, which could be achieved with a setup featuring two CMOS cameras. Such a setup would enable a comprehensive analysis to address whether the blister flattens again, or at least partially, at high temperatures.

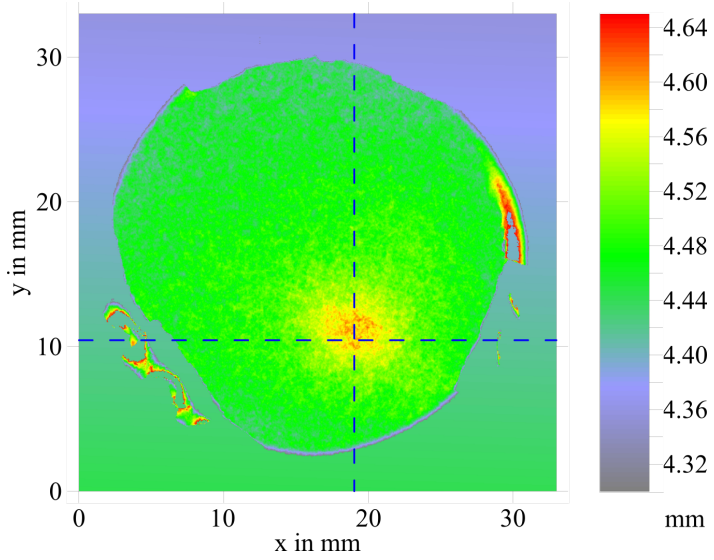

Fig. 6.41 Profilometer measurement showing blister at the point of detected change in local strain of Figures 6.39 and 6.40

After the sample was measured in the white light topographer, it was futher cycled until failure. The continued growth of the blister is evident in Figure 6.42, as the reference image is that of the first cycle after the topography measurement. The progression of the blister is characterized by continued local growth, followed by a sudden crack propagation extending to the edge of the sample. This crack led to the complete detachment of the lower right area of the surface coating. This delamination crack occurred during the heating of the coating in the 1621 cycle.

With these tests, it has been demonstrated that both SPS and APS coating systems experience local failures leading to blistering of the coating in the affected areas. Continuous growth of these defects over the cycles then lead to failure. This is reflected in the local strain changes measured with DIC and the formation of local hotspots on the sample surface. In these areas, the heat introduced can no longer be transferred to the substrate due to the air gap formed, causing the temperature to rise. After a certain number of cycles and progressive growth of the blister, a sudden crack propagates to the edge of the sample and causes the coating to fail. Whether this occurs at a particular blister size or TGO thickness has not yet been clarified. In particular, a 3D camera setup could be used to accurately determine blister height and size at high temperatures, providing valuable insights into the factors influencing coating failure.

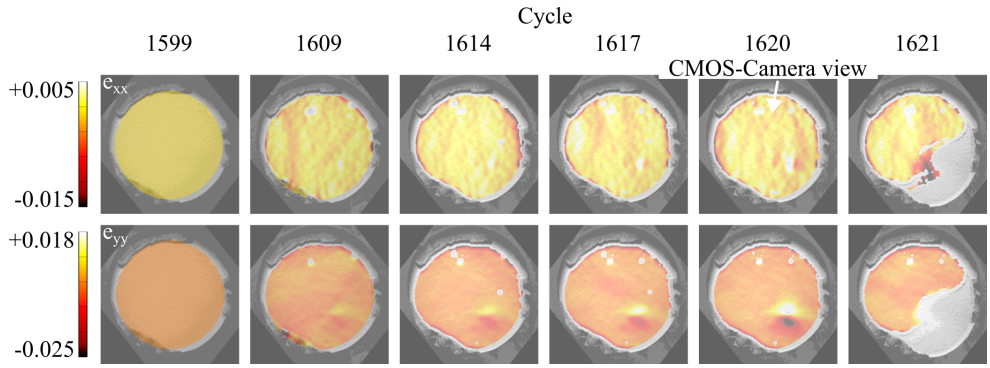

Fig. 6.42 Calculation of the local strain changes on the sample with blister (Figure 6.41) in the x (top) and y (bottom) directions after investigation of the blister with white light topographer

6.4 Laser Shock Adhesion Testing (LASAT)

The LASAT experiments were conducted in this thesis for two main reasons. First, the interfacial strength was investigated for different types of bond coat surfaces and different plasma sprayed topcoats in the as-sprayed state and after thermal cycling. Therefore, pre-tests were initially performed to assess the transferability of the process from EB-PVD coatings to plasma sprayed coatings. Based on this, two systematic studies were performed to test the interface toughness of the different coating systems. To evaluate the damage caused by the laser shocks, infrared thermographic images were taken and the defect size was measured from the images. Additionally, cross-sectional studies of the defects were conducted using SEM.
The knowledge gained from these studies can be used in the future to introduce targeted defects into the bond to topcoat and TGO to topcoat interfaces. Subsequently, the damaged specimens can be subjected to thermal cycling during the burner rig tests to analyze and evaluate the growth of the introduced defects. This comprehensive approach aims to determine the interfacial toughness of TBCs and the evolution of introduced defects during thermal cycling, which constitutes the second purpose for LASAT on plasma-sprayed coatings. Thus, this combined LASAT approach is pursued, building on its successful application for EB-PVD coatings [205].

6.4.1 Pre-tests and systematic study of APS cycling samples

In the preliminary tests, the effect of laser shocks on porous APS thermal barrier coatings was investigated. These were deposited on IN738 substrates of different thicknesses (diameter 30 mm). Additionally, some samples were coated with a Standard Bond Coat, while others had the ceramic layer applied directly to the grit-blasted substrate. An overview of the samples tested is provided in Table 6.6. Since this test series was not designed to evaluate the direct influence of substrate thickness or bond coat presence, but rather to test the suitability of the LASAT under different sample conditions, the results obtained are not directly comparable. On these samples, the laser was focused

Tab. 6.6 Properties of the LASAT pre-test samples

Sample	Thickness Sub. [mm]	Thickness BC [µm]	Thickness TC [µm]
BC1	1.9	~130	~370
X1	1.3	-	~370
BC2	1.9	~130	~140
X2	1.3	-	~140

to apply a shock with a diameter of 3 mm to both the metal and ceramic sides of the samples. For the shocks applied to the metallic side, the surface energy ranged from 0.5 to approximately 4.7 GW/cm^2. On the ceramic side, the shocks were applied with an energy of approximately 1.0 to 4.9 GW/cm^2.
Defects were detected in all samples examined by infrared imaging. In the case of the thick ceramic layers, the defects appeared very faint and blurred, as shown in Figure 6.43 (a). One contributing factor is that thermal radiation encounters more pores along its path to the surface, resulting in greater scattering. Moreover, cracks formed in the thick coatings, although detectable in cross-sections, were notably thinner compared to those in thinner top coats, resulting in reduced insulating effects and surface temperature differences. An example of such a fine crack in a thick coating is depicted in Figure 6.43 (b), where it was introduced at the maximum possible surface energy with a shock diameter of 3 mm. This contributes to the challenge of detecting cracks in infrared images. Applying shocks to the ceramic side of the sample resulted in multiple cracks forming in the coating, as shown in Figure 6.43 (c), which are undesired. Due to these challenges, it was not feasible to generate LASAT curves for the thick top coatings to determine the LASAT threshold and defect sizes as a function of applied laser energy.

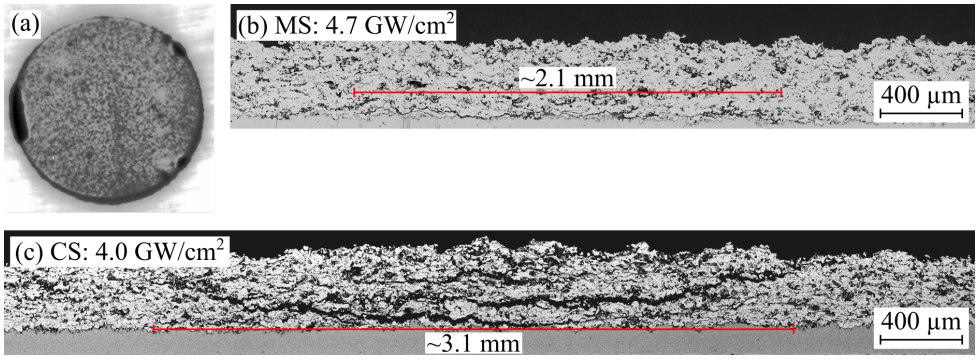

Fig. 6.43 (a) Infrared image of the X1 sample and cross-sectional images of shock induced defects in the sample: (b) shock from the metallic substrate side, (c) shock from the ceramic top coat side

In contrast, the cracks in the thin topcoat layers were clearly visible on the IR images and could be measured to determine a LASAT threshold. The IR images and the LASAT curves generated from those are shown in Figure 6.44. The results reveal lower adhesion of the ceramic layer on the sample without a bond coat. The LASAT Threashold is between about 0.5 and 1.0 GW/cm^2 for the sample without bond coat and between about 1.0

and 2.0 GW/cm^2 for the sample with bond coat. This is most likely due to the lower roughness without the bond coat and the resulting lower mechanical interlocking of the topcoat. However, the different substrate thickness plus bond coat thickness may also have influenced the shock wave propagation and thus the location of the maximum tensile stress. In addition, good agreement was found between the defects measured on the IR images and the cross-sections examined for all shocks of the BC2 specimen. These crack sizes measured in the cross sections are also shown in the LASAT curve in Figure 6.44.

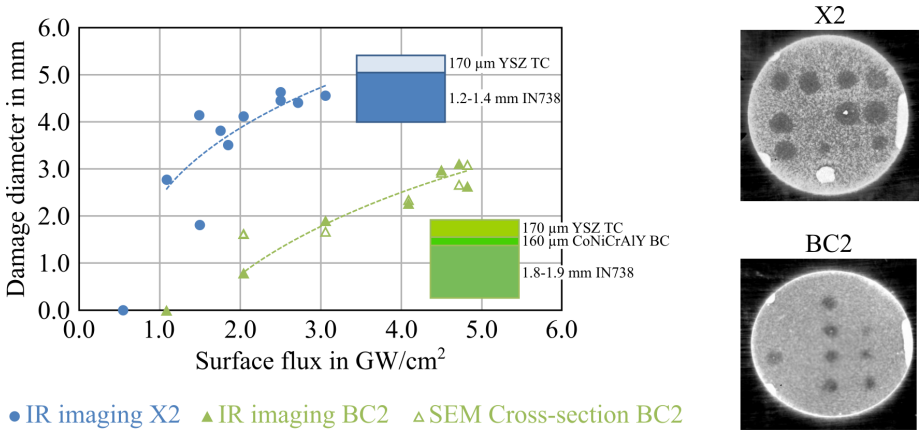

Fig. 6.44 Lasat curves and infrared images of samples with a thin top coat (X2, BC2)

Investigating the cross-sections revealed that for the thin coatings, a crack could be initiated at the substrate to topcoat interface or near the bond coat to topcoat interface. Exemplary images of a shock-induced defects in the samples with a thin top coat are presented in Figure 6.45. The lower adhesion of the top coat on the sample without a bond coat is also evident there. Despite the lower surface energy of the laser pulse, the resulting defect is significantly larger than in the sample with a bond coat. Moreover, it is noticeable that in many cases, the shocks applied to the system with a bond coat resulted in multiple cracks in the ceramic layer, rather than just a single crack at the interface as observed in the sample without a bond coat. However, it is uncertain whether the bond coat alone is responsible for this effect, as the different substrate thicknesses could also have an influence.

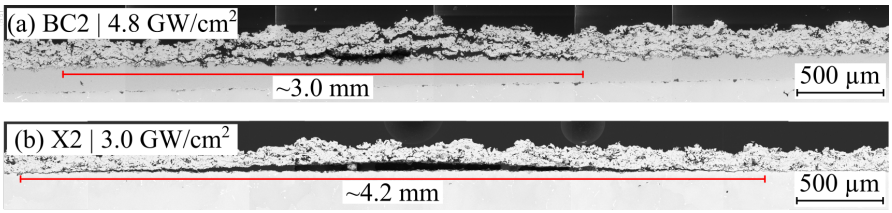

Fig. 6.45 Cross-sections of samples with thin top coat: (a) with Bond Coat - BC2, (b) without Bond Coat - X2

Tab. 6.7 Properties of the LASAT samples of the fist systematic study

Sample	Thickness TC [µm]	Heat treatment
LCS1	~200	No
LCS2	~450	No
LCS3	~200	Yes
LCS4	~450	Yes

These results demonstrated that defects can be introduced into APS coating systems at or near the interface. The LASAT approach was particularly successful for coating systems with a thin topcoat in the absence of a bond coat layer. However, these coating systems are not representative as the bond coat layer is always present in TBC systems and the plasma sprayed layers are typically thicker. Therefore, another test series was conducted with representative coating systems. This involved using typical substrate thicknesses for cycling samples of 3 mm. Additionally, all samples were coated with a bond coat approximately 110 µm thick. For the top coatings, a comparison was made between a thinner APS top coating, roughly 200 µm thick, and a thicker coating, roughly 450 µm thick. Although the preliminary tests with the thicker coatings did not yield promising results for the systematic investigation of LASAT-induced defects, this approach was chosen to investigate a potential positive effect of furnace cycling, which could lead to sintering of the ceramic and the formation of a TGO, weakening the interface. For this purpose, two of the four samples tested were subjected to a heat treatments as listed in Table 6.7. The samples were subjected to thermal cycling over 100 cycles in an air atmosphere in a furnace. Each cycle consisted of a one-hour heating period in the furnace at 1100 ℃ followed by a 15-minute cooling period in air in front of a fan.

The results of this first systematic test series demonstrated a significant influence of substrate thickness and heat treatment on the results obtained. In the sample with the thin top coat without heat treatment, defects could still be induced at a surface energy of > 1.6 GW/cm^2 for a shock diameter of 3 mm and > 1.4 GW/cm^2 for a shock diameter of 3.5 mm. The cross-sections revealed fine cracks running through the ceramic near the interface and along roughness peaks of the bond coat. Often these cracks also appeared within the ceramic only, or multiple cracks were formed. Since these defects do not allow a clear determination of the interface toughness, a LASAT curve was not generated. Furthermore, the results exhibited a high deviation in defect size due to coating inhomogeneity. Since the possibilities of introducing defects of different sizes in this type of sample were very limited, the variant of shocks on the ceramic side was also tested. However, these tests resulted either in no defect localization or in complete spallation of the coating in the area of the shock.

After heat treatment, the sample with the thin top coating consistently spalled near the interface when shocks were applied from the ceramic side, while no cracks could be induced when shocks were applied from the metal side, regardless of the laser energy. The lack of cracking with shocks applied from the metal side may be due to improved bonding of the ceramic as a result of sintering. However, it is not clear why the coating always delaminated when the shocks were applied to the ceramic side. This discrepancy suggests that the shock wave propagation and reflection also changed as a result of the TGO growth

and sintering of the ceramic. The different results could be attributed to a shift in the localization of the maximum tensile stresses, although this hypothesis requires validation by simulations.
In the samples with the thick top coat, no cracks were induced within the coating or at the interface, either in the as-sprayed state or after heat treatment, when the laser was focused on the metallic substrate side. However, when the shocks were applied to the ceramic side, multiple cracks in different coating layers were produced, sometimes leading to partial delamination of the coating. Since no relevant cracks could be produced with the combination of thick substrate and thick coating, this system is not considered further. It is assumed that with this thickness combination, the localization of the maximum tensile stresses does not occur in the required areas of the interface when the shock is applied to the metal side. The multiple cracks observed when applying the shocks on the ceramic side are also not desired.
The results of the initial systematic test series revealed that introducing defects was hindered not only by thermal cycling in air but also by the presence of the thick substrate material. Additionally, due to the thick substrates and partially thick coatings, it appears that the maximum tensile stress is either insufficient to create defects or localized at an incorrect location. Consequently, achieving a wide range of defect sizes with different laser energy, shock diameters, or shock types (metal, ceramic) was not possible. As a result, correlating the coating adhesion of different plasma-sprayed coating systems with the applied surface energy in LASAT curves is not feasible.

6.4.2 Systematic study of LASAT on different coating microstructures

Based on the pre-test results and the first systematic test series, a second systematic test series was conducted to better understand the LASAT process when applied to thermally sprayed coatings. In this series, substrates with a thickness of 2 mm were utilized, which closely resembles the thickness of the thicker substrates used in the preliminary tests. Although the results obtained are not directly transferable to thermal cycling samples, it is possible to gain insight into the formation of LASAT-induced cracks in plasma sprayed coatings. The transferability to thicker substrates would require verification, or thermocycling specimens with modified geometry (thinner substrates) would need to be produced. With these samples it would be possible to observe and analyze the evolution of specifically introduced defects during thermal cycling.
Various bond and top coats, produced using different processes, were applied to the 2 mm thick IN738 substrates. An overview of the coating systems investigated in the second systematic study is given in Table 6.8. For samples with an APS topcoat, two different bond coats with different roughnesses were tested, as well as two different topcoats with different porosities and thus elastic moduli. The rough bond coat corresponds to the Flash Bond Coat, while the smoother one is referred to as the Smooth BC. The parameters for producing these can be found in Chapter 3.3 in Table 3.6. The topcoat parameters are described in Chapter TC Parameters under the names LASAT porous and LASAT dense (Table 3.8). This selection aims to provide insights into the effect of bond coat roughness on the adhesion energy in the interface. Additionally, the different top coat densities should reveal whether they affect shock wave propagation and thus the localization of

Tab. 6.8 Properties of the LASAT samples of the second systematic study

Sample	BC roughness R_a [µm]	TC porcess	Thickness TC [µm]	Porosity TC [%]	Heat treatment
L1	~15	APS	~260	~6	No
L2	~15	APS	~260	~6	Yes
L3	~15	APS	~210	~20	No
L4	~15	APS	~210	~20	Yes
L5	~15	SPS	~170	n.a.	No
L6	~15	SPS	~170	n.a.	Yes
L7	~5	APS	~260	~6	No
L8	~5	APS	~260	~6	Yes
L9	~5	APS	~160	~20	No
L10	~5	APS	~160	~20	Yes
L11	<1	PS-PVD	~150	n.a.	No
L12	<1	PS-PVD	~150	n.a.	Yes

maximum tensile stresses. The four possible combinations of bond and top coats were tested both in the as-sprayed state and after thermal cycling in the furnace.
In addition to these eight APS samples, two columnar topcoat systems were also investigated. One was an optimized SPS coating (Table 3.8) deposited on the rough Flash Bond Coat, and the other was a PS-PVD coating (Table 3.8) deposited on a polished bond coat. In particular, the PS-PVD system was expected to be the most similar to the EB-PVD system in terms of its properties. These two different columnar coating systems were also studied in the as-sprayed state and after thermal cycling in a furnace. The topcoat deposition parameters were used as described for all coating systems. However, based on the pre-tests, the target thickness for the topcoats was 200 µm, so the number of passes was adjusted to achieve the desired thickness. Due to the nature of the process, the actual coating thicknesses achieved differed from the target value, so the actual coating thicknesses achieved are also shown in Table 6.8.
The aim of this test series was to investigate the effect of bond coat roughness and coating density of APS coatings on the LASAT results. In addition, it aimed to verify the suitability of the LASAT method for the different columnar coating systems and the ability to identify and evaluate defects using IR images. Due to the large number of samples and, above all, the number of shocks, only the key findings of the experiments on the individual coating systems are summarized in the following subsections.

Dense APS Coatings as-sprayed
In the dense APS coatings with a porosity of about 6 %, cracks were detected in the IR images for both the rough (a) and smooth (b) bond coat samples (Figure 6.46). These cracks are particularly evident in the sample with the smooth bond coat (b). However, an accurate determination of the defect size from the IR images is limited because many defects are not symmetrical in shape. Therefore, it is necessary to take a closer look at the cross sections to analyze the defects caused by the laser shocks.
Figure 6.47 shows sections of the IR images of the samples ((a) and (b)), each indicating the position of the cross-sections shown. The figure includes two images with defects in the sample with the rough bond coat ((c), (d)) and two images with defects in the sample with the smooth bond coat ((e), (f)). These cross sections clearly show that the cracks caused by the laser shocks were not localized in the interface, but in the ceramic coating

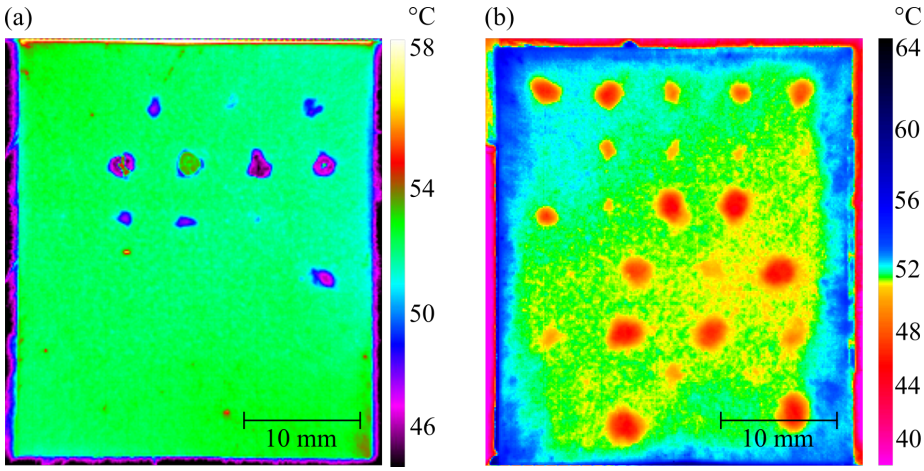

Fig. 6.46 Infrared images of L1 and L7 sample with dense top coat and different bond coats

itself. In the sample with the rough bond coat, the defects always occur at a constant distance of about 80 µm below the coating surface. This suggests that the maximum tensile stress caused by the laser shocks occurred in this region. Some of the shocks with a high surface energy exceeding 3 GW/cm^2 also caused the coating to delaminate.
In the sample with the smooth bond coat, there was no spalling of the coating, but rather the phenomenon of multicracking. This is particularly evident in Figure 6.47 (e). It is even possible to count the number of passes of the torch during production based on the layers between the cracks. This observation suggests poor bonding between the individual layers of the coating. Since the two samples with the dense top layer were produced in two different runs but with the same parameters, it is not clear whether this effect is due to process fluctuations or to a different transition of the shock wave through the interface of the smooth bond coat. To verify this, two samples from one coating run would have to be examined on the different bond coats. The poor bonding between the individual layers of the coating could potentially result from overspray, wherein unmolten particles are deposited between the layers. Such poor adhesion, despite high deposition temperatures during production of the dense coating, could also explain the horizontal cracking found in the vertically cracked DVC and SPS coatings during process optimization.
Regarding the dense coatings in the as-sprayed state, it can be summarized that the effects of the bond coat roughness cannot be clearly defined, as there may also be a difference between the two top coats, even though they were produced with the same parameters. Furthermore, it was shown that the maximum tensile stresses in the dense layers localized in the ceramic itself. As a result, it was possible to measure the ceramic toughness rather than the interface toughness, which is why no LASAT curves were plotted for these coating systems.

Porous APS Coatings as-sprayed
The porous coatings had a negative effect on the visual evaluation of defects (Figure 6.48 (a) and (b)). This is consistent with the poor visualization of defects in the thick

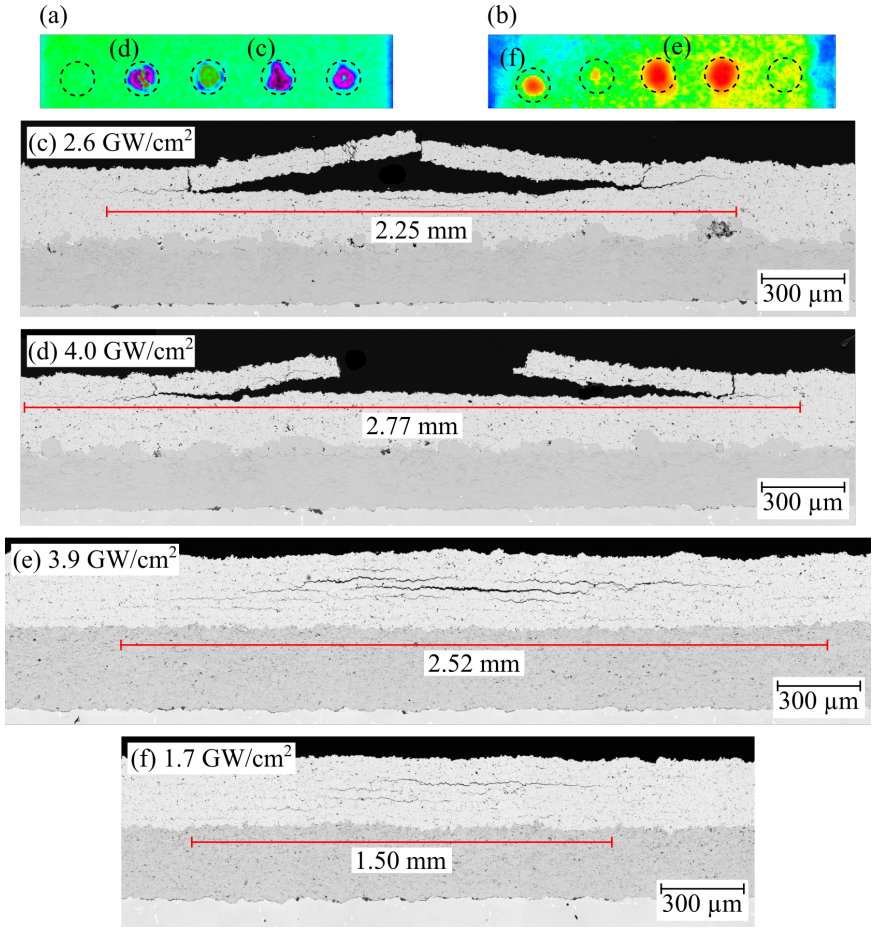

Fig. 6.47 Sections of the infrared images of L1 (a) and L7 (b) specimen with dense top coat and different bond coats; (c) and (d) cross-sections of L1 specimen, (e) and (f) cross-sections of L7 specimen

coatings from the pre-tests and the first systematic tests. The scattering of thermal radiation by pores reduces the pronounced effect of different thermal conduction at defects. Furthermore, as in previous experiments, the defects are thinner at higher porosities ((c) and (d)), reducing their influence on the temperature difference that appears. This could be due to the fact that some energy of the laser shock waves is reflected at the pores before being reflected and reversed at the free surface, reducing the energy of the wave. In addition, the porous layers with a lower elastic modulus may be better at absorbing the shock wave, resulting in small defects.

Examination of the cross-sections showed that the cracks in the porous coatings formed closer to the interface for both bond coat types, compared to the cracks in dense coatings. Some ran along roughness peaks, as shown in Figure 6.48 (c), while others ran completely through the ceramic (d). However, the main crack was always close to the interface. This

could be due to a change in shock wave propagation compared to the dense coatings, but would need to be verified with simulations. Due to the inhomogeneity of the microstructure of the coating and the weak points at microcracks and poorly bonded particles, branching cracks often form from the interface to the ceramic. Although this type of crack microstructure does not allow a direct determination of the interface toughness, it was investigated whether the roughness of the bond coat has an influence on the size of the defects caused by the shocks close to the interface.

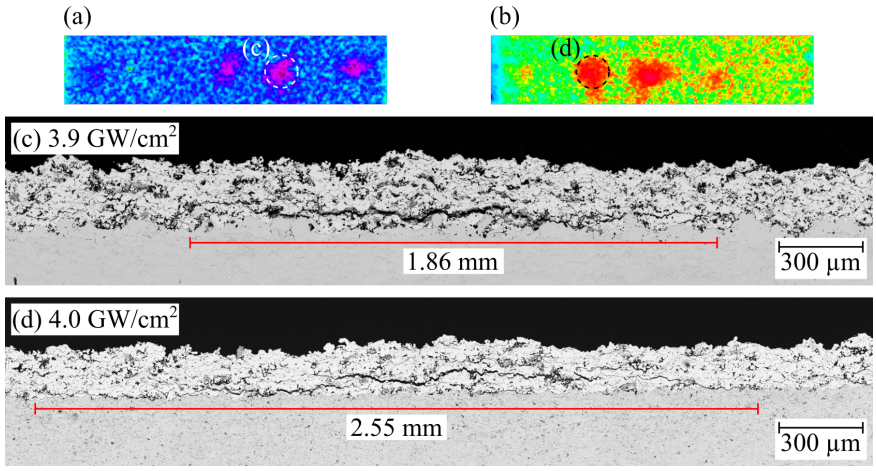

Fig. 6.48 Sections of the infrared images of L3 (a) and L9 (b) sample with porous top layer and different bond coats; (c) cross-section of L3 sample, (d) cross-section of L7 sample

Taking IR images at higher magnification with a changed camera lens allowed for a more detailed analysis of defect sizes influenced by the bond coat surface roughness. The defect sizes were measured using temperature profiles extracted from the images. Using this data, LASAT curves were plotted for the porous coatings with the two different bond coats, categorized by laser shock diameter. One curve was generated for each bond coat, considering a shock diameter of 3 mm (Figure 6.49 (a)) and another for a shock diameter of 4 mm (Figure 6.49 (b)).

All LASAT curves indicate that the defect size increases with the surface energy applied by the laser pulse, with limited influence from the bond coat. Only at a shock diameter of 3 mm, the defect size is higher with the smooth bond coat compared to the rough bond coat, suggesting potentially lower bonding strength due to less interlocking of the coating. However, since there is no clear difference between the bond coats, this suggests that the ceramic toughness rather than interface toughness was measured. Due to the inhomogeneous coating microstructure, laser shocks tend to cause crack branching in the ceramic, which is why there is no difference between samples with the same coating but different bond coats. Another possibility is that the evaluation of porous coatings using IR thermography reaches its limits for porous plasma sprayed coatings. A more detailed analysis of cross-sections could confirm this, but has not yet been conducted due to time constraints.

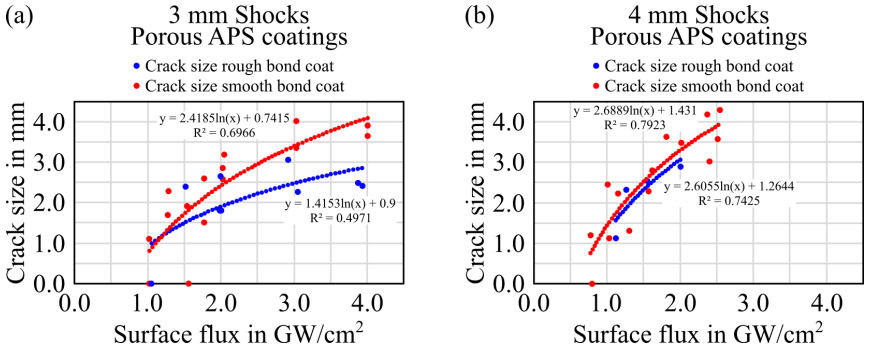

Fig. 6.49 LASAT curves of samples with a porous top layer and different bond coats: (a) shock diameter 3mm, (b) shock diameter 4mm

LASAT on APS Coatings after Heat Treatment

The heat treatment of the coatings, similar to the first systematic test series, affected the LASAT results. With the dense coating on the rough bond coat, part of the coating spalled off after 100 cycles of 1 hour at 1100 ℃. Consequently, the number of cycles for thermal cycling of the APS coatings on the smooth bond coat was reduced to 50 cycles. However, even with this reduction, the dense coating still experienced spalling of a large area of the coating.

The IR images again showed that the defects caused by the laser shocks were barely visible in the porous layers after heat treatment, and not visible at all in the dense layers. However, defects were still present in the coatings. As shown in Figure 6.50, the crack generated in the dense layer of the rough bond coat (a) moved closer to the interface. This shift may have been caused by a relocation of the region with the weakest adhesion due to sintering and pre-existing damage from cycling. The presence of defects in the coating near the interface after thermal cycling are indicated by the partial delamination of the coating. Additionally, Figure 6.50 (a) exhibits a crack on the right side of the image, likely induced by thermal cycling as no shock was applied there. This crack aligns with the height of the crack created or expanded by the laser shock. Apart from horizontal cracks, vertical cracks have also emerged for stress relief. As defects are already present due to the thermal cycling, this can also be a reason why the defects introduced by LASAT cannot be identified on the IR images.

In the porous LASAT APS coatings, the induced cracks ran near the interface in both samples, as illustrated in Figure 6.50 (b) for the rough bond coat and (c) for the smooth bond coat. However, the cracks do not strictly follow the interface, but branched out into the ceramic. Therefore, it is not possible to determine the interface toughness. Nevertheless, since the crack paths shown in the sample with the Flash Bond Coat (Figure 6.50 (b)) were also also found in the failed burner rig specimens with this bond coat (Figure 5.7), such defects could be used for investigation of the defect growth in cycling tests. However, it would be necessary to determine whether the defects could be detected by the IR camera on the burner rigs during thermal cycling.

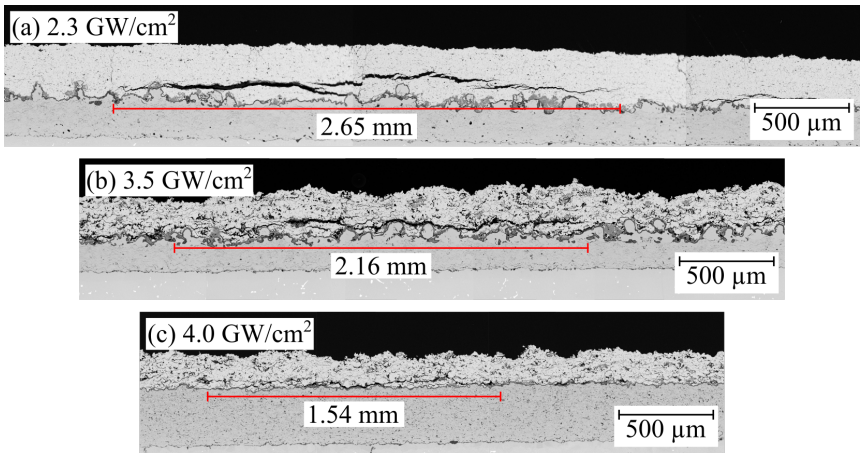

Fig. 6.50 Cross-sections of samples after thermal cycling and subsequent shock application: (a) L2 sample, (b) L4 sample, (c) L10 sample; Thermal cycling with 1 hour cycles at 1100 °C (a) and (b) 100 cycles, (c) 50 cycles

LASAT on Columnar Microstructured Samples

The results of the LASAT tests on the columnar SPS and PS-PVD coatings were combined into one section as the damage mechanisms were comparable. In the case of the SPS coatings, the IR images revealed either areas of spallation or no detectable defects, both in the as-sprayed state and after heat treatment. In contrast, blurry defect shapes could be identified on the IR images of the PS-PVD coatings for the samples in both states.
Analysis of the cross-sections also showed either no damage or direct spalling of coating areas in the SPS samples, both in the as-sprayed state and after 100 cycles of thermal cycling. No cracks occurred where the coating remained on the bond coat. Individual failure of single or multiple neighboring columns was often observed (Figure 6.51 (a)). The localized removal of columns suggests either very localized stress peaks, possibly caused by the rough bond coat and inhomogeneous coating microstructure causing a change in shock wave propagation, or differences in the bonding of the columns themselves.
The same phenomenon was observed with the PS-PVD coatings (Figure 6.51 (b)). In some cases, individual columns were detached from the coating, but the PS-PVD coatings also frequently cracked in the area where the elongated grain growth of the columns begins. This crack nucleation point is also known from LASAT in EB-PVD coatings. However, most of the columns remained in the coating.

Summary of LASAT on different plasma-sprayed microstructures

Summarizing the LASAT trials, it can be stated that IR thermography can be used to detect laser-induced defects in a wide variety of plasma sprayed coating microstructures. The thicker the coating or the higher the defect density in the coating due to microcracks and pores, the less accurate the IR thermogram generated and the more difficult it is to analyze. Possible improvements in the results could be achieved with pulsed IR analysis, in which short pulses of infrared light are emitted onto the sample [251].

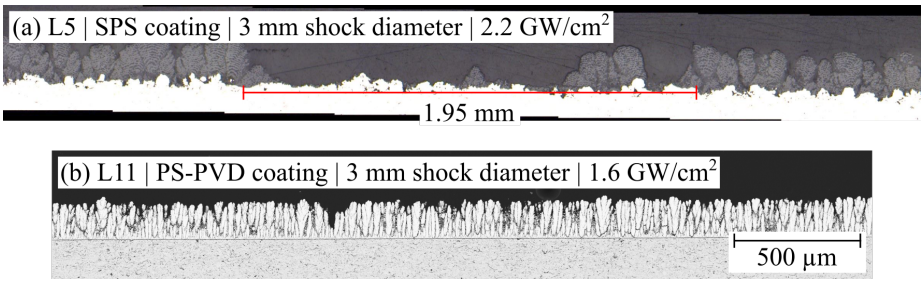

Fig. 6.51 Cross-sections of samples with columnar microstructure in the as-sprayed state after shock application: (a) L5 sample, (b) L11 sample

The examinations of the cross-sections of the dense APS coatings revealed that the localization of the maximum tensile stresses induced by the laser shocks occured at a constant distance from the coating surface. This indicates uniform shock wave propagation. Furthermore, the presence of multiple cracks in the coating system exposed an interpass weakness, potentially attributed to overspray during the coating process. Thermal cycling at maximum temperatures of 1100 °C resulted in changes in the coating system. The weakest point of the system shifted to an area near the interface where cracks had already formed in the coating as a result of thermal cycling.

In contrast, the shock wave propagation was less uniform in the porous coatings, often resulting in multiple cracks in the ceramic and significant branching of the cracks along poorly bonded splats or unmolten particles and micro cracks. Moreover, the cracks tended to be localize closer to the interface, suggesting a potentially different shock wave propagation through the porous layer with a different Young's modulus.

The columnar microstructures did not show long horizontal cracks, but the formation of local cracks in individual columns. In SPS coatings, this cracking always resulted in delamination of the column, whereas in the PS-PVD coating, most of the columns remained intact despite the cracks.

In the future, the shock wave propagation should be simulated to better understand the formation of the defects. To achieve this, it is important to determine the exact density and Young's moduli of the coatings. Furthermore, the simulations should consider the different surface roughnesses across different samples.

Furthermore, using the LASAT method, defects could be introduced into the porous layers after heat treatment that are similar to the failure mechanism of these coating systems during thermal cycling. This makes it possible to introduce local defects into thermal cycling samples (with a substrate thickness of 2 mm). Their growth can then be observed during thermal cycling, giving further insights into the failure of TBCs.

7 Summary and Outlook

Thermal barrier coating systems are designed to protect components from high temperatures, oxidation and corrosion in the hot sections of a turbine. Typically, these consist of a ceramic insulating layer and a metallic bond coat layer deposited on the turbine components. Due to the different material properties of these layers, stresses occur in the coating system during temperature changes. Additionally, factors such as oxidation of the bond coat and temperature-induced changes in the ceramic top coat further contribute to these stresses. Consequently, these factors are primarily responsible for the failure of thermal barrier coating systems during operation, where high operational flexibility of the turbines is a particular challenge. However, this will be required of power plant turbines in the future as they are used to compensate for fluctuations in electricity demand and generation due to the volatility of renewable energy sources.
Therefore, the focus of this work was to optimize the thermal barrier coating system for better cyclability and to gain insight into the failure behavior of TBCs with different microstructures. By optimizing the manufacturing process, the influence of the properties of the manufactured coatings on the thermal cycling results was investigated. Additionally, an image correlation and a laser shock method were used to better understand the failure of the differently structured topcoats. Image correlation was employed to monitor strains on the sample surface during thermal cycling and correlate them with failure. Laser shock tests were used to study the adhesion of the ceramic topcoats. Several research questions have emerged from these approaches, which are described in Chapter 1. These are addressed and answered below, indicated by the numbers assigned in Chapter 1.

The investigation of different bond coats was aimed at increasing the service life of the coating systems either by surface modifications or by using an innovative bond coat alloy with a significantly reduced coefficient of thermal expansion to reduce out-of-plane stresses. This led to the question of how different bond coat roughness profiles and the altered thermal expansion coefficient of the alternative bond coat alloy affect the durability of the TBC system under rapid temperature changes (i).
It was shown that roughening the surface of the bond coat could shift the crack propagation path responsible for failure from the interface of the system between the TGO and the topcoat into the ceramic topcoat and along the roughness peaks of the bond coat. However, this did not necessarily improve the lifetime of the system. In particular, particles that were not molten due to process changes and were therefore poorly bonded to the coating, which could contribute to surface roughening, but favored failure of the coating system. These particles were often isolation from the rest of the bond coat and, therefore, quickly depleted from aluminum. This, in turn, lead to the growth of mied oxides and promoted an early failure.
The samples produced with the alternative bond coat alloy with a reduced coefficient of thermal expansion showed a comparable failure mechanism to the Standard Bond Coats without surface modification. This can be explained by their comparable surface roughness. In terms of service life, the Oerlikon Metco Standard Bond Coat, the Flash Bond Coat

and the bond coat produced with the alternative alloy all showed comparable service life. However, it was significantly longer than that of FZJ's Standard Bond Coat, which was used as the reference system for this thesis. The reasons for the significant differences in service life between the Standard Bond Coats from FZJ and Oerlikon Metco will be investigated in the future using EBSD and TEM. An accurate evaluation of the bond coat performance with respect to the influence of roughness and thermal expansion could not be made since the bond coats were either partially or completely depleted of aluminum due to the long service life. It is possible that coating systems with a thicker bond coat and thus a larger Al-reservoir would have achieved an even longer service life.
Targeted pre-oxidation of the bond coat in an argon atmosphere (ii) improved the life of the APS and SPS coating systems. While the increase in life of the APS coatings was moderate, the life of the SPS coatings was approximately doubled. This enhancement is attributed to the slower oxide growth during cycling facilitated by the previously formed dense Al_2O_3 layer. If the Al_2O_3 layer is not formed until the topcoat is applied, the growth during thermal cycling is faster [75]. Previous research has already demonstrated the effectiveness of targeted pre-oxidation for both APS coatings [75], [83] and SPS coatings [80]. Therefore, the purpose of this study was to provide a direct comparison of pre-oxidation on APS and SPS systems. The effect of pre-oxidation on the service life increase was greater for the SPS coatings as the effect of the initial high growth stresses of the TGO on the ceramic could be prevented. Nevertheless, the overall lifetime of the APS coatings after pre-oxidation of the bond coats was higher than of the SPS coatings. This is due to the fact that the APS system only failed when the fracture toughness of the interface was exceeded. The SPS coatings, in contrast, stored a large amount of elastic energy in the ceramic close to the interface. In addition, near to the interface, there were areas of low critical energy release rates in the porosity bands of the coating. Therefore, failure occurred within these porosity bands before the critical energy release rate of the interface was exceeded.
Studies investigating the impact of various parameters on oxide formation during pre-oxidation have highlighted the importance of factors such as applied temperature, holding times [74], and oxygen partial pressure (pO_2). The studies indicated that an intermediate pO_2 level is optimal for pre-oxidation [75], [78]. Insufficient pressure did not facilitate the formation of a dense Al_2O_3 layer, while excessively high pressure led to mixed oxide formation. Therefore, future studies should develop optimized parameters under controlled pO_2 for the coating systems used to see if different conditions are optimal for APS and SPS.
In addition to these specifically investigated factors, strong pore formation in the bond coat was also detected at high sample lifetimes in thermal cycling tests. This could be attributed to a depletion of aluminum as well as cobalt.

The effect of the different top coating microstructures produced (iii) can hardly be evaluated directly from the results obtained. This is because many systems failed due to the formation of mixed oxides after partial or complete aluminum depletion of the bond coat. For a better comparison of the lifetimes of the different top coats, a more resistant bond coat is required, or a thicker bond coat that can provide a larger aluminum reservoir for the formation of the Al_2O_3 layer.

Nevertheless, the thermal cycling results showed different failure mechanisms for the different coating systems. While coatings with an APS top coat failed at the interface along the TGO, the DVC and SPS coatings developed a crack that propagated from the roughness peaks of the bond coat through the ceramic. The APS coatings are assumed to have a higher critical energy release rate than the TGO, leading to failure of the TGO when mixed oxides form due to aluminum depletion of the bond coat. In contrast, the dense areas between the segmentation cracks in the DVC coatings are assumed to store a lot elasic energy during cycling, due to their high Young's modulus. As a result, the elastic energy stored in these segments exceeds the critical energy release rate after a certain number of cycles, and the cracks in the ceramic begin to propagate. This crack propagation occurs before the cracks develop in the TGO/coating interface, which is why this coating also has a lower thermal shock resistance than the APS coated samples. In the SPS coatings, the cracks that form over the roughness peaks propagate through the porosity bands of the coating, which have low adhesion due to the many solidified particles deposited in these porous bands. This also results in a shorter service life compared to coatings with an APS top layer. Futhermore, it was observed that the sintering tendency of the considered coating systems is significantly higher when there are finely distributed defects and pores in the specimens. This increased sintering tendency was found for DVC and SPS coatings and might contribute to the early failure due to a stiffening of the coatings. Failure of PS-PVD coatings is caused by rumpling, where the polished bond coat is subsequently roughened during operation, causing parts of the coating to detach at the interface. Since the flat surface of the bond coat does not prevent crack growth, these delaminations quickly connect, leading to large-scale delamination of the coating along the TGO/coating interface.
The examination of the failed coatings revealed the segregation of the metastable tetragonal t'-phase into cubic and tetragonal phases. However, the rapid cooling of the coating system prevented the formation of the critical monoclinic phase in most cases. Weak peaks of the monoclinic phase were only detected in XRD in the optimized APS coating, indicating the transformation of a small amount of the tetragonal phase.

The setup developed for digital image correlation allowed the acquisition of images over complete cycles during burner rig testing, suitable for image correlation. With these images it is possible to perform qualitative analyses of local strain changes on the sample (iv). However, since the detected strains are overestimated, quantitative strain determination and thus stress calculation is not possible. Nevertheless, the system was able to show that the substrate alone is responsible for the expansion behavior of the entire coating system. Furthermore, it was shown that SPS and APS coatings form blisters during thermal cycling. These blisters are present at room and high temperatures, indicating plastic deformation of the coating. At the location of blister formation, the coating later failed, making the system suitable for damage prediction as well (v). However, it is not possible to determine the precise dimensions of the blister at high temperatures. To achieve this, a 3D camera setup for image acquisition and subsequent image processing is proposed. This approach aims to accurately determine blister height at high temperatures, providing additional insights into the underlying failure mechanisms.

Attempts to transfer the achievements of the LASAT process with EB-PVD coatings to plasma sprayed systems have shown that this is only possible for a small range of coating systems (vi). Direct interface defects could only be introduced on thin substrates (< 2 mm), with no bond coat and an APS top layer < 150 µm. For other coatings, cracks were always found to have branching cracks in the ceramic or to be completely formed in the ceramic rather than in the interface.
IR thermography could be used to detect laser-induced defects across a wide range of plasma sprayed coating microstructures. The thicker the coating or the higher the defect density in the coating due to microcracks and pores, the less accurate the IR thermogram generated and the more difficult it is to analyze. Possible improvements in results could be achieved with pulsed IR analysis, where short pulses of infrared light are directed onto the sample [251]. The examination of cross-sections of the dense APS coatings revealed that the maximum tensile stresses induced by laser shocks localized consistently at a fixed distance from the coating surface, initiating crack formation at this position. This indicates a uniform propagation of the shock waves. Additionally, the presence of multiple cracks in the coating system indicates a weak bond between individual layers of the coating, possibly due to overspray during the deposition process. Thermal cycling at maximum temperatures of 1100 ℃ caused changes in the coating system. The weakest point of the system shifted to an area near the interface where cracks had already formed in the coating as a result of the thermal cycling.
In contrast, the shock wave propagation in the porous coatings was less uniform, often resulting in multiple cracks in the ceramic. These cracks exhibited significant branching along poorly bonded splats or unmolten particles and microcracks. Moreover, the cracks tended to localize closer to the interface, possibly indicating different shock wave propagation through the porous layer with a different elastic modulus.
The columnar microstructures did not show long horizontal cracks, but rather the formation of localized cracks in individual columns. With the SPS coatings, these cracks always led to delamination of single columns, whereas with the PS-PVD coating, most of the columns remained intact despite the cracks.
LASAT tests revealed limitations in inducing targeted crack sizes within the interface of thermocycling samples due to substrate thicknesses of 3 mm. Additionally, the typical coating thicknesses of these samples were also too high. However, for specific coating systems with a substrate of 2 mm and a top layer of ~200 µm, it is possible to induce defects that behave like the cracks that occur during thermal cycling. It would therefore be possible to observe the growth of such defects during thermal cycling using adapted cycling samples.

Based on the overall results of this work, it is proposed to develop a double-layer coating system of YSZ layers, attempting to maximize the cyclability of the thermal barrier coating systems. This should combine the advantages of different coatings as shown in the furnace cycling tests with different materials. It is proposed to investigate a double layer APS/SPS YSZ system on a bond coat pre-oxidized under controlled pO_2 as an ideal coating system. This would ensure the advantage of a slowly growing oxide layer due to the pre-oxidation as well as the good bonding of the APS layer and the high strain tolerance and erosion resistance of the SPS layer. With the SinplexPro torch, this could also be achieved without a high loss of time and thus cost. One injector could deliver the powder for depositing

the APS layer and another injector could deliver the suspension for the SPS layer. This would allow the production of the double-layer system in a time and cost efficient manner without the need to change the gun setup or remove the components to be coated.

Bibliography

[1] Tobias Bossmann, Barberi Paul, and Laurent Fournié. *Effect of high shares of renewables on power systems: Study S11*. Brussels, 2018.

[2] Alexander Schiemann. So läuft der ausbau der erneuerbaren energien in deutschland, 2024.

[3] Alexander Schiemann. Das zeitalter der erneuerbaren energien, 2024.

[4] Artur Mertens, Klaus-Michael Ahrend, Anke Kopsch, and Werner Stork, editors. *Smart Region*. Springer Fachmedien Wiesbaden, Wiesbaden, 2021.

[5] Martin Dehli. *Energieeffizienz in Industrie, Dienstleistung und Gewerbe*. Springer Fachmedien Wiesbaden, Wiesbaden, 2020.

[6] Johannes Lambertz, Hans-Wilhelm Schiffer, Ivan Serdarusic, and Hendrik Voß. Flexibilität von kohle- und gaskraftwerken zum ausgleich von nachfrage- und einspeiseschwankungen. *Energiewirtschaftliche Tagesfragen*, 62(7):16–32, 2012.

[7] Daniela Ewers. Einigung zur kraftwerksstrategie, 2024.

[8] Giovanni Cerri, Marco Gazzino, Fabio Botta, and Coriolano Salvini. Production planning with hot section life prediction for optimum gas turbine management. *International Journal of Gas Turbine, Propulsion and Power Systems*, 2(1):9–16, 2008.

[9] Herbert Sigloch. *Strömungsmaschinen: Grundlagen und Anwendungen : mit 358 Bildern, 36 Tabellen sowie einer Multimedia-CD-ROM*. Hanser, München, 6., aktualisierte auflage edition, 2018.

[10] Burkhard Heine. Nickelbasis-superlegierungen für flugzeugantriebe aus metallkundlicher sicht. *WOMag: Kompetenz in Werkstoff und funktioneller Oberfläche*, (1), 2014.

[11] Albert Feuerstein, James Knapp, Thomas Taylor, Adil Ashary, Ann Bolcavage, and Neil Hitchman. Technical and economical aspects of current thermal barrier coating systems for gas turbine engines by thermal spray and ebpvd: A review. *Journal of Thermal Spray Technology*, 17(2):199–213, 2008.

[12] Robert Vaßen, Alexandra Stuke, and Detlev Stöver. Recent developments in the field of thermal barrier coatings. *Journal of Thermal Spray Technology*, 18(2):181–186, 2009.

[13] Robert Vaßen, Maria Ophelia Jarligo, Tanja Steinke, Daniel Emil Mack, and Detlev Stöver. Overview on advanced thermal barrier coatings. *Surface and Coatings Technology*, 205(4):938–942, 2010.

[14] Robert Vaßen, Emine Bakan, Daniel Emil Mack, and Olivier Guillon. A perspective on thermally sprayed thermal barrier coatings: Current status and trends. *Journal of Thermal Spray Technology*, 31(4):685–698, 2022.

[15] Amrinder Mehta, Hitesh Vasudev, and Sharanjit Singh. Recent developments in the designing of deposition of thermal barrier coatings – a review. *Materials Today: Proceedings*, 26:1336–1342, 2020.

[16] Daniel Thomas and Andy Gleadall. Advanced metal transfer additive manufacturing of high temperature turbine blades. *The International Journal of Advanced Manufacturing Technology*, 120(9-10):6325–6335, 2022.

[17] Nitin P. Padture, Maurice Gell, and Eric H. Jordan. Thermal barrier coatings for gas-turbine engine applications. *Science (New York, N.Y.)*, 296(5566):280–284, 2002.

[18] D. R. Clarke and C. G. Levi. Materials design for the next generation thermal barrier coatings. *Annual Review of Materials Research*, 33(1):383–417, 2003.

[19] David R. Clarke, Matthias Oechsner, and Nitin P. Padture. Thermal-barrier coatings for more efficient gas-turbine engines. *MRS Bulletin*, 37(10):891–898, 2012.

[20] Hans-Josef Allelein, Elmar Bollin, Helmut Oehler, Udo Schelling, and Richard Zahoransky. *Energietechnik*. Vieweg+Teubner, Wiesbaden, 2010.

[21] Karl Strauß. *Kraftwerkstechnik*. Springer Berlin Heidelberg, Berlin, Heidelberg, 2009.

[22] William W. Bathie. *Fundamentals of gas turbines*. Wiley, New York, 2. ed. edition, 1996.

[23] Christof Lechner and Jörg Seume. *Stationäre Gasturbinen*. VDI-Buch. Springer, Berlin, Heidelberg, 2., neu bearbeitet auflage edition, 2010.

[24] Sahil Popli, Peter Rodgers, and Valerie Eveloy. Trigeneration scheme for energy efficiency enhancement in a natural gas processing plant through turbine exhaust gas waste heat utilization. *Applied Energy*, 93:624–636, 2012.

[25] Zongming Yang, Mykola Radchenko, Andrii Radchenko, Dariusz Mikielewicz, and Roman Radchenko. Gas turbine intake air hybrid cooling systems and a new approach to their rational designing. *Energies*, 15(4):1474, 2022.

[26] Thamir K. Ibrahim and M. M. Rahman. Effect of compression ratio on performance of combined cycle gas turbine. *International Journal of Energy Engineering*, 2(1):9–14, 2012.

[27] Emine Bakan. *Yttria-stabilized zirconia/gadolinium zirconate double-layer plasma-sprayed thermal barrier coating systems (TBCs)*. Dissertation, Forschungszentrum Jülich GmbH, 2015.

[28] Umesh Unnikrishnan and Vigor Yang. A review of cooling technologies for high temperature rotating components in gas turbine. *Propulsion and Power Research*, 11(3):293–310, 2022.

[29] W. N. Harrison, D. G. Moore, and J. C. Richmond. Review of an investigation of ceramic coatings for metallich turbine parts and other high-temperature applications. *National Advisory Committee for Aeronautics*, (NACA Technical Note No. 1186), 1947.

[30] Floyd B. Garrett and Charles A. Gyorgak. Adhesive and protective characteristics of ceramic coating a-417 and its effect on engine life of forged refractaloy-26 (ams 5760) and cast stellite 21 (ams5385) turbine blades. *National Advisory Committee for Aeronautics*, Research Memorandum RM E52L30, 1953.

[31] Edward R. Bartoo and John L. Clure. Experimental investigation of air-cooled turbine blades in turbojet engine. *National Advisory Committee for Aeronautics*, Research Memorandum RM E53E18, 1953.

[32] Stephan Stecura. Two-layer thermal barrier coating for high temperature components. *Am. Ceram. Soc. Bull*, 56(12):1082–1085, 1977.

[33] Ralf Bürgel, Hans Jürgen Maier, and Thomas Niendorf. *Handbuch Hochtemperatur-Werkstofftechnik: Grundlagen, Werkstoffbeanspruchungen, Hochtemperaturlegierungen und -beschichtungen*. Vieweg+Teubner Verlag / Springer Fachmedien Wiesbaden GmbH Wiesbaden, Wiesbaden, 4., überarbeitete auflage edition, 2011.

[34] Uwe Leushake. *Design, Herstellung und Lebensdauer gradierter elektronenstrahlgedampfter Wärmedämmschichten im System Aluminiumoxid/Zirkonoxid*. 2001.

[35] Robert B. Heimann. *Plasma spray coating: Principles and applications*. Wiley-VCH, Weinheim, 2., completely rev. and enl. ed. edition, 2008.

[36] Kiyoshi Fujimoto, Yuya Fukunaga, Satoshi Hada, Toshishige Ai, Masanori Yuri, and Junichiro Masada. Technology application to mhps large flame f series gas turbine. In *Volume 3: Coal , Biomass, and Alternative Fuels; Cycle Innovations; Electric Power; Industrial and Cogeneration; Organic Rankine Cycle Power Systems*, pages 1–8. American Society of Mechanical Engineers, 2018.

[37] Tresa M. Pollock and Sammy Tin. Nickel-based superalloys for advanced turbine engines: Chemistry, microstructure and properties. *Journal of Propulsion and Power*, 22(2):361–374, 2006.

[38] Roger C. Reed. *The superalloys: Fundamentals and applications*. Cambridge University Press, Cambridge, 2006.

[39] Chester Thomas Sims, Norman S. Stoloff, and William C. Hagel. *Superalloys II: High-temperature materials for aerospace and industrial power*, volume 2 of *Superalloys / ed. by Chester T. Sims*. Wiley, New York, NY, 1987.

[40] J. R. Nicholls. Designing oxidation-resistant coatings. *JOM*, 52(1):28–35, 2000.

[41] W. G. Sloof and T. J. Nijdam. On the high-temperature oxidation of mcraly coatings. *International Journal of Materials Research*, 100(10):1318–1330, 2009.

[42] J. R. Nicholls. Advances in coating design for high-performance gas turbines. *MRS Bulletin*, 28(9):659–670, 2003.

[43] W. Beele, N. Czech, W. J. Quadakkers, and W. Stamm. Long-term oxidation tests on a re-containing mcraly coating. *Surface and Coatings Technology*, 94-95:41–45, 1997.

[44] B. H. Pilsner. Eeffects of mar-m247 substrate (modified) composition on coating oxidation coating/substrate interdiffusion. *NASA Contract Report 174851*, N85-19073*#, 1985.

[45] D. Delaunay and A. M. Huntz. Mechanisms of adherence of alumina scale developed during high-temperature oxidation of fe-ni-cr-al-y alloys. *Journal of Materials Science*, 17(7):2027–2036, 1982.

[46] Bruce A. Pint, Anthony J. Garratt-Reed, and Linn W. Hobbs. Possible role of the oxygen potential gradient in enhancing diffusion of foreign ions on α-al$_2$o$_3$ grain boundaries. *Journal of the American Ceramic Society*, 81(2):305–314, 1998.

[47] A. Gil, D. Naumenko, R. Vassen, J. Toscano, M. Subanovic, L. Singheiser, and W. J. Quadakkers. Y-rich oxide distribution in plasma sprayed mcraly-coatings studied by sem with a cathodoluminescence detector and raman spectroscopy. *Surface and Coatings Technology*, 204(4):531–538, 2009.

[48] J. Toscano, R. Vaßen, A. Gil, M. Subanovic, D. Naumenko, L. Singheiser, and W. J. Quadakkers. Parameters affecting tgo growth and adherence on mcraly-bond coats for tbc's. *Surface and Coatings Technology*, 201(7):3906–3910, 2006.

[49] T. J. Nijdam and W. G. Sloof. Effect of reactive element oxide inclusions on the growth kinetics of protective oxide scales. *Acta Materialia*, 55(17):5980–5987, 2007.

[50] Emmanuel Perez. Development of aps mcraly dense bond coats. *Report; University of Central Florida: Orlando, FL, USA,*, 2006.

[51] Georg Mauer, Doris Sebold, Robert Vaßen, Elham Hejrani, Dmitry Naumenko, and Willem J. Quadakkers. Impact of processing conditions and feedstock characteristics on thermally sprayed mcraly bondcoat properties. *Surface and Coatings Technology*, 318:114–121, 2017.

[52] M. Gupta, N. Markocsan, X.-H. Li, and L. Östergren. Influence of bondcoat spray process on lifetime of suspension plasma-sprayed thermal barrier coatings. *Journal of Thermal Spray Technology*, 27(1-2):84–97, 2018.

[53] M. Gupta, N. Markocsan, X.-H. Li, and B. Kjellman. Development of bondcoats for high lifetime suspension plasma sprayed thermal barrier coatings. *Surface and Coatings Technology*, 371:366–377, 2019.

[54] Nitish Kumar, Mohit Gupta, Daniel E. Mack, Georg Mauer, and Robert Vaßen. Columnar therma barrier coatings produced by different thermal spray processes. *Journal of Thermal Spray Technology*, 30(6):1437–1452, 2021.

[55] Georg Mauer, Karl-Heinz Rauwald, Yoo Jung Sohn, and Robert Vaßen. The potential of high-velocity air-fuel spraying (hvaf) to manufacture bond coats for thermal barrier coating systems. *Journal of Thermal Spray Technology*, 2023.

[56] Moritz Elsaß, Martin Frommherz, Alfred Scholz, and Matthias Oechsner. Interdiffusion in mcraly coated nickel-base superalloys. *Surface and Coatings Technology*, 307:565–573, 2016.

[57] A. Rabiei. Failure mechanisms associated with the thermally grown oxide in plasma-sprayed thermal barrier coatings. *Acta Materialia*, 48(15):3963–3976, 2000.

[58] M. Elsaß, M. Frommherz, and M. Oechsner. The influence of the coating deposition process on the interdiffusion behavior between nickel-based superalloys and mcraly bond coats. *Journal of Thermal Spray Technology*, 27(3):379–390, 2018.

[59] J. A. Nesbitt and R. W. Heckel. Modeling degradation and failure of ni-cr-al overlay coatings. *Thin Solid Films*, 119(3):281–290, 1984.

[60] W. S. Walston, J. C. Schaeffer, and W. H. Murphy. A new type of microstructural instability in superalloys - srz. *Superalloys*, pages 9–18, 1996.

[61] H. Chen, J. Li, L. Li, W. Zhu, L. Wei, Y. Yin, and X. Wang. Experimental and modelling study on the β-phase depletion behaviour under the growth of spinel oxides and alumina in a conicraly coating. *Surface and Coatings Technology*, 429:127859, 2022.

[62] D. Seo, K. Ogawa, Y. Suzuki, K. Ichimura, T. Shoji, and S. Murata. Comparative study on oxidation behavior of selected mcraly coatings by elemental concentration profile analysis. *Applied Surface Science*, 255(5):2581–2590, 2008.

[63] P. Poza and P. S. Grant. Microstructure evolution of vacuum plasma sprayed conicraly coatings after heat treatment and isothermal oxidation. *Surface and Coatings Technology*, 201(6):2887–2896, 2006.

[64] D. Salehi Doolabi, M. R. Rahimipour, M. Alizadeh, S. Pouladi, S.M.M. Hadavi, and M. R. Vaezi. Effect of high vacuum heat treatment on microstructure and cyclic oxidation resistance of hvof-conicraly coatings. *Vacuum*, 135:22–33, 2017.

[65] H. Chen, A. Rushworth, X. Hou, J. He, and H. Guo. Effects of temperature on the β-phase depletion in mcralys: A modelling and experimental study towards designing new bond coat alloys. *Surface and Coatings Technology*, 363:400–410, 2019.

[66] P. Niranatlumpong, C. B. Ponton, and H. E. Evans. The failure of protective oxides on plasma-sprayed nicraly overlay coatings. *Oxidation of Metals*, 53(3/4):241–258, 2000.

[67] W. Brandl, H. J. Grabke, D. Toma, and J. Krüger. The oxidation behaviour of sprayed mcraly coatings. *Surface and Coatings Technology*, 86-87:41–47, 1996.

[68] W. Brandl, D. Toma, J. Krüger, H. J. Grabke, and G. Matthäus. The oxidation behaviour of hvof thermal-sprayed mcraly coatings. *Surface and Coatings Technology*, 94-95:21–26, 1997.

[69] Xiaoju Liu, Teng Wang, Caicai Li, Zhenhuan Zheng, and Qiang Li. Microstructural evolution and growth kinetics of thermally grown oxides in plasma sprayed thermal barrier coatings. *Progress in Natural Science: Materials International*, 26(1):103–111, 2016.

[70] Karl Wefers and Chanakya Misra. *Oxides and Hydroxides of Aluminum*. Alcoa Laboratories, 1987.

[71] M. W. Brumm and H. J. Grabke. The oxidation behaviour of nial-i. phase transformations in the alumina scale during oxidation of nial and nial-cr alloys. *Corrosion Science*, 33(11):1677–1690, 1992.

[72] Dmitry Naumenko, Vladimir Shemet, Lorenz Singheiser, and Willem Josef Quadakkers. Failure mechanisms of thermal barrier coatings on mcraly-type bondcoats associated with the formation of the thermally grown oxide. *Journal of Materials Science*, 44(7):1687–1703, 2009.

[73] F. Traeger, M. Ahrens, R. Vaßen, and D. Stöver. A life time model for ceramic thermal barrier coatings. *Materials Science and Engineering: A*, 358(1-2):255–265, 2003.

[74] W. Lih E. Chang, B. C. Wu, and C. H. Chao. Effects of bond coat preoxidation on the properties of zro2-8wt.% y2o3/ni-22cr-10al-1y thermal-barrier coatings. *Oxidation of Metals*, 36(3-4):221–238, 1991.

[75] Mineaki Matsumoto, Kazuyuki Hayakawa, Satoshi Kitaoka, Hideaki Matsubara, Hiroshi Takayama, Yukio Kagiya, and Yuuji Sugita. The effect of preoxidation atmosphere on oxidation behavior and thermal cycle life of thermal barrier coatings. *Materials Science and Engineering: A*, 441(1-2):119–125, 2006.

[76] V. K. Tolpygo, D. R. Clarke, and K. S. Murphy. The effect of grit blasting on the oxidation behavior of a platinum-modified nickel-aluminide coating. *Metallurgical and Materials Transactions A*, 32(6):1467–1478, 2001.

[77] R. Prescott and M. J. Graham. The formation of aluminum oxide scales on high-temperature alloys. *Oxidation of Metals*, 38(3-4):233–254, 1992.

[78] T. J. Nijdam and W. G. Sloof. Combined pre-annealing and pre-oxidation treatment for the processing of thermal barrier coatings on nicocraly bond coatings. *Surface and Coatings Technology*, 201(7):3894–3900, 2006.

[79] Satoshi Kitaoka, Tomohiro Kuroyama, Mineaki Matsumoto, Rumi Kitazawa, and Yutaka Kagawa. Control of polymorphism in al2o3 scale formed by oxidation of alumina-forming alloys. *Corrosion Science*, 52(2):429–434, 2010.

[80] Jana Joeris, Walter Sebastian Scheld, Sven Uhlenbruck, Yoo Jung Sohn, Doris Sebold, Olivier Guillon, and Robert Vaßen. Preparation of highly durable columnar suspension plasma spray (sps) coatings by pre-oxidation of the conicraly bondcoat. *Coatings*, 13(9):1575, 2023.

[81] Dapeng Zhou, Olivier Guillon, and Robert Vaßen. Development of ysz thermal barrier coatings using axial suspension plasma spraying. *Coatings*, 7(8):120, 2017.

[82] Masahiro Negami, Shinya Hibino, Akihito Kawano, Yoshimichi Nomura, Ryozo Tanaka, and Kenichiroh Igashira. Development of highly durable thermal barrier coating by suppression of thermally grown oxide. In *Volume 6: Ceramics; Controls, Diagnostics and Instrumentation; Education; Manufacturing Materials and Metallurgy*. American Society of Mechanical Engineers, 2017.

[83] Masahiro Negami, Kohei Kyuma, Makoto Azuma, Tomoki Taniguchi, and Yoko Yamabe-Mitarai. Improvement of the durability of thermal barrier coating by pre-oxidation. *Corrosion Science*, 227:111806, 2024.

[84] Masahiro Negami and Yoko Yamabe-Mitarai. The oxidation behaviors of nicocraly coatings after pre-oxidation treatment during high-temperature oxidation at 800 ℃ and 900 ℃. *High Temperature Corrosion of Materials*, 101(3):511–527, 2024.

[85] F. Cernuschi, P. Bianchi, M. Leoni, and P. Scardi. Thermal diffusivity/microstructure relationship in y-psz thermal barrier coatings. *Journal of Thermal Spray Technology*, 8(1):102–109, 1999.

[86] X. Q. Cao, R. Vassen, and D. Stoever. Ceramic materials for thermal barrier coatings. *Journal of the European Ceramic Society*, 24(1):1–10, 2004.

[87] Stephan Stecura. Effects of compositional changes on the performance of a thermal barrier coating system. *Technical report, NASA TM-78976, National Aeronautics and Space Administration*, 1978.

[88] K. D. Sheffler and J. T. DeMasi. Thermal barrier coating life prediction model development. *NASA Contract Report 175087*, 1985.

[89] Robert A. Miller. Current status of thermal barrier coatings — an overview. *Surface and Coatings Technology*, 30(1):1–11, 1987.

[90] Robert Vaßen, Xueqiang Cao, Frank Tietz, Debabrata Basu, and Detlev Stöver. Zirconates as new materials for thermal barrier coatings. *Journal of the American Ceramic Society*, 83(8):2023–2028, 2000.

[91] John R. Nicholls, K. J. Lawson, A. Johnstone, and David Rickerby. Low thermal conductivity eb-pvd thermal barrier coatings. *Materials Science Forum*, 369-372:595–606, 2001.

[92] Srinivasan Raghavan, Hsin Wang, Ralph B. Dinwiddie, Wallace D. Porter, and Merrilea J. Mayo. The effect of grain size, porosity and yttria content on the thermal conductivity of nanocrystalline zirconia. *Scripta Materialia*, 39(8):1119–1125, 1998.

[93] Lech Pawlowski, Didier Lombard, and Pierre Fauchais. Structure-thermal properties—relationship in plasma sprayed zirconia coatings. *Journal of Vacuum Science & Technology A: Vacuum, Surfaces, and Films*, 3(6):2494–2500, 1985.

[94] R. Vaßen, G. Kerkhoff, and D. Stöver. Development of a micromechanical life prediction model for plasma sprayed thermal barrier coatings. *Materials Science and Engineering: A*, 303(1-2):100–109, 2001.

[95] Dongming Zhu and Robert A. Miller. Thermal conductivity and elastic modulus evolution of thermal barrier coatings under high heat flux conditions. *Journal of Thermal Spray Technology*, 9(2):175–180, 2000.

[96] Jérôme Chevalier, Laurent Gremillard, Anil V. Virkar, and David R. Clarke. The tetragonal-monoclinic transformation in zirconia: Lessons learned and future trends. *Journal of the American Ceramic Society*, 92(9):1901–1920, 2009.

[97] Petra A. Langjahr, Rainer Oberacker, and Michael J. Hoffmann. Long-term behavior and application limits of plasma-sprayed zirconia thermal barrier coatings. *Journal of the American Ceramic Society*, 84(6):1301–1308, 2001.

[98] H. G. Scott. Phase relationships in the zirconia-yttria system. *Journal of Materials Science*, 10(9):1527–1535, 1975.

[99] Masahiro Yoshimura. Phase stability of zirconia. *American Ceramic Society Bulletin*, (67):1950–1955, 1988.

[100] Anil V. Virkar and Roger L. K. Matsumoto. Ferroelastic domain switching as a toughening mechanism in tetragonal zirconia. *Journal of the American Ceramic Society*, 69(10), 1986.

[101] Gajawalli V. Srinivasan, Jan-Fong Jue, Shih-Yee Kuo, and Anil V. Virkar. Ferroelastic domain switching in polydomain tetragonal zirconia single crystals. *Journal of the American Ceramic Society*, 72(11):2098–2103, 1989.

[102] Robert Vaßen. *Entwicklung neuer oxidischer Wärmedämmschichten für Anwendungen in stationären und Flug-Gasturbinen: Zugl.: Bochum, Univ., Habil.-Schr., 2004*, volume 33 of *Schriften des Forschungszentrums Jülich Reihe Energietechnik*. Forschungszentrum Zentralbibliothek, Jülich, 2004.

[103] Kuttanellur Muraleedharan, Jandhyala Subrahmanyam, and Sarit B. Bhaduri. Identification of t' phase in zro 2 –7.5 wt% y 2 o 3 thermal–barrier coatings. *Journal of the American Ceramic Society*, 71(5), 1988.

[104] Robert A. Miller, James L. Smialek, and Ralph G. Garlick. Phase stability in plasma-sprayed, partially stabilized zirconia-yttria. In A. H. Heuer and L. W. Hobbs, editors, *Advances in Ceramics - Volume 3*, pages 241–253. American Ceramic Society, Inc. All rights reserved., USA, 1981.

[105] M. Leoni, R.L Jones, and P. Scardi. Phase stability of scandia–yttria-stabilized zirconia tbcs. *Surface and Coatings Technology*, 108-109:107–113, 1998.

[106] Archana Loganathan and Ashutosh S. Gandhi. Effect of phase transformations on the fracture toughness of t′ yttria stabilized zirconia. *Materials Science and Engineering: A*, 556:927–935, 2012.

[107] John R. Nicholls, K. J. Lawson, D. S. Rickerby, and P. Morrell. Advanced processing of tbc's for reduced thermal conductivity. *NATO Workshop on Thermal Barrier Coatings, Aalborg, Denmark*, (AGARD-R-823), 1998.

[108] L. Braginsky, V. Shklover, G. Witz, and H.-P. Bossmann. Thermal conductivity of porous structures. *Journal of Thermal Spray Technology*, 75(9):241, 2007.

[109] Weiguang Chi, Sanjay Sampath, and Hsin Wang. Microstructure–thermal conductivity relationships for plasma–sprayed yttria–stabilized zirconia coatings. *Journal of the American Ceramic Society*, 91(8):2636–2645, 2008.

[110] Sebastian Mihm. *Methodik und ganzheitliche Prozessoptimierung zur Effizienzsteigerung des atmosphärischen Plasmaspritzens von Wärmedämmschichten*. Dissertation, Technische Universität Ilmenau, 2017.

[111] M. Ahrens, S. Lampenscherf, R. Vaßen, and D. Stöver. Sintering and creep processes in plasma-sprayed thermal barrier coatings. *Journal of Thermal Spray Technology*, 13(3):432–442, 2004.

[112] Gwendolin Blandin and Rolf Willi Steinbrecher. *PhD Thesis, Thermomechanisches Verhalten von plasmagespritzten Schichtsystemen zur Wärmedämmung*, volume Berichte des Forschungszentrums Jülich ; 3954 of *Zugleich: Dissertation, Rheinisch-Westfälische Technische Hochschule Aachen, 2002*. 2002.

[113] Jens Igel, Georg Mauer, Olivier Guillon, and Robert Vaßen. Systematic approach to optimize technological and economical aspects of atmospheric plasma sprayed thermal barrier coatings. *Advanced Engineering Materials*, 2023.

[114] Benjamin Bernard, Aurélie Quet, Luc Bianchi, Aurélien Joulia, André Malié, Vincent Schick, and Benjamin Rémy. Thermal insulation properties of ysz coatings: Suspension plasma spraying (sps) versus electron beam physical vapor deposition (eb-pvd) and atmospheric plasma spraying (aps). *Surface and Coatings Technology*, 318:122–128, 2017.

[115] Emine Bakan and Robert Vaßen. Ceramic top coats of plasma-sprayed thermal barrier coatings: Materials, processes, and properties. *Journal of Thermal Spray Technology*, 26(6):992–1010, 2017.

[116] Robert Vaßen. Internal communication: Overall labega project description: Innovative lastflexible beschichtungssysteme für gasturbinen, 2020.

[117] R. Vaßen, F. Traeger, and D. Stöver. New thermal barrier coatings based on pyrochlore/ysz double–layer systems. *International Journal of Applied Ceramic Technology*, 1(4):351–361, 2004.

[118] A. Karaulov and E. I. Zoz. Phase formation in the zro2 - hfo2 - gd2o3 and zro2 - hfo2 - yb2o3 systems. *Refractories and Industrial Ceramics*, 40:479–483, 1999.

[119] Henry Lehmann, Dieter Pitzer, Gerhard Pracht, Robert Vassen, and Detlef Stöver. Thermal conductivity and thermal expansion coefficients of the lanthanum rare–earth–element zirconate system. *Journal of the American Ceramic Society*, 86(8):1338–1344, 2003.

[120] Lei Guo, Hongbo Guo, Hui Peng, and Shengkai Gong. Thermophysical properties of yb2o3 doped gd2zr2o7 and thermal cycling durability of (gd0.9yb0.1)2zr2o7/ysz thermal barrier coatings. *Journal of the European Ceramic Society*, 34(5):1255–1263, 2014.

[121] J. Lian, L. Wang, J. Chen, K. Sun, R. C. Ewing, J. Matt Farmer, and L. A. Boatner. The order–disorder transition in ion-irradiated pyrochlore. *Acta Materialia*, 51(5):1493–1502, 2003.

[122] B. Wuensch. Connection between oxygen-ion conductivity of pyrochlore fuel-cell materials and structural change with composition and temperature. *Solid State Ionics*, 129(1-4):111–133, 2000.

[123] R. M. Leckie, S. Krämer, M. Rühle, and C. G. Levi. Thermochemical compatibility between alumina and zro2–gdo3/2 thermal barrier coatings. *Acta Materialia*, 53(11):3281–3292, 2005.

[124] Dapeng Zhou, Daniel Emil Mack, Emine Bakan, Georg Mauer, Doris Sebold, Olivier Guillon, and Robert Vaßen. Thermal cycling performances of multilayered yttria–stabilized zirconia/gadolinium zirconate thermal barrier coatings. *Journal of the American Ceramic Society*, 103(3):2048–2061, 2020.

[125] Emine Bakan, Daniel E. Mack, Georg Mauer, and Robert Vaßen. Gadolinium zirconate/ysz thermal barrier coatings: Plasma spraying, microstructure, and thermal cycling behavior. *Journal of the American Ceramic Society*, 97(12):4045–4051, 2014.

[126] Robert Vaßen, Emine Bakan, Daniel Mack, Sigrid Schwartz-Lückge, Doris Sebold, Yoo Jung Sohn, Dapeng Zhou, and Olivier Guillon. Performance of ysz and gd2zr2o7/ysz double layer thermal barrier coatings in burner rig tests. *Journal of the European Ceramic Society*, 40(2):480–490, 2020.

[127] Vaishak Viswanathan, Gopal Dwivedi, and Sanjay Sampath. Multilayer, multimaterial thermal barrier coating systems: Design, synthesis, and performance assessment. *Journal of the American Ceramic Society*, 98(6):1769–1777, 2015.

[128] Satyapal Mahade, Nicholas Curry, Stefan Björklund, Nicolaie Markocsan, Per Nylén, and Robert Vaßen. Functional performance of gd2zr2o7/ysz multi-layered thermal barrier coatings deposited by suspension plasma spray. *Surface and Coatings Technology*, 318:208–216, 2017.

[129] Pierre L. Fauchais, Joachim V.R. Heberlein, and Maher I. Boulos. *Thermal Spray Fundamentals*. Springer US, Boston, MA, 2014.

[130] R. Vaßen. Entstehung und auswirkung von spannungen in thermisch gespritzten schichten. *8. GRV Kolloquium Thermisches Spritzen & Laser Cladding*, 2022.

[131] Robert Vaßen, Daniel Emil Mack, Martin Tandler, Yoo Jung Sohn, Doris Sebold, and Olivier Guillon. Unique performance of thermal barrier coatings made of yttria–stabilized zirconia at extreme temperatures (>1500°c). *Journal of the American Ceramic Society*, 104(1):463–471, 2021.

[132] M. Ahrens, R. Vaßen, and D. Stöver. Stress distributions in plasma-sprayed thermal barrier coatings as a function of interface roughness and oxide scale thickness. *Surface and Coatings Technology*, 161(1):26–35, 2002.

[133] George C. Chang, W. Phucharoen, and Robert A. Miller. Behavior of thermal barrier coatings for advanced gas turbine blades. *Surface and Coatings Technology*, 30(1):13–28, 1987.

[134] Hui Dong, Guan-Jun Yang, Cheng-Xin Li, Xiao-Tao Luo, and Chang-Jiu Li. Effect of tgo thickness on thermal cyclic lifetime and failure mode of plasma–sprayed tbc s. *Journal of the American Ceramic Society*, 97(4):1226–1232, 2014.

[135] W. Nowak, D. Naumenko, G. Mor, F. Mor, D. E. Mack, R. Vassen, L. Singheiser, and W. J. Quadakkers. Effect of processing parameters on mcraly bondcoat roughness and lifetime of aps–tbc systems. *Surface and Coatings Technology*, 260:82–89, 2014.

[136] Dapeng Zhou, Daniel Emil Mack, Pintsuk Gerald, Olivier Guillon, and Robert Vaßen. Architecture designs for extending thermal cycling lifetime of suspension plasma sprayed thermal barrier coatings. *Ceramics International*, 45(15):18471–18479, 2019.

[137] Jana Joeris. *Abscheidung kolumnarer Wärmedämmschichten mittels Suspensionsplasmaspritzen (SPS) und Plasma Spray – Physical Vapor Deposition (PS-PVD) Prozess*. Dissertation, Forschungszentrum Jülich GmbH, 2023.

[138] Leonardo Ajdelsztajn, Josep A. Picas, George E. Kim, Fernando L. Bastian, Julie Schoenung, and V. Provenzano. Oxidation behavior of hvof sprayed nanocrystalline nicraly powder. *Materials Science and Engineering: A*, 338(1-2):33–43, 2002.

[139] T. J. Marrow, S. G. Roberts, and A. K. Pearce-Higgins. The brittle/ductile transition in cubic stabilised zirconia. *Journal of the European Ceramic Society*, 14(5):447–453, 1994.

[140] C. Mercer, J.R Williams, D.R Clarke, and A.G Evans. On a ferroelastic mechanism governing the toughness of metastable tetragonal-prime (t ′) yttria-stabilized zirconia. *Proceedings of the Royal Society A: Mathematical, Physical and Engineering Sciences*, 463(2081):1393–1408, 2007.

[141] J. A. Thompson and T. W. Clyne. The stiffness of plasma sprayed zirconia top coats in tbcs. *Proc. UTSC'99, Dusseldorf, DVM*, 1999.

[142] Li-Shuang Wang, Zhi-Yuan Wei, Bo Cheng, Mei-Jun Liu, Guang-Rong Li, Hui Dong, and Guan-Jun Yang. Gradient stiffening induced interfacial cracking and strain tolerant design in thermal barrier coatings. *Ceramics International*, 46(2):2355–2364, 2020.

[143] Robert Vaßen, Franziska Traeger, and Detlev Stöver. Correlation between spraying conditions and microcrack density and their influence on thermal cycling life of thermal barrier coatings. *Journal of Thermal Spray Technology*, 13(3):396–404, 2004.

[144] Matthias Oechsner. *Ein Beitrag zur Lebensdauervorhersage von keramischen Wärmedämmschichten: Zugl.: Karlsruhe, Univ., Diss., 2000*, volume 263 of *Fortschritt-Berichte VDI Reihe 18, Mechanik, Bruchmechanik*. VDI Verl., Düsseldorf, als ms. gedr edition, 2001.

[145] R.G Wellman and J.R Nicholls. Some observations on erosion mechanisms of eb pvd tbcs. *Wear*, 242(1-2):89–96, 2000.

[146] R. G. Wellman and J. R. Nicholls. Erosion, corrosion and erosion–corrosion of eb pvd thermal barrier coatings. *Tribology International*, 41(7):657–662, 2008.

[147] Manfred Peters, Christoph Leyens, Uwe Schulz, and Wolfgang A. Kaysser. Eb-pvd thermal barrier coatings for aeroengines and gas turbines. *Advanced Engineering Materials*, 3(No. 4), 2001.

[148] R. L. Jones. Some aspects of the hot corrosion of thermal barrier coatings. *Journal of Thermal Spray Technology*, 6(1):77–84, 1997.

[149] Stephan Krämer, James Yang, Carlos G. Levi, and Curtis A. Johnson. Thermochemical interaction of thermal barrier coatings with molten cao–mgo–al 2 o 3 –sio 2 (cmas) deposits. *Journal of the American Ceramic Society*, 89(10):3167–3175, 2006.

[150] B. R. Marple, R. S. Lima, C. Moreau, S. E. Kruger, L. Xie, and M. R. Dorfman. Yttria-stabilized zirconia thermal barriers sprayed using n2-h2 and ar-h2 plasmas: Influence of processing and heat treatment on coating properties. *Journal of Thermal Spray Technology*, 16(5-6):791–797, 2007.

[151] Rogerio S. Lima, Bruno M. H. Guerreiro, Nicholas Curry, Matthias Leitner, and Karl Körner. Environmental, economical, and performance impacts of ar-h2 and n2-h2 plasma-sprayed ysz tbcs. *Journal of Thermal Spray Technology*, 29(1-2):74–89, 2020.

[152] Bruno Guerreiro, Rogerio S. Lima, Nicholas Curry, Matthias Leitner, and Karl Körner. The influence of plasma composition in the thermal cyclic performance of yttria-stabilized zirconia (8ysz) thermal barrier coatings (tbcs). *Journal of Thermal Spray Technology*, 30(1-2):59–68, 2021.

[153] Maher I. Boulos, Pierre Fauchais, and Emil Pfender. *Thermal Plasmas*. Springer US, Boston, MA, 1994.

[154] P. Fauchais and M. Vardelle. Plasma spraying: Present and future. *Pure and Applied Chemistry*, 66(6):1247–1258, 1994.

[155] Maher I. Boulos, Pierre L. Fauchais, and Emil Pfender. Plasma-particle momentum, heat and mass transfer. In Maher I. Boulos, Pierre L. Fauchais, and Emil Pfender, editors, *Handbook of Thermal Plasmas*, pages 1–73. Springer International Publishing, Cham, 2018.

[156] Thomas Duda. *Beitrag zum Einsatz diagnostischer Verfahren bei thermischen Spritztechnologien: Zugl.: Dortmund, Univ., Diss., 2002*. Mainz, Aachen, 1. aufl. edition, 2002.

[157] Juraj Ružbarský and Anton Panda. *Plasma and Thermal Spraying*. Springer International Publishing, Cham, 2017.

[158] Y. P. Wan, V. Prasad, G.-X. Wang, S. Sampath, and J. R. Fincke. Model and powder particle heating, melting, resolidification, and evaporation in plasma spraying processes. *Journal of Heat Transfer*, 121(3):691–699, 1999.

[159] S. Sampath, X.Y Jiang, J. Matejicek, A.C Leger, and A. Vardelle. Substrate temperature effects on splat formation, microstructure development and properties of plasma sprayed coatings part i: Case study for partially stabilized zirconia. *Materials Science and Engineering: A*, 272(1):181–188, 1999.

[160] S. Karthikeyan, V. Balasubramanian, and R. Rajendran. Developing empirical relationships to estimate porosity and young's modulus of plasma sprayed ysz coatings. *Applied Surface Science*, 296:31–46, 2014.

[161] B. Z. Janos, E. Lugscheider, and P. Remer. Effect of thermal aging on the erosion resistance of air plasma sprayed zirconia thermal barrier coating. *Surface and Coatings Technology*, 113(3):278–285, 1999.

[162] C. S. Ramachandran, V. Balasubramanian, and P. V. Ananthapadmanabhan. Erosion of atmospheric plasma sprayed rare earth oxide coatings under air suspended corundum particles. *Ceramics International*, 39(1):649–672, 2013.

[163] Satyapal Mahade, Abhilash Venkat, Nicholas Curry, Matthias Leitner, and Shrikant Joshi. Erosion performance of atmospheric plasma sprayed thermal barrier coatings with diverse porosity levels. *Coatings*, 11(1):86, 2021.

[164] Ahmet Kucuk, Rogerio S. Lima, and Christopher C. Berndt. Influence of plasma spray parameters on in–flight characteristics of zro 2 –8 wt% y 2 o 3 ceramic particles. *Journal of the American Ceramic Society*, 84(4):685–692, 2001.

[165] Lech Pawlowski. *The Science and Engineering of Thermal Spray Coatings*. Wiley, 2008.

[166] C. S. Ramachandran, V. Balasubramanian, and P. V. Ananthapadmanabhan. Multiobjective optimization of atmospheric plasma spray process parameters to deposit yttria-stabilized zirconia coatings using response surface methodology. *Journal of Thermal Spray Technology*, 20(3):590–607, 2011.

[167] M. Karger, R. Vaßen, and D. Stöver. Microstructure and thermal cycling behavior of atmospheric plasma sprayed thermal barrier coatings with high segmentation crack densities. In B. R. Marple, M. M. Hyland, Y.-C. Lau, C.-J. Li, R. S. Lima, and G. Montavon, editors, *Thermal Spray 2009: Proceedings from the International Thermal Spray Conference*, International Thermal Spray Conference, pages 34–39. ASM International, 2009.

[168] M. Karger, R. Vaßen, and D. Stöver. Atmospheric plasma sprayed thermal barrier coatings with high segmentation crack densities: Spraying process, microstructure and thermal cycling behavior. *Surface and Coatings Technology*, 206(1):16–23, 2011.

[169] Lech Pawlowski. Suspension and solution thermal spray coatings. *Surface and Coatings Technology*, 203(19):2807–2829, 2009.

[170] Alexandre Guignard, Georg Mauer, Robert Vaßen, and Detlev Stöver. Deposition and characteristics of submicrometer-structured thermal barrier coatings by suspension plasma spraying. *Journal of Thermal Spray Technology*, 21(3-4):416–424, 2012.

[171] Nicholas Curry, Zhaolin Tang, Nicolaie Markocsan, and Per Nylén. Influence of bond coat surface roughness on the structure of axial suspension plasma spray thermal barrier coatings — thermal and lifetime performance. *Surface and Coatings Technology*, 268:15–23, 2015.

[172] Jana Joeris, Ashutosh Tiwari, Steffen Brinckmann, Frank Kurze, Olivier Guillon, and Robert Vaßen. Evaluation of major factors influencing the tbc topcoat formation in axial suspension plasma spraying (sps). *International Journal of Applied Ceramic Technology*, 20(2):884–895, 2023.

[173] J. Oberste Berghaus, S. Bouaricha, J.-G. Legoux, and C. Moreau. Injection conditions and in-flight particle states in suspension plasma spraying of alumina and zirconia nano-ceramics. In E. Lugscheider, editor, *Thermal Spray 2005: Proceedings from the International Thermal Spray Conference*, International Thermal Spray Conference, pages 512–518. Verlag für Schweißen und verwandte Verfahren DVS-Verlag GmbH, 2005.

[174] Nicholas Curry, Kent VanEvery, Todd Snyder, Johann Susnjar, and Stefan Bjorklund. Performance testing of suspension plasma sprayed thermal barrier coatings produced with varied suspension parameters. *Coatings*, 5(3):338–356, 2015.

[175] C. Delbos, J. Fazilleau, V. Rat, J. F. Coudert, P. Fauchais, and B. Pateyron. Phenomena involved in suspension plasma spraying part 2: Zirconia particle treatment and coating formation. *Plasma Chemistry and Plasma Processing*, 26(4):393–414, 2006.

[176] Ashish Ganvir, Rosa Filomena Calinas, Nicolaie Markocsan, Nicholas Curry, and Shrikant Joshi. Experimental visualization of microstructure evolution during suspension plasma spraying of thermal barrier coatings. *Journal of the European Ceramic Society*, 39(2-3):470–481, 2019.

[177] Leszek Latka, Sergey B. Goryachev, Stefan Kozerski, and Lech Pawlowski. Sintering of fine particles in suspension plasma sprayed coatings. *Materials (Basel, Switzerland)*, 3(7):3845–3866, 2010.

[178] L. Łatka. Thermal barrier coatings manufactured by suspension plasma spraying - a review. *Advances in Materials Science*, 18(3):95–117, 2018.

[179] G. Mauer, A. Hospach, N. Zotov, and R. Vaßen. Process conditions and microstructures of ceramic coatings by gas phase deposition based on plasma spraying. *Journal of Thermal Spray Technology*, 22(2-3):83–89, 2013.

[180] Wenting He, Georg Mauer, Yoo Jung Sohn, Alexander Schwedt, Olivier Guillon, and Robert Vaßen. Investigation on growth mechanisms of columnar structured ysz coatings in plasma spray-physical vapor deposition (ps-pvd). *Journal of the European Ceramic Society*, 39(10):3129–3138, 2019.

[181] Georg Mauer, Andreas Hospach, and Robert Vaßen. Process development and coating characteristics of plasma spray-pvd. *Surface and Coatings Technology*, 220:219–224, 2013.

[182] S. Rezanka, G. Mauer, and R. Vaßen. Improved thermal cycling durability of thermal barrier coatings manufactured by ps-pvd. *Journal of Thermal Spray Technology*, 23(1-2):182–189, 2014.

[183] Stefan Rezanka. *Abscheidung von Wärmedämmschichtsystemen mit dem Plasma Spray-Physical Vapor Deposition- (PS-PVD-) Prozess*. Dissertation, Ruhr-Universität Bochum, 2015.

[184] A. Yamauchi. Evaporation of cr2o3 in atmospheres containing h2o. *Oxidation of Metals*, 59(5/6):517–527, 2003.

[185] John P. Collier, Paul W. Keefe, and John K. Tien. The effects of replacing the refractory elements w, nb, and ta with mo in nickel-base superalloys on microstructural, microchemistry, and mechanical properties. *Metallurgical Transactions A*, 17(4):651–661, 1986.

[186] A. G. Evans, D. R. Mumm, J. W. Hutchinson, G. H. Meier, and F. S. Pettit. Mechanisms controlling the durability of thermal barrier coatings. *Progress in Materials Science*, 46(5):505–553, 2001.

[187] Jianhong He. Advanced mcraly alloys with doubled tbc lifetime. *Surface and Coatings Technology*, 448:128931, 2022.

[188] Tao Zhang, Gilles Mariaux, Armelle Vardelle, and Chang-Jiu Li. Numerical analysis of the interactions between plasma jet and powder particles in ps-pvd conditions. *Coatings*, 11(10):1154, 2021.

[189] Andreas Hospach. *Untersuchung zum Thin Film Low Pressure Plasma Spraying (LPPS-TF) Prozess: Zugl.: Bochum, Univ., Diss., 2012*, volume 140 of *Schriften des Forschungszentrums Jülich Reihe Energie & Umwelt*. Forschungszentrum Jülich, Jülich, 2012.

[190] C.R.C. Lima and J. M. Guilemany. Adhesion improvements of thermal barrier coatings with hvof thermally sprayed bond coats. *Surface and Coatings Technology*, 201(8):4694–4701, 2007.

[191] Robert Vaßen, Stephan Giesen, and Detlev Stöver. Lifetime of plasma-sprayed thermal barrier coatings: Comparison of numerical and experimental results. *Journal of Thermal Spray Technology*, 18(5-6):835–845, 2009.

[192] Basel Mulhem and Gunther Schulte. Effect of solid particle characteristics on suspension atomization. *Atomization and Sprays*, 13(2-3):23, 2003.

[193] Régine Rampon, Claudine Filiatre, and Ghislaine Bertrand. Suspension plasma spraying of ypsz coatings: Suspension atomization and injection. *Journal of Thermal Spray Technology*, 17(1):105–114, 2008.

[194] Robert Vaßen, Emine Bakan, and Sigrid Schwartz-Lückge. Influence of substrate removal method on the properties of free-standing ysz coatings. *Coatings*, 11(4):449, 2021.

[195] G02 Committee. Test method for conducting erosion tests by solid particle impingement using gas jets.

[196] Gregory Fabre, Vincent Guipont, Michel Jeandin, M. Boustie, J. P. Cuq-Lelandais, L. Berthe, A. Pasquet, and Jean Yves Guédou. Laser shock adhesion test (lasat) of electron beam physical vapor deposited thermal barrier coatings (eb-pvd tbcs). *Advanced Materials Research*, 278:509–514, 2011.

[197] Vincent Maurel, Vincent Guipont, Mélanie Theveneau, Basile Marchand, and Florent Coudon. Thermal cycling damage monitoring of thermal barrier coating assisted with lasat (laser shock adhesion test). *Surface and Coatings Technology*, 380:125048, 2019.

[198] Vincent Guipont, Michel Jeandin, Sebastien Bansard, Khiam Aik Khor, Mariette Nivard, Laurent Berthe, Jean-Paul Cuq-Lelandais, and Michel Boustie. Bond strength determination of hydroxyapatite coatings on ti-6al-4v substrates using the laser shock adhesion test (lasat). *Journal of biomedical materials research. Part A*, 95(4):1096–1104, 2010.

[199] Lara Mahfouz. *Evolution du système barrière thermique AM1/(Ni,Pt)Al/YPSZ en conditions de fatigue thermo-mécanique*. 2022.

[200] Thibaut De, Jean-Paul Cuq-Lelandais, Michel Boustie, Emilien Lescoute, and Laurent Berthe. Wave propagation and dynamic fracture in laser shock-loaded solid materials. In Andrey Petrin, editor, *Wave Propagation in Materials for Modern Applications*. InTech, 2010.

[201] Jean-Paul Cuq-Lelandais. *Etude du comportement dynamique de matériaux sous choc laser subpicoseconde*. 2010.

[202] G. Bégué, G. Fabre, V. Guipont, M. Jeandin, P. Bilhe, J. Y. Guédou, and F. Lepoutre. Laser shock adhesion test (lasat) of eb-pvd tbcs: Towards an industrial application. *Surface and Coatings Technology*, 237:305–312, 2013.

[203] C. Bolis. Visar pull-back signals as a diagnostic for the laser adherence test applied to copper coating on aluminum substrate. In *AIP Conference Proceedings*, pages 1373–1376. AIP, 2004.

[204] C. Bolis, L. Berthe, M. Boustie, M. Arrigoni, S. Barradas, and M. Jeandin. Physical approach to adhesion testing using laser-driven shock waves. *Journal of Physics D: Applied Physics*, 40(10):3155–3163, 2007.

[205] Vincent Guipont, Geoffrey Bégué, Grégory Fabre, and Vincent Maurel. Buckling and interface strength analyses of thermal barrier coatings combining laser shock adhesion test to thermal cycling. *Surface and Coatings Technology*, 378:124938, 2019.

[206] Lara Mahfouz, Basile Marchand, Vincent Guipont, Florent Coudon, and Vincent Maurel. Driving forces in thermal barrier coatings blistering. *Materialia*, 28:101728, 2023.

[207] N. C. Anderholm. Laser-generated stress waves. *Applied Physics Letters*, 16(3):113–115, 1970.

[208] Hélène Sapardanis, Vincent Maurel, Alain Köster, Steve Duvinage, François Borit, and Vincent Guipont. Influence of macroscopic shear loading on the growth of an interfacial crack initiated from a ceramic blister processed by laser shock. *Surface and Coatings Technology*, 291:430–443, 2016.

[209] F. Traeger, R. Vaßen, K.-H. Rauwald, and D. Stöver. Thermal cycling setup for testing thermal barrier coatings. *Advanced Engineering Materials*, 5(6):429–432, 2003.

[210] J. I. Eldridge, C. M. Spuckler, K. W. Street, and J. R. Markham. Infrared radiative properties of yttria–stabilized zirconia thermal barrier coatings. In Hau-Tay Lin and Mrityunjay Singh, editors, *26th Annual Conference on Composites, Advanced Ceramics, Materials, and Structures: B: Ceramic Engineering and Science Proceedings, Volume 23, Issue 4*, volume 23 of *Ceramic Engineering and Science Proceedings*, pages 417–430. John Wiley & Sons, Inc, Hoboken, NJ, USA, 2002.

[211] Nicholas Curry, Kent VanEvery, Todd Snyder, and Nicolaie Markocsan. Thermal conductivity analysis and lifetime testing of suspension plasma-sprayed thermal barrier coatings. *Coatings*, 4(3):630–650, 2014.

[212] Bing Pan, Kemao Qian, Huimin Xie, and Anand Asundi. Two-dimensional digital image correlation for in-plane displacement and strain measurement: a review. *Measurement Science and Technology*, 20(6):062001, 2009.

[213] F. Hild and S. Roux. Digital image correlation: from displacement measurement to identification of elastic properties – a review. *Strain*, 42(2):69–80, 2006.

[214] T. Niendorf, J. Dadda, D. Canadinc, H. J. Maier, and I. Karaman. Monitoring the fatigue-induced damage evolution in ultrafine-grained interstitial-free steel utilizing digital image correlation. *Materials Science and Engineering: A*, 517(1-2):225–234, 2009.

[215] Thomas Niendorf, Christian Burs, Demircan Canadinc, and Hans J. Maier. Early detection of crack initiation sites in tial alloys during low-cycle fatigue at high temperatures utilizing digital image correlation. *International Journal of Materials Research*, 100(4):603–608, 2009.

[216] Jorge Abanto-Bueno and John Lambros. Investigation of crack growth in functionally graded materials using digital image correlation. *Engineering Fracture Mechanics*, 69(14-16):1695–1711, 2002.

[217] B. Gorny, T. Niendorf, J. Lackmann, M. Thoene, T. Troester, and H. J. Maier. In situ characterization of the deformation and failure behavior of non-stochastic porous structures processed by selective laser melting. *Materials Science and Engineering: A*, 528(27):7962–7967, 2011.

[218] B. Wattrisse, A. Chrysochoos, J.-M. Muracciole, and M. Némoz-Gaillard. Analysis of strain localization during tensile tests by digital image correlation. *Experimental Mechanics*, 41(1):29–39, 2001.

[219] Bernhard Gorny. *Einsatzmöglichkeiten und Anwendungsgrenzen der digitalen Bildkorrelation zur Frühdetektion struktureller und funktioneller Schädigungen und Versagensvorhersage in metallischen Werkstoffen, Werkstoffverbunden und Verbundwerkstoffen*. Dissertaition, Universität Paderborn, Paderborn, 2013.

[220] Michael A. Sutton, Stephen R. McNeill, Jeffrey D. Helm, and Yuh J. Chao. Advances in two-dimensional and three-dimensional computer vision. In Claus E. Ascheron, Hans J. Kölsch, Werner Skolaut, and Pramod K. Rastogi, editors, *Photomechanics*, volume 77 of *Topics in Applied Physics*, pages 323–372. Springer Berlin Heidelberg, Berlin, Heidelberg, 2000.

[221] Sun Yaofeng and John H.L. Pang. Study of optimal subset size in digital image correlation of speckle pattern images. *Optics and Lasers in Engineering*, 45(9):967–974, 2007.

[222] Aurélie Vande Put, Djar Oquab, Eve Péré, Aymeric Raffaitin, and Daniel Monceau. Beneficial effect of pt and of pre-oxidation on the oxidation behaviour of an nicocralyta bond-coating for thermal barrier coating systems. *Oxidation of Metals*, 75(5-6):247–279, 2011.

[223] M. A. Hernández-Rodríguez, V. Monteseguro, A. D. Lozano-Gorrín, F. J. Manjón, J. González-Platas, P. Rodríguez-Hernández, A. Muñoz, V. Lavín, I. R. Martín, and U. R. Rodríguez-Mendoza. Structural, vibrational, and elastic properties of yttrium orthoaluminate nanoperovskite at high pressures. *The Journal of Physical Chemistry C*, 121(28):15353–15367, 2017.

[224] Juddha Thapa, Bo Liu, Steven D. Woodruff, Benjamin T. Chorpening, and Michael P. Buric. Raman scattering in single-crystal sapphire at elevated temperatures. *Applied optics*, 56(31):8598–8606, 2017.

[225] Giovanni Bolelli, Christoph Vorkötter, Luca Lusvarghi, Stefania Morelli, Veronica Testa, and Robert Vaßen. Performance of wear resistant mcraly coatings with oxide dispersion strengthening. *Wear*, 444-445:203116, 2020.

[226] A. El-Turki, G. C. Allen, C. M. Younes, and J. C. C. Day. An investigation of the effect of thermal cycling on plasma–sprayed zirconia/nicocraly thermal barrier coating. *Materials and Corrosion*, 55(1):24–29, 2004.

[227] Anand Kulkarni, A. Vaidya, A. Goland, S. Sampath, and H. Herman. Processing effects on porosity-property correlations in plasma sprayed yttria-stabilized zirconia coatings. *Materials Science and Engineering: A*, 359(1-2):100–111, 2003.

[228] P. Fauchais, J. F. Coudert, M. Vardelle, A. Vardelle, and A. Denoirjean. Diagnostics of thermal spraying plasma jets. In R. Suryanarayanan, editor, *Plasma Spraying: Theory and Applications*, pages 61–92. WORLD SCIENTIFIC, 1993.

[229] S. Karthikeyan, V. Balasubramanian, and R. Rajendran. Developing empirical relationships to estimate porosity and microhardness of plasma-sprayed ysz coatings. *Ceramics International*, 40(2):3171–3183, 2014.

[230] Ashok K. Ray and Rolf W. Steinbrech. Crack propagation studies of thermal barrier coatings under bending. *Journal of the European Ceramic Society*, 19(12):2097–2109, 1999.

[231] Rogerio S. Lima. Perspectives on thermal gradients in porous zro2-7–8 wt.% y2o3 (ysz) thermal barrier coatings (tbcs) manufactured by air plasma spray (aps). *Coatings*, 10(9):812, 2020.

[232] Dianying Chen, Riston Rocchio-Heller, and Christopher Dambra. Segmented thermal barrier coatings for id and od components using the sinplexpro plasma torch. *Journal of Thermal Spray Technology*, 28(7):1664–1673, 2019.

[233] Dianying Chen, Christopher Dambra, and Mitchell Dorfman. Deposition, microstructure and thermal cycling performance of strain-tolerant thermal barrier coatings. *Journal of Thermal Spray Technology*, 32(4):1108–1114, 2023.

[234] H. E. Eaton and R. C. Novak. Particulate erosion of plasma-sprayed porous ceramic. *Surface and Coatings Technology*, 30(1):41–50, 1987.

[235] Nicholas Curry, Satyapal Mahade, Abhilash Venkat, and Shrikant Joshi. Erosion performance of suspension plasma spray thermal barrier coatings — a comparison with state of art coatings. *Surface and Coatings Technology*, 437:128311, 2022.

[236] Rogerio S. Lima, Bruno M. H. Guerreiro, and Maniya Aghasibeig. Microstructural characterization and room-temperature erosion behavior of as-deposited sps, eb-pvd and aps ysz-based tbcs. *Journal of Thermal Spray Technology*, 28(1-2):223–232, 2019.

[237] F. Cernuschi, L. Lorenzoni, S. Capelli, C. Guardamagna, M. Karger, R. Vaßen, K. von Niessen, N. Markocsan, J. Menuey, and Carlo Giolli. Solid particle erosion of thermal spray and physical vapour deposition thermal barrier coatings. *Wear*, 271(11-12):2909–2918, 2011.

[238] Caroline Wännman. *Erosion Behaviour of Thermal Barrier Coatings*. 2021.

[239] P. Fauchais, M. Vardelle, S. Goutier, and A. Vardelle. Key challenges and opportunities in suspension and solution plasma spraying. *Plasma Chemistry and Plasma Processing*, 35(3):511–525, 2015.

[240] Robert Vaßen, Holger Kaßner, Georg Mauer, and Detlev Stöver. Suspension plasma spraying: Process characteristics and applications. *Journal of Thermal Spray Technology*, 19(1-2):219–225, 2010.

[241] Madhura Bellippady, Manon Florent, Stefan Björklund, Xin Hai Li, Frykholm Robert, Bjorn Kjellman, Shrikant Joshi, and Nicolaie Markocsan. Characteristics and performance of suspension plasma sprayed thermal barrier coatings on additively manufactured superalloy substrates. *Surface and Coatings Technology*, 472:129926, 2023.

[242] D. Renusch, M. Schorr, and M. Schütze. The role that bond coat depletion of aluminum has on the lifetime of aps–tbc under oxidizing conditions. *Materials and Corrosion*, 59(7):547–555, 2008.

[243] Emine Bakan, Daniel Emil Mack, Georg Mauer, Robert Mücke, and Robert Vaßen. Porosity–property relationships of plasma–sprayed gd 2 zr 2 o 7 / ysz thermal barrier coatings. *Journal of the American Ceramic Society*, 98(8):2647–2654, 2015.

[244] M.J.D. Rushton, Christopher R. Stanek, Antony R. Cleave, Blas P. Uberuaga, Kurt E. Sickafus, and Robin W. Grimes. Simulation of defects and defect processes in fluorite and fluorite related oxides: Implications for radiation tolerance. *Nuclear Instruments and Methods in Physics Research Section B: Beam Interactions with Materials and Atoms*, 255(1):151–157, 2007.

[245] Ulrich Bast and Eckart Schumann. Development of novel oxide materials for tbc's. In Hau-Tay Lin and Mrityunjay Singh, editors, *26th Annual Conference on Composites, Advanced Ceramics, Materials, and Structures: B: Ceramic Engineering and Science Proceedings, Volume 23, Issue 4*, volume 23 of *Ceramic Engineering and Science Proceedings*, pages 525–532. John Wiley & Sons, Inc, Hoboken, NJ, USA, 2002.

[246] Martin Frommherz, Alfred Scholz, Matthias Oechsner, Emine Bakan, and Robert Vaßen. Gadolinium zirconate/ysz thermal barrier coatings: Mixed-mode interfacial fracture toughness and sintering behavior. *Surface and Coatings Technology*, 286:119–128, 2016.

[247] J. S. Lyons, J. Liu, and M. A. Sutton. High-temperature deformation measurements using digital-image correlation. *Experimental Mechanics*, 36(1):64–70, 1996.

[248] Bing Pan, Dafang Wu, and Yong Xia. High-temperature deformation field measurement by combining transient aerodynamic heating simulation system and reliability-guided digital image correlation. *Optics and Lasers in Engineering*, 48(9):841–848, 2010.

[249] Bing Pan, Dafang Wu, and Liping Yu. Optimization of a three-dimensional digital image correlation system for deformation measurements in extreme environments. *Applied optics*, 51(19):4409–4419, 2012.

[250] T. S. CHENG, C.-Y. WU, Y.-H. LI, and Y.-C. CHAO. Chemiluminescence measurements of local equivalence ratio in a partially premixed flame. *Combustion Science and Technology*, 178(10-11):1821–1841, 2006.

[251] Steven M. Shepard. Advances in pulsed thermography. In Andres E. Rozlosnik and Ralph B. Dinwiddie, editors, *Thermosense XXIII*, SPIE Proceedings, pages 511–515. SPIE, 2001.

List of Figures

List of Tables

Acknowledgements

I would like to express my heartfelt gratitude to everyone who supported, guided, and encouraged me throughout my journey toward completing this dissertation. Each contribution — whether professional, personal, or emotional — played a vital role in the success of this work.
First and foremost, I am deeply thankful to my doctoral supervisor, Prof. Dr. Robert Vaßen, whose professional expertise, constant support, and trust in my abilities, has given me the opportunity to successfully complete this work. His open-door policy led to numerous valuable discussions in which he motivated and helped me to make decisive progress with constructive criticism, helpful advice, and anecdotes.
I would also like to sincerely thank my second supervisor, Dr. Vincent Guipont, for his kind review of my work and for enabling me to spend time researching at the Centre des Matériaux of Mines ParisTech. Our discussions were highly informative and provided me with important input for the preparation of my dissertation.
Special thanks go to Projektträger Jülich, which laid the foundation for this work through its coordination of the LABEGA project, which was funded by the Federal Ministry of Economic Affairs and Climate Action (BMWK), Germany, within the framework of the 7th Energy Research Program (FKZ 03EE5045A). Furthermore, I would also like to thank the project partners at Oerlikon Metco, Mines ParisTech, and Safran for their constructive and trusting cooperation.
My colleagues at IMD-2 and IMD-1 also played an essential role in my doctoral journey. Whether in the lab, in the office, during coffee and lunch breaks, or while commuting between Aachen and the research center, I was fortunate to be surrounded by so many supportive individuals. Though too many to name here, please know that I am sincerely grateful for every encounter, whether it was a professional exchange, overcoming small and large challenges of everyday research life together, motivating conversations, or private chats.
I would also like to express my special thanks to Maike, Johannes, and Tim, for taking the time to proofread parts of my work and thereby helping to enhance its quality. My gratitude also extends to the entire XYZ department — particularly Daniel, Martin, Karl-Heinz, Frank, and Ralf — for their continuous support. And of course, a big thank you to my office colleagues Alex and Walter from “Room 152”, the best office in the world. You have given me a great time in which we had a lot of fun, but also had constructive and motivating conversations.
I would also like to express my special thanks to Maike, Johannes, and Tim, for taking the time to proofread parts of my work and thereby helping to enhance its quality. My gratitude also extends to the entire department of "Materials for High-Temperature Technologies" of the IMD-2 — particularly Daniel, Martin, Karl-Heinz, Frank, and Ralf — for their continuous support. And of course, a big thank you to my office colleagues Alex and Walter from “Room 152”, the best office in the world. You have given me a great time in which we had a lot of fun, but also had constructive and motivating conversations.
In addition, I am deeply grateful to my family, who have always believed in me and offered their unwavering support. Your encouragement has been very important to me. I also want to thank my friends for their patience, understanding, and the much-needed distractions outside of academic life.
Last but certainly not least, my heartfelt thanks go to my partner, Hannah. Your love, patience, and constant encouragement were invaluable throughout this entire time. Without your support, your listening ear, and your confidence in me, especially during the difficult times, this would have been a far more challenging journey.

Appendix

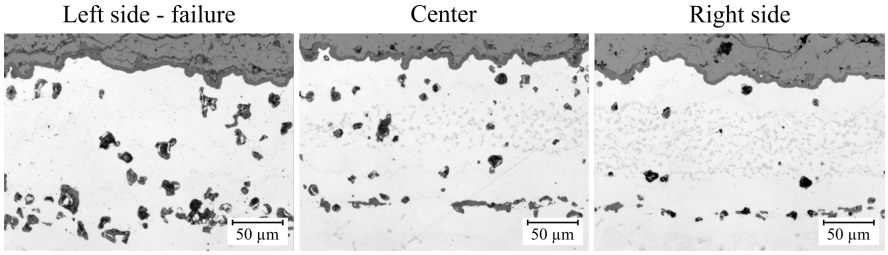

Fig. 7.1 **AF1:** Cross-sections of bond coat and TGO with depletion zones of the reference system

Run	Factor 1 (C), current [A]	Factor 2 (SD), spraying distance [mm]	Factor 3 (H), hydrogen [nlpm]
1	400	190	5
2	450	190	6.5
3	450	220	5
4	450	190	6.5
5	500	160	6.5
6	400	220	6.5
7	450	190	6.5
8	450	160	8
9	500	220	6.5
10	450	220	8
11	400	160	6.5
12	500	190	5
13	400	190	8
14	500	190	8
15	450	160	5

Fig. 7.2 **AF2:** Experimental matrix according to the Box–Behnken design optimizing the APS process

No [#]	Power [kW]	Spray Distance [mm]	Feed Rate [g/min]	Robot speed [mm/s]	Passes [#]	Cooling
1	51	120	100	1000	8	B
2	51	120	100	1000	8	B + F
3	51	120	50	1000	16	B
4	51	120	50	1000	16	B + F
5	72	70	50	500	8	B
6	72	70	50	500	8	B + F
7	72	70	100	500	4	B
8	72	70	100	500	4	B + F

Fig. 7.3 AF3: Experimental plan for DVC development using long injector holder (B = back side substrate cooling, B + F = back and front side cooling at the same time)

No [#]	Power [kW]	Spray Distance [mm]	Feed Rate [g/min]	Robot speed [mm/s]	Passes [#]
9	64	70	100	500	4
10	64	70	50	500	8
11	51	70	50	1000	16
12	51	70	100	1000	8
13	51	120	100	1000	8
14	51	120	50	1000	16
15	64	120	50	500	8
16	64	120	100	500	4

Fig. 7.4 AF4: Experiment plan for DVC development using short injector holder (back side cooling only)

Name	Current [A]	Argon	Hydrogen	Standoff	Feedrate	Robot speed	Passes
DVC1	575	60	7,5	75	60	1000	18
DVC2	600	80	10	110	35	350	16
DVC3	675	80	10	110	35	350	16
DVC4	525	80	10	110	35	350	16

Fig. 7.5 AF5: Experiment plan for DVC using Metco 214A

Band / Volume 652
Modelling Secondary Circulation in Convective Boundary Layer Using Large Eddy Simulation
L. Zhang (2024), 84 pp
ISBN: 978-3-95806-799-8

Band / Volume 653
Optionen zur Umsetzung der Klimaschutzziele im Verkehrssektor
S. Kraus (2025), XI, 317 pp
ISBN: 978-3-95806-802-5

Band / Volume 654
Modellierung der flächendifferenzierten Grundwasserneubildung für Schleswig-Holstein im Beobachtungszeitraum 1961 – 2021 und für Klimaszenarien bis 2100
I. McNamara, B. Tetzlaff, F. Wendland, T. Wolters (2025), 191 pp
ISBN: 978-3-95806-803-2

Band / Volume 655
Entwicklung alternativer Brenngaselektroden für die Hochtemperatur-Elektrolyse
F. E. Winterhalder (2025), vii, 161 pp
ISBN: 978-3-95806-805-6

Band / Volume 656
Oxide-based All-Solid-State Batteries for and from Recycling Processes
V. M. Kiyek (2025), viii, 128 pp, xix
ISBN: 978-3-95806-806-3

Band / Volume 657
Investigation of current and future anthropogenic chemical regimes in simulation chamber experiments
M. Färber (2025), 213 pp
ISBN: 978-3-95806-809-4

Band / Volume 658
Dynamischer Betrieb von Polymer-Elektrolyt-Membran Wasserelektrolyseuren
E. Rauls (2025), XIV, 239 pp
ISBN: 978-3-95806-811-7

Band / Volume 659
Pore-scale reactive transport modeling in cementitious materials: Development and application of a high-performance computing code based on the Lattice-Boltzmann method
S. Rohmen (2025), X, 295 pp
ISBN: 978-3-95806-812-4

Band / Volume 660
Recyclingmöglichkeiten für die Keramikkomponenten einer Festoxidzelle
S. Sarner (2025), VIII, 122 pp
ISBN: 978-3-95806-816-2

Band / Volume 661
Methodological Approach Enabling the Two-phase Flow Investigation in Alkaline Electrolysis under Demanding Conditions
S. Renz (2025), IX, 252 pp
ISBN: 978-3-95806-821-6

Band / Volume 662
Variable renewable energy potential estimates based on high-resolution regional atmospheric modelling over southern Africa
S. Chen (2025), XIII, 141 pp
ISBN: 978-3-95806-822-3

Band / Volume 663
Advances in Understanding Nitrate Aerosol Formation and the Implications for Atmospheric Radiative Balance
A. Milousis (2025), 195 pp
ISBN: 978-3-95806-823-0

Band / Volume 664
Optimization of NaSICON-type lithium-ion conductors for solid-state batteries
A. Loutati (2025), viii, 104 pp
ISBN: 978-3-95806-824-7

Band / Volume 665
Innovative Plasma Sprayed Thermal Barrier Coatings for Enhanced Flexibility in Gas Turbine Operation
J. Igel (2025), V, 153, XXXVI pp
ISBN: 978-3-95806-827-8

Energie & Umwelt / Energy & Environment
Band / Volume 665
ISBN 978-3-95806-827-8

Mitglied der Helmholtz-Gemeinschaft

JÜLICH
Forschungszentrum